N73-11970

NASA CR-120926

HYDROGEN FILM/CONDUCTIVE COOLING

CASE FILE COPY

by

R. L. Ewen

Aerojet Liquid Rocket Company
Sacramento, California 95812

prepared for

NATIONAL AERONAUTICS AND SPACE ADMINISTRATION

NASA Lewis Research Center
Contract NAS 3-14343
E. A. Edelman, Project Manager

Requests for copies of this report should be referred to

National Aeronautics and Space Administration
Scientific and Technical Information Facility
P.O. Box 33
College Park, Md. 20740

1. Report No. NASA CR-120926	2. Government Accession No.	3. Recipient's Catalog No.
4. Title and Subtitle HYDROGEN FILM/CONDUCTIVE COOLING		5. Report Date November 1972
		6. Performing Organization Code
7. Author(s) R. L. Ewen		8. Performing Organization Report No.
9. Performing Organization Name and Address Aerojet Liquid Rocket Company Sacramento, California		10. Work Unit No.
		11. Contract or Grant No. NAS 3-14343
12. Sponsoring Agency Name and Address National Aeronautics and Space Administration Washington, D. C. 20546		13. Type of Report and Period Covered Contractor Report
		14. Sponsoring Agency Code

15. Supplementary Notes

Project Manager, E. A. Edelman, NASA Lewis Research Center, Cleveland, Ohio

16. Abstract

Small scale nozzle tests using heated nitrogen were run to obtain effectiveness and wall heat transfer data with hydrogen film cooling. Effectiveness data are compared with a new entrainment model developed from previous plane, unaccelerated flow results; present results indicate significant effects due to flow turning and acceleration. With injection velocity effects accounted for explicitly, heat transfer correlation coefficients were found to be the same with and without film cooling when properties are evaluated at an appropriate reference temperature for the local gas composition defined by the coolant effectiveness.

A design study for an O_2/H_2 application with 300 psia (207 N/cm^2) chamber pressure and 1500 lbs (6670 N) thrust indicates an adiabatic wall design requires 4-5 percent of the total flow as hydrogen film cooling. Internal regenerative cooling designs were found to offer no reduction in coolant requirements.

17. Key Words (Suggested by Author(s)) Film Cooling Heat Transfer	18. Distribution Statement Unclassified - Unlimited

19. Security Classif. (of this report) Unclassified	20. Security Classif. (of this page) Unclassified	21. No. of Pages 219	22. Price* $3.00

FOREWORD

The work described herein was conducted by the Aerojet Liquid Rocket Company under NASA Contract NAS 3-14343; the period of performance was 29 June 1970 through 30 September 1971. E. A. Edelman, NASA-Lewis Research Center, was the NASA Project Manager.

This report was originally issued as Aerojet Liquid Rocket Company Report 14343-F, 29 October 1971.

TABLE OF CONTENTS

Page

I. Summary 1

II. Introduction 3

III. Test Hardware 5

- A. Coolant Injectors 5
- B. Test Nozzles 7
- C. Turbulence Screens 9
- D. Related Hardware 10

IV. Test Facility and Instrumentation 11

V. Laboratory Testing 16

- A. Injector Flow Distribution Tests 21
- B. Hot-Wire Anemometer Test 23
- C. Film Cooling Checkout Tests 25
- D. Ambient Hydrogen Tests 29
- E. Cold Hydrogen Tests 31
- F. Rectangular Geometry Test 32
- G. Liquid Hydrogen Tests 33

VI. Analytical Model 37

- A. Film Coolant Effectiveness 37
- B. Heat Transfer 43
- C. Computer Program 44

VII. Correlation and Discussion of Laboratory Test Data 46

- A. Film Coolant Effectiveness 46
- B. Heat Transfer Data 56

VIII. Design Feasibility Investigation 62

- A. Adiabatic Walls 62
- B. Internal Regenerative Cooling 71

IX. Conclusions 78

- A. Laboratory Tests 78
- B. Design Feasibility Investigation 79

References 81

APPENDICES

Appendix		Page
A	Gas Film Cooling Entrainment Model	83
B	Data Analysis	89
C	Nomenclature	107
D	Distribution	113

LIST OF TABLES

Table		Page
I	Fluid Temperature Thermocouples	14
II	Laboratory Test Summary	17
III	Test Condition Summary	19
IV	Test Data Summary	20
V	Film Cooling Data Parameters	38
VI	Comparison of Cylindrical Combustion Chamber Configurations	69
VII	Heat Loss Coefficients	93
VIII	Cylindrical Chamber Heating Transient - Test 3	96
IX	Cylindrical Chamber Cooling Transient - Test 3	98
X	Electrical Heating Data - Test 5A	101
XI	Cylindrical Chamber Effectiveness Data - Test 7A	103

LIST OF FIGURES

Figure		Page
1	Test Assembly	129
2	Film Coolant Slot Design - Ambient Hydrogen	130
3	Film Coolant Slot Design - 140°R Hydrogen	131
4	Film Coolant Injector Assembly	132
5	Film Coolant Injector - Inner Ring	133
6	Film Coolant Injector - Outer Ring	134
7	Inner Ring - 0.015 in. Injector	135
8	Outer Ring - 0.015 in. Injector	136
9	0.060 in. Film Coolant Slot	137
10	0.015 in. Film Coolant Slot	138
11	Square Injector Assembly	139
12	Square Injector - Plate No. 1 Assembly	140
13	Square Injector - Plate No. 2 Assembly	141
14	Five-Channel Metering Section and Cover Plate	142
15	Four-Channel Metering Section and Cover Plate	143
16	Square Injector Coolant Slot	144
17	Liquid Coolant Injector Design	145
18	Liquid Coolant Injector	146
19	Cylindrical Chamber	147
20	Conical Chamber	148
21	Rectangular Chamber Assembly	149
22	Rectangular Chamber	150
23	Rectangular Test Assembly Components	151
24	Adapter Housing	152
25	Flow Transition Sleeve	153
26	Overall View of the Test Area	154
27	Test System Schematic Diagram	155
28	Liquid Hydrogen Vessel and Transfer Line	156
29	Liquid Hydrogen Test Setup	157

LIST OF FIGURES (cont.)

Figure		Page
30	Spring Loaded Thermocouple	158
31	Test Assembly Before Insulation	159
32	Cylindrical Chamber Thermocouple Locations	160
33	Conical Chamber Thermocouple Locations	161
34	Rectangular Chamber Thermocouple Locations	162
35	Injector Flow Distribution Test Setup	163
36	Axial Position of Probe Without Sleeve	164
37	Flow Distribution - 0.060 in. Slot (No Sleeve)	165
38	Flow Distribution - 0.060 in. Slot (With Sleeve)	166
39	Flow Distribution Test of 0.015 in. Injector	167
40	Flow Distribution - 0.015 in. Slot	168
41	Square Injector Flow Distribution	169
42	Liquid Injector Water Flow Test	170
43	Liquid Injector Two-Phase Flow Test	171
44	Test Procedure Schematic	172
45	Test Assembly with Conical Chamber	173
46	Density Ratio Correlation	174
47	Velocity Ratio Correlating Function	175
48	Gas Film Cooling Effectiveness Correlation for Plane, Unaccelerated Flow	176
49	Mixing Layer Profile Shape Factors	177
50	Gas Film Cooling Program	178
51	Comparison of Predicted and Measured Adiabatic Wall Temperatures	179
52	Cylindrical Chamber Adiabatic Wall Temperatures - Test 5	180
53	Effect of Velocity Ratio, Coolant Reynolds Number and Slot Height on Coolant Effectiveness - Cylindrical Section	181
54	Effect of Velocity Ratio and Coolant Reynolds Number on Coolant Effectiveness - Nozzle Section	182
55	Entrainment Fraction Multipliers - Cylindrical Chamber Tests 3 and 4	183

LIST OF FIGURES (cont.)

Figure		Page
56	Entrainment Fraction Multipliers - Cylindrical Chamber Test 5	184
57	Entrainment Fraction Multiplier - Cylindrical Chamber	185
58	Film Coolant Effectiveness - Cylindrical Chamber, Ambient Coolant	186
59	Comparison of Conical and Cylindrical Chamber Adiabatic Wall Temperatures	187
60	Conical Chamber Adiabatic Wall Temperatures	188
61	Entrainment Fraction Multiplier - Conical Chamber	189
62	Film Coolant Effectiveness - Conical Chamber	190
63	Film Coolant Effectiveness - Rectangular Chamber	191
64	Wall Temperatures with Cold Gaseous Coolant	192
65	Entrainment Fraction Multipliers - Tests 8 and 10	193
66	Wall Temperatures with Supercritical Liquid Hydrogen	194
67	Wall Temperatures with Subcritical Liquid Hydrogen	195
68	Entrainment Fraction Multipliers - Nozzle 3, Ref. 12	196
69	Entrainment Fraction Multiplier Due to Flow Turning	197
70	Heat Transfer Coefficients Without Film Cooling - Cylindrical Chamber Tests 3, 4 and 5A	198
71	Heat Transfer Correlation Coefficients Without Film Cooling - Cylindrical Chamber Tests 3, 4, and 5A	199
72	Heat Transfer Coefficients with Film Cooling - Cylindrical Chamber Tests 3 and 5	200
73	Heat Transfer Correlation Coefficients with Film Cooling - Cylindrical Chamber Tests 3 and 5	201
74	Heat Transfer Correlation Coefficients - Cylindrical Chamber Test 6	202
75	Heat Transfer Correlation Coefficients - 0.015 in. Slot Without Coolant	203
76	Heat Transfer Correlation Coefficients - 0.015 in. Slot, Ambient Coolant	204
77	Heat Transfer Correlation Coefficients - 0.015 in. Slot, Cold Coolant	205

LIST OF FIGURES (cont.)

Figure		Page
78	Heat Transfer Coefficients Without Film Cooling - Conical Chamber	206
79	Heat Transfer Correlation Coefficients Without Film Cooling - Conical Chamber	207
80	Heat Transfer Coefficients With Film Cooling - Conical Chamber	208
81	Heat Transfer Correlation Coefficients With Film Cooling - Conical Chamber	209
82	Velocity Decay Function - Cylindrical Chamber	210
83	Design Study Chamber Contours	211
84	Design Study Entrainment Fraction Multipliers	212
85	Adiabatic Wall Coolant Requirements - Throat Temperature Limit	213
86	Adiabatic Wall Coolant Requirements - 1800°F Maximum Temperature	214
87	Adiabatic Wall Temperature Axial Variation	215
88	Adiabatic Wall Coolant Requirements With a Sleeve	216
89	Effect of Velocity Ratio on Coolant Flow Requirements	217
90	Performance Loss due to Film Cooling	218
91	Adiabatic Wall Throat Temperature Variation with Coolant Flow	219
92	Effect of Overall Mixture Ratio on Coolant Flow and Performance	220
93	Adiabatic Wall Coolant Requirement Variation with Combustion Chamber Length	221
94	Internal Regenerative Cooling Node Network	222
95	Comparison of Beryllium and Copper Chambers	223
96	Beryllium Chamber Axial Temperature Variation	224
97	Copper Chamber Axial Temperature Variation	225
98	Effect of Wall Thickness on Copper Chambers	226
99	Entrainment Model Schematic	227

LIST OF FIGURES (cont.)

Figure		Page
100	Wall Temperature Reduction due to Heat Loss	228
101	Determination of Chamber Pressure Time Constant	229
102	Test Section Electrical Resistance - High Temperature Range	230
103	Test Section Electrical Resistance - Low Temperature Range	231
104	Correlation of the Relative AC RMS Voltage	232

I. SUMMARY

Adiabatic wall temperatures and heat fluxes from non-adiabatic walls were measured with hydrogen film cooling in three convergent-divergent nozzle configurations using 900°F (755 K) nitrogen as the primary flow. Heat fluxes were measured in two ways: during wall temperature transients with the thin nozzle wall acting as a calorimeter, and by electrically heating the cylindrical inlet section of one of the nozzles. Heat fluxes without film cooling were measured for comparison. The electrically heated nozzle had a short convergent section, the second nozzle had a very short cylindrical inlet and a long conical convergent section, and the third provided a rectangular cross-section; their contraction ratios and the axial distances between the injection point and throat were identical. Tests with gaseous coolant investigated the effects of coolant/core injection velocity ratio, density ratio, coolant slot height, coolant Reynolds number and chamber configuration. Liquid film cooling tests were conducted at both supercritical and subcritical pressures.

Adiabatic wall temperatures are interpreted in terms of a coolant effectiveness based on total enthalpy and are compared with a new gas film cooling model in which the entrainment flux of core flow into a mixing layer containing all the film coolant is represented as a fraction of the core axial mass velocity. A correlation for this entrainment fraction was developed from five sets (four coolants) of existing flat plate effectiveness data; it was found to be independent of the distance from the injection point. Present results confirm the entrainment fraction dependence on injection velocity ratio, but indicate a lesser dependence on coolant Reynolds number. However, the cylindrical section values are about 60 percent greater than the flat plate results, presumably due to the 4 percent core turbulence intensity and a small wall discontinuity between the coolant injection ring and the test section. In addition, significant turning and acceleration effects on the entrainment fraction were observed in the nozzle sections; the turning effects are attributed to the imbalance in centrifugal forces caused by density differences between the coolant and core flows. Entrainment in the expansion section was very small, so that the imperfect recovery of kinetic energy caused the adiabatic wall temperature to decrease. Wall temperature measurements with cold gas and liquid film cooling were affected by heat transfer from the chamber forward flange, and nitrogen condensation in the mixing layer occurred during subcritical liquid testing.

Heat transfer coefficients based on the adiabatic wall enthalpy indicate that except for injection velocity effects near the injection point, correlating coefficients are the same with and without gas film cooling when properties are evaluated for the local gas composition at the wall at the arithmetic mean of the adiabatic and non-adiabatic wall temperatures. Local gas compositions are determined by analogy from the coolant effectiveness.

A design feasibility study for a 300 psia (207 N/cm^2) chamber pressure application with 1500 lbs (6670 N) thrust and O_2/H_2 propellants indicates an adiabatic wall design requires 4-5 percent of the total flow as hydrogen film coolant and results in minor performance losses. Internal regenerative cooling designs were also investigated, but were found to offer no advantage relative to adiabatic wall designs.

II. INTRODUCTION

The purpose of the present program was to obtain hydrogen film cooling effectiveness and heat transfer data in both axisymmetric and rectangular nozzle configurations, using both gaseous and liquid coolant. These results were then to be applied to oxygen/hydrogen thrust chambers to investigate the feasibility of adiabatic wall and internal regenerative cooling designs. In the latter concept heat is conducted axially through the chamber wall from the throat region to the low temperature film coolant at the forward end of the chamber. This concept has been demonstrated for low pressure, low thrust applications with earth storable propellants using liquid fuel film cooling; the present program considers the feasibility of extending this concept to hydrogen and to gas film cooling. The Space Shuttle APS application was selected for the chamber design studies.

Previous laboratory film cooling experimenta have provided ample effectiveness data for plane, unaccelerated flow, although in only one instance was hydrogen used as the coolant; in the latter case the effectiveness data were well below the range of liquid rocket design interest due to the low coolant flow rates employed. A limited amount of film cooling data are available for nozzle configurations, but not enough to interpret and correlate possible flow turning and acceleration effects. Heat transfer data with film cooling have been obtained in a few instances, but not for foreign gas cooling with significant temperature differences between the core and coolant flows.

In this program small scale laboratory tests using heated nitrogen as the core flow in thin-walled nozzle configurations were utilized to measure both adiabatic wall temperatures and heat transfer with hydrogen film cooling. Heat transfer data were obtained in two ways: by electrically heating the cylindrical inlet section of one of the nozzles and by using the wall as a calorimeter during thermal transients. The effects of injection velocity ratio, density ratio, slot height, coolant Reynolds number and convergent section configuration were investigated for gaseous coolant in axisymmetric nozzles. One rectangular nozzle was tested with gaseous coolant, and one axisymmetric nozzle was tested with liquid hydrogen at both subcritical and supercritical pressures.

Another objective of the present effort was to develop a fundamental framework or analytical model for correlating existing film cooling data and the data to be obtained herein which could readily be extended to account for the chemical reactions, turbulence intensity and coolant injection configurations associated with actual rocket engine application. The laboratory tests with gaseous coolant were to provide idealized continuous slot injection for the sake of generality.

III. TEST HARDWARE

The type of test assembly used in all film cooling tests is illustrated in Figure 1. It consists of an adapter section, a film coolant injector and a test nozzle or chamber. The adapter section provided for flow transition from the nitrogen supply line to the inside diameter of the film coolant injector. Use of a split sleeve in the adapter allowed a turbulence screen to be located between sleeves (View B) or at the downstream end of the adapter. Other test configurations, using a conical chamber or a rectangular flow geometry, employed component assemblies analogous to that of Figure 1; however, the conical and rectangular chambers did not provide for electrical heating. A similar test assembly was used in a hot-wire anemometer test, except the film coolant injector was replaced by an anemometer holder which located the anemometer axially at a position corresponding to the coolant slot exit. Design and fabrication details for key components in the various test assemblies are presented in this section.

A. COOLANT INJECTORS

Four film coolant injectors were utilized in the laboratory test program: a circular injector for ambient coolant, a circular injector for cold gaseous coolant, a square injector with the same slot height as the first circular unit, and a liquid hydrogen injector. The second circular injector was also used with ambient coolant to determine the effect of slot height independent of the effect of density ratio. The procedure used for selection of slot heights for the ambient and cold gas film coolant injectors is shown in Figures 2 and 3, respectively. Slot heights required to obtain a range of film coolant effectiveness at the throat are shown for a coolant/core injection velocity ratio of 1.1. These curves are based on the most appropriate effectiveness data considered in developing the flat plate correlation of Section VI,A and applying the density ratio correction of that correlation. An injection velocity ratio of 1.1 is near the middle of the range tested, provides an effectiveness near the maximum and is close to the optimum design value. In order to account for anticipated coolant injection and core turbulence intensity effects the dimensionless lengths corresponding to each effectiveness were divided by 1.5. To simulate a design application, it would be desirable to test at a throat effectiveness of about 0.4. However, designing for this effectiveness presented a problem in temperature measurement. Figures 2 and 3 show that at an effectiveness value of 0.4, the adiabatic wall temperature differences between the throat and the film coolant injection point would be about 90°F (50 K) and 130°F (72 K) for the two cases. In order to obtain an adequate measurement of the entire adiabatic wall temperature distribution, it was considered necessary to make this difference about 200°F (110 K) and accept a reduced effectiveness. The slot height selection shown on each figure is based on this criterion; the resultant slot heights are 0.060 in. (0.152 cm) for ambient hydrogen and 0.015 in. (0.038 cm) for cold hydrogen.

The ambient hydrogen film coolant injector design is shown in detail in Figures 4-6. Particular care was taken to provide a uniform flow distribution to each channel through the use of deflectors at each inlet and of 0.020 in. (0.051 cm) deep metering slots for pressure drop control upstream of each channel (Figure 6). Tapered ribs provide a uniform coolant flow at the slot exit (Figure 5). The cold gas coolant injector design is similar, but provides a 0.015 in. (0.038 cm) slot height; in addition, the metering channel width was reduced from 0.046 in. (0.117 cm) to 0.023 in. (0.058 cm) because of the somewhat lower coolant flow rates and higher slot pressure drops. Electrical discharge machining was used on each component of both injectors. Figures 7 and 8 show the inner and outer rings, respectively, of the cold gas injector. These figures show the key features of both injectors: the tapered ribs of the film coolant slot on the inner ring, and the inlet deflectors and metering channels for flow distribution control on the outer ring. The hole in the foreground of Figure 8 is the manifold instrumentation port. Figures 9 and 10 provide closeup views of the complete injectors showing the 0.060 in. (0.152 cm) and 0.015 in. (0.038 cm) slots, respectively, and the ends of the tapered ribs.

Figure 11 shows the square film coolant injector design, which has a 0.060 in. (0.152 cm) slot height to match the first circular injector. It consists of four segments, two each of the Plate No. 1 Assembly shown in Figure 12 and the Plate No. 2 Assembly shown in Figure 13. Figures 14 and 15 provide photographs of the metering sections and cover plates used to make the subassemblies of Figures 12 and 13, respectively. A closeup of the coolant slot in the completed injector is shown in Figure 16.

The design of the liquid coolant injector is shown in Figure 17. In order to obtain uniform liquid coverage on the wall with discrete injection holes, it is necessary to either impinge the liquid on the wall at an angle of about 30° or provide a tangential injection velocity component. An impinging design in the present case would result in the core flow seeing a very large wall discontinuity. Therefore, a swirl flow design was selected with the wall discontinuity limited to that of the ambient hydrogen gas injector. Twenty-four injection holes with a diameter of 0.042 in. (0.107 cm) provide a liquid injection velocity of 100 ft/sec (30 m/s) at the maximum coolant flow rate. Since it was likely that a two-phase mixture would enter the injector manifold, tangential inlets were provided to minimize phase separation. A closeup view of the liquid injector is shown in Figure 18.

B. TEST NOZZLES

Figure 19 shows the design for the test nozzle with an electrically heated cylindrical chamber. The throat diameter was selected to provide a stagnation pressure of 250 psia (172 N/cm^2) with no film cooling and the nominal heated nitrogen flow of 1.0 lb/sec (0.45 kg/s). A higher pressure would require smaller test sections and was, therefore, not desirable; a significantly lower pressure is not possible for testing with supercritical liquid film coolant. The chamber diameter of 1.218 in. (3.094 cm) gives a contraction ratio of 4.0, a typical value for internal regenerative designs, and also accommodates commercially available Hastelloy-X tubing with 0.020 in. (0.051 cm) wall thickness. Hastelloy-X was selected because of its high electrical resistivity and great strength at high temperatures. The latter feature allows a thinner wall, which is desired to increase electrical resistance and minimize transient temperature gradients (thereby facilitating transient data analysis). A cylindrical section length of 3.5 in. (8.9 cm) provides for an adequate electrically heated length and simulates a typical design L* of 16. The expansion section contour was dictated by flow separation and instrumentation considerations; it is not typical of internal regenerative cooling applications. Figure 20 shows the conical chamber design; it provides the same axial distance to the throat and the same throat and expansion section configurations as the cylindrical chamber design.

Both the cylindrical and conical chambers were spun; subsequent grinding of the throat section provided a nearly uniform wall thickness. The wall thickness of the cylindrical chamber was 0.022 in. (0.056 cm) in the throat and 0.020 in. (0.051 cm) elsewhere; the wall of the conical chamber was 0.019 in. (0.048 cm) at the throat and 0.015-0.018 in. (0.038-0.046 cm) elsewhere. Two early attempts to spin the conical chamber resulted in cracking near the throat. Additional Hastelloy-X tubing was ordered along with CRES 347 tubing. The latter material was an acceptable alternate for this chamber, since the conical design was not electrically heated. Two conical chambers were then spun successfully, one from each material. However, the internal surface of the Hastelloy-X conical chamber was damaged during final machining. Therefore, the flange was removed and brazed to the CRES 347 chamber.

The rectangular chamber assembly design is shown in Figure 21, while Figure 22 provides the chamber wall details. A square inlet was selected, with convergence in one plane resulting in a throat aspect ratio of 4:1. The nozzle throat and exit areas, along with the injector core flow area, are identical to those in the circular system. The instrumented walls were made from 0.019 in. (0.048 cm) CRES 347 sheet stock. Transverse stiffeners were added to the chamber to prevent deflection of the side walls; these stiffeners did not contact the thin test walls and allowed room for the expected deflection of these walls. The actual chamber with stiffeners is shown in Figure 23 along with the other components of the rectangular assembly.

C. TURBULENCE SCREENS

A range of square mesh screens was used in an attempt to influence the turbulence intensity of the nitrogen core flow at the coolant injection location. The characteristics of these screens are tabulated below.

Mesh	Wire Dia. in.	% Open Area	$\frac{x}{M}$	Criteria
10	.02	64.0	5	Coarse Mesh
14	.017	57.2	7	10% Intensity
22	.0075	69.7	11	Intermediate Mesh
30	.0065	64.8	15	Uniformity
40	.0065	54.8	20	Finer Mesh

The primary criteria for screen size selection was to simulate the turbulence intensity near an injector face. Data from Ref. 1 indicate that the turbulence intensity near an injector is about 10 percent. An extrapolation of the screen turbulence data given in Ref. 2 indicates that a 10 percent intensity level can be expected at an x/M ratio of about 7, where x is the distance downstream of the screen and M is the mesh size. This criteria leads to a mesh size of 14 for the downstream position of the turbulence grid (1/2 inch or 1.3 cm upstream of the film coolant inlet); therefore, the 14 mesh screen was chosen for one of the turbulence grids. A 10 mesh screen was also used in case a more coarse grid was necessary to obtain the desired turbulence.

Flow uniformity in the radial direction was also a desirable characteristic of the flow downstream of the turbulence grid. Ref. 2 gives an x/M value of 15 as a flow uniformity criteria and this led to the selection of the 30 mesh screen. An intermediate sized screen, 22 mesh, and a finer screen, 40 mesh, were also used so that a wide range of screens could be characterized.

One other criteria considered in selecting the screen sizes was flow stability downstream of the screen. Data in Ref. 3 correlate the occurrence of flow instabilities with the portion of flow area "blocked" by the wire of the mesh; a minimum value of about 55 to 60 percent open area was desirable for stability.

D. RELATED HARDWARE

A laminated Grafoil-mica-Grafoil seal was used between the film coolant injector and the cylindrical chamber; it also provided electrical isolation of the chamber. Mica was also used to prevent electrical contact between the chamber and the smaller shoulder on the injector (see Figures 1 and 4). This mica was carefully matched to the chamber dimensions in order to provide a smooth surface for the film coolant.

Figure 24 shows the coolant channel provided in the adapter housing in order to reduce heating of the film coolant prior to its injection. Ambient nitrogen was used in this circuit during ambient hydrogen testing; there was no flow in this circuit during tests with the cold film coolants. A similar cooling circuit was provided in the adapter for the rectangular assembly. Transition from the circular nitrogen supply line to the square film coolant injector was provided by the upstream sleeve in the adapter section; this sleeve is shown in Figure 25.

IV. TEST FACILITY AND INSTRUMENTATION

Test Bay 5 of the Research Physics Laboratory was utilized for the film cooling tests. This bay was selected because of adjacent liquid hydrogen feed system facilities and the accessibility of a gaseous nitrogen heating unit and a high wattage dc power supply. A special stand was installed to provide unimpeded channeling of power leads and gas facilities as shown in Figure 26. Nitrogen at 500 and 3600 psi (345 and 2480 N/cm^2) and gaseous hydrogen at 3000 psi (2070 N/cm^2) were provided to the stand.

The cylindrical chamber was heated by connecting the cylindrical section as an electrical resistance heater to a 40 kW power supply. A pair of 2/0 copper leads were run from the bus bars to the test stand; another pair was used for the ground circuit. A dc shunt was installed to permit measurement of power input to the test section during the heat transfer tests.

The primary flow heater was also electrical resistance heated; it is just visible in the upper right corner of Figure 26. This unit consists of two series-connected runs. The first is constructed of 1 in. (2.5 cm) diameter stainless steel tubing and the second of 1-1/2 in. (3.8 cm) Inconel 600 tubing. A total power of approximately 340 kW was available to heat the incoming nitrogen. The heater delivers 1.0 lb/sec (0.45 kg/s) of nitrogen at temperatures in excess of 1100°F (866 K) for short durations or at 900°F (755 K) continuously.

Gaseous hydrogen as film coolant was supplied from the 3000 psi (2070 N/cm^2) system, with a 1/2 in. (1.3 cm) regulator and 1/2 in. (1.3 cm) extended stem valve for control. Flow rates were measured by use of a critical nozzle installed immediately upstream of the valve. A schematic flow diagram of the test system is shown in Figure 27 and includes the subsystems for cold gas and liquid coolant testing. In order to obtain rapid hydrogen flow transients the flow control valve was located close to the test assembly, and the pilot valve was close-coupled to the flow control valve with 3/8 in. (0.95 cm) diameter tubing. Hydrogen flow rates were controlled by presetting the pressure regulator upstream of the critical flow nozzle. Nitrogen supply to the heater was through a 1.0 in. (2.5 cm) stainless steel line, with a 1.5 in. (3.8 cm) connection to the test section from the heater. Hydrogen lines were 0.50 in. (1.3 cm) stainless steel tubing. System pressure drops at required flow rates were minimal except for the cold gas heat exchanger, which was calculated to have a pressure drop in the 100-200 psi (69-138 N/cm^2) range.

The heater exchanger for the cold gaseous hydrogen tests consisted of 180 ft (55 m) of 3/4 in. (1.9 cm) diameter stainless steel tubing installed in three parallel coils. During operation the coils were submerged in liquid nitrogen in a cylindrical cryostat. They were assembled in a manner to provide for natural convective circulation in a counter-current heat transfer mode. Rated capacity was 0.1 lb/sec (0.045 kg/s) of ambient temperature hydrogen. This method of temperature conditioning was selected over the LH_2 vaporization method because it produces better temperature control under variable flow rate conditions. The heat exchanger was installed downstream of the flow measurement nozzle, and a subsonic venturi was used downstream of the heat exchanger. This arrangement provided for accurate setting of the flow into the heat exchanger with a separate measurement of the flow out of the heat exchanger. The venturi was calibrated against the critical flow nozzle using ambient hydrogen.

For the liquid hydrogen testing a vacuum-jacketed line was installed between a 100 gallon (0.38 m^3) LH_2 run vessel and the valve at the test stand, as shown in Figure 28. The inner line was wrapped with one layer of aluminized Mylar, one layer of fiberglass cloth and then seven layers of alternating Dimplar and aluminized Mylar. Micarta discs were used as spacers at 4-foot (1.2 m) intervals. Components not readily jacketed were insulated with polyurethane foam. Figure 29 shows the test stand set up for liquid hydrogen testing with all insulation in place.

The flow control device for these tests was a venturi serving both as a cavitating venturi for liquid flow and as a critical nozzle for gas flow. Hydrogen temperature at the venturi was measured with a platinum resistance temperature transducer. Actual flow rates were determined from a separate calibration test, in which the hydrogen was heated to near ambient temperature after leaving the venturi and then flowed through a critical flow nozzle. This test was also used to calibrate the copper-constantan thermocouple used to measure the hydrogen temperature in the coolant injector manifold.

Fluid static pressure and stagnation temperature were measured at the following locations: (1) upstream of the critical flow nozzle in the nitrogen supply line, (2) upstream of the critical flow nozzle in the hydrogen circuit, (3) at the flange in the nitrogen line to which the test assembly mates (see Figure 1), and (4) in the manifold of the film coolant injector. Table I indicates the types of thermocouple used in each case. Additional pressure taps were used to provide the pressure drop across the venturis used in the cold gas and liquid hydrogen testing. Turbulence intensity was measured in a special test using a two-wire, constant temperature hot-wire anemometer with a range of 0-300 ft/sec (0-91 m/s) for standard air; the oscillatory component of the anemometer signal was measured with an rms voltmeter.

Each chamber was instrumented with 26 thermocouples using 40 gauge (.008 cm dia.) chromel-alumel wires. The ten thermocouples in the electrically heated section of the cylindrical chamber were spring loaded in tension against 0.0005 in. (0.0013 cm) thick mica using the cantilever system illustrated in Figure 30; all other thermocouples were spot-welded to the wall. Figure 31 provides a closeup of the test assembly; five of the cantilever springs can be seen in the left center of the figure. Just to the right of these thermocouples is the film coolant injector, with inlet lines near the top and bottom. Immediately to the right of the bottom inlet line is the outlet from the adapter coolant circuit, which exhausts ambient nitrogen to the atmosphere.

TABLE I - FLUID TEMPERATURE THERMOCOUPLES

Location	Materials	Wire Dia., in.	Type of Junction
N_2 Flow Nozzle	Chromel-Alumel	.009	Shielded
H_2 Flow Nozzle	Copper-Constantan	.020	Exposed
N_2 Supply Flange*	Chromel-Alumel	.020	Exposed
H_2 Injector Manifold	Copper-Constantan	.009	Shielded

* Inserted about 1/4 in. Others are approximately in the center of the flow.

After the second checkout test, the spring-loaded thermocouples in the electrically heated section were changed to 30 gauge (.025 cm diameter) wire to reduce breakage. Thermocouple locations on each chamber are shown in Figures 32 - 34.

All data were recorded on magnetic tape, with subsequent analog/digital conversion providing 80 samples/sec for each item; computer cards were punched automatically from the digital data for the wall temperature transients. Selected output were also recorded on an oscillograph, and digital display of parameters used to control each test was provided in the control room.

V. LABORATORY TESTING

Small scale laboratory tests were run using 900°F (755 K) nitrogen as the core flow with hydrogen film coolant. Two basic results were obtained: adiabatic wall temperature distributions and heat fluxes between the film coolant and a non-adiabatic wall, thereby defining the film coolant effectiveness and the heat transfer coefficient between the coolant and the wall. Heat fluxes were obtained in two ways: with the wall acting as a calorimeter during a cooling transient, and by electrically heating the chamber wall. In addition, heating transients were used to obtain heat transfer coefficients without coolant for comparison purposes.

All laboratory tests are summarized in Table II. Tests 1A-D were ambient nitrogen flow tests which determined if the gas film coolant injectors flowed uniformly. Test 1E was a water flow test of the liquid film coolant injector. Test 1F calibrated the venturi used in Tests 13 and 14. Test 1G provided hotwire anemometer characterization of various turbulence grid configurations. Tests 2, 3 and 4 provided for system checkout and practicing the test procedure; the program was not dependent on data from these test, although useful results were obtained from Tests 3 and 4.

Tests 5 - 10 represent a systematic, although very limited, study of the effect of velocity ratio, density ratio, slot height and coolant Reynolds number. These are the fundamental injection parameters used in Section VI,A to correlate plane, unaccelerated gaseous film coolant effectiveness data. Coolant flow designations A, B, C and D in Table II refer to nominal injection velocity ratios of 0.85, 1.0, 1.25, and 1.5, respectively. These velocity ratios were selected to span the range of optimum design, the maximum in the velocity ratio correlating function of Section VI,A and the maximum test effectiveness. The S designations represent special test segments at reduced nitrogen temperatures as described in Section V,D. In Test 6 the coolant Reynolds number was half that of Test 5. Test 7 used the coolant injector with a smaller slot height, thereby allowing the effect of slot height to be

TABLE II. - LABORATORY TEST SUMMARY

Test	Test Type	Coolant Ring	Hydrogen Flow	Pressure, psia (4)	No. Power Levels	Geometry
1A	Flow Dist.	0.060 in. (1)	--	--	--	Cylindrical
1B	Flow Dist.	0.060 in.	--	--	--	Cylindrical
1C	Flow Dist.	0.015 in.	--	--	--	Cylindrical
1D	Flow Dist.	Rect.	--	--	--	Rectangular
1E	Flow Dist.	Liquid (1)	--	--	--	Cylindrical
1F	Flow Calib.	--	(2)	--	--	--
1G	Anemometer (3)	--	--	--	--	Cylindrical
2	Checkout	0.060 in.	A, B, D	250	6	Cylindrical
3	Checkout	0.060 in.	A	250	1	Cylindrical
4	Checkout	0.060 in.	A	250	1	Cylindrical
5	530°R	0.060 in.	A,B,C,D, S-1,S-2	250	12	Cylindrical
6	530°R	0.060 in.	A, B, C	125	9	Cylindrical
7	530°R	0.015 in.	A,B,C,S	250	9	Cylindrical
8	140°R	0.015 in.	A	250	3	Cylindrical
9	140°R	0.015 in.	B	250	3	Cylindrical
10	140°R	0.015 in.	C	250	3	Cylindrical
11	530°R	0.060 in.	A,B,C,D	250	--	Conical
12	530°R	Rect.	A,B,C,D	250	--	Rectangular
13	Liquid	Liquid	E, F, G	250	13	Cylindrical
14	Liquid	Liquid	E, F, G	100	13	Cylindrical

---

(1) Without sleeve
(2) Duplicating Tests 13 and 14
(3) Ambient GN_2

(4) Nominal values without coolant flow. GN_2 flow is 1.0 lb/sec for 250 psia.

investigated independent of the density ratio change accompanying the use of this injector in Tests 8 - 10 with cold hydrogen gas.

Test 11 provided a second chamber contour and thus different flow turning and acceleration characteristics compared to Test 5. Test 12 employed a rectangular test section. Except for this geometry change, Test 12 was identical to Tests 5 and 11; it provided for comparison of plane and axisymmetric flows. Tests 13 and 14 attempted to provide liquid hydrogen coolant at supercritical and subcritical pressures, respectively.

Table III summarizes the test conditions achieved in Tests 3-14. Nominal nitrogen flow was 1.04 lb/sec (0.47 kg/s) except in the low pressure tests, and resulted in chamber pressures of 250 - 300 psia (172-207 N/cm^2). Table III indicates that the coolant flow was usually 4-8 percent of the total flow. Nitrogen flow rates in Tests 6 and 14 were 0.53 and 0.43 lb/sec (0.24 and 0.20 kg/s), respectively.

Table IV summarizes the various test data obtained. Normally, the adiabatic wall temperature was processed as part of the electrical heating or cooling transient results. A detailed discussion of the data reduction is given in Appendix B.

Helium and a hydrogen-nitrogen mixture were considered as alternate core flows to replace nitrogen and provide better density ratio simulation. The planned use of ambient and 140°R (78 K) hydrogen with 900°F (755 K) nitrogen provides density ratios of 0.19 and 0.70, respectively, compared with design applications of 1.7 or higher. Use of hydrogen coolant at 265°R (147 K) with helium at 900°R (500 K) (set by electrical heating limits) would yield a density ratio of 1.7. However, this approach would be very costly and would require a 0.010 in. (0.025 cm) slot height. Use of a hydrogen-nitrogen mixture

TABLE III. - TEST CONDITION SUMMARY

Test	Nitrogen Flow, lb/sec	Nitrogen Temperature, °F	Hydrogen Flow, lb/sec	Hydrogen Temperature, °F	Chamber Pressure, psia	Velocity Ratio, u_c/ue	Density Ratio, ρ_c/ρ_e	Slot Height, in.	Coolant Reynolds Numbers
3	1.044	914	0.0405	70	278	0.838	0.187	0.060	22,700
4	1.046	921	0.0397	61	282	0.802	0.191		22,500
5A	1.042	916	0.0396	53	281	0.794	0.193		22,700
5B	1.036	921	0.0470	57	285	0.952	0.192		26,800
5C	1.032	932	0.0583	60	292	1.182	0.193		33,100
5D	1.052	907	0.0706	57	305	1.422	0.190		40,300
6A	0.520	922	0.0204	57	137	0.822	0.192		11,600
6B	0.530	896	0.0242	60	141	0.981	0.188		13,800
6C-1	0.526	947	0.0286	57	145	1.119	0.196		16,300
6C-2	0.535	911	0.0291	58	147	1.151	0.190		16,600
7A	1.041	914	0.0085	77	256	0.837	0.184	0.0145	4,530
7B	1.041	924	0.0101	81	258	0.998	0.184		5,380
7C	1.042	927	0.0124	79	260	1.217	0.185		6,620
7S	1.041	211	--	--	177	--	--		--
8	1.054	902	0.0262	-260	263	0.960	0.490		27,100
10	1.061	906	0.0376	-292	268	1.147	0.585		43,700
11A	1.045	910	0.0396	67	281	0.817	0.187	0.060	22,300
11B	1.040	915	0.0474	71	285	0.986	0.186		26,600
11C	1.041	918	0.0584	64	294	1.195	0.189		33,000
11D	1.037	923	0.0701	65	302	1.438	0.190		39,600
12A	1.055	899	0.0428	75	253	0.777	0.183	0.063	22,200
12A*	1.038	930	0.0430	76	250	0.777	0.187		22,300
12B	1.051	909	0.0511	75	258	0.924	0.184		26,500
12B*	1.042	926	0.0508	75	257	0.915	0.186		26,400
12C	1.048	918	0.0636	74	266	1.144	0.186		33,000
12D	1.044	924	0.0761	73	273	1.365	0.187		39,600
13A	1.038	930	0.0382	-378	259	--	--	--	--
13B	1.025	939	0.0548	-380	262	--	--	--	--
13C	1.040	925	0.0714	-365	268	--	--	--	--
14A	0.425	903	0.0384	-380	108	--	--	--	--
14B	0.438	891	0.0547	-393	114	--	--	--	--
14C	0.434	906	0.0726	-375	118	--	--	--	--

---

*Separate transient test.

TABLE IV. - TEST DATA SUMMARY

	Heated Section					Unheated Section		
	Electrical(1)							
Test	Cooled	Uncooled	Heating Transient	Cooling Transient	T_{AW} Only	Heating Transient	Cooling Transient	T_{AW} Only
3	1		X	X		X	X	
4	1					X	X	
5A	3					X	X	
5B	3					-(2)	X	
5C	3					-	X	
5D	3					-	X	
5S-1(3)					-	-	-	
5S-2(4)					-	-	-	
6A	3					X	X	
6B	3					-	X	
6C-1					X	-	X	
6C-2	3					-	X	
7A	2					-		X
7B	2					-		X
7C	3					-		X
7S(5)		2						
8	3				X(6)	X		X
9(7)	-				-	-		-
10	3				X(6)	-		X
11A						X	X	
11B						-	X	
11C						-	X	
11D						-	X	
12A						-	X	X
12B						X	X	X
12C								X
12D								X
13A	3					-	X	
13B	5					-	X	
13C	5					-	X	
14A	3					-	X	
14B	5					-	- (8)	
14C	5					-	- (8)	

---

(1) Number of power levels is indicated.
(2) Dash indicates available data which were not processed.
(3) Nitrogen at 650°F.
(4) Nitrogen at 400°F.
(5) Nitrogen at 200°F.
(6) Processed separately from electrical data due to coolant temperature variation.
(7) Not processed due to data anomaly.
(8) Data not analyzed due to problem in automatic card punching.

with 140°R (78 K) hydrogen coolant can also provide a density ratio of 1.7, but requires an even smaller slot height. Furthermore, the results of Section VI,A, indicating the density ratio and velocity ratio effects to be separable (with the former correlated by a simple power law) were considered to provide a sound basis for extrapolating the laboratory test data. Therefore, nitrogen was retained as the core flow. However, the significant turning effects described in Section VII,A are dependent on coolant-core density differences. Therefore, future testing should simulate design density ratios; this can easily be accomplished using nitrogen as the coolant.

A. INJECTOR FLOW DISTRIBUTION TESTS

Quantitative flow distribution tests were conducted on the three gaseous film coolant injectors. Ambient nitrogen flowed through the coolant circuit, exhausting to the atmosphere with no core flow through the center of the injector. For the circular injectors a gear-driven angle measuring device was mounted in a bench vise as shown in Figure 35. The injector was bolted concentrically beneath it, and a total pressure probe attached rigidly to the geared plate. The probe tip was located at the radial center of the coolant slot and the plate rotated to provide a circumferential survey of the velocity head. The U-tube water manometer used to measure the velocity head can be seen in Figure 35 along with the two nitrogen lines to the injector and the pressure gauge which monitored an upstream venturi pressure.

Two tests were run with the 0.060 in. (0.152 cm) slot; in each the nitrogen flow rate was set to provide approximate simulation of the hydrogen Mach number. In the first test the chamber wall was not simulated and the probe tip was located near the slot exit as shown in Figure 36. In Figure 37 the square root of the measured velocity head is plotted vs. azimuthal position; data points are shown as small balck dots. In general, data were obtained adjacent to the ribs and at maximum and minimum velocity head locations between the ribs; a few additional points shown as large open circles were obtained directly in front of slot ribs. Although Figure 37 indicates a substantial velocity depression adjacent to many ribs, the channel-to-channel flow distribution appears to be quite uniform. The rib depression is probably due to the boundary layer which builds up along the rib, although tapering of the ribs may not have completely eliminated the wake region which otherwise would be present.

In order to investigate the dissipation of the rib effect, a 1.5 in. (3.8 cm) long sleeve was used to simulate the chamber wall in the second test of the 0.060 in. (0.152 cm) slot injector. The probe tip was located 0.725 in. (1.84 cm) downstream of the slot exit, corresponding to the first thermocouple location on the cylindrical chamber. A circumferential survey was made to find maximum and minimum velocity heads, the results of which are shown in Figure 38. All but four points fall within a ± 10 percent velocity range, and comparison with Figure 37 indicates the rib depressions have disappeared in most cases. In mating this injector to the cylindrical chamber, the complete rows of chamber thermocouples were aligned with the 90 and 270 degree positions on Figures 37 and 38.

The 0.015 in. (0.038 cm) slot injector was tested using the chamber sleeve with the probe tip again 0.725 in. (1.84 cm) from the slot exit; the probe and sleeve are shown in place in Figure 39. In this test the probe was necked down to a 0.005 in. (0.013 cm) inside diameter in order to make the region of pressure averaging smaller relative to the slot width; the previous probe had an inside diameter of 0.010 in. (0.025 cm) at the tip. With the slow response of the smaller tip it was no longer possible to search for maximum and minimum velocity head locations. Therefore, measurements were taken at each rib location and in the center of each slot. In order to obtain a high enough differential pressure to read accurately, the nitrogen flow was set at about twice the value required for Mach number simulation. A careful check of the upstream pressure verified that the metering channels in the injector were not near a choked flow condition.

Results of the 0.015 in. (0.38 cm) slot injector test are shown in Figure 40. The velocity scatter is within a ± 10 percent band for each half of the circumference, but a small maldistribution between the two sides of the injector is apparent. This may have been caused by either the chamber sleeve or the probe mount not being exactly concentric with the coolant slot. In case an injector maldistribution actually existed this injector was mated to the chamber such that the primary thermocouples were at the nodes of the velocity distribution. Data were also obtained at 2-degree increments between the 100 and 140 degree locations on Figure 40. These results follow the trend of Figure 40 except for a minimum point at 116 degrees, where the normalized velocity was 1.25.

The square coolant injector's flow distribution was measured with a total pressure probe in a similar manner, A plastic rectangular sleeve was used, with the probe located axially at the first thermocouple position. Figure 41 gives the relative velocity distribution measured; it is quite uniform on the two five-channel sides which were used for chamber instrumentation.

The liquid hydrogen coolant injector was flow tested with water and then with a water-nitrogen mixture, as shown in Figures 42 and 43, respectively. Visual observations indicated the water flow distribution was excellent. In the two-phase case a slightly reduced liquid flow was noted as the flow in each half of the manifold reached the other inlet (see Figure 17). The injector was oriented relative to the chamber such that the primary thermocouple rows were away from the inlets.

B. HOT-WIRE ANEMOMETER TEST

The test assembly for Test 1G was like that for the first group of film cooling tests except an anemometer holder replaced the film coolant injector and positioned a hot-wire anemometer probe at the same axial position as the film coolant slot exit. Seven turbulence intensity measurements were made, each at the center of the ambient nitrogen flow: with no screen, with each of the five screens described in Section III located 0.5 in. (1.3 cm) upstream of the anemometer probe and with the 10 mesh screen retracted approximately 2 in. (5 cm) to the position between adapter sleeves (see Figure 1).

Due to the mass velocity limitation of the anemometer these tests were run at essentially atmospheric pressure, i.e., with subsonic flow in the nozzle. Three measurements were made for each configuration, at velocities of about 115, 170 and 200 ft/sec (35, 52, and 61 m/s). The two higher velocities indicated slightly lower turbulence intensities than the 115 ft/sec (35 m/s) value, but the anemometer fluctuation calibration is much less accurate at the higher velocities. Therefore, the results reported herein are at 115 ft/sec (35 m/s) which corresponds to a Reynolds number of 70,000. In the film cooling tests the heated nitrogen velocity was 300 ft/sec (91 m/s) with a Reynolds number of 600,000.

The turbulence intensities measured at 115 ft/sec (35 m/s) were as follows:

Screen	Intensity, %
None	4.1
40 mesh	4.1
30 mesh	4.0
22 mesh	4.1
14 mesh	4.5
10 mesh	4.7
10 mesh retracted	4.0

The increase in turbulence intensity with the coarse mesh screens was much less than anticipated. Extrapolation of the data of Ref. 2 had indicated a 10 percent intensity might be obtained with a 14 mesh screen. As a result of the small variation in intensity, film cooling tests to investigate the effect of turbulence were dropped from the test plan, and all tests were conducted with no screen.

C. FILM COOLING CHECKOUT TESTS

Three checkout tests were run using the electrically heated cylindrical chamber, .060 in. (0.152 cm) film coolant slot and ambient hydrogen coolant. The test procedure practiced in the checkout tests is illustrated in Figure 44; it was easily run and was used in all film coolant testing. Coolant flow was initiated during the nitrogen preheating period in order to prevent heating of the film coolant injector and to provide the adiabatic wall temperature distribution in the chamber after the nitrogen temperature reached steady state at 900°F (755 K). The hydrogen valve was then closed to obtain a wall temperature transient from which heat transfer coefficients without film cooling could be inferred. Opening the hydrogen valve then gave a cooldown transient from which the corresponding heat transfer coefficients with film cooling could be inferred. At the end of this transient a second measurement of the adiabatic wall temperatures was obtained in some cases. Electrical heating of the cylindrical section of the chamber followed, with steady-state wall temperatures usually obtained at three power levels. The maximum power level was established by limiting the wall temperature to about 1100°F (866 K). However, maximum power was not attained in the checkout tests, as described below.

In the case of ambient gaseous coolant each test consisted of multiple coolant flow rates. Therefore, after the chamber power was cut off the hydrogen regulator pressure was adjusted to provide the new coolant flow rate. When steady conditions were obtained the test sequence was repeated starting with closure of the hydrogen valve. Analog-to-digital conversion of all data was obtained from just before hydrogen valve closure until near the end of the cooldown transient and also for a short interval with steady conditions during each chamber power level.

The first checkout test revealed several problems, the most serious being a large leak at the hydrogen valve. This valve was an extended stem globe valve that had been specially equipped with a stem vent fitting below the stem seal. The valve was installed with pressure below the seat, and it was consequently not noted that leakage would occur from the stem vent even though the system was leak tested thoroughly prior to the run. There was a check valve between the film coolant injector and the valve preventing flow to the valve when the chamber assembly was pressurized. Thus the valve lost a substantial volume of the total flow but only when in the open or run position. Subsequent to sealing the vent no further problem of this nature occurred. This vent can be seen in Figure 26 about midway on a vertical line between the top of the valve and the top of the heated nitrogen supply line; it points in the direction of the test assembly. The leak precluded use of the chamber thermocouple data due to the unknown coolant flowrate. Following a test segment at the maximum hydrogen flowrate and subsequent electrical heating of the chamber during the next segment, this leak resulted in a minor explosion which terminated the test. Maximum chamber temperature at the time of the explosion was approximately 1100°F (866 K).* Damage was limited to scorched wire insulation and breakage of all spring-loaded chamber thermocouples.

---

*Maximum chamber temperature during electrical heating at the maximum hydrogen flow rate was 890°F (750 K).

Two electrical problems were also revealed. Maximum current obtained through the test section was only 1500 amps, compared to a 2400 amp or greater capability by the power supply. It was determined that excessive resistance in the cables to and from the test section resulted in reaching the voltage limit of the power supply at the reduced current. Failure to obtain data from most of the spot-welded thermocouples was also attributed to excessive resistance in the ground circuit and the resultant voltage on the unheated section of the chamber. As a result the cross-section of both the ground and input cabling was doubled for the second test. The length of these cables was also reduced, and several diodes in the power supply were replaced. Based on subsequent testing, these modifications resolved the problems described above.

The second checkout test accomplished only part of the test procedure of Figure 44, at a coolant flow rate corresponding to a velocity ratio of 0.85. Good data were obtained for the transient portion and the first power level at 1400 amps; the second power level was to be at 2000 amps. However, when the current reached about 1900 amps a fire broke out in the vicinity of the chamber, and the test was terminated. Maximum chamber temperature at the time of the fire was approximately 650°F (615 K). Damage was limited to breakage of some of the spring-loaded chamber thermocouples. The fire was attributed to leakage developing during the test at the chamber-injector interface; such a leak would supply almost pure hydrogen to the region between the test section and the quartz wool insulation surrounding it. Post-test inspection revealed that the seal at this interface was installed improperly* and was damaged in one region. It was also found that the chamber flange was warped.

---

*Installed as mica-Grafoil-mica instead of Grafoil-mica-Grafoil.

A third checkout test was run in an attempt to resolve the injector-chamber interface leakage problem noted in the second test. Prior to assembly the chamber flange was machined flat, and the chamber thermocouples were replaced. The spring-loaded thermocouples in the electrically heated section were changed to 30 gauge (.025 cm diameter) wire to reduce breakage. This change sacrificed the transient data from these thermocouples as a secondary source of heat transfer coefficients in this section; steady-state data with electrical heating of the wall was always the primary source. The injector-chamber seal for this test was a Grafoil-Grafoil-mica-Grafoil laminate.

The results of the third checkout test were virtually identical to the second. At the initial coolant flow rate, transient testing and the first power level (1400 amps) were completed successfully. However, at a test section current of about 1900 amps an interface leak and fire occurred. Subsequent pressure testing with the nozzle plugged pinpointed the leak between two of the three current-carrying bolts. Since this type of leak occurred on two tests at the same power level, but not on the initial checkout test* which was limited to lower power levels, it was concluded that expansion of the bolts due to their internal electrical heating caused the leak. The ground connection for the test section had been moved upstream of the adapter flange to provide more room for the spring-loaded thermocouple assembly. Following the third checkout test this connection was moved to its originally planned location on the chamber flange using a specially contoured bus connector; no leakage problems were encountered in subsequent tests with this connection.

The checkout tests revealed a number of secondary problems. Steady-state thermocouple readings without coolant flow just prior to the childown transients revealed that external heat losses and axial conduction were not negligible, with the chamber flanges acting as fins and reducing adjacent wall

---

*The initial test ran longer and at generally higher temperatures due to the hydrogen valve leak.

temperature measurements by about 40°F (22 K). Therefore, Tests 5S-1 and 5S-2 were added to obtain similar data at reduced nitrogen temperatures in order to determine external boundary conditions for use in film cooling data analysis. A second problem was the large a-c ripple in the test section voltage drop; as a result, rms measurements of the a-c component as a function of power level were obtained in a subsequent test. Use of these data in calculating the electrical heat flux is described in Appendix B. In addition, it was observed that the chamber pressure transient was slow after opening or closing the hydrogen valve, i.e., the pressure transient duration was comparable to that of the wall temperature transient. However, the hydrogen flow transient appears to be very fast, as indicated by the differential between the coolant injector manifold pressure and the chamber pressure. The nitrogen flow variation implied by the chamber pressure transients is analyzed in Appendix B and used in calculating correlation coefficients from the transient heat transfer coefficients.

D. AMBIENT HYDROGEN TESTS

Tests 5 and 6 used the 0.060 in. (0.152 cm) coolant slot with the cylindrical chamber. In Test 6 the core and coolant flows were half the Test 5 values in order to investigate the effect of coolant Reynolds number. Test 7 used the coolant injector with a 0.015 in. (0.038 cm) slot height, thereby allowing the effect of slot height to be investigated independent of the density ratio change accompanying the use of this injector in subsequent tests with cold hydrogen.

Tests 5S-1 and 5S-2 were run with nominal nitrogen temperatures of 650°F and 400°F (615 and 480 K), respectively, in order to obtain additional heat loss data. In each case the normal transient test sequence was employed, using about 0.03 lb/sec (0.014 kg/s) of hydrogen; no electrical heating data were obtained. Use of the steady-state results obtained without coolant just prior to the cooldown transients is described in Appendix B. Test 6C was run twice (note Tables III and IV), since the initial attempt was interrupted after the transient sequence by an electrical problem with the nitrogen heater.

The liquid nitrogen heat exchanger used in Test 8 - 10 was installed prior to running Test 7. Since a by-pass was not provided, the coolant in Test 7 passed through the empty heat exchanger. Pressure data at the subsonic hydrogen venturi and in the injector manifold indicate the heat exchanger volume was sufficient to cause a long-duration flow transient after opening the hydrogen valve. Therefore, heat transfer coefficients were not inferred from the cooldown transients of this test.

Nominal test section currents were 1400, 2000 and 2400 amps for Test 5 and 1100, 1550 and 1900 amps for Test 6. Only two electrical heating measurements, at 1000 and 1500 amps, were made for each of the two lower coolant flow rates in Test 7; planned operation at 1800 amps was eliminated because of the high wall temperatures observed at 1500 amps*. A third point, at 1700 amps, was obtained at the highest coolant flow. At the end of this test the nitrogen temperature was reduced to approximately 200°F (370 K), and steady-state heat transfer data were obtained without coolant flow at 1000 and 1400 amps (Test 7S).

Test 11 used the conical chamber and thus provided different flow turning and acceleration characteristics compared to Test 5. This comparison is of great importance in view of the turning effects observed in Test 5 and discussed in Section VII,A. Figure 45 shows the conical chamber on the test stand with the insulation removed.

---

*Maximum test section power was limited based on preventing the wall temperature from exceeding 1100°F (866 K).

E. COLD HYDROGEN TESTS

Tests 8 - 10 used the same component assembly as Test 7, but provided higher injection density ratios by using cold hydrogen gas as the film coolant. Ambient hydrogen entered a tubular heat exchanger consisting of three parallel coils submerged in liquid nitrogen as discussed in Section IV. This heat exchanger performed about as expected, although the long flow transient after hydrogen valve opening eliminated the wall cooldown transient as a source of heat transfer coefficient data as in Test 7. No flow oscillations were observed at the subsonic venturi measuring flow from the heat exchanger, even though parallel circuits were used in the heat exchanger. However, the outlet temperature decreased somewhat within each test and from test to test; coolant temperatures obtained in the injector manifold early in each test when the adiabatic wall temperatures were recorded were as follows:

Test	H_2 Temperature, °R	Density Ratio
8	200	0.490
9	184	0.535
10	168	0.585

The resulting density ratios compare with a value of about 0.19 for ambient coolant. Variation of the coolant temperature within each test was accounted for by adjusting the adiabatic wall temperature for use in the analysis of the electrical heating data based on constant effectiveness.

Nominal test section currents were 1400, 2000 and 2200 amps in Tests 8 and 9 and 1400, 2000 and 2400 amps in Test 10. The third power level in Tests 8 and 9 was restricted due to high wall temperatures. Following Test 10 a thermocouple calibration test of the assembled chamber with all thermocouples in place was made. This test consisted of a two-point check of the chamber, at 59°F (288 K) and totally immersed and equilibrated in liquid nitrogen. Maximum deviation from base temperature was 12°F (7 K) on voltage substitution calibrated thermocouples. Some of the thermocouples could not be balanced for each test run because of the limited number of calibration channels available, and in these channels a maximum shift of 34°F (19 K) was observed. Linear correction relationships were developed to permit adjustment of the temperatures as read.

Data from Test 9 were found to be inconsistent and were not analyzed. Adiabatic wall temperatures from the two primary rows of thermocouples, measured early in the test, are higher than those from Test 8 in spite of a higher coolant flow rate and lower coolant temperature in Test 9. In Test 10, a further increase in coolant flow and decrease in coolant temperature resulted in temperatures significantly lower than in Test 8 (as expected). At the end of the transient sequence and during electrical heating, however, these same Test 9 wall temperature measurements were between those of Tests 8 and 10, as are the adiabatic wall temperatures from the secondary rows of thermocouples (90° from the primary rows). Therefore, the data from Test 9 are not self-consistent. It would appear that an unusual coolant flow distribution existed early in Test 9, but this distribution was not re-established when coolant flow was initiated during the transient sequence. Unfortunately, the new steady-state adiabatic wall condition was not attained during the data recording sequence due to the long flow transients noted above. Therefore, adiabatic wall temperatures were not available for analysis of the electrical heating data.

F. RECTANGULAR GEOMETRY TEST

A short preliminary run of Test 12 resulting in no data acquisition revealed two problems: an abrupt rather than gradual reduction in the thin wall deflection approaching the throat, and a significant loss of thermocouples due to the thermal expansion and contraction of these walls. As a result of the former, subsequent data obtained at and beyond the throat are of little value due to the significant flow turning just upstream of the throat. As a result of the second problem, the chamber thermocouples were repaired and the test procedure for Test 12 was revised. Steady-state data at four coolant flow rates were obtained first, corresponding to the velocity ratios used in Tests 5 and 11. The normal transient test sequence was then run at the two lower coolant flows. By this time about half of the chamber thermocouples had been lost, so the test was terminated.

G. LIQUID HYDROGEN TESTS

The following table summarizes the flow conditions obtained in the liquid hydrogen film cooling tests.

Test	Hydrogen Flow Rate lb/sec	Hydrogen Temperature at Venturi °R	Hydrogen Temperature in Injector °R
13A	.0382	54	85 - 76
13B	.0548	63	82 - 76
13C	.0714	69	101 - 91
14A	.0384	66	88 - 76
14B	.0547	65	67 - 64
14C	.0726	75	88 - 76 - 91

Note that the hydrogen temperature in the injector manifold varied slightly within each test segment. Nominal nitrogen flow rates in Tests 13 and 14 were 1.04 and 0.43 lb/sec (0.47 and 0.20 kg/s), respectively.

Test section electrical power was limited during Tests 13 and 14 due to a shortage of diodes for the power supply; maximum heat flux was about 0.3 Btu/in.^{2}-sec (49 W/cm^2). For the first two coolant flow rates in each test, nominal test section currents were 750, 1100 and 1500 amps. However, in the second segment of each test these power levels were run in descending as well as ascending order in order to detect any pseudo boiling phenomena. For the third or high flow segment of each test, nominal currents were 750, 950, 1100, 1300 and 1500 amps, thereby providing a more detailed heat flux vs. wall temperature curve if a pseudo boiling behavior were obtained; these power levels were run in ascending order only.

Laboratory testing was completed with running of the liquid hydrogen flow calibration test (1F in Table II). In this test a critical flow nozzle was installed in series with the venturi used for hydrogen flow control in Tests 13 and 14. The heat exchanger used previously in cold hydrogen gas testing, in this case filled with water, was installed downstream of the venturi and the run valve; it heated the hydrogen to approximately 500°R (280 K) before entering the critical flow nozzle. System flow, as measured by the critical flow nozzle, was correlated with the pressure and density upstream of the venturi by the equation

$$W_c = C_1 \sqrt{P \rho}$$

in which

W_c = hydrogen flow, lb/sec
P = pressure upstream of venturi, psia
ρ = density upstream of venturi, lb/ft^3

The correlation coefficient C_1 was found to be very slightly pressure dependent, ranging from 0.528 x 10^{-3} at 1100 psia (760 N/cm^2) to 0.519 x 10^{-3} at 4200 psia (2900 N/cm^2). As in the actual film cooling tests, the hydrogen temperature upstream of the venturi was measured with a platinum resistance temperature transducer; the resultant temperature range during the calibration test was 64 - 75°R (36 - 42 K). The copper-constantan thermocouple used to measure the hydrogen temperature in the film coolant injector manifold was installed adjacent to the resistance temperature transducer during Test 1F in order to calibrate the former.

Interpretation and analysis of the "liquid" hydrogen data from Tests 13 (supercritical) and 14 (subcritical) were hampered in some cases by the unsteady nature of some wall temperatures during the adiabatic wall and electrical heating measurements and by occasional inconsistencies among the wall temperatures measured prior to transient testing, near the end of the cooling transient* and during the lowest electrical power level. These problems are attributed to jet instability or quasi-stability (i.e., more than one relatively stable operating mode) associated with injection of the coolant through discrete holes and to heat transfer from the forward chamber flange to the coolant. The latter occurrence was also observed with the cold hydrogen gas data, as discussed in Section VII,A, but would be of even greater magnitude in the liquid tests. In order to process the data and provide approximate results, best estimates of the wall temperatures were utilized whenever unsteady or inconsistent data were encountered. When the inside wall temperature with electrical heating minus the adiabatic wall temperature was less than 5°F (3 K), no heat transfer coefficient was calculated.

Some of the adiabatic wall temperatures obtained in Test 14 were low enough to indicate the likelihood of nitrogen condensation, which precludes determination of the film coolant effectiveness. In addition, the simple

---

*Data were usually not recorded long enough to reach steady state after the cooling transients.

nitrogen property formulations used in calculating mixture properties at the wall could not be extrapolated below 250°R (140 K); therefore, heat transfer correlation coefficients were not calculated when the property reference temperature was below 250°R (140 K). Automatic card punching of the cooling transient temperatures for Tests 14B and C was not possible due to a time scale problem; the computer program modification required to rectify this problem was beyond the scope of the present effort.

VI. ANALYTICAL MODEL

A. FILM COOLANT EFFECTIVENESS

Before conducting the present test program, existing laboratory gas film cooling effectiveness data from Refs. 4-6 for plane, unaccelerated flow were correlated using the following dimensionless length:

$$\xi = \frac{x}{\left(\frac{\rho_c}{\rho_e}\right)^{1.15} f\left(\frac{u_c}{u_e}\right) Re_c^{0.25} s_c} \quad (1)$$

These data were obtained using air, helium, argon and Arcton 12 as the film coolants, with air as the mainstream flow in each case. They were selected for correlation because of the wide density ratio range provided (0.26 - 4.2), and because each set includes a meaningful range of velocity ratio. In addition, each investigator used a good slot design to provide film coolant flow parallel to the wall. Table V indicates the parameter ranges associated with each of the five sets of data. Use of the air-air data of Ref. 7 was also planned, since they represent density ratios of about 1.8 and 2.6; these ratios bracket the design range of interest and fill the gap between 1.4 and 4.2 in the other data. However, comparisons of Ref. 7 with the other five data sets were discouraging; further comparison evidently requires correcting for the preheating of the film coolant of Ref. 7.

The coolant effectiveness used herein is the total enthalpy effectiveness (see Appendix A), which is equal to the element concentration effectiveness assuming a turbulent Lewis number of unity. Therefore, it was possible to use the concentration measurements of Ref. 6 on the same basis as the wall temperature measurements of Refs. 4 and 5.

The above form for the correlating length ξ, but with a general function of density ratio and velocity ratio in the denominator, was assumed a

TABLE V. - FILM COOLING DATA PARAMETERS

Author (Ref.)	Coolant	Slot Height in.	Density Ratio	Velocity Ratio	Coolant Reynolds No.	Comments
Hatch & Papell (4)	Helium	.125-.5	.26-.39	.36-1.6	2820-45,000	Data for $1.49 \leq U_c/U_e \leq 3.83$ with $s_c = .125$ do not fit correlation. Mainstream at 1000°F.
Seban (5)	Air	.063-.25	.85-1.02	.29-9.5	930-6960	Data for $\eta < 0.3$ with $U_c/U_e \geq 3.5$ do not fit correlation.
Pai & Whitelaw (6)						Measured C_w instead of T_{aw}
	Air	0.1	1.0	.37-3.1	1285-10,500	
	Argon	0.1	1.38	.29-2.5	1065-8720	Data for $\eta < 0.3$ with $U_c/U_e = 0.29$ do not fit correlation
	Arcton 12	0.1	4.17	.28-1.65	2450-14,250	Data for $\eta < 0.5$ with $U_c/U_e = 0.28$ do not fit correlation

priori based on existing correlations and theory. In view of existing velocity ratio correlating functions valid for specific density ratios (e.g., Ref. 5), the primary purpose of the present effort was to clarify density ratio effects and, in particular, determine any interaction between density ratio and velocity ratio. The first step in developing the new correlation was to define the effect of density ratio at velocity ratios near unity. This was accomplished by plotting $x/(Re_c^{0.25} s_c)$ vs. density ratio for a given effectiveness. Figure 46 is a composite of three such plots (η = 0.5, 0.6 and 0.84) in which the air data of Ref. 6 have been used to normalize the ordinate. A linear fit of these results (log coordinates) yields a power-law exponent of about 1.15; note that the boundary layer entrainment model of Ref. 8 gives an exponent of unity, while Refs. 5 and 9 use an exponent of 1.5

Plotting $x/(Re_c^{0.25} s_c)$ vs. velocity ratio for a given effectiveness and density ratio indicated a 1.5 power dependence for all data with velocity ratios less than unity, thereby confirming the exponent of Ref. 5 and determining that velocity ratio and density ratio effects are separable in this range. Figure 47 is a composite of all these plots such that the 1.5 power fits for each effectiveness-density ratio combination coincide. Data for velocity ratios greater than unity have been included in Figure 47, except as noted below, and indicate the same behavior for all density ratios. Although such separability of velocity ratio and density ratio effects in this region is used herein, with the velocity ratio function given by the solid curve in Figure 47, additional data are required for confirmation. Figure 47 includes only 8 points with velocity ratios greater than 1.1 for which the density ratios are not near unity. In addition, the helium data (Ref. 4) are contradictory. Those for a slot height of 0.5 in. (1.3 cm) indicate a peak in $x/(Re_c^{0.25} s_c)$ near a velocity ratio of 1.2 consistent with the other data of Figure 47, while the 0.125 in. (0.32 cm) slot height data (not shown for u_c/u_e > 1.1) peak at a velocity ratio of almost two.

Figures 46 and 47 determined the correlating length of Eq. (1) based on data comparisons at a limited number of effectiveness values. Figure 48 shows all effectiveness data greater than 0.1 as a function of this length. The correlation obtained is quite good considering that the data represent three sources using two different measurement techniques and covering very wide ranges of density ratio, velocity ratio, coolant Reynolds number and slot height. Note that the helium data (Ref. 4) are generally higher than the rest for $\xi < 15$, but are slightly lower for $\xi > 20$. The greater lengths obtained at high effectiveness are undoubtedly due to differences in slot design and upstream core flow characteristics, while the ultimately lower effectiveness may be due to the high core temperature (810 K) used in Ref. 4. Some of the data (not shown) do not fit the correlation of Figure 48. In addition to the high velocity ratio helium data noted in the preceeding paragraph, these include the following: (1) the argon data below an effectiveness of about 0.3 for a velocity ratio of 0.29, (2) the Arcton 12 data below an effectiveness of about 0.5 for a velocity ratio of 0.28, and (3) the Seban air data below an effectiveness of about 0.3 for velocity ratios of 3.5 and greater. With the exception of the helium data these omissions are not considered to be significant, since they represent velocity ratios well outside the range of good design practice.

As expected, the data of Figure 48 indicate three distinct regimes. For $\xi < 0.6$ the mixing of core flow and film coolant has not penetrated to the wall, and the effectiveness remains at unity. A transition region is followed by the characteristic nearly-linear asymptotic region (slope ≈ -0.8) observed many times before; the latter starts at about $\xi = 20$. It was necessary to fit the data of Figure 48 with a fundamental model in order to provide a basis for extension to axisymmetric, accelerated flow with rocket engine turbulence intensities, combustion effects and coolant injection techniques. For this purpose, the entrainment model detailed in Appendix A was selected. This model represents explicitly the entrainment of core flow into a mixing layer which contains all of the film coolant; an enthalpy profile shape factor relates bulk mixing layer and adiabatic wall enthalpies. Therefore, an energy balance on the mixing layer gives the film cooling effectiveness as

$$\eta = \frac{W_c}{\Theta\,(W_c + W_E)} \qquad (2)$$

In the initial free-jet region of unity effectiveness, the increasing entrainment flow W_E merely reduces the shape factor Θ. At some distance from the film coolant injection point, the mixing layer profiles should become similar, in which case the shape factor is constant. Between these limits, core entrainment affects both the shape factor and the effectiveness.

The entrainment mass flux is represented as a fraction k of the axial mass velocity of the mainstream. This entrainment fraction was assumed to be independent of the distance from the injection point in correlating the plane, unaccelerated flow data. Therefore, the total entrainment flow at any location for these data is

$$W_E = k_o \rho_e u_e \, x$$

and the coolant effectiveness is

$$\eta = \frac{1}{\theta \left(1 + \dfrac{k_o x}{\dfrac{\rho_c}{\rho_e} \cdot \dfrac{u_c}{u_e} \, s_c} \right)} \qquad (3)$$

The solid curve of Figure 48 is the proposed entrainment model fit of the plane, unaccelerated flow data. For $\xi \geq 14$ the data of Figure 48 are fit by

$$\eta = \frac{1.32}{1 + 0.1\ \xi} \qquad (\xi \geq 14) \tag{4}$$

which by comparison with Eq. (3) gives an asymptotic shape factor of 0.76 and the following entrainment fraction:

$$k_o = \frac{0.1\ u_c/u_e}{\left(\frac{\rho_c}{\rho_e}\right)^{0.15} f\left(\frac{u_c}{u_e}\right) Re_c^{\ 0.25}} \tag{5}$$

The curve between $\xi = 0.6$ ($\eta = 1$) and $\xi = 14$, along with Eq. (3), defines the shape factor variation in the transition region; note that the shape factor is 0.94 at the start of this region.

In extending this model beyond the plane unaccelerated flow case, it was assumed that all results remain valid in terms of W_E/W_c. Therefore, since $W_E/W_c = 0.1\ \xi$ above,

$$\begin{aligned} \eta &= 1 && W_E/W_c \leq 0.06 \\ &= \frac{1}{\Theta\left(1 + \frac{W_E}{W_c}\right)} && 0.06 < W_E/W_c < 1.4 \\ &= \frac{1.32}{1 + \frac{W_E}{W_c}} && W_E/W_c \geq 1.4 \end{aligned} \tag{6}$$

with the transition region shape factor Θ defined by Figure 49. Generalization of the entrainment flow rate is presented in Appendix A along with the determination of the adiabatic wall temperature when chemical reactions occur. It remains to determine the effects of flow turning and acceleration, mainstream combustion and turbulence, and coolant injection geometry on the entrainment fraction k. Therefore, of primary interest in interpreting the present laboratory data and the firing data of Refs. 10 and 11 is the ratio k/k_o, i.e., the entrainment fraction multiplier required to account for those effects not present in plane, unaccelerated flow laboratory data with continuous slot coolant injection.

B. HEAT TRANSFER

The convective heat flux to a non-adiabatic wall with film cooling is calculated herein as

$$q = G \, St \, (H_{aw} - H_w) \, \rho_{ref}/\rho_e \tag{7}$$

in which H_{aw} is the adiabatic wall enthalpy defined by the coolant effectiveness (see Appendix A) and H_w is the enthalpy of the local gas mixture at the wall at the non-adiabatic wall temperature. The mixture ratio at the wall is also defined by the coolant effectiveness. Use of H_{aw} as the driving enthalpy is based on the assumption that the thermal boundary layer due to wall cooling or heating is small relative to the coolant mixing layer.

The Stanton number is evaluated from a modified turbulent pipe flow correlation,

$$St = C_{g_1}(x) \left[1 + g \left(\frac{u_c}{u_e} - 1\right)\right]^{0.8} Re_D^{-0.2} \, Pr_{ref}^{-0.6} \tag{8}$$

in which

C_{g_1} = position dependent correlation coefficient for a velocity ratio of unity

g = velocity mixing function, to be determined by the present laboratory data

Re_D = Reynolds number based on flow diameter, $\rho_{ref}\ GD/\rho_e \mu_{ref}$

Pr = Prandtl number

The reference properties (ρ, μ and Pr) are evaluated at the wall mixture ratio defined by the coolant effectiveness and at a reference temperature. Two reference temperatures were considered, the adiabatic wall temperature and the arithmetic mean of the adiabatic and non-adiabatic wall temperatures.

Based on previous experience it was expected that the laboratory heat transfer data would show that the above formulation would allow the same correlation coefficients to be used with and without film cooling. The effect of film cooling is accounted for by the use of the local gas composition in evaluating properties and by the velocity correction near the injection point. Analysis of the laboratory data in Section VII,B confirms this hypothesis.

C. COMPUTER PROGRAM

The computer program used in the design feasibility studies consists of four major parts, linked as shown in Figure 50: (1) a thermochemical subroutine THERM which calculates the mainstream expansion and is also used to compute gas mixture compositions and properties at the wall, (2) the film cooling module BARFC which uses the entrainment model of Appendix A to determine the coolant effectiveness and the resulting adiabatic wall enthalpy and wall mixture ratio, (3) the boundary condition subroutine TCALHG which calculates the wall heat transfer coefficient, and (4) the SINDA network analyzer. For adiabatic wall designs only THERM and BARFC are required.

None of these program components was developed originally on this contract. However, BARFC was modified to provide the entrainment fraction and shape factor correlations developed in Section VIA and to include a data analysis mode of operation to calculate average values of k/k_o between data stations. In addition, TCALHG was modified to include bracketed term in Eq. (8), which accounts for the effect of coolant injection velocity on the wall heat transfer coefficient.

VII. CORRELATION AND DISCUSSION OF LABORATORY TEST DATA

A separate data analysis program was developed to determine the adiabatic wall temperature and film coolant effectiveness from the steady-state wall temperature with film cooling and to calculate heat transfer coefficients and corresponding correlation coefficients from the transient and electrical heating data. A detailed discussion of these calculations is given in Appendix B, and the results are discussed in this section. Many of the adiabatic wall temperatures have been input to the data mode of the film cooling program, and the resulting entrainment fraction data are also presented below.

A. FILM COOLANT EFFECTIVENESS

1. Cylindrical Chamber with Ambient Coolant

Figure 51 shows the typical axial variation of adiabatic wall temperature obtained with the cylindrical chamber and ambient coolant. Shown for comparison is the predicted distribution from the model of Section VI,A using a uniform entrainment fraction multiplier of 1.5; this is essentially the prediction used to design the film coolant injector, with the 1.5 factor used to account for the expected turbulence intensity. Although the measured turbulence intensity (Section V,B) was less than expected, this prediction is in excellent agreement with the data in the cylindrical section. However, the measured temperatures in the convergent section and at the throat are much higher than predicted. This is attributed to turning effects at the start of convergence, which are subsequently investigated in detail. Predicted temperatures downstream of the throat change very little, since the additional mixing is offset by the imperfect recovery of kinetic energy. The significant decrease in measured wall temperatures downstream of the throat indicates that very little mixing occurs in this region. If the throat temperature is used to infer a stagnation temperature for the gas mixture at the wall in the throat, the expansion region temperatures can be predicted quite well assuming no further mixing and a recovery factor equal to the one-third power of the wall mixture Prandtl number.

Figure 52 shows the adiabatic wall temperatures from Test 5 and indicates the effect of injection velocity ratio. In general, these temperatures decrease as the velocity ratio increases in the range 0.79 to 1.18; however, increased temperatures are observed for a velocity ratio of 1.42 consistent with the model of Section VI,A. Figures 53 and 54 show the effects of injection velocity ratio and coolant Reynolds number on coolant effectiveness for all thermocouples in the cylindrical and nozzle sections, respectively, of the cylindrical chamber; the data scatter would be much less if each axial location were shown individually. The predicted effects of both parameters are shown for comparison; in Test 6, the coolant Reynolds number is half that of Test 5. Both the data and the predictions have been normalized by the results for lowest velocity ratio of Test 5. These data show a slightly greater reduction in effectiveness at the highest velocity ratio than predicted; the data indicate little or no effect of coolant Reynolds number for a fixed slot height. Figure 53 also shows the measured and predicted effect of slot height (0.038 cm for Test 7 compared with 0.152 cm for Test 5), with the predicted effectiveness slightly higher than the data; therefore, the coolant Reynolds number dependence of the entrainment model is required to predict the observed effect of slot height.

In order to examine in detail the magnitude and axial variation of the entrainment fractions implied by the results of Figures 51 and 52, the corresponding adiabatic wall temperatures were input to the data mode of the film cooling program. This mode determines the factor by which the entrainment fraction for plane, unaccelerated flow must be multiplied for the model to match the data. By using data from an entire row of thermocouples, these entrainment multipliers are obtained as averages between data stations.

Figure 55 shows the resulting entrainment fraction multipliers for the cylindrical chamber from Tests 3 and 4; the injection velocity ratio was about 0.8 in both tests. A multiplier of about 1.6 applies in the cylindrical section and presumably results from differences in turbulence intensity and injection geometry between the present tests and those used in defining the plane, unaccelerated entrainment fraction; in addition, mating of the injector and chamber in the present tests may have introduced a slight surface discontinuity. A multiplier of 1.5 was used in the design of the coolant injectors in this program. Very large entrainment multipliers are obtained in the first half of the convergent section. This is attributed to the turn at the start of convergence, which also affects the results shown at about 3.2 in. (8.1 cm) since the downstream thermocouple for this region is about 0.05 in. (0.13 cm) past the start of convergence. Since the core flow in these tests was much heavier than the coolant, the former cannot turn as easily. Therefore, at the start of convergence the coolant turns into the core, resulting in much greater mixing. Conversely, at the throat the coolant turns away from the core, resulting in the very low multipliers shown in Figure 55 for the first part of the expansion section. Analysis of convergent section effectiveness data from Ref. 12, for which the coolant was heavier than the core, shows greatly reduced mixing in the initial turn and increased mixing in the throat curve consistent with the above explanation of turning effects; these results are presented in Section VII,A,6. Figure 55 shows two different trends in the second part of the expansion section, one indicating sharply increased mixing and the other yielding negative entrainment mass fluxes.

Figure 56 presents the entrainment multipliers inferred from Test 5 for all velocity ratios. Essentially the same trends observed above in Figure 55 are repeated. However, for the first two axial locations, an increase in coolant injection velocity increases the multiplier, perhaps indicating that a wall discontinuity at the injector-chamber interface is affecting the mixing process. No data in the second part of the divergent section are available from this test.

A more detailed spatial variation of the entrainment fraction multiplier was inferred by supplying graphically interpolated adiabatic wall temperatures to the data mode of the film cooling program. The resulting entrainment fraction multiplier curve selected for the cylindrical chamber is shown in Figure 57. It illustrates the significant effects of flow turning, both at the start of convergence and in the throat, for the case in which the coolant is much less dense than the core flow. Using this multiplier variation, Figure 58 shows the correlation of all film coolant effectiveness results from the cylindrical chamber with ambient coolant (Tests 3 to 7), encompassing variations in injection velocity ratio, coolant Reynolds number and slot height. The solid curve in Figure 58 is the correlation developed in Section VI,A from plane, unaccelerated flow data. Therefore, use of a single entrainment fraction multiplier curve allows all cylindrical chamber effectiveness data to be correlated on the same basis as plane, unaccelerated flow data, and the present results extend the validity of this correlation from an effectiveness of 0.1 to a value of 0.02.

2. Conical Chamber

Figure 59 compares the axial variation of the adiabatic wall temperatures for the conical and cylindrical chambers. The higher temperatures in the conical chamber convergent section compared to the cylindrical part of the cylindrical chamber are to be expected due to the higher core mass velocities and possibly increased mixing resulting from the turn into the conical section. Core entrainment into the mixing layer is low enough upstream of the throat in the conical chamber to allow the imperfect recovery of kinetic energy at the throat to reduce the adiabatic wall temperature there to the same value obtained 0.6 in. (1.5 cm) upstream. The significant decrease in measured wall temperature downstream of the throat is repeated for the conical chamber. Figure 60 shows all adiabatic wall temperatures for the conical chamber. In contrast to the cylindrical chamber data, these temperatures continue to decrease slightly for the highest injection velocity ratio tested.

Figure 61 gives the entrainment fraction multipliers for the conical chamber. The initial results again indicate an increase with velocity ratio. These initial multipliers are consistently somewhat higher than those for the cylindrical chamber, again indicating increased mixing due to the turn at the start of convergence. For the conical chamber, the entrainment multiplier decreases throughout the convergent section, reaching a value of unity just upstream of the throat. A multiplier of unity is maintained just downstream of the throat in contrast to the much lower values obtained with the cylindrical chamber. This difference may be caused by the much smaller turning angle coming into the throat of the conical chamber; both chambers have the same turn downstream of the throat. The results in the second part of the divergent section are again inconsistent; some large negative multipliers in this region have been omitted from Figure 61.

Figure 61 also shows the entrainment fraction multiplier curve selected for the conical chamber. Beyond the first thermocouple location (1.85 cm), this curve was obtained directly from the data shown. The initial multiplier was taken as the mean of the two values obtained between the inlet and the first thermocouple location for the cylindrical chamber with an injection velocity ratio of 0.95 (see Figure 56). The effect of the turn at the start of convergence in the conical chamber was then inferred by requiring the peak multiplier in the turn to yield an integrated average between the inlet and the first thermocouple location equal to the mean of the two values shown for a velocity ratio of 0.99. For all comparable velocity ratios, the average multiplier in this region is higher for the conical chamber, presumably due to the turn. Although this procedure is crude and not unique for the correlation of the initial thermocouple data, it does provide some insight into possible turning effects in the conical chamber. Note that the throat turn has little effect on the entrainment fraction. Figure 62 shows the resulting correlation of conical chamber effectiveness data using the entrainment fraction multiplier curve of Figure 61.

3. Rectangular Chamber

Although the distortion of the rectangular chamber (Section V,F) reduced the quantity and quality of the adiabatic wall temperature data, a comparison has been made of the resultant coolant effectiveness data with those presented above for the conical chamber. Rectangular chamber data obtained at and downstream of the throat were not considered due to the turning effects introduced by the change in distortion just upstream of the throat. Assuming no sidewall interaction, an entrainment flow analysis for the rectangular chamber analogous to that of Section VI,A for axisymmetric chambers yields:

$$\frac{W_E}{W_c} = \frac{k_o \bar{x}}{\frac{\rho_c}{\rho_e} \cdot \frac{u_c}{u_e} s_o}$$

in which

$$\bar{x} = \int_o^x \frac{d_o}{d} k_m \, dx$$

Uncertainty in the local chamber height d due to distortion should have a relatively small effect on the entrainment prediction. Figure 63 shows the effectiveness data as a function of the above entrainment flow ratio, with the correlation of Section VI,A shown for comparison. The entrainment fraction multiplier k_m for the conical chamber (solid curve of Figure 61) was used in order to compare the rectangular and conical results. If this multiplier curve were also valid for the rectangular configuration, which has similar convergence characteristics, the rectangular data would agree with the correlation curve. It is apparent from Figure 63 that this is not the case, with most of the rectangular data indicating a higher effectiveness than that predicted based on conical chamber entrainment characteristics. Additional data, without chamber distortion, are required to define the turning and acceleration characteristics of rectangular chambers.

4. Cold Gaseous Coolant

Figure 64 shows the adiabatic wall temperature data obtained in Tests 8 and 10 with the cylindrical chamber using film coolant conditioned by a liquid nitrogen heat exchanger before entering the 0.015 in. (0.038 cm) coolant ring, thereby providing a higher injection density ratio. All corresponding coolant effectiveness data are considerably lower than would be predicted based on the model of Section VI,A and the previous ambient coolant entrainment fraction multipliers. There is no reason to suspect such a prediction in the cylindrical section, since the correlation for the plane, unaccelerated entrainment fraction k was developed from data covering a wide range of density ratio, including the ratios obtained herein with cold gas. Furthermore, since the calculated coolant temperature rise in the injection slot is less than 10°F (6°K), the injection temperature is considered to be reasonably well known.

These data were input to the data analysis mode of the film cooling program in order to generate average entrainment fraction multipliers between data stations. As shown in Figure 65, very high multipliers were obtained between the injection point and the first data station, while downstream values were more typical of the results obtained with ambient coolant. If a coolant temperature effect were missing in the entrainment fraction correlation, or if the present density ratio effect were incorrect, all multipliers would have been higher than those obtained previously with ambient coolant. Therefore, the high wall temperatures at the first thermocouple location are not attributed to any unexpected mixing phenomenon, but rather to heat transfer from the forward chamber flange to the cold coolant and from the flange through the chamber wall to the thermocouples.

5. Liquid Hydrogen Coolant

The "liquid" hydrogen adiabatic wall temperature data are undoubtedly affected by the same flange problem noted above for cold gaseous coolant. These temperatures are shown in Figures 66 and 67 for the supercritical and subcritical tests, respectively. A second problem is apparent in the latter test, i.e., the possibility that nitrogen from the core flow was condensing in the mixing layer or on the wall. Such an occurrence would impose a lower limit on the measured temperature in the range observed in Figure 67; in several cases, this limit is observed for three successive thermocouples and, in one case, for four. When nitrogen condensation occurs, the adiabatic wall temperature does not define a coolant effectiveness.

6. Correlation of Turning and Acceleration Effects

The empirical entrainment fraction multipliers derived above from the present film coolant effectiveness data indicate significant flow turning effects, which have been attributed to the imbalance in centrifugal forces resulting from density differences between the coolant and core flows. However, these multipliers also include any effect on the entrainment fraction of flow acceleration, which must be identified separately in order to segregate the effects of turning. An acceleration correlation suggested by the work of Deissler (Refs. 13 and 14) on transverse turbulent transport in a homogeneous fluid was considered herein; Ref. 15 indicates that this approach adequately represents the effect of acceleration on Stanton number measured in Ref. 16. The proposed correlation is

$$k_a = \left[\frac{\rho_e u_e}{(\rho_e u_e)_o}\right]^{-n}$$

with Deissler's work indicating an exponent n of about 0.6. This correlation fits quite well with the gradual entrainment fraction decay observed in Figure 61 for most of the conical chamber convergent section, with the exponent n equal to 0.67. Also compared with this correlation were the effectiveness data of Ref. 17, in which blisters on the wall opposite the film-cooled plate were used to provide core acceleration without coolant turning. However, these data were inconsistent; some indicated very strong acceleration effects ($n > 1$), some indicated augmentation of the entrainment fraction due to acceleration (n negative), and in one case the data upstream of the blister were not consistent with the present entrainment model. Therefore, additional data are required to isolate the effects of flow acceleration on entrainment fraction.

In order to confirm the turning effects observed herein and their postulated dependence on coolant-core density differences, the adiabatic wall temperature data of Ref. 12 were analyzed. In these tests, the coolant was considerably heavier than the core, thereby providing the opposite situation from the present tests. Only one of the three configurations of Ref. 12 was considered; this nozzle has a 0.6 in. (1.5 cm) long cylindrical section, followed by a convergent section consisting of two circular arcs (10 cm radius of curvature) with no conical section between. The maximum convergence angle is 35 degrees, and the contraction ratio is 15.3. The other nozzle was not considered because its very large convergence angles (74° maximum) are well outside the range of rocket engine application. Axial conduction effects in the cylindrical configuration precluded the use of data without flow acceleration and turning to determine an entrainment fraction multiplier associated with turbulence intensity and injection effects. Figure 68 shows the entrainment fraction multipliers inferred for the highest injection velocity ratio (0.67). Comparison of these results with Figure 57 indicates the turning effects are reversed from those observed herein, which is exactly what would be expected when the coolant density exceeds that of the core. An entrainment fraction reduction in the turn at the start of convergence in this case is confirmed by the data of Ref. 10, which is discussed in detail in Section VIII,A,3.

The parameter proposed to correlate turning effects on the entrainment fraction is one defining the magnitude of the differential centrifugal force resulting from the density difference across the mixing layer relative to the turbulent shear force which otherwise accounts for the mixing process. This centrifugal force is proportional to

$$(\rho_e - \rho_w) \frac{V^2}{R}$$

in which V is some characteristic velocity in the mixing layer and R is the turn radius of curvature; the conventional turbulent shear force is proportional to

$$\frac{\bar{\rho} \; \varepsilon \; V}{s^2}$$

A common representation of the eddy viscosity ε assumes it is proportional to sV, which indicates the ratio of centrifugal to turbulent shear forces is proportional to

$$\frac{\rho_e - \rho_w}{\bar{\rho}} \cdot \frac{s}{R}$$

This is the parameter proposed for the correlation of turning effects. Figure 69 shows the limited turning data developed herein as a function of this parameter*. The trends are correct but much more data, including details within the turns as in Ref. 12, are required to develop a correlation.

---

*These data include any acceleration effects.

B. HEAT TRANSFER DATA

The data analysis program generated two correlation coefficients from the inferred heat transfer coefficients (see Section 6 of Appendix B) using the pipe-flow correlation of Eq. (8); they differ only in the reference temperature used for properly evaluation and correspond to the product of the first two terms in Eq. (8). One is based on the adiabatic wall temperature, and the other is based on the arithmetic mean of the adiabatic and nonadiabatic wall temperatures. The correlation coefficients discussed herein are based on the arithmetic mean temperature. With gaseous coolant, this reference temperature was found to provide an excellent correlation of the wall temperature effect observed from the electrical heating data, and it allows use of the same correlation with and without film cooling.

Figure 70 shows the nitrogen heat transfer coefficients for the high pressure tests (3, 4 and 5A) with the cylindrical chamber and 0.060 in. (0.152 cm) coolant slot; Figure 71 gives the corresponding correlation coefficients. Individual data points are shown in the electrically heated section, since Test 3 was the only test with fast response thermocouples in this section. Downstream of the electrical section the circles represent the average of the data, while the bars indicate the data range. The high initial coefficients and subsequent decay are caused by the 0.080 in. (0.203 cm) wall discontinuity which occurs at the end of the coolant injector without coolant flow. However, 2.8 in. (7.1 cm) downstream of this step the correlation coefficient has reached the fully developed turbulent pipe flow range. The higher coefficients obtained just after the start of convergence may be due to the switch from spring-loaded to spot-welded thermocouples or may indicate flow separation, a phenomenon that has been observed previously (Ref. 18). Much lower correlating coefficients, typical of highly accelerated flows, are obtained midway through the convergent section. The subsequent large increase in correlating coefficient at the throat, to values slightly above the pipe-flow range, is a surprise; a much smaller increase was anticipated. At the throat a decrease in heat transfer coefficient with time was observed, which is considered to be due to axial wall conduction effects since the throat responds so much faster than neighboring regions. Throat data are from early in the transient; later results would represent a net coefficient including the axial conduction effects.

Figure 72 shows the cooling transient heat transfer coefficients from Tests 3 and 5 along with the steady-state coefficients from Test 5 for the highest electrical power level; the electrically heated data consistently show a decrease in the coefficient as the power level and wall temperature increases. The transient data follow the spatial dependence of the nitrogen coefficients, but are much higher as expected. Coefficients near the coolant injector, where the hydrogen concentration at the wall is high, are more than twice the nitrogen values even though the coolant was injected at a lower velocity. The steady-state coefficients at the lowest coolant flow rate are even higher than the transient values. This discrepancy cannot be attributed to local wall temperature differences; it may be due to the mica and the contact resistances between the spring-loaded thermocouples and the electrically heated wall. Figure 72 shows a dramatic effect near the injector of the coolant injection velocity, which is advantageous for the internal regenerative design concept. At the first data location, the heat transfer coefficient is approximately proportional to the 0.8 power of the injection velocity. Mixing of the coolant and core flows gradually dissipates this dependence farther downstream; although injection effects are still apparent at the last measurement in the electrically heated section, they have essentially disappeared at the start of convergence.

Figure 73 shows the correlation coefficients for all data of Figure 72. This coefficient provides an excellent correlation of the electrically heated data; therefore, the average value for the three power levels is shown. Comparison of the cooling transient coefficients with the heating transient values of Figure 71 reveals these results are the same except for a reduction with cooling at the throat. This result demonstrates the basic premise that, except for the effect of injection velocity near the injection point, the effect of film cooling on the heat transfer coefficient can be accounted for by using the wall mixture properties defined by the coolant effectiveness. Correlation of the effect of injection velocity is considered later in this section. Correlation coefficients with cooling for the low pressure test with the cylindrical chamber (Test 6) are shown in Figure 74; they are very similar to those of Figure 73, although the throat values are somewhat lower (0.016 to 0.018). This difference is consistent with the fact that acceleration effects are more pronounced at lower chamber pressures.

Figures 75 to 77 present the correlation coefficients obtained from the cylindrical chamber with the 0.015 in. (0.038 cm) coolant slot. Figure 75 shows the coefficients without coolant flow, which may be compared with Figure 71 for the 0.060 in. (0.152 cm) slot height. However, in the cylindrical section the results of Figure 75 are from electrical heating data, while those in Figure 71 are from heating transient data. These results are the same at the initial data locations, but the 0.015 in. (0.038 cm) slot data are then higher; Figures 72 and 73 indicated that electrical heating coefficients would tend to be higher than transient values. In the convergent section, the coefficients for the 0.015 in. (0.038 cm) slot height are slightly lower than those for the 0.060 in. (0.152 cm) slot. At the throat and beyond the two results are virtually identical. Figure 76 shows the correlation coefficients obtained with ambient coolant, while Figure 77 shows those obtained with cold hydrogen gas (Tests 8 and 10). These results are essentially the same, but are a little lower than those in Figure 75 without coolant and those in Figure 73 with the 0.060 in. (0.152 cm) slot. Note that a high velocity ratio does not yield a high coefficient in Figure 76 as it does in Figures 73, 74 and 77. This result is consistent with the fact that the combination of ambient coolant with the small slot height results in much greater mixing and lower coolant effectiveness (see Figure 53); therefore, injection velocity effects are dissipated much faster. No cooling transient data for the nozzle section are available from these tests due to poor coolant system flow transient response, as discussed in Section V.

Figures 78 and 79 show the heat transfer coefficients and corresponding correlation coefficients for the conical chamber without coolant flow. Figures 80 and 81 give the same results with ambient coolant flow. These results are analogous to those in Figures 70 to 73 for the cylindrical chamber, although all conical results were obtained from transient data; the same coolant injector was used with both chambers. The conical chamber results again illustrate the much greater heat transfer coefficients obtained with hydrogen film cooling and the significant effect of coolant injection velocity; in this chamber, the injection velocity effects persist all the way to the throat. Heat transfer coefficients 0.6 in. (1.5 cm) upstream of the throat are essentially the same as those at the throat. Correlation coefficients with film cooling for a velocity ratio of unity are somewhat higher than those without cooling for the first few axial locations, but then are essentially the same.

Correlation of the effect of coolant injection velocity on the wall heat transfer coefficient was investigated using the relation of Eq. (8), i.e.,

$$C_g = C_{g_1} \left[1 + g\ (W_E/W_c)\ (\frac{u_c}{u_e} - 1)\right]^{0.8}$$

in which C_{g_1} is the heat transfer correlation coefficient for an injection velocity ratio (u_c/u_e) of unity. The function g defines the decay due to mixing of the velocity differential between the coolant and core flows. If the turbulent Prandtl number were unity, the analogy between momentum and energy mixing would establish g as being equal to the coolant effectiveness for the case of small temperature differentials. The first five data locations in Tests 5 and 6 were used to infer g from the measured C_g values. Figure 82 shows these results as a function of the entrainment flow ratio, with the effectiveness correlation shown for comparison. Significant scatter in g and an inability to calculate small values results from the fact that g is very sensitive to small variations in the measured heat transfer coefficients.

In order to account for injection velocity effects on the heat transfer coefficients used in the subsequent design study of the internal regenerative cooling concept, the velocity decay function data of Figure 82 were correlated using the same three-region entrainment framework employed in Section VI,A for the coolant effectiveness. This correlation is shown as the solid curve in Figure 82. It was assumed that the momentum entrainment ratio was proportional to the energy entrainment ratio W_E/W_c; the proportionality constant was found to be 0.9, which is consistent with typical turbulent Prandtl numbers. Therefore, the velocity decay correlation is

$$g = \frac{1}{\theta_v \left(1 + 0.9 \frac{W_E}{W_c}\right)} \qquad (9)$$

with the velocity profile shape factor θ_v defined in three regions analogous to its enthalpy profile counterpart θ. In the initial free-jet region, defined by $W_E/W_c \leq 0.85$, g is unity and Eq. (9) defines θ_v; note that the data of Figure 82 require this region to be much longer than in the case of the coolant effectiveness. However, the asymptotic region has been defined consistent with the effectiveness correlation, i.e., $0.9\ W_E/W_c \geq 1.4$. In the asymptotic region θ_v is 0.5, and in the short transition region it is defined by Eq. (9) and the correlation curve of Figure 82. Figure 49 includes the velocity profile shape factor variation with W_E/W_c. A cursory study of the conical chamber heat transfer data indicated g decayed less rapidly and could not be represented by the above correlation.

Heat transfer coefficients and the corresponding correlation coefficients with film cooling in the rectangular chamber are significantly lower than those in the conical chamber. This result may be due to the increase in flow area caused by deflection and thermal expansion of the two thin walls, in which case the calculated correlation coefficients are in error since they were calculated for the cold, unpressurized geometry. Heat transfer coefficients without film cooling are closer to the conical chamber values but are still lower than the latter.

Tests 13 and 14 heat transfer data are inconsistent for the first two or three thermocouple locations, a result undoubtedly related to the problems discussed in Section V,G. Some of the correlation coefficients at other locations are in reasonable agreement with those of Test 5 for ambient gaseous coolant. However, the correlation coefficient does not account in many cases for the wall temperature effects observed with electrical heating, although these effects are frequently not consistent between runs and between the increasing and decreasing heat flux segments of Tests 13B and 14B.

VIII. DESIGN FEASIBILITY INVESTIGATION

Two chamber cooling concepts were investigated in the design feasibility study: film-cooled adiabatic walls and internal regenerative cooling. The applicability of each concept was considered only for the Space Shuttle APS Engine conditions of 1500 lbs (6670 N) thrust at 300 psia (207 N/cm^2) chamber pressure, with gaseous oxygen and gaseous hydrogen as the propellants at 375°R and 250°R (210 and 140 K), respectively.

A. ADIABATIC WALLS

The adiabatic wall design study was conducted in three parts. In the first part the coolant injection temperature, velocity ratio and location were varied for a fixed chamber contour and an overall mixture ratio of 4. When combined with the heat transfer characteristics of specific propellant injectors, these results provide for the design of chambers in which the film coolant flows through a sleeve or shroud prior to injection. In the second part the effect of overall mixture ratio on the required coolant flow was determined for a fixed injection temperature and location but at several velocity ratios. Finally, the combustion chamber contour was varied with all other design parameters fixed; thirteen configurations, both cylindrical and conical, were considered.

A conical combustion chamber with an L' of 5.75 in. (14.6 cm) was selected for the injection parameter and mixture ratio studies, since the results of Contract NAS 3-14354 (Refs. 10 and 11) and related IR&D work indicated this was a high-performance configuration for the APS application. The expansion section contour was identical to that used for altitude simulation testing on Contract NAS 3-14354; this contour and the three conical combustion chamber configurations used in the adiabatic wall study are shown in Figure 83. All adiabatic wall temperature calculations were terminated 4 in. (10 cm) downstream of the throat, since internal radiation losses through the exit of a 40:1

nozzle start to affect the wall temperature in this region. In most cases, the adiabatic wall temperature is increasing very slowly at the 4 in. (10 cm) point so that the actual wall temperature will decrease downstream due to the radiation loss.

Entrainment fraction multipliers k/k_o used in the design studies were determined from the adiabatic wall temperature data of Contract NAS 3-14354, Refs. 10 and 11. These data were processed by the data analysis mode of the film cooling program used herein. The resulting entrainment fraction multipliers account for the effects of propellant injection and combustion, practical coolant slot configuration and flow turning and acceleration. Insufficient data were available to separate turning and acceleration effects from injection characteristics, and as noted in Section VII,A general correlations accounting for turning and acceleration are not available. Therefore, the combined entrainment fraction multipliers of Refs. 10 and 11 were used directly in the present design study. They are considered to be representative of practical designs, but cannot account in detail for specific combustion chamber contour variations considered herein.

Entrainment fraction multipliers used with the conical combustion chambers are illustrated in Figure 84 for a chamber with an L' of 4 in. (10 cm). In all conical cases the multiplier was varied linearly with axial distance, from 3.5 at the coolant injection point to 1.75 at the throat. This variation is based on the data of Ref. 11 for coolant injection in a conical section, with the injection point 1.25 in. (3.2 cm) upstream of the throat; the expansion section multipliers shown in Figure 84 are also based on these data. Note that such a conical convergent section variation is also consistent with the acceleration correlation discussed in Section VII,A,6.

1. Injection Parameter Study

In the injection parameter study the coolant injection temperature was varied from 250°R to 800°R (140-440K) for injection locations 0, 2 and 4 in. (0, 5 and 10 cm) downstream of the propellant injector in a 5.75 in. (14.6 cm) conical combustion chamber. For each combination of injection temperature and location, the coolant/core (combustion gas) velocity ratio was varied from 0.75 to 1.25; for selected combinations this variation was 0.5-1.5. The upper injection temperature of 800°R (440 K) was set by enthalpy limitations in the present computer program.

Figure 85 shows the film coolant flows required to maintain throat wall temperatures of 1500°F and 1800°F (1090 and 1260K) for an injection velocity ratio of unity.* Structural analyses indicate a throat temperature limit of about 1500°F (1090 K) is required to meet Space Shuttle APS life and cycle requirements. However, life requirements could be met with a higher temperature and thicker wall in applications with less severe cycle requirements; for this reason the 1800°F (1260 K) limit has also been shown. If throat temperatures are limited to the 1500-1800°F (1090-1260 K) range, the maximum wall temperature occurs downstream in the nozzle section. However, stresses are much lower here so higher wall temperatures can be accommodated. With a 1500°F (1090 K) throat, all nozzle wall temperatures were calculated to be less than 1900°F (1310 K), which could be accommodated with appropriate material selection. Therefore, the most pertinent wall temperature limit is considered to be the 1500°F (1090 K) throat limit shown in Figure 85. However, depending on material selection and cycle requirements, nozzle temperatures could be limiting. Therefore, Figure 86 gives the coolant flows required to limit nozzle temperatures to 1800°F (1260 K) for an injection velocity ratio of unity. For injection at the propellant injector or 2 in. (5 cm) downstream, these flows are slightly higher than the corresponding values for an 1800°F (1260 K) throat; however, for injection 4 in. (10 cm) downstream they are slightly higher than those for a 1500°F (1090K) throat limit.

---

*Results for an 1800°F (1260 K) limit with a 4 in. (10 cm) sleeve are not available.

It is apparent from the latter result that the wall temperature increase downstream of the throat is greater as the injection point moves closer to the throat. With the injection point close to the throat, the entrainment flow downstream of the throat is a much larger percentage of the total and results in a greater change in coolant effectiveness. Figure 87 illustrates the axial variation of the adiabatic wall temperature for the two extreme coolant injection locations. Note that with injection 5.75 in. (14.6 cm) upstream of the throat (i.e., at the propellant injector), the imperfect recovery of kinetic energy almost completely compensates for the relatively small additional entrainment below the throat and results in very little increase in the adiabatic wall temperature. The coolant requirements of the Figure 86 are based on correcting the adiabatic wall temperatures for radiation losses through the exit of a 40:1 nozzle assuming a inside surface emmissivity of 0.8. As noted previously, this reduction is small at the point 4 in. (10 cm) downstream of the throat where the calculations were terminated; for example, it is 30°F (17 K) for the downstream injection case in Figure 87. Therefore, Figure 87 indicates the predicted nozzle wall temperatures may be slightly lower than the maximum values reached farther downstream in those cases where coolant injection is 4 in. (10 cm) downstream of the propellant injector.

In order to utilize the results of Figures 85 and 86 for designs in which the coolant flows through a shroud or sleeve from the propellant injector to the point at which it is injected as film coolant, it is necessary to use the coolant energy balance in the sleeve to define the injection temperature. Since this energy balance is dependent on the coolant flow rate, it must be solved simultaneously with the results of Figure 85 or 86 to determine the coolant flow required. This situation is illustrated in Figure 88 using typical combustion chamber heat fluxes from Contract NAS 3-14354 test data, a coolant temperature of 250°R (140 K) at the sleeve inlet and a limiting throat temperature of 1500°F (1090 K) from Figure 85. Under these conditions, the following film coolant requirements are determined as a function of sleeve length:

Sleeve Length, in.	Coolant Flow, % of Fuel
0	25.1
2	23.5
4	17.6

Figures 85 and 86 provide for the analysis of sleeve inlet temperatures as high as 650°R and 325°R (360 and 180K) for sleeve lengths of 2 and 4 in. (5 and 10 cm), respectively.

All results presented above are for a coolant/core injection velocity ratio of unity. It was found that the effect of velocity ratio is essentially independent of all other design parameters, including overall mixture ratio. Figure 89 shows the percentage increase in coolant flow, relative to a velocity ratio of unity, required to maintain a specified adiabatic wall temperature at a specified location. The range of calculated coolant requirements at each velocity ratio investigated is seen to be quite small. However, the effect of velocity ratio is very significant and indicates the importance of proper coolant slot sizing.

Performance losses attributable to the film coolant requirements presented herein may be determined from Figure 90. These results were predicted using the Aerojet-developed Thermal Exchange Film Coolant Performance Model, the validity of which has been demonstrated over a wide range of coolant flows and overall mixture ratios on both the low and high pressure phases of Contract NAS 3-14354 (Ref. 11). This performance loss results from a combination of three factors: off-design combustion kinetics due to the core mixture ratio shift, unequal stream tube specific impulse and energy removal from the core flow. The latter factor accounts for the specific impulse reduction which occurs in the core gases as the film coolant is heated along the chamber and nozzle walls, thereby simulating the lower specific impulse of the entrained flow in the actual mixing process.

2. Overall Mixture Ratio Effect

The above results and those presented in the next section for various combustion chamber configurations are for an overall mixture ratio of 4. Mixture ratio effects were considered for a coolant inlet temperature of 250°F (140 K), with injection at the propellant injector of the 5.75 in. (14.6 cm) conical combustion chamber considered above. Figure 91 shows the throat wall temperature as a function of coolant flow for an injection velocity ratio of unity* with overall mixture ratios of 3, 4 and 5; it indicates the expected increase in wall temperature as the mixture ratio is increased for a fixed coolant flow. Coolant flow requirements as a function of mixture ratio for a throat temperature of 1500°F (1090 K) are shown in Figure 92a, both as a percentage of total flow and of fuel flow. Increasing the mixture ratio from 3 to 5 requires a 29 percent increase in the absolute coolant flow rate.

Figure 92b combines the results of Figures 90 and 92a to show coolant performance loss as a function of overall mixture ratio with the coolant flow varying to provide a 1500°F (1090 K) throat wall temperature. The specific impulse obtained by subtracting this loss from the ideal performance is also shown. It indicates an overall mixture ratio of 3 is near optimum; however, the mixture ratio dependence of other performance losses could shift the optimum value.

---

*Velocity ratio effects for the additional mixture ratios considered here are included in Figure 89.

3. Combustion Chamber Contour Study

Two additional conical combustion chambers and eleven cylindrical configurations were considered for injection of 250°R (140 K) coolant at the propellant injector with an injection velocity ratio of unity; the overall mixture ratio was 4. The additional conical chambers are included in Figure 83; they provide longer and shorter combustion chamber lengths with the same contraction ratio (3.15) used above. Figure 93 gives the resultant coolant flow requirement as a function of chamber length (L') for a throat wall temperature of 1500°F (1090 K); increasing L' from 4 to 7.5 inches (10 to 19 cm) increases the absolute coolant flow required by 67 percent.

The various cylindrical combustion chambers investigated represent five different convergent section contours; various chamber lengths were obtained by using different cylindrical section lengths with each convergent section contour. Table VI gives the combinations of convergence angle and contraction ratio investigated. In each case the radius of curvature at the start of convergence was 2.88 in. (7.31 cm or 2.5 r_t), and that leading into the throat was 1.92 in. (4.88 cm or 2 r_t) as for the conical chambers. The convergence angle of 23 degrees was selected to match the configuration tested in Contract NAS 3-14354, Ref. 10. Selection of the smaller angle was based on obtaining a combustion chamber length of 4 in. (10 cm) without a cylindrical section, while the larger angle results in no conical section between the circular arcs. The smallest contraction ratio in Table VI corresponds to that of the conical chambers, while the value of 3.59 matches that tested in Ref. 10. The latter contour is included in Figure 83 for a chamber length of 4 in. (10 cm), and the corresponding entrainment fraction multipliers inferred from Ref. 10 are shown in Figure 84. An entrainment fraction multiplier of 4 was used throughout all cylindrical sections. For the shorter convergent sections the regions of decreasing and constant entrainment fraction multiplier were assumed to be in the same proportion as in Figure 84, while for the longer convergent sections the length of the constant entrainment multiplier section was maintained at 1.4 in. (3.6 cm).

TABLE VI. - COMPARISON OF CYLINDRICAL COMBUSTION CHAMBER CONFIGURATIONS

Convergence Angle, Degrees	Contraction Ratio	Coolant Flow*, % of Fuel	
		L' = 4	L' = 7.5
12.03	3.15	17.4	32.8
23.05	3.15	18.3	33.6
	3.59**	17.6	32.1
	4.13	17.1	31.0
32.35	3.15	18.5	34.0

---

*For a throat adiabatic wall temperature of 1500°F.

**This combination tested in Contract NAS 3-14354.

Development of the cylindrical chamber entrainment fraction multipliers of Figure 84 from the data of Ref. 10 reflects turning effects consistent with the data of Figure 68. An average entrainment multiplier of 3.5 was obtained over a 1.5 in. (3.8 cm) cylindrical section plus the first 1.6 in. (4.1 cm) of the convergent section. When the injection point was moved forward to the start of convergence, a multiplier of 2.5 was obtained over the first 1.6 in. (4.1 cm) of the convergent section. This reduction is consistent with the initial turn effect shown in Figure 68 and the increased coolant/core density ratio at the start of the turn, which would enhance the turning effect. Because of the density ratio effect, the average multiplier in this section with upstream injection would be greater than 2.5. Therefore, to interpret the average multiplier of 3.5 obtained with upstream injection in the light of demonstrated turning effects, requires an average multiplier greater than 3.5 in the cylindrical section with an average value less than 3.5 but greater than 2.5 in the first 1.6 in. (4.1 cm) of the convergent section. The entrainment multiplier variation in Figure 84 was selected to provide the average value of 3.5 noted above within these constraints and to merge with the multiplier of 1.75 measured over the final 1.4 in. (3.1 cm) of the convergent section.

Table VI gives the effects of convergent section contour on coolant requirements for combustion chamber lengths of 4 and 7.5 in. (10 and 19 cm) based on a throat wall temperature of 1500°F (1090 K). A slight increase in coolant flow is required with increasing convergence angle due to the longer application of the high initial entrainment fraction. However, it must be remembered that the present entrainment fraction multipliers are based on data for a single convergence angle, so the present results relative to convergence angle are speculative. Note that the 12 degree chamber with a 4 inch (10 cm) length has no cylindrical section, so that except for the curvature at the start of convergence it is like the conical chamber considered previously but with alternate entrainment fraction multipliers (Figure 84). Figure 93 indicates a coolant flow requirement of 18.7 percent of the fuel for the conical chamber compared with 17.4 percent for the so-called cylindrical chamber of Table VI, a result of the higher entrainment multipliers near the throat for the former. Table VI shows the coolant requirement decreases slightly with increasing contraction ratio, due to the reduction in length and mass velocity for the cylindrical section with its high entrainment multiplier. An intermediate chamber length was also analyzed for the second configuration in Table VI, and the coolant requirement as a function of L' for this chamber is included in Figure 93. Increases in chamber length in this case are increases in the cylindrical section length with its high entrainment multiplier, so the coolant requirement increases faster than for the conical chambers.

B. INTERNAL REGENERATIVE COOLING

In the internal regenerative cooling concept heat is conducted axially from the throat region and part of the nozzle through a thick high conductivity wall to the forward end of the chamber, where it is transferred by convection to the low temperature film coolant; the downstream effectiveness of the film coolant also reduces the heat transfer to the throat region and nozzle, thereby reducing the amount of heat which must be conducted axially through the wall. This concept has been demonstrated for low pressure ($\leq$ 150 psia), low thrust ($\leq$ 1000 lbs) applications with earth storable propellants using liquid film cooling. Its extension to gaseous hydrogen film cooling is of interest in view of the very high heat transfer coefficients obtained near the coolant injection point in the present laboratory tests and the potential coolant flow reductions relative to adiabatic wall chambers.

The present investigation studied the effects of coolant injection velocity, chamber wall thickness and wall thickness profile, wall material and combustion chamber contour. In all cases except those studying chamber contour perturbations, the 4 inch conical combustion chamber included in Figure 83 was used in order to minimize the conduction length from the throat region to the film coolant sink and to maximize the downstream effectiveness of the coolant. The internal regenerative section was assumed to extend 6 in. (15 cm) downstream of the throat. In actual application it would be terminated at the point where internal and external radiation, coupled with the residual effectiveness of the film coolant, could maintain a thin wall at acceptable temperatures; present results indicate this point is a maximum of 6 in. (15 cm) downstream of the throat. In the SINDA network representation of the wall, 9 nodes were used axially from the injector through the throat, with 7 nodes in the nozzle section where temperature gradients are smaller. In all cases 5 nodes were used radially, for a total of 80 nodes (5 radial x 16 axial); this node network is shown in Figure 94. Both ends of the wall and the external surface were assumed to be adiabatic, but internal radiation losses through the exit of a 40:1 nozzle were included assuming an emissivity of 0.61. Based on the results of Figure 81 and Ref. 10, the heat transfer correlation coefficient C_{g_1} of Eq. (8) was assumed to be 0.052 for the first 0.5 in. (1.3 cm), was reduced to 0.026 over the region 0.5-2.0 in. (1.3-5 cm) from the injection point, and then was held constant over the rest of the chamber and nozzle.

1. Coolant Injection Velocity

As noted previously in Figure 89, a coolant/core injection velocity ratio of unity is optimum for adiabatic wall temperature control. However, it was of interest to consider higher velocity ratios for internal regenerative cooling because of the resultant higher heat transfer coefficients in the heat sink region near the injection point, Figures 72 and 80. A beryllium wall with a uniform 1.75 in. (4.45 cm) thickness was used to study the net effect of injection velocity ratio; the coolant flow rate was maintained constant at 20 percent of the fuel flow with an overall mixture ratio of 4. As shown in the following tabulation, the sink heat transfer coefficient increase was not sufficient to compensate for the higher adiabatic wall temperatures:

Injection Velocity Ratio	Injection Point Heat Transfer Coefficient Btu/in.^{2} sec °F	Throat Adiabatic Wall Temperature °F	Throat Gas-Side Wall Temperature °F
1.0	.0098	1389	1284
1.25	.0117	1569	1466
1.5	.0133	1973	1861

Therefore, an injection velocity ratio of unity was used in all subsequent internal regenerative cooling analyses.

2. Chamber Wall Material

Both beryllium and copper were considered as candidate wall materials. Most of the internal regenerative cooling development to date has utilized beryllium; however, its cycle life with large temperature variations during each cycle is very limited. Copper is obviously of interest because of its high thermal conductivity. These materials were compared directly over a range of coolant flows using a uniform 2.5 in. (6.4 cm) wall thickness; as the coolant flow varied the core mixture ratio was inadvertantly held constant (at a value of 5) instead of the overall mixture ratio. Figure 95 shows the variation with coolant flow of adiabatic wall temperature and of the gas-side surface temperature for both materials at both the throat and the end of the internal regenerative section. Although the wall temperatures are higher at the latter point, coolant flow requirements in many applications would be set by throat conditions due to cycle requirements. Since a material comparison based on cycle life considerations was beyond the scope of the present effort, a comparison of beryllium and copper coolant requirements can only be made on the basis of maximum steady-state operating temperatures which provide adequate material strengths, i.e., about 1200°F (920 K) for copper and 1700-1800°F (1200-1260 K) for beryllium. On this basis it is apparent from Figure 95 that the greater internal regenrative cooling capability of copper is not sufficient to compensate for its lower temperature limitation. Specifically, Figure 95b indicates 3.6 percent of the total flow is required as coolant for beryllium at 1700°F (1200 K) compared with 4.2 percent for copper at 1200°F (920 K).

Figure 95 also indicates the extent to which internal regenerative cooling can reduce the gas-side wall temperature below the adiabatic wall temperature. Unfortunately, this reduction is small for beryllium; even if a beryllium chamber could be operated at the same temperature as a thin-walled adiabatic design, the small coolant flow saving (about 0.2 percent of the total flow or 1 percent of the fuel flow) would hardly offset the significant weight penalty of the internal regenerative concept.

Figures 96 and 97 show the axial variations of the gas-side and external wall temperatures for beryllium and copper chambers, respectively, with 4 percent of the total flow (20 percent of the fuel) as film coolant; the adiabatic wall temperature is shown for comparison. The length of the heat sink region, in which the gas-side wall temperature is greater than the adiabatic wall temperature, is about 1.6 in. (4.1 cm) for the beryllium wall and 2.1 in. (5.3 cm) for copper. Sink heat transfer rates are 15.4 and 28.8 Btu/sec (16.2 and 30.4 kW) for the beryllium and copper chambers, respectively. Radial temperature gradients are smaller in the copper wall due to its higher thermal conductivity.

3. Chamber Wall Thickness

Figure 98 shows the effect of copper wall thickness on the throat and maximum gas-side wall temperatures as a function of coolant flow for an overall mixture ratio of 4, with the corresponding adiabatic wall temperatures shown for comparison. If the maximum temperature is limited to 1200°F (920 K) the following coolant flow rates are required.

Copper Chamber Uniform Wall Thickness, in.	Coolant Flow % of Fuel
1.0	23.8
1.75	22.4
2.5	21.2

Thus the coolant flow requirement is relatively insensitive to the thickness of a copper chamber wall.

Increasing the thickness of a beryllium chamber wall from 1.75 to 2.5 in. (4.45 to 6.35 cm), decreases the throat temperature by only 11°F (6 K) and the maximum temperature by 48°F (27 K) for a coolant flow equal to 20 percent of the fuel flow with an overall mixture ratio of 4.

4. Wall Thickness Profile

All internal regenerativel cooling results presented above are for a uniform wall thickness. At the start of this study a comparison was made for beryllium between a chamber with a uniform 1.75 inch (4.45 cm) wall and the tapered wall shown in Figure 94. The latter is 1.0 inch (2.5 cm) thick at each end and 2.5 in. (6.4 cm) thick at the throat, thereby providing approximately the same average thickness in both the combustion chamber and nozzle sections as in the uniform wall case. Throat and maximum gas-side wall temperatures were within 2°F (1 K) of the corresponding temperatures for the uniform wall chamber, indicating the distribution of thermal conductance is not critical for this particular application.

The effect of tapering the wall thickness in the nozzle section to save weight was investigated for a copper chamber. A uniform wall thickness of 2.5 in. (6.4 cm) was used in the combustion chamber, with the wall thickness tapered to 1.0 inch (2.5 cm) at the end of the internal regenerative section; therefore, the nozzle section was identical to that in Figure 94. This reduction in nozzle wall thickness resulted in a 9°F (5 K) decrease in throat temperature compared to a 2.5 in. (6.4 cm) uniform wall thickness but a 49°F (27 K) increase in the maximum wall temperature, i.e., at the end of the nozzle section. The latter increase is due, of course, to the reduction in overall axial thermal conductance. This comparison is with 20 percent of the fuel flow used as film coolant at an overall mixture ratio of 4.

5. Combustion Chamber Contour

Two additional combustion chamber contours were considered with uniform 2.5 in. (6.4 cm) copper walls: the 5.75 inch (14.6 cm) conical and 4 inch (10 cm) cylindrical chambers shown previously in Figure 83. A 23-degree convergence angle was selected for the cylindrical chamber since entrainment fraction multipliers were available for this angle as discussed previously. Selection of the same contraction ratio as the 4 inch (10 cm) conical chamber considered above was not of interest for two reasons: the results of Section VIII,A,3 (Figure 92) indicate the adiabatic wall temperatures for these chambers are nearly equal, and with such thick chamber walls the axial conduction characteristics of the two configurations would be virtually identical. Therefore, the 3.59 contraction ratio chamber of Section VIII,A,3 was selected to determine if the reduced heat transfer coefficients in the heat sink region would offset the lower adiabatic wall temperatures in the source region. The following tabulation compares the film coolant requirements for the three chamber configurations based on a maximum wall temperature of 1220°F (930 K) and a core mixture ratio of 5:

Combustion Chamber	Coolant Flow % of Total Flow
4 in. cylindrical	4.0
4 in. conical	4.2
5.75 in. conical	5.3

It is apparent that the reduced heat transfer coefficients in the sink region of the cylindrical chamber do not offset the lower adiabatic wall temperatures obtained in the throat and nozzle regions compared with the 4 inch (10 cm) conical chamber.

The number of axial nodes in the combustion chamber was increased from 9 to 12 for the 5.75 inch (14.6 cm) chamber, bringing the total number of nodes to 95 for this case (5 radial x 19 axial). As the chamber length increases the coolant flow requirement increases for two reasons: to offset increased throat and nozzle adiabatic wall temperatures and to compensate for the greater thermal resistance between the source and sink regions of the wall.

IX. CONCLUSIONS

A. LABORATORY TESTS

Gaseous hydrogen film cooling effectiveness data from the present laboratory test program agree with a new entrainment model developed herein from previous data for air, argon, helium and Arcton 12 relative to the effects of injection velocity ratio and coolant slot height. Although the hydrogen data exhibit essentially no dependence on coolant Reynolds number for a fixed slot height, the Reynolds number dependence of the entrainment model is required to predict the effect of slot height. The present data indicate the new entrainment model is valid for effectiveness values as low as 0.02, or a ratio of entrained core flow to coolant flow of 70.

These effectiveness data reveal significant flow turning effects at the start of convergence and at the throat, which are attributed to the imbalance in centrifugal forces across the mixing layer resulting from the density difference between the coolant and core flows. A proposed parameter for the correlation of turning effects indicates the proper trends; however, much more data from various nozzle configurations are required to develop a correlation. This parameter is the product of a dimensionless local density difference and the ratio of local mixing layer thickness to wall radius of curvature. Data from the conical chamber indicate the effect of flow acceleration on the ratio of entrainment mass flux to core mass velocity is very similar to that determined previously for transverse turbulent transport in a homogeneous fluid. Downstream of the throat there is little entrainment of core flow into the mixing layer, and the observed reduction in adiabatic wall temperature is adequately predicted by the imperfect recovery of kinetic energy.

Coolant effectiveness results with cold gaseous hydrogen and with liquid hydrogen were affected by heat transfer from the massive flange at the forward end of the chamber, and thus are not representative of adiabatic wall conditions. In addition, some wall temperatures in the subcritical liquid hydrogen test indicate nitrogen condensation in the mixing layer, in which case a coolant effectiveness cannot be defined from the adiabatic wall temperature.

In most cases the effect of gaseous film cooling on heat transfer from the wall could be accounted for merely by using the composition at the wall defined by the coolant effectiveness in evaluating properties. Exceptions were near the injection point, where the effect of injection velocity must be superimposed, and at the throat of the cylindrical chamber, where film cooling reduced the Stanton number correlating coefficient. A reference temperature for property evaluation equal to the arithmetic mean of the adiabatic and non-adiabatic wall temperatures allows the use at other locations of the same correlating coefficient with and without film cooling and accounts for the wall temperature effects observed with electrical heating. The decay of injection velocity perturbations can be correlated by a model similar to that used for coolant effectiveness, but with a slightly lower entrainment rate and a lower asymptotic mixing layer profile shape factor.

B. DESIGN FEASIBILITY INVESTIGATION

Adiabatic wall designs are feasible for application at 300 psia (207 N/cm^2) chamber pressure and 1500 lbs (6670 N) thrust; gas film cooling requirements are in the range of 4-5 percent of the total flow for a combustion chamber length of 5.75 in. (14.6 cm). Coolant flow requirements can be reduced by the use of a shroud or sleeve between the coolant inlet and injection points. Considering only losses due to film cooling, specific impulse is maximized for an overall mixture ratio near 3. Coolant slots should be sized to provide a coolant/core injection velocity ratio of unity. The increase in flow requirement for other velocity ratios is essentially independent of other design parameters and is 35-40 percent when the injection velocity differs from the core velocity by ± 50 percent. Although coolant requirements are nearly proportional to combustion chamber length, the effect of other chamber contour parameters is small. However, the latter conclusion may be the result of the incomplete correlation of the effect of flow turning and acceleration on entrainment by the mixing layer.

Internal regenerative cooling is not an attractive alternate to adiabatic wall design. The small reduction in film cooling provided by a thick beryllium wall is not likely to offset its significant weight penalty, and the greater internal regenerative cooling capability of copper (about twice that of beryllium) is not sufficient to compensate for its lower temperature limitation. Coolant flow requirements are relatively insensitive to wall thickness and are essentially independent of the wall thickness profile for a fixed average thickness. When the internal regenerative cooling effect is small, the increase in sink region heat transfer coefficients obtained by using injection velocity ratios greater than unity does not compensate for the increased adiabatic wall temperatures in the throat region.

REFERENCES

1. Hersch, M.,"Experimental Method of Measuring Intensity of Turbulence in a Rocket Chamber", ARS Journal, January 1961, pp. 39-45.

2. Dryden, H. L. and others, "Measurements of Intensity and Scale of Wind - Tunnel Turbulence and Their Relation to the Critical Reynolds Number of Spheres", NASA Report No. 581, 1937.

3. Cousin, S., "Turbulence: Experimental Methods", Handbook der Physik, VIII/2, 1963, pp. 524-590.

4. Hatch, J. E. and Papell, S. S., "Use of a Theoretical Flow Model to Correlate Data for Film Cooling or Heating an Adiabatic Wall by Tangential Injection of Gases of Different Fluid Properties", NASA TN D-130, November 1959.

5. Seban, R. A., "Heat Transfer and Effectiveness for A Turbulent Boundary Layer with Tangential Fluid Injection", J. Heat Transfer, Vol. 82, No. 4, 1960, pp. 303-312.

6. Pai, B. R. and Whitelaw, J. H., "The Influence of Density Gradients on the Effectiveness of Film Cooling", ARC CP 1013, December 1967.

7. Papell, S. S. and Trout, A. M., "Experimental Investigation of Air Film Cooling Applied to an Adiabatic Wall by Means of an Axially Discharging Slot", NASA TN D-9, August 1959.

8. Stollery, J. L. and El-Ehwany, A. A. M., "A Note on The Use of a Boundary Layer Model for Correlating Film Cooling Data", Int. J. Heat and Mass Transfer, Vol. 8, 1965, pp. 55-65.

9. Chin, J., et al., "Adiabatic Wall Temperature Downstream of a Single Injection Slot", ASME Paper No. 58-A-104, 1958.

10. Schoenman, L. and Oare, A., "Hydrogen-Oxygen High P_c APS Engines", Aerojet Liquid Rocket Co., Report 14354-Q-3, 14 April 1971.

11. Schoenman, L. and Oare, A., "Hydrogen-Oxygen APS Engines", Final Report, Contract NAS 3-14354, to be published.

12. Williams, J. J., "The Effect of Gaseous Film Cooling on the Recovery Temperature Distribution in Rocket Nozzles", PhD. Thesis, University of California at Davis, May 1969. Also ASME Paper No. 70-HT/SpT-42.

References (cont.)

13. Deissler, R. G., "Weak Locally Homogeneous Turbulence in Idealized Flow Through a Cone", NASA TN D-3613, 1966.

14. Deissler, R. G., "Weak Locally Homogeneous Turbulence and Heat Transfer with Uniform Normal Strain", NASA TN D-3779, January 1967.

15. Graham, R. W. and Deissler, R. G., "Prediction of Flow Acceleration Effects on Turbulent Heat Transfer", J. Heat Transfer, Vol. 89, No. 4, 1967, pp. 371-372.

16. Moretti, P. M. and Kays, W. M., "Heat Transfer to a Turbulent Boundary Layer with Varying Freestream Velocity and Varying Surface Temperature - An Experimental Study", Int J Heat and Mass Transfer, Vol 8, 1965. pp. 1187-1202.

17. Seban, R. A. and Back, L. H., "Effectiveness and Heat Transfer for a Turbulent Boundary Layer with Tangential Injection and Variable Free-Stream Velocity", J. Heat Transfer, Vol. 84, No. 3, 1962, pp. 235-244.

18. Back, L. H., Massier, P. F., and Cuffel, R. F., "Flow Phenomena and Convective Heat transfer in a Conical Supersonic Nozzle", J Spacecraft, Vol 4, No. 8, 1967, pp. 1040-1047.

APPENDIX A

GAS FILM COOLING ENTRAINMENT MODEL

Appendix A

GAS FILM COOLING ENTRAINMENT MODEL

Although gas film cooling models have historically provided a temperature effectiveness, e.g., Ref. 4, a more fundamental enthalpy effectiveness is used herein. Using an energy transfer - mass transfer analogy based on a turbulent Lewis number of unity, it is assumed that the element concentration effectiveness is equal to the total enthalpy effectiveness; thus

$$\eta = \frac{H_{o_e} - H_{o_{aw}}}{H_{o_e} - H_c} = \frac{c_e - c_w}{c_e - 1} \tag{A1}$$

in which c represents the mass fraction of H_2 when all species are broken down into the elements H_2 and O_2. The elemental hydrogen mass fraction may be related to the mixture ratio to obtain

$$\eta = \frac{1}{MR_e} \left(\frac{1 + MR_e}{1 + MR_w} - 1 \right) \tag{A2}$$

Thus, the film coolant effectiveness η defines both the wall mixture ratio and $H_{o_{aw}}$, which is the total enthalpy at the edge of the viscous region of the wall boundary layer for an adiabatic wall. It is assumed that this viscous region represents a very small part of the total thickness of the mixing layer. The adiabatic wall or recovery enthalpy is given by

$$H_{aw} = H_{o_{aw}} - (1 - Pr_w^{1/3}) (H_{o_e} - H_e) \tag{A3}$$

in which $Pr_w^{1/3}$ is the recovery factor applied to the free-stream kinetic energy. An equilibrium chemical composition subroutine determines the resultant adiabatic wall temperature.

It is necessary to describe the region along the wall in which the characteristics of the flow differ from those of the mainstream due to the presence of the film coolant and mixing of the mainstream with it. Since the flow in this mixing layer is greater than the injected coolant flow, the mixing process can be considered to represent entrainment of mainstream flow by the mixing layer as shown schematically in Figure 99. In the present model framework, this entrainment is represented explicitly, but its effect on conditions at the wall is described on a lumped parameter basis (i.e., without a distributed representation of the transport phenomena within the mixing layer). Therefore, while such a framework recognizes the existence of changing enthalpy and concentration profiles within the mixing layer, it does not provide a basis for their calculation.

The entrainment mass flux is represented as a fraction k of the axial mass velocity of the mainstream. Thus, the total entrainment flow up to any contour position is

$$W_E = \int_o^x 2\pi\ (r - s \cos \alpha)\ k\ \rho_e\ u_e\ dx \tag{A4}$$

The cooling effectiveness is related to this flow, the coolant flow, and a shape factor describing the enthalpy profile in the mixing layer. An energy balance on the mixing layer gives

$$\frac{H_{o_e} - H_{o_b}}{H_{o_e} - H_c} = \frac{W_c}{W_c + W_E} \tag{A5}$$

from which

$$\eta = \frac{W_c}{\theta\ (W_c + W_E)} \tag{A6}$$

with the profile shape factor θ defined as

$$\theta = \frac{H_{o_e} - H_{o_b}}{H_{o_e} - H_{o_{aw}}} \tag{A7}$$

Eqs. (A4) and (A6) represent the broad framework on which the present model is based. Many specific models can be derived depending on the development of the entrainment fraction k (x) and shape factor θ (x).

Appendix A

The entrainment fraction is assumed to be of the form

$$k = k_o \, k_m(x) \tag{A8}$$

in which k_o is the entrainment fraction with laboratory conditions and no turning or flow acceleration as defined by Eq. (5) of Section VI,A. Thus $k_m(x)$ is a multiplier which accounts for flow turning and acceleration, mainstream combustion and turbulence, coolant injection from discontinuous slots and any other effects not present in k_o. The present laboratory data and the firing data of Refs. 10 and 11 have been interpreted in terms of $k_m(x)$.

A momentum balance on the total nozzle flow should be used to account for the effect of the mixing layer on the freestream mass velocity $\rho_e u_e$. However, for the sake of simplicity, the present model assumes the mainstream accelerates as if there were no film cooling

$$\rho_e u_e = (\rho_e u_e)_o \left(\frac{r_o}{r}\right)^2 F_{2D} \tag{A9}$$

in which r_o is the nozzle radius at the injection point. A nozzle mass balance (integral continuity equation) then gives the mixing layer thickness from

$$\left(1 - \frac{s}{r}\cos\alpha\right)^2 = \left(1 - \frac{s_o}{r_o}\right)^2 \left(1 - \frac{W_E}{W - W_c}\right) \tag{A10}$$

Substituting Eqs. (A8), (A9) and (A10) in Eq. (A4) gives

$$W_E = 2\pi\,(r_o - s_o)\,k_o(\rho_e u_e)_o \int_o^x \left(1 - \frac{W_E}{W-W_c}\right)^{0.5} \left(\frac{r_o}{r}\right) F_{2D}\, k_m \, dx \tag{A11}$$

Solving this integral equation and relating $(\rho_e u_e)_o$ to s_o and the flow rates yields*

---

*Note that the initial mixing layer thickness s_o is not equal to the slot height s_c when a finite lip separates the core and coolant flows at the injection point. In order to determine s_o, it is assumed herein that the velocity ratio u_c/u_e existing just prior to injection is maintained immediately downstream of the slot.

$$\frac{W_E}{W - W_c} = 2\,\frac{k_o\,\bar{x}}{r_o - s_o} - \left(\frac{k_o\,\bar{x}}{r_o - s_o}\right)^2 \tag{A12}$$

in which

$$\bar{x} = \int_o^x \frac{r_o}{r}\,F_{2D}\,k_m\,dx \tag{A13}$$

Thus Eq. (A12) gives the entrainment flow and Eq. (A6) then determines the film cooling effectiveness provided the local mixing layer shape factor $\theta(x)$ is known.

The shape factor is determined by the above model in an initial free-jet region ($x \leq x'$), since the effectiveness remains at unity; i.e., the sole effect of the entrainment in this region is to change the mixing layer profiles without affecting the conditions at the wall. From Eq. (A6) with η equal to unity

$$\theta = \frac{W_c}{W_c + W_E} \quad (x \leq x') \tag{A14}$$

A transition region follows in which the shape factor continues to decrease while the effectiveness starts to decrease because of the penetration of mixing effects to the wall. It is assumed that the normalized mixing layer profiles do not change beyond the end of the transition region ($x = x''$) so that the shape factor is then constant. In the present model, these regions and x' and x'' are defined by $W_E/W_c = 0.06$ and 1.4, respectively, as developed in Section VI,A. The shape factor variation with W_E/W_c is given in Figure 49.

APPENDIX B

DATA ANALYSIS

Appendix B

DATA ANALYSIS

1. LOCAL HEAT LOSSES

As noted in Section V,C, wall temperature measurements without coolant flow indicated significant local heat losses due to external cooling and axial heat conduction in the chamber wall. As a result, Tests 5S-1 and 5S-2 at reduced nitrogen temperatures were run with the cylindrical chamber. These data along with the high temperature data from Tests 3, 4 and 5 were used to determine external boundary conditions, which were incorporated into the data analysis program. Figure 100 shows the wall temperature reduction due to heat losses at the fourth thermocouple position as a function of the measured wall temperature; the adiabatic wall temperature was determined from the measured nitrogen temperature. At each location, these data are reasonably well represented by the equation*

$$T_{aw} - T_w = \left(\frac{1}{h_g} + \frac{\Delta}{K}\right) \left\{ h\,(T_w - T_{amb}) + 0.0033 \left[\left(\frac{T_w + 460}{1000}\right)^4 - \left(\frac{T_{amb} + 460}{1000}\right)^4 \right] \right\}$$

in which

T_{aw} = adiabatic wall temperature as determined from the nitrogen temperature and a nozzle flow analysis

T_w = measured wall temperature, °F

h_g = internal heat transfer coefficient from the wall heating transient analysis

Δ = wall thickness

K = wall thermal conductivity

h = heat loss coefficient, to be determined from data fit

T_{amb} = ambient temperature (60°F)

---

*At the exit thermocouple location, the coefficient 0.0033 was increased to 0.0050 to account for internal radiation losses.

The curve in Figure 100 corresponds to a loss coefficient h of 0.48×10^{-4} Btu/in.^{2}-sec-°F (0.014 W/cm^2-°K); the heat loss coefficients for all ten cylindrical chamber thermocouple locations are given in Table VII. A similar procedure was followed for the conical chamber, the results of which are also shown in Table VII. In addition to accounting for heat losses in the heat transfer coefficient analyses, the data analysis program uses the above formulation to obtain adiabatic wall temperatures with film cooling; in this case, h_g is the internal coefficient with cooling as determined by the cooling transient or electrical heating analyses.

2. CHAMBER FLOW TRANSIENT

Section V,C noted the slow chamber pressure transients obtained after opening or closing the hydrogen valve. This transient is attributed to the large volume in the nitrogen system between the critical flow nozzle and the test section. Although the flow into this system is constant, the nitrogen flow out through the test section can vary due to the mass storage transient in this large volume. Assuming the ratio of chamber pressure to total chamber flow adjusts instantaneously, the chamber pressure and total flow (including hydrogen) transients are given by

$$P_c = P_{c_f} + (P_{c_i} - P_{c_f})\, e^{-t/\tau}$$

$$W = W_f \left[1 + \frac{P_{c_i} - P_{c_f}}{P_{c_f}}\, e^{-t/\tau}\right]$$

in which subscript i refers to the initial chamber pressure before hydrogen valve operation and subscript f refers to the final steady-state condition. This flow transient has been included in the data analysis program calculation of correlation coefficients from transient heat transfer coefficients. The time constant τ is related to the nitrogen system volume and was determined from transient chamber pressure measurements, as shown in Figure 101, to be 0.595 sec.

Appendix B

TABLE VII - HEAT LOSS COEFFICIENTS

Cylindrical Chamber		Conical Chamber	
Axial Distance, In.	$h \times 10^4$ Btu/in^2-sec-$^\circ$F	Axial Distance, In.	$h \times 10^4$ Btu/in^2-sec-$^\circ$F
0.79	1.11	0.73	0.59
1.19	0.74	1.33	0.31
1.69	0.53	1.93	0.28
2.19	0.48	2.53	0.32
2.74	0.54	3.13	0.26
3.69	0.76	3.73	0.33
4.04	0.34	4.33	0.53
4.39	0.58	4.93	0.12
4.94	0.23	5.33	0.42
5.44	0.45		

3. TRANSIENT DATA ANALYSIS

Transient heat transfer coefficients have been determined by a lumped parameter analysis in which the heat transfer coefficient is assumed to be constant over each temperature increment analyzed. The wall specific heat is assumed to vary linearly with temperature; thus, the basic energy balance solved is

$$M\ (C_o + C_1 T)\ \frac{dT}{dt} = h_g\ (T_{aw} - T) - h_a\ (T - T_{amb}) \tag{B1}$$

in which the effective loss coefficient h_a is defined by

$$h_a = (1 + \frac{\Delta}{r_i}) \left\{ h + \frac{0.0033}{\bar{T} - T_{amb}} \left[\left(\frac{\bar{T} + 460}{1000} \right)^4 - \left(\frac{T_{amb} + 460}{1000} \right)^4 \right] \right\} \tag{B2}$$

and

M = wall mass per unit of inner surface area
C_o = specific heat at zero °F
C_1 = specific heat derivative with respect to temperature
T = instantaneous wall temperature, °F
T_{aw} = adiabatic wall temperature, °F
$\bar{T}$ = average temperature over the increment, °F
r_i = inner radius of the wall
t = time

Solution of Equation (B1) yields

$$h_g + h_a = \frac{M}{t_1 - t_o} \left[(C_o + C_1\ T_s)\ \ln \frac{(T_o - T_s)}{(T_1 - T_s)} + C_1\ (T_o - T_1) \right] \tag{B3}$$

in which subscripts o and 1 refer to the beginning and end, respectively, of the temperature-time increment, and T_s is the ultimate steady-state wall temperature.

Appendix B

The data analysis program determines the time increment in the transient analyses based on obtaining a temperature increment equal to or greater than 40°F (22°K). This value appeared to be large enough to filter out "noise" in the data, but small enough to give a reasonable number of increments. Transient heat transfer coefficients determined by the lumped parameter analysis are corrected for the temperature variation across the wall. This was accomplished by applying the analysis to "data" from distributed wall temperature transient solutions to generate a table of actual vs calculated heat transfer coefficients. The range of heat transfer coefficients obtained herein is such that this correction is generally less than 10 percent.

For the heating transients both T_{aw} and T_s are known, so that if h_g is relatively constant an effective loss coefficient is defined by

$$h_a = \frac{h_g (T_{aw} - T_s)}{T_s - T_{amb}}$$

This relation was combined with Equation (B3) to yield h_g without an a priori determination of the heat loss coefficient h as outlined in Section 1 of this appendix. Since the latter requires an h_g without coolant, a simultaneous solution was thus avoided. Consequently, the analysis sequence for each chamber was heating transient analysis, determination of the heat loss coefficients as indicated in Section 1, then analysis of the cooling transient and electrical heating data using these loss coefficients. If the wall temperature was less than the ambient temperature, the loss coefficient was assumed to be zero.

Table VIII is a sample printout from the data analysis program for a heating transient. The first column indicates the number of the data time steps required to meet the 40°F (22°K) temperature increment criterion; each data time step is 0.0125 sec. A maximum of 20 time steps per analysis increment was usually allowed on heating transients in order to eliminate the less accurate tail of the transient. In all transient printouts, the averaging of the heat transfer and correlation coefficients omits the first value. The correlation coefficients are defined in Section 6 below.

TABLE VIII. - CYLINDRICAL CHAMBER HEATING TRANSIENT TEST 3

```
                              THERMOCOUPLE    TB-4


   CORE FLOW             1,044  LB/SEC         AXIAL LENGTH                 2,19  IN
   CORE TEMP,             914,  DEG F          CONTOUR LENGTH               2,19  IN
   COOLANT FLOW          ,0000  LB/SEC         RADIUS                       ,609  IN
   COOLANT TEMP,            0,  DEG F          STATIC TEMP, FACTOR          ,000
   CHAMBER PRESSURE       247,  PSIA           WALL THICKNESS              ,0200  IN


  ADIABATIC WALL TEMP,  914,  DEG F
  VISCOSITY           ,193-05  LB/IN-SEC

                         TRANSIENT DATA ANALYSIS

  NO, OF     INITIAL     AVERAGE     HEAT FLUX    COEFFICIENT        CORRELATION
  STEPS       TEMP,       TEMP,       BTU PER       BTU PER          COEFFICIENT
              DEG F       DEG F     SQ IN-SEC    SQ IN-SEC-F      T-AW          T-AM

   11         190,6       214,3       -,233        ,000337       ,0159         ,0132
    7         238,1       260,5       -,354        ,000552       ,0277         ,0222
    6         282,9       303,5       -.387        ,000647       ,0326         ,0266
    7         324,0       345,9       -.361        ,000648       ,0328         ,0272
    8         367,7       390,5       -,337        ,000657       ,0334         ,0281
    9         413,2       436,0       -,308        ,000659       ,0336         ,0288
   10         458,8       479,2       -,257        ,000602       ,0308         ,0268
   11         499,7       519,8       -,238        ,000615       ,0316         ,0278
   12         540,0       560,3       -,227        ,000656       ,0338         ,0302
   15         580,6       601,8       -,200        ,000653       ,0337         ,0306
   19         623,1       644,7       -,170        ,000643       ,0333         ,0306

                                       AVERAGE     ,000633       ,0323         ,0279
```

Table IX is a sample cooling transient printout. The adiabatic wall temperature is obtained by correcting the steady-state temperatures with film cooling for the heat losses of Section 1, i.e.

$$T_{aw} = T_s + h_a\ (T_s)\ (\frac{1}{h_g} + \frac{\Delta}{K})\ (T_s - T_{amb}) \tag{B4}$$

In this case, h_g is the average heat transfer coefficient from the cooling transient analysis. Section 5 describes the coolant effectiveness calculation; all properties printed by the data analysis program are at the adiabatic wall temperature for the gas composition defined by the coolant effectiveness. A maximum of 12 data time steps per analysis increment was usually allowed on cooling transients.

Table IX is for a throat thermocouple and illustrates the decrease in heat transfer coefficient with time which was obtained at the throat for both heating and cooling transients. This decrease is attributed to axial conduction in the wall since the throat responds much faster than neighboring regions. At the first thermocouple in the expansion section, increases in the heat transfer coefficient were frequently observed which can again be attributed to axial conduction. In such cases where the coefficient varies significantly, results from early in the transient were used in data plotting and correlation; later results represent a net coefficient including axial conduction.

4. ELECTRICAL HEATING DATA

The electrical heat generation calculation accounts for the dependence of test section resistance on temperature and for the a-c voltage component. Figures 102 and 103 show the test section resistance vs temperature as obtained from overall voltage drop and average temperature; use of these correlations allows local heat fluxes to be calculated in place of the average flux determined by the voltage drop. Figure 104 shows the a-c rms voltage normalized by the d-c voltage. Using these results, the electrical heat flux is given by:

TABLE IX. - CYLINDRICAL CHAMBER COOLING TRANSIENT TEST 3

```
                              THERMOCOUPLE    TC-3


   CORE FLOW              1,044  LB/SEC        AXIAL LENGTH                    4,39   IN
   CORE TEMP,              914,  DEG F         CONTOUR LENGTH                  4,46   IN
   COOLANT FLOW           ,0405  LB/SEC        RADIUS                          ,308   IN
   COOLANT TEMP,            70,  DEG F         STATIC TEMP, FACTOR             ,167
   CHAMBER PRESSURE        278,  PSIA          WALL THICKNESS                 ,0220   IN


                              TRANSIENT DATA ANALYSIS

  NO, OF       INITIAL       AVERAGE      HEAT FLUX      COEFFICIENT           CORRELATION
   STEPS        TEMP,         TEMP,       BTU PER        BTU PER              COEFFICIENT
                DEG F         DEG F      SQ IN-SEC     SQ IN-SEC-F         T-AW           T-AM

    3           798,4         774,0        1,071        ,002910            ,0230          ,0265
    3           749,7         728,6         ,913        ,002785            ,0219          ,0249
    4           707,6         683,3         ,775        ,002701            ,0211          ,0236
    5           659,1         633.9         ,631        ,002606            ,0202          ,0223
    6           608,7         587,7         ,423        ,002102            ,0162          ,0175
    7           566,8         546,6         ,341        ,002090            ,0160          ,0170
   12           526,5         505,6         .194        ,001565            ,0119          ,0125

                                         AVERAGE    ,002308            ,0179          ,0196

                                         ADIABATIC WALL TEMP,          371,   DEG F
  VELOCITY RATIO          ,838           COOLANT EFFECTIVENESS         ,101
  DENSITY RATIO           ,187           MOLECULAR WEIGHT             12,09
  SLOT HEIGHT             ,060   IN      SPECIFIC HEAT                 .576   BTU/LB-F
  COOLANT REYNOLDS                       VISCOSITY                 ,125-05   LB/IN-SEC
               NUMBER   22725,           PRANDTL NUMBER                ,383
```

$$q_{el} = \frac{0.948 \times 10^{-6}}{\pi D_i L} I^2 R_{el} \left[1 + \left(\frac{rms}{E}\right)^2\right]$$

in which

D_i = inside diameter of the electrically heated section, in.
L = length of the electrically heated section, in.
I = test section current, amps
T_w = wall temperature, °F
rms/E = normalized a-c voltage component from Figure 104
R_{el} = test section electrical resistance, 10^{-3} ohms
$= 1.374 + 0.639 \times 10^{-3} T_w$ ($T_w < 241°F$)
$= 1.454 + 0.307 \times 10^{-3} T_w$ ($T_w \geq 241°F$)

The internal heat flux, accounting for external heat losses, is

$$q_i = q_{el} - h_a (T_{w_o}) (T_{w_o} - T_{amb})$$

in which T_{w_o} is the measured outside wall temperature. The inside wall temperature is given by

$$T_{w_i} = T_{w_o} - \frac{\Delta}{K}\left[0.5\, q_{el} - h_a (T_{w_o})(T_{w_o} - T_{amb})\right]$$

Since the heat transfer coefficient is defined by

$$h_g = \frac{q_i}{T_{w_i} - T_{aw}}$$

and the adiabatic wall temperature is again defined by Equation (B4), a simultaneous solution for h_g and T_{aw} is required. This solution yields

$$h_g = \frac{q_i + h_a (T_s) (T_s - T_{amb})}{T_{w_i} - T_s - \frac{\Delta}{K} h_a (T_s) (T_s - T_{amb})}$$

Table X is a sample printout of the data analysis program for electrical heating data. The adiabatic wall temperature, Equation (B4), is based on the average heat transfer coefficient for all power levels. No heat transfer coefficient was calculated if $T_{w_i} - T_{aw}$ was less than 5°F (3°K), which occurred for some of the data of Tests 13 and 14.

5. COOLANT EFFECTIVENESS AND GAS COMPOSITION AT THE WALL

The data analysis program determined the film coolant effectiveness from the adiabatic wall temperature and defined the gas composition and properties at the wall. The effectiveness calculation is iterative since it depends on the recovery factor, which depends in turn on the gas mixture Prandtl number.

Film cooling effectiveness is defined herein on a total enthalpy (H_o) basis as

$$\eta = \frac{H_{o_e} - H_{o_{aw}}}{H_{o_e} - H_c}$$

in which subscript e refers to the core or freestream flow and subscript c refers to the coolant at injection. The static enthalpy for an adiabatic wall with film cooling is assumed to be

$$H_{aw} = H_{o_{aw}} - (1 - Pr_w^{1/3})(H_{o_e} - H_e)$$

in which the recoverable kinetic energy is that of the core, but the recovery factor is based on the Prandtl number of the gas mixture at the wall. By analogy between energy and species mixing, the effectiveness η is also equal to the hydrogen mass fraction at the wall, so that

$$H_{aw} = \eta\, H_{H_2}(T_{aw}) + (1 - \eta)\, H_{N_2}(T_{aw})$$

TABLE X. - ELECTRICAL HEATING DATA TEST 5A

```
                              THERMOCOUPLE    TA-5

    CORE FLOW             1,042  LB/SEC         AXIAL LENGTH                   2,74   IN
    CORE TEMP,             916,  DEG F          CONTOUR LENGTH                 2,74   IN
    COOLANT FLOW          ,0396  LB/SEC         RADIUS                         ,609   IN
    COOLANT TEMP,           53,  DEG F          STATIC TEMP, FACTOR            ,000
    CHAMBER PRESSURE       281,  PSIA           WALL THICKNESS                ,0200   IN

                         ELECTRICAL HEATING DATA ANALYSIS

CURRENT       OUTER        INNER      HEAT FLUX     COEFFICIENT        CORRELATION
              TEMP,        TEMP,       BTU PER       BTU PER           COEFFICIENT
  AMPS        DEG F        DEG F     SQ IN-SEC    SQ IN-SEC-F       T-AW          T-AM

 1410,        426,0        410,0        ,310         ,001508         ,0272         ,0299
 1990,        702,0        675,6        ,621         ,001320         ,0238         ,0290
 2385,        957,0        923,9        ,912         ,001269         ,0229         ,0304

                                    AVERAGE     ,001366           ,0247         ,0297

                                    ADIABATIC WALL TEMP,            205,    DEG F
VELOCITY RATIO          ,794        COOLANT EFFECTIVENESS          ,250
DENSITY RATIO           ,193        MOLECULAR WEIGHT               6,58
SLOT HEIGHT             ,060   IN   SPECIFIC HEAT                 1,062    BTU/LB-F
COOLANT REYNOLDS                    VISCOSITY                  ,913-06    LB/IN-SEC
          NUMBER      22709,        PRANDTL NUMBER                 ,431
```

Combining these relationships yields, for a constant core specific heat,

$$\eta = \frac{T_{o_e} - T_{aw} - (1 - Pr_w^{1/3})(T_{o_e} - T_e)}{T_{o_e} - T_{aw} + \frac{1}{C_{p_e}}[H_{H_2}(T_{aw}) - H_c]}$$

This equation is solved iteratively since the Prandtl number at the wall depends on η. The static temperature factor printed by the data analysis program (e.g., see Table IX) is defined as $1 - (T_e/T_{oe})$. Table XI is a sample printout for cases in which only the adiabatic wall temperature calculation of Equation (B4) and the above effectiveness calculation are made. All thermocouples at a given axial location are processed as a group, and h_g in Equation (B4) is calculated by the formulation of Section 6 using an input correlation coefficient. In Test 14, some of the adiabatic wall temperatures were below -300°F; in these cases, no coolant effectiveness was calculated due to the possibility of nitrogen condensation.

Since the hydrogen mass fraction at the wall equals the coolant effectiveness, the hydrogen mole fraction at the wall is

$$y = \frac{14\eta}{1+13\eta}$$

and the mixture molecular weight at the wall

$$MW = \frac{28}{1+13\eta}$$

The mixture viscosity at the wall is calculated by the method of Wilke and the thermal conductivity by the analogous method of Mason and Saxena; thus,

$$\mu_w, K_w = \frac{y\ (\mu, K)_{H_2}}{y+(1-y)\phi_{12}} + \frac{(1-y)(\mu, K)_{N_2}}{1-y + y\ \phi_{21}}$$

TABLE XI. - CYLINDRICAL CHAMBER EFFECTIVENESS DATA TEST 7A

CORE FLOW	1.041	LB/SEC	AXIAL LENGTH	3.69	IN
CORE TEMP.	914.	DEG F	CONTOUR LENGTH	3.69	IN
COOLANT FLOW	.0085	LB/SEC	RADIUS	.607	IN
COOLANT TEMP.	77.	DEG F	STATIC TEMP. FACTOR	.000	
CHAMBER PRESSURE	256.	PSIA	WALL THICKNESS	.0200	IN
VELOCITY RATIO	.837		SLOT HEIGHT	.015	IN
DENSITY RATIO	.184		COOLANT REYNOLDS NUMBER	4533.	

THERMOCOUPLE	ADIABATIC WALL TEMP. (DEG F)	COOLANT EFFECTIVENESS
TC-1	635.	.035
TD-1	671.	.028
TE-1	609.	.039

in which

$$\phi_{12} = \frac{1}{2.93} \left[1 + 1.934 \left(\frac{\mu_{H_2}}{\mu_{N_2}}\right)^{0.5}\right]^2$$

$$\phi_{21} = \frac{1}{10.95} \left[1 + 0.517 \left(\frac{\mu_{N_2}}{\mu_{H_2}}\right)^{0.5}\right]^2$$

The mixture Prandtl number at the wall is given by

$$Pr_w = \frac{\mu_w}{K_w} \left[\eta\, C_{p_{H_2}} + (1-\eta)\, C'_{p_e}\right]$$

6. HEAT TRANSFER CORRELATION COEFFICIENT

A correlation coefficient C_g was calculated from the measured heat transfer coefficient and the following correlation equation:

$$h_g = C_g\, G \left(\frac{MW}{28} \frac{T_e}{T_{ref}}\right)^{0.8} \left(\frac{H_{aw} - H_w}{T_{aw} - T_w}\right) Re_D{}^{-0.2}\, Pr_w{}^{-0.6}$$

in which

h_g = measured heat transfer coefficient
G = mass velocity (total flow rate per unit area)
MW = molecular weight of the gas mixture at the wall
T_e = freestream temperature
T_{ref} = reference temperature for property evaluation
H_{aw} = adiabatic wall enthalpy
T_{aw} = adiabatic wall temperature
H_w = gas mixture enthalpy at the nonadiabatic wall temperature
T_w = wall temperature
Re_D = Reynolds number based on diameter or equivalent diameter (GD/μ_w)
Pr_w = Prandtl number

Appendix B

Two reference temperatures are used, the adiabatic wall temperature and the arithmetic mean of T_{aw} and T_w. All properties are based on the gas composition at the wall defined by the coolant effectiveness. No correlation coefficient was calculated if the reference temperature was less than -210°F, due to limitations of the property formulations.

APPENDIX C

NOMENCLATURE

Appendix C

NOMENCLATURE

1. ENGLISH LETTERS

c	Elemental hydrogen mass fraction
C_p	Specific heat
C_g	Heat transfer correlation coefficient; C_{g_1} is for a velocity ratio of unity
d	Rectangular chamber flow height
D	Chamber or nozzle flow diameter
F_{2D}	Ratio of two-dimensional to one-dimensional mass velocity
g	Velocity mixing function, defined by Eq. (9)
G	Axial mass velocity based on total flow
h	External convective heat loss coefficient
h_a	External total heat loss coefficient
h_g	Gas-side convective heat transfer coefficient
H	Static enthalpy
H_o	Total enthalpy
k	Entrainment fraction
k_o	Laboratory entrainment fraction for straight, unaccelerated flow with continuous slot injection
k_m	Entrainment fraction multiplier
K	Thermal conductivity
L'	Combustion chamber axial length
M	Screen mesh size
MR	Mixture ratio
MW	Molecular weight

Appendix C

n	Acceleration exponent
P_c	Chamber pressure
Pr	Prandtl number
q	Heat flux
r	Local chamber or nozzle radius
R	Radius of curvature; positive when the wall turns into the flow
Re_c	Coolant Reynolds number based on slot height, $\rho_c u_c s_c/\mu_c$
Re_D	Overall Reynolds number, $\rho_{ref}\, GD/\rho_e \mu_{ref}$
s	Mixing layer thickness
s_c	Coolant slot height
St	Stanton number
t	Time
T	Static temperature
T_o	Total temperature
u	Axial velocity
V	Mixing layer characteristic velocity
W	Total flow rate
W_c	Film coolant flow rate
W_E	Entrainment flow rate
x	Contour distance from the film coolant injection point
$\bar{x}$	Contour integral defined by Eq. (A13)

2. GREEK LETTERS

α	Angle between the nozzle centerline and the wall tangent
Δ	Test section wall thickness
ε	Eddy viscosity
η	Film cooling effectiveness, defined by Eq. (A1)
θ	Enthalpy and elemental mass fraction profile shape factor for the mixing layer
θ_v	Velocity profile shape factor
μ	Viscosity
ξ	Correlating length, Eq. (1)
ρ	Density; $\overline{\rho}$ is defined as 0.5 $(\rho_e + \rho_w)$
τ	Chamber pressure transient time constant

3. SUBSCRIPTS

o	Film coolant injection location (except H_o, T_o, k_o)
amb	Ambient temperature
aw	Adiabatic wall condition
b	Bulk value for the mixing layer
c	Coolant inlet
e	Freestream or core
ref	Gas composition at the wall at the reference temperature
s	Steady state
t	Throat
w	At the chamber wall

APPENDIX D

DISTRIBUTION

Appendix D

Report Copies R	D	Recipient	Designee
		National Aeronautics & Space Administration Lewis Research Center 21000 Brookpark Road Cleveland, Ohio 44135	
1		Attn: Contracting Officer, MS 500-313	
5		E. A. Bourke, MS 500-203	
1		Technical Report Control Office, MS 5-5	
1		Technology Utilization Office, MS 3-16	
2		AFSC Liaison Office, 501-3	
2		Library	
1		Office of Reliability & Quality Assurance, MS 500-111	
1		J. W. Gregory, Chief, MS 500-	
13		D. E. Sokolowski, Project Manager, MS 500	
1		E. A. Edelman, MS 501-6	
1		R. A. Duscha, MS 500-203	
1		Director, Shuttle Technology Office, RS Office of Aeronautics & Space Technology NASA Headquarters Washington, D.C. 20546	
2		Director Space Prop. and Power, RP Office of Aeronautics & Space Technology NASA Headquarters Washington, D.C. 20546	
1		Director, Launch Vehicles & Propulsion, SV Office of Space Science NASA Headquarters Washington, D.C. 20546	
1		Director, Materials & Structures Div, RW Office of Aeronautics & Space Technology NASA Headquarters Washington, D.C. 20546	
1		Director, Advanced Manned Missions, MT Office of Manned Space Flight NASA Headquarters Washington, D.C. 20546	
20		National Technical Information Service Springfield, Virginia 22151	

Appendix D

Report Copies			
R	D	Recipient	Designee
1		National Aeronautics & Space Administration Ames Research Center Moffett Field, California 94035 Attn: Library	Hans M. Mark Mission Analysis Division
1		National Aeronautics & Space Administration Flight Research Center P.O. Box 273 Edwards, California 93523 Attn: Library	
1		Director, Technology Utilization Division Office of Technology Utilization NASA Headquarters Washington, D.C. 20546	
1		Office of the Director of Defense Research & Engineering Washington, D.C. 20301 Attn: Office of Asst. Dir. (Chem Technology)	
2		NASA Scientific and Technical Information Facility P.O. Box 33 College Park, Maryland 20740 Attn: NASA Representative	
1		National Aeronautics & Space Administration Goddard Space Flight Center Greenbelt, Maryland 20771 Attn: Library	Merland L. Moseson, Code 620
1		National Aeronautics & Space Administration John F. Kennedy Space Center Cocoa Beach, Florida 32931 Attn: Library	Dr. Kurt H. Debus
1		National Aeronautics & Space Administration Langley Research Center Langley Station Hampton, Virginia 23365 Attn: Library	E. Cortwright Director

Appendix D

Report Copies			
R	D	Recipient	Designee
1		National Aeronautics & Space Administration Manned Spacecraft Center Houston, Texas 77001 Attn: Library	J. G. Thiobodaux, Jr. Chief, Propulsion & Power Division
1		National Aeronautics & Space Administration George C. Marshall Space Flight Center Huntsville, Alabama 35912 Attn: Library	Hans G. Paul Leon J. Hastings James Thomas Dale Burrows I. G. Yates Clyde Nevins J. Blumrich
1		Jet Propulsion Laboratory 4800 Oak Grove Drive Pasadena, California 91103	Henry Burlage, Jr. Duane Dipprey
	1	Attn: Library	Robert Riebling, 125-224
1		Defense Documentation Center Cameron Station Building 5 5010 Duke Street Alexandria, Virginia 22314 Attn: TISIA	
1		RTD (RTNP) Bolling Air Force Base Washington, D.C. 20332	
1		Arnold Engineering Development Center Air Force Systems Command Tullahoma, Tennessee 37389 Attn: Library	Dr. H. K. Doetsch
1		Advanced Research Projects Agency Washington, D.C. 20525 Attn: Library	
1		Aeronautical Systems Division Air Force Systems Command Wright-Patterson Air Force Base, Dayton, Ohio Attn: Library	D. L. Schmidt Code ARSNC-2

Appendix D

Report Copies		Recipient	Designee
R	D		
1		Air Force Missile Test Center Patrick Air Force Base, Florida Attn: Library	L. J. Ullian
1		Air Force Systems Command Andrews Air Force Base Washington, D.C. 20332 Attn: Library	Capt. S. W. Bowen SCLT
1		Air Force Rocket Propulsion Laboratory (RPR) Edwards, California 93523 Attn: Library	
1		Air Force Rocket Propulsion Laboratory (RPM) Edwards, California 93523 Attn: Library	
1		Air Force FTC (FTAT-2) Edwards Air Force Base, California 93523 Attn: Library	Donald Ross
1		Air Force Office of Scientific Research Washington, D.C. 20333 Attn: Library	SREP, Dr. J. F. Masi
1		Space & Missile Systems Organization Air Force Unit Post Office Los Angeles, California 90045 Attn: Technical Data Center	
1		Office of Research Analyses (OAR) Holloman Air Force Base, New Mexico 88330 Attn: Library RRRD	
1		U.S. Air Force Washington, D.C. Attn: Library	Col C. K. Stambaugh, Code AFRST
1		Commanding Officer U.S. Army Research Office (Durham) Box CM, Duke Station Durham, North Carolina 27706 Attn: Library	

Appendix D

Report Copies R	Report Copies D	Recipient	Designee
1		U.S. Army Missile Command Redstone Scientific Information Center Redstone Arsenal, Alabama 35808 Attn: Document Section	Dr. W. Wharton
1		Bureau of Naval Weapons Department of the Navy Washington, D.C. Attn: Library	J. Kay, Code RTMS-41
1		Commander U.S. Naval Missile Center Point Mugu, California 93041 Attn: Technical Library	
1		Commander U.S. Naval Weapons Center China Lake, California 93557 Attn: Library	
1		Commanding Officer Naval Research Branch Office 1030 E. Green Street Pasadena, California 91101 Attn: Library	
1		Director (Code 6180) U.S. Naval Research Laboratory Washington, D.C. 20390 Attn: Library	H. W. Carhart J. M. Krafft
1		Picatinny Arsenal Dover, New Jersey 07801 Attn: Library	I. Forsten
1		Air Force Aero Propulsion Laboratory Research & Technology Division Air Force Systems Command United States Air Force Wright-Patterson AFB, Ohio 45433 Attn: APRP (Library)	R. Quigley C. M. Donaldson

Appendix D

Report Copies			
R	D	Recipient	Designee
1		Electronics Division Aerojet-General Corporation P.O. Box 296 Azusa, California 91703 Attn: Library	W. L. Rogers
1		Space Division Aerojet-General Corporation 9200 East Flair Drive El Monte, California 91734 Attn: Library	S. Machlawski
1		Aerojet Ordnance and Manufacturing Aerojet-General Corporation 11711 South Woodruff Avenue Fullerton, California 90241 Attn: Library	
1		Aerojet Liquid Rocket Company P.O. Box 15847 Sacramento, California 95813 Attn: Technical Library 2484-2015A	R. Stiff
1		Aeronutronic Division of Philco Ford Corp. Ford Road Newport Beach, California 92663 Attn: Technical Information Department	Dr. L. H. Linder
1		Aerospace Corporation 2400 E. El Segundo Blvd. Los Angeles, California 90045 Attn: Library-Documents	J. G. Wilder
1		Arthur D. Little, Inc. 20 Acorn Park Cambridge, Massachusetts 02140 Attn: Library	
1		Astropower Laboratory McDonnell-Douglas Aircraft Company 2121 Paularino Newport Beach, California 92163 Attn: Library	

Appendix D

Report Copies R	D	Recipient	Designee
1		ARO, Incoporated Arnold Engineering Development Center Arnold AF Station, Tennessee 37389 Attn: Library	
1		Susquehanna Corporation Atlantic Research Division Shirley Highway & Edsall Road Alexandria, Virginia 22314 Attn: Library	
1		Beech Aircraft Corporation Boulder Facility Box 631 Boulder, Colorado Attn: Library	Douglas Pope
1	1	Bell Aerosystems, Inc. Box 1 Buffalo, New York 14240 Attn: Library	John Seneff
1		Instruments & Life Support Division Bendix Corporation P.O. Box 4508 Davenport, Iowa 52808 Attn: Library	W. M. Carlson
1		Bellcomm 955 L'Enfant Plaza, S.W. Washington, D.C. Attn: Library	H. S. London
1		Boeing Company Space Division P.O. Box 868 Seattle, Washington 98124 Attn: Library	J. D. Alexander C. F. Tiffany
1		Boeing Company 1625 K Street, N.W. Washington, D.C. 20006	

Appendix D

Report Copies			
R	D	Recipient	Designee
1		Boeing Company P.O. Box 1680 Huntsville, Alabama 35801	Ted Snow
1		Chemical Propulsion Information Agency Applied Physics Laboratory 8621 Georgia Avenue Silver Spring, Maryland 20910	Tom Reedy
1		Chrysler Corporation Missile Division P.O. Box 2628 Detroit, Michigan Attn: Library	John Gates
1		Chrysler Corporation Space Division P.O. Box 29200 New Orleans, Louisiana 70129 Attn: Librarian	
1		Curtiss-Wright Corporation Wright Aeronautical Division Woodridge, New Jersey Attn: Library	G. Kelley
1		University of Denver Denver Research Institute P.O. Box 10127 Denver, Colorado 80210 Attn: Security Office	
1		Fairchild Stratos Corporation Aircraft Missiles Division Hagerstown, Maryland Attn: Library	
1		Research Center Fairchild Hiller Corporation Germantown, Maryland Attn: Library	Ralph Hall

Appendix D

Report Copies		Recipient	Designee
R	D		
1		Republic Aviation Fairchild Hiller Corporation Farmington, Long Island New York	
1		General Dynamics/Convair P.O. Box 1128 San Diego, California 92112 Attn: Library	Frank Dore
1		Missiles and Space Systems Center General Electric Company Valley Forge Space Technology Center P.O. Box 8555 Philadelphia, Pa. 19101 Attn: Library	A. Cohen F. Schultz
1		General Electric Company Flight Propulsion Lab. Department Cincinnati, Ohio Attn: Library	D. Suichu Leroy Smith
1		Grumman Aircraft Engineering Corporation Bethpage, Long Island, New York Attn: Library	Joseph Gavin
1		Hercules Powder Company Allegheny Ballistics Laboratory P.O. Box 210 Cumberland, Maryland 21501 Attn: Library	
1		Honeywell, Inc. Aerospace Division 2600 Ridgeway Road Minneapolis, Minnesota Attn: Library	
1		IIT Research Institute Technology Center Chicago, Illinois 60616 Attn: Library	C. K. Hersh

Appendix D

Report Copies			
R	D	Recipient	Designee
1		Kidde Aerospace Division Walter Kidde & Company, Inc. 476 Main Street Belleville, N. J.	R. J. Hanville
1		Ling-Temco-Vought Corporation P.O. Box 5907 Dallas, Texas 75222 Attn: Library	
1		Lockheed Missiles and Space Company P.O. Box 504 Sunnyvale, California 94087 Attn: Library	
1		Lockheed Propulsion Company P.O. Box 111 Redlands, California 92374 Attn: Library, Thackwell	H. L. Thackwell
1		Marquardt Corporation 16555 Saticoy Street Box 2013 - South Annex Van Nuys, California 91409	L. R. Bell, Jr.
1		Martin-Marietta Corporation (Baltimore Division) Baltimore, Maryland 21203 Attn: Library	
1		Denver Division Martin-Marietta Corporation P.O. Box 179 Denver, Colorado 80201 Attn: Library	Dr. Morganthaler F. R. Schwartzberg
1		Orlando Division Martin-Marietta Corporation Box 5827 Orlando, Florida Attn: Library	J. Fern

Appendix D

Report Copies			
R	D	Recipient	Designee
1		Western Division McDonnell Douglas Astronautics 5301 Bolsa Avenue Huntington Beach, California 92647 Attn: Library	R. W. Hallet G. W. Burge P. Klevatt
1		McDonnell Douglas Aircraft Corporation P.O. Box 516 Lambert Field, Missouri 63166 Attn: Library	R. A. Herzmark
1		Rocketdyne Division North American Rockwell, Inc. 6633 Canoga Avenue Canoga Park, California 91304 Attn: Library, Department 596-306	Dr. R. J. Thompson S. F. Lacobellis
1		Space & Information Systems Division North American Rockwell 12214 Lakewood Blvd. Downey, California Attn: Library	
1		Northrop Space Laboratories 3401 West Broadway Hawthorne, California Attn: Library	Dr. William Howard
1		Purdue University Lafayette, Indiana 47907 Attn: Library (Technical)	Dr. Bruce Reese
1		Radio Corporation of American Astro-Electronics Products Princeton, New Jersey Attn: Library	
1		Rocket Research Corporation Willow Road at 116th Street Redmond, Washington 98052 Attn: Library	F. McCullough, Jr.

Appendix D

Report Copies		Recipient	Designee
R	D		
1		Stanford Research Institute 333 Eavenswood Avenue Menlo Park, California 94025 Attn: Library	Dr. Gerald Marksman
1		Thiokol Chemical Corporation Redstone Division Huntsville, Alabama Attn: Library	John Goodloe
1		TRW Systems, Inc. 1 Space Park Redondo Beach, California 90278 Attn: Tech. Lib. Doc. Acquisitions	D. H. Lee
1		TRW TAPCO Division 23555 Euclid Avenue Cleveland, Ohio 44117	P. T. Angell
1		United Aircraft Corporation Corporation Library 400 Main Street East Hartford, Connecticut 06108 Attn: Library	Dr. David Rix Erle Martin Frank Owen Wm. E. Taylor
1		United Aircraft Corporation Pratt & Whitney Division Florida Research & Development Center P.O. Box 2691 West Palm Beach, Florida 33402 Attn: Library	R. J. Coar Dr. Schmitke
1		United Aircraft Corporation United Technology Center P.O. Box 358 Sunnyvale, California 94038 Attn: Library	Dr. David Altman
1		Vickers Incorporated Box 302 Troy, Michigan	
1		Vought Astronautics Box 5907 Dallas, Texas Attn: Library	

FIGURES

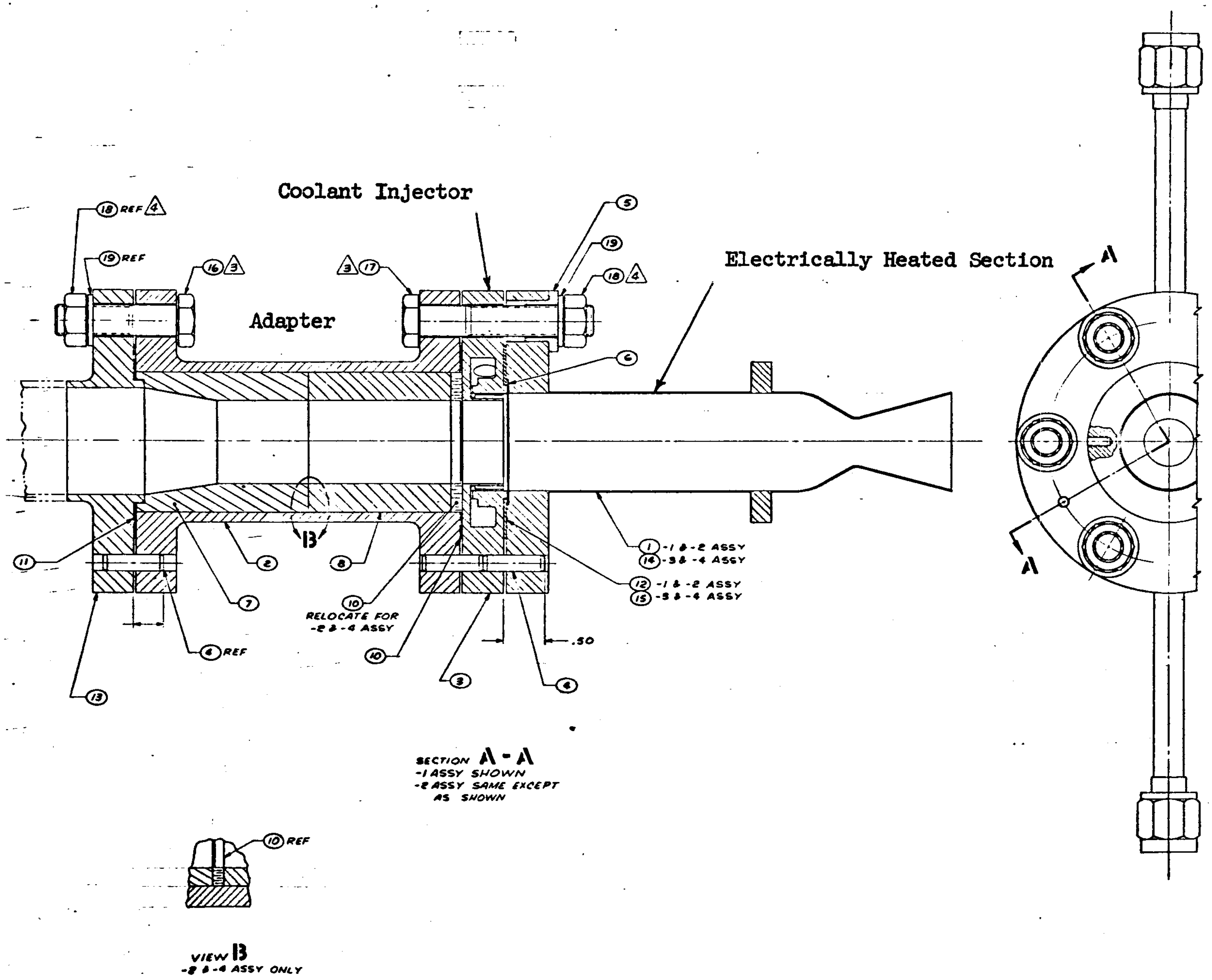

Figure 1. Test Assembly

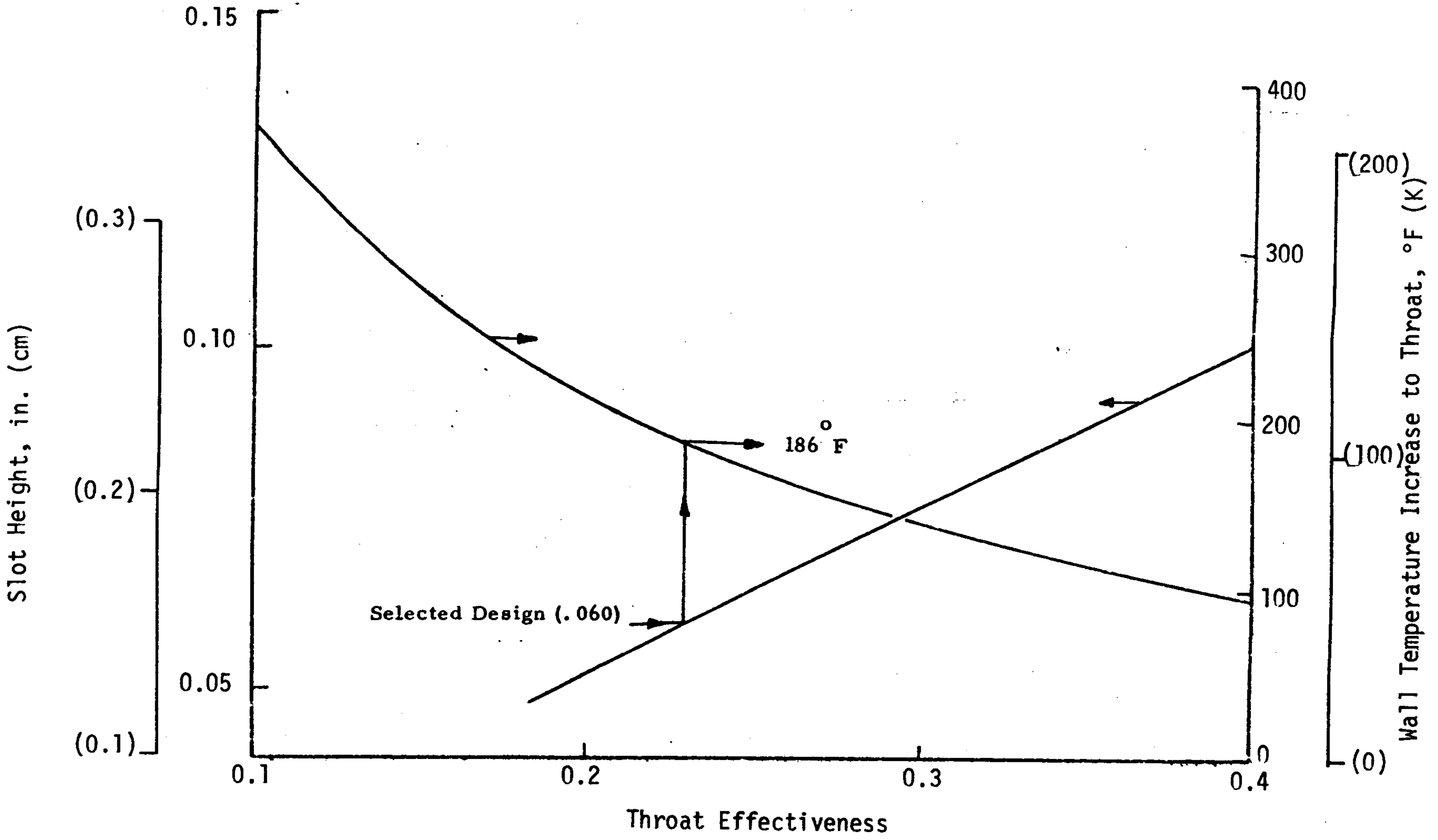

Figure 2. Film Coolant Slot Design - Ambient Hydrogen

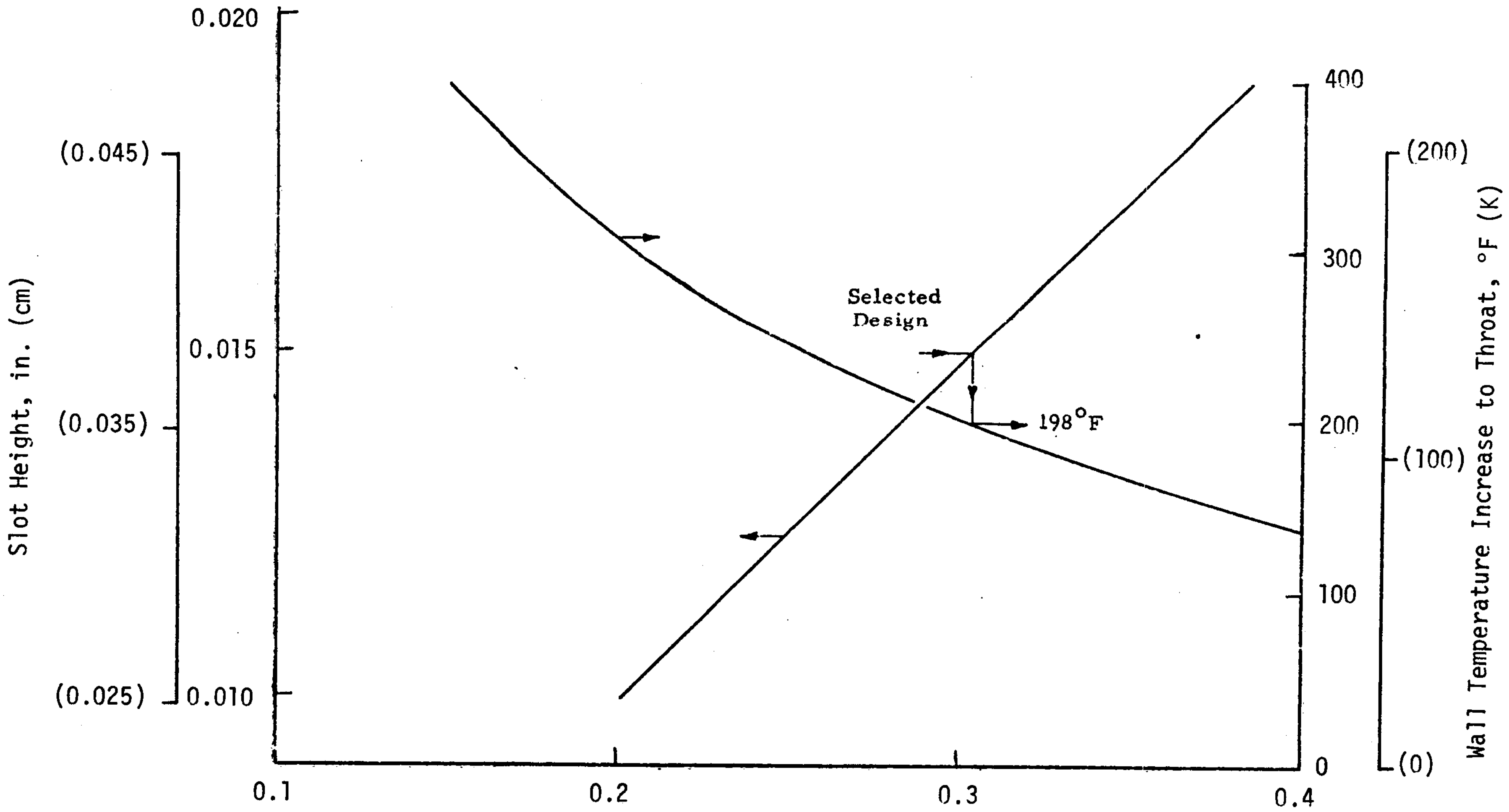

Figure 3. Film Coolant Slot Design - 140°R Hydrogen

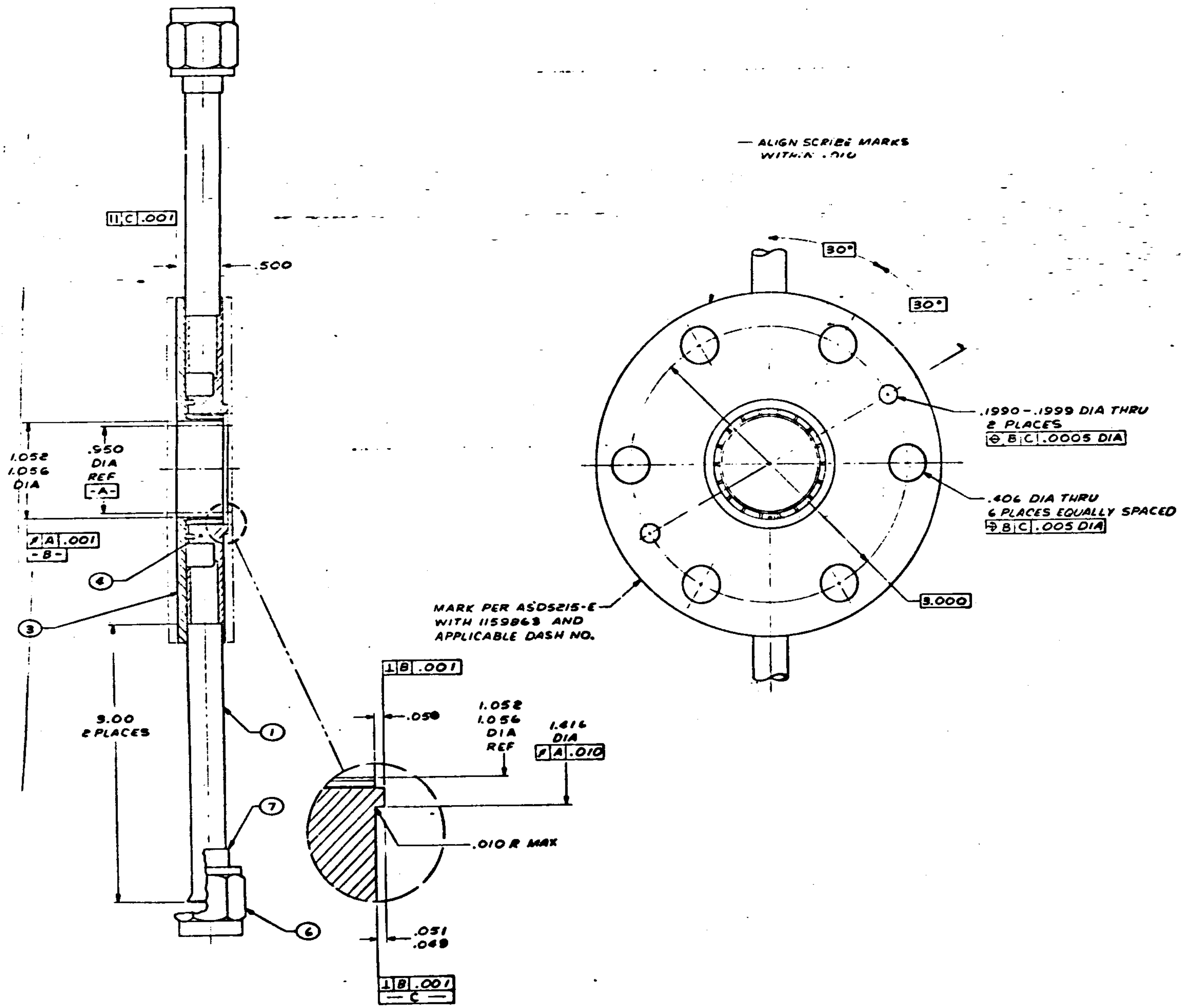

Figure 4. Film Coolant Injector Assembly

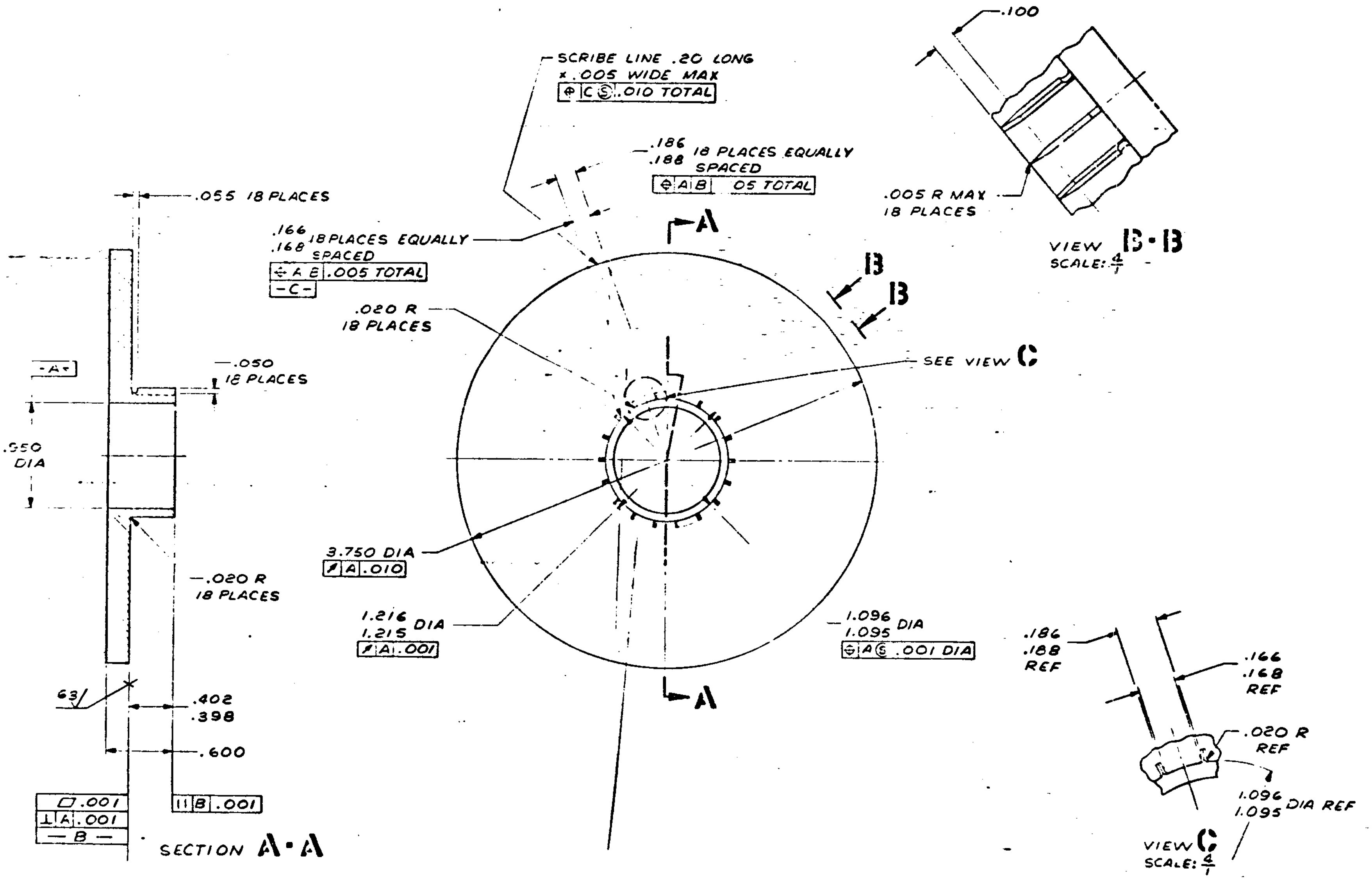

Figure 5. Film Coolant Injector - Inner Ring

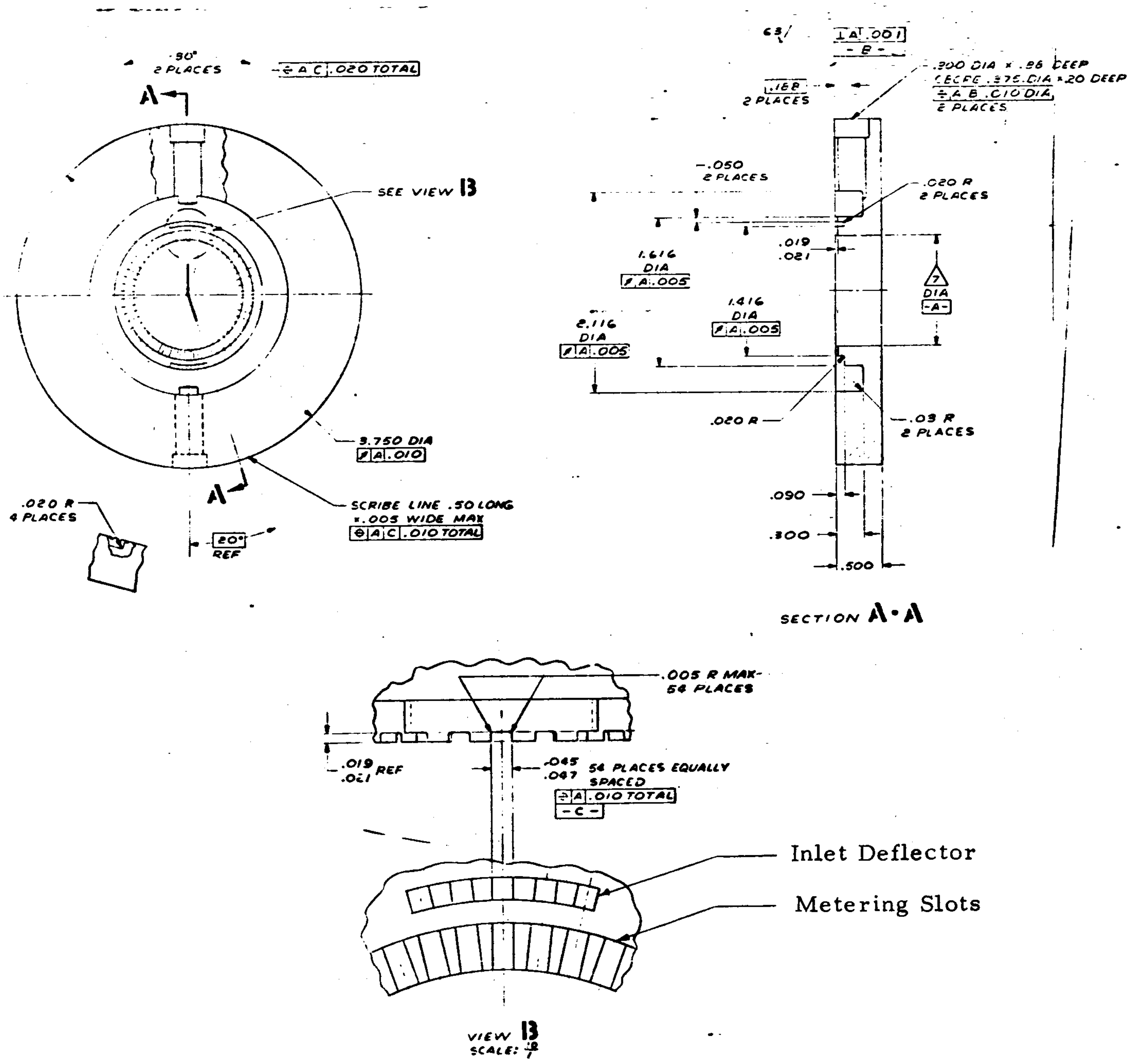

Figure 6. Film Coolant Injector - Outer Ring

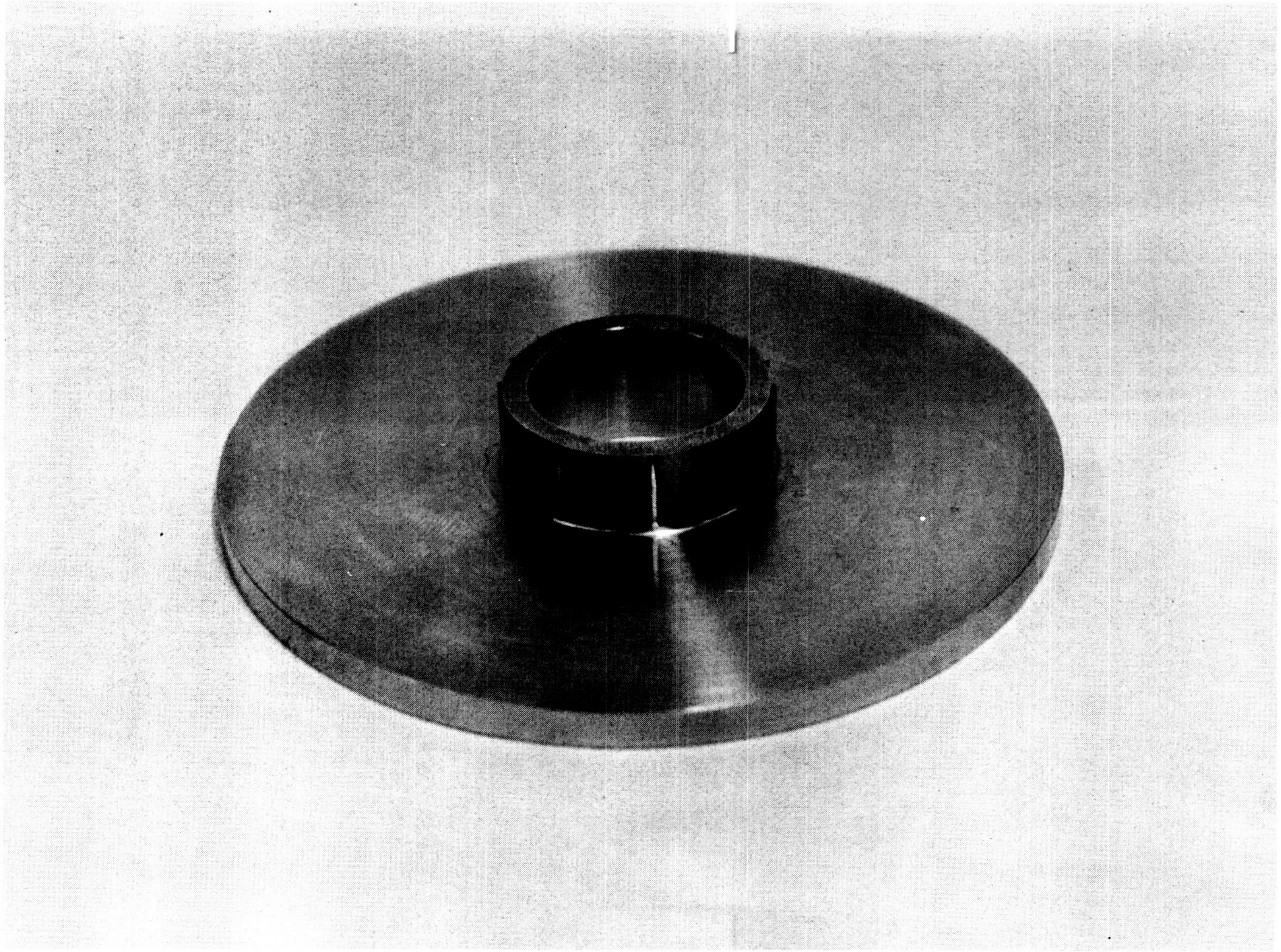

Figure 7. Inner Ring - 0.015 in. Injector

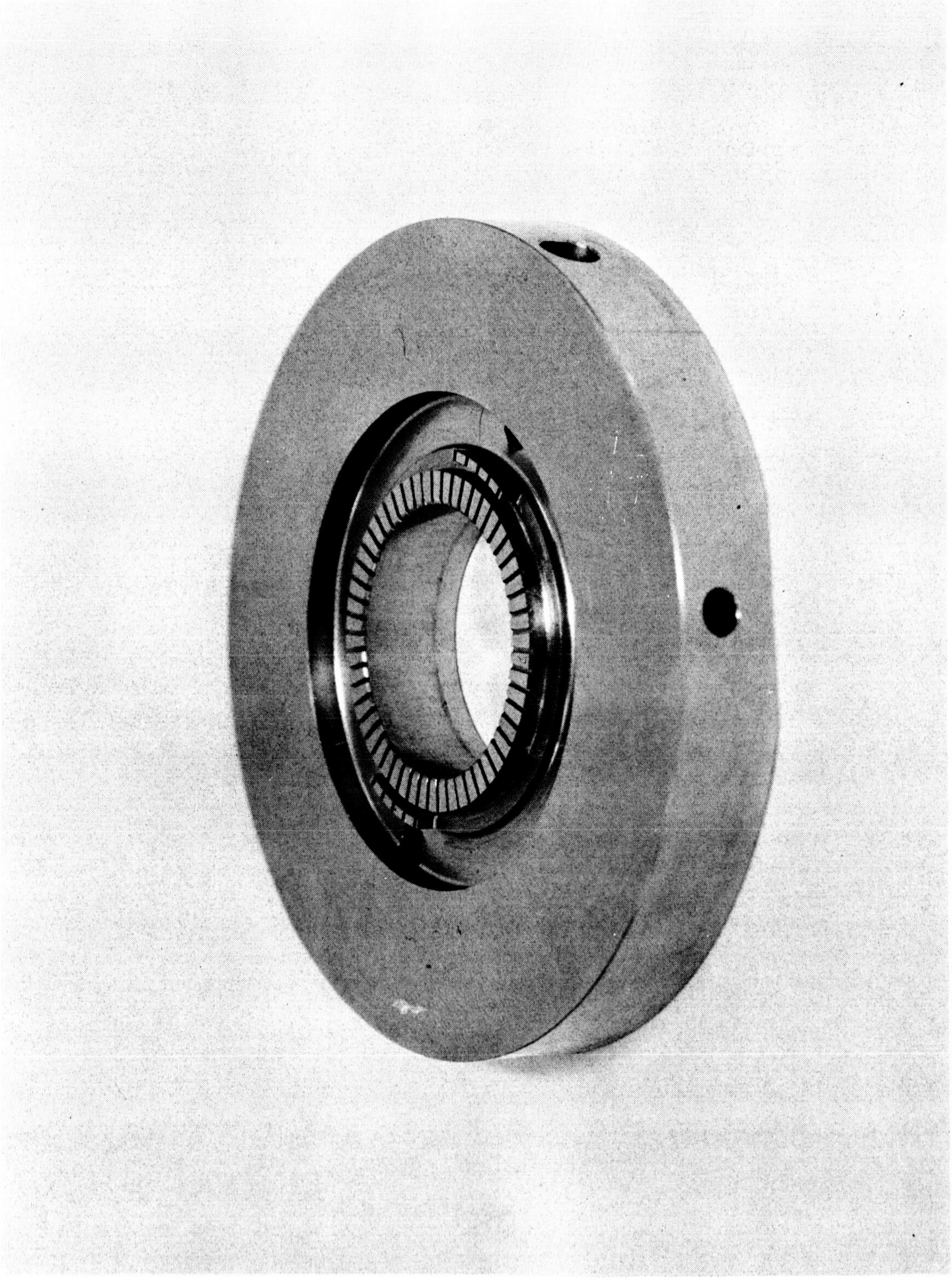

Figure 8. Outer Ring - 0.015 in. Injector

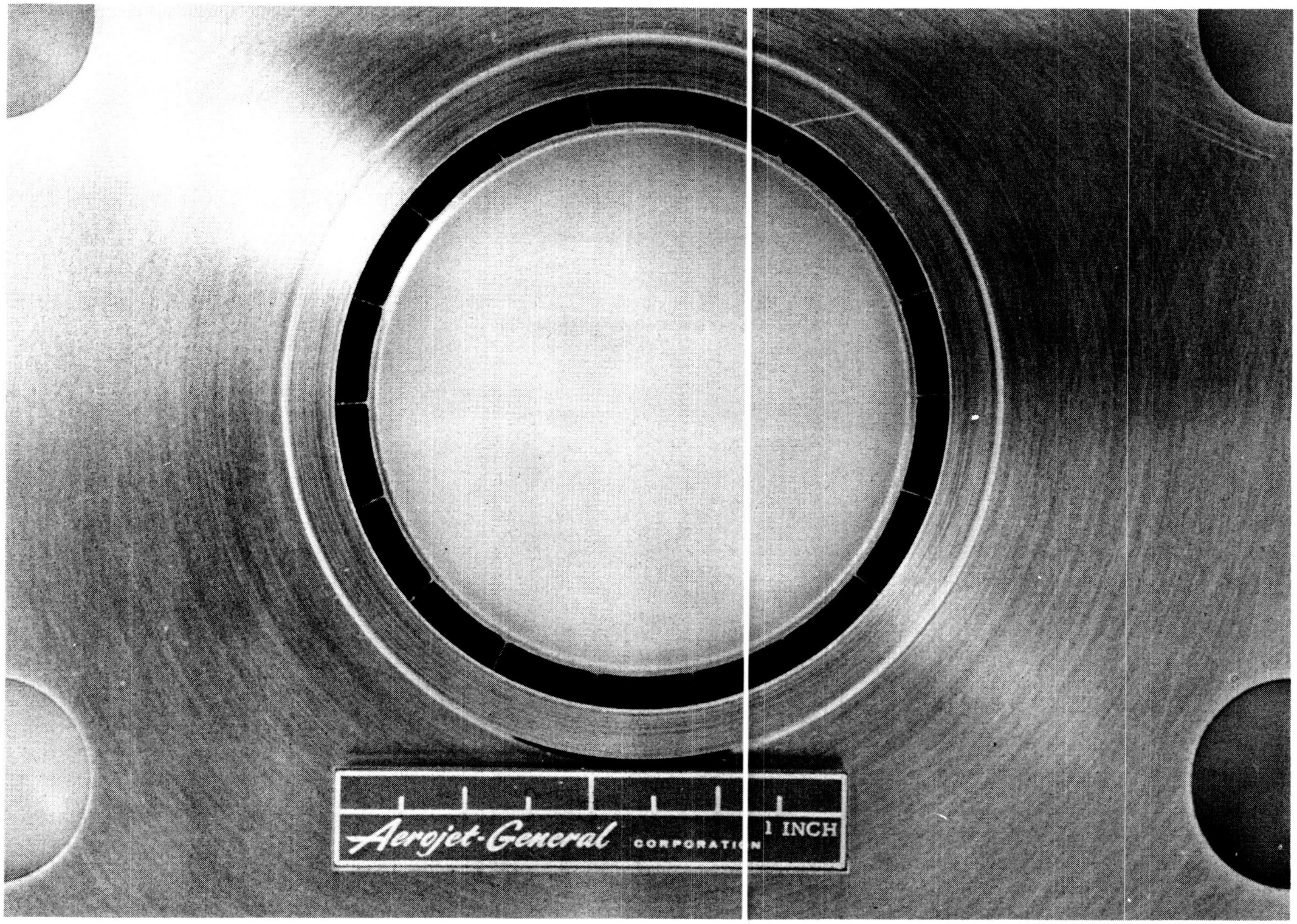

Figure 9. 0.060 in. Film Coolant Slot

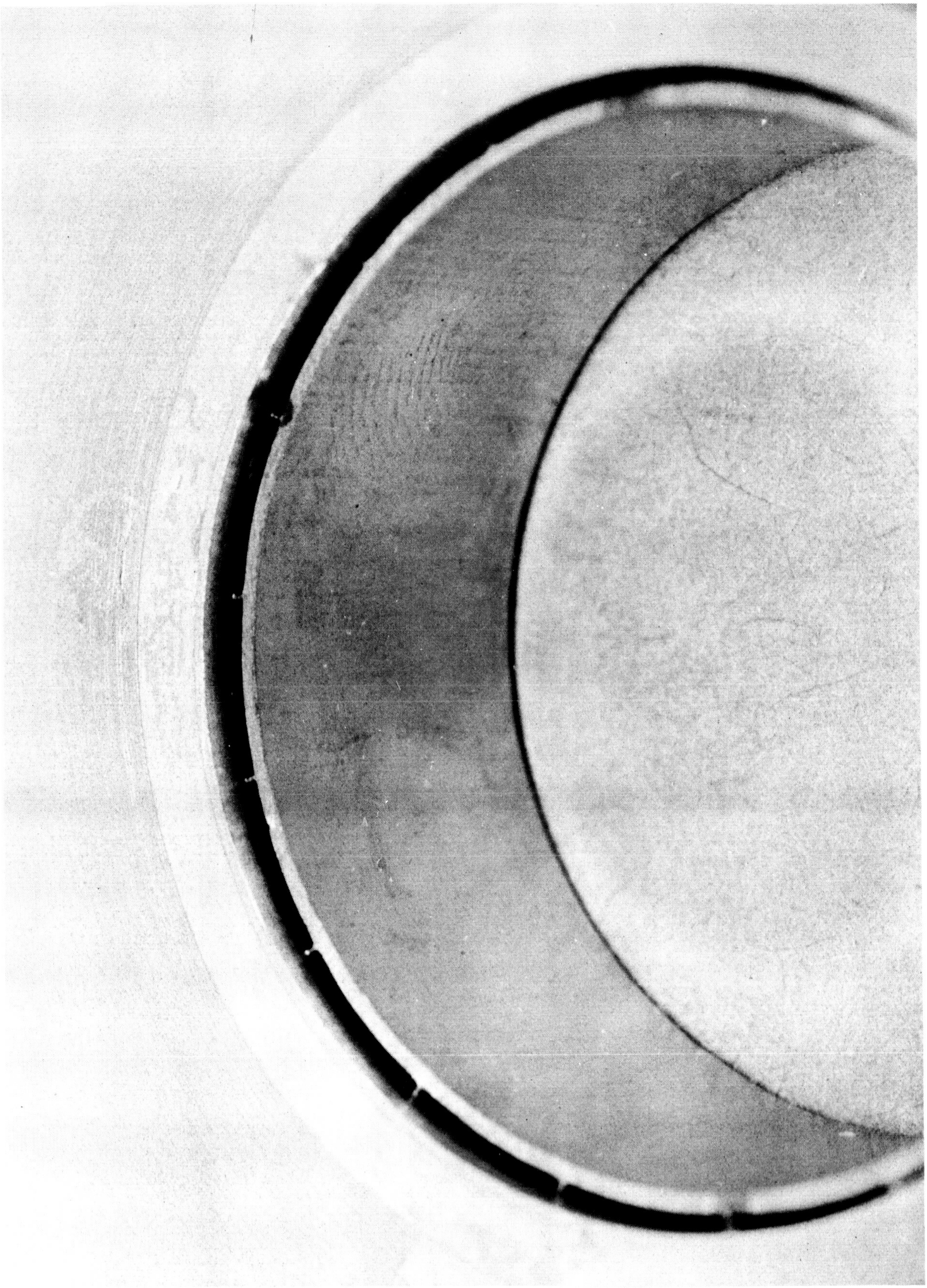

Figure 10. 0.015 in. Film Coolant Slot

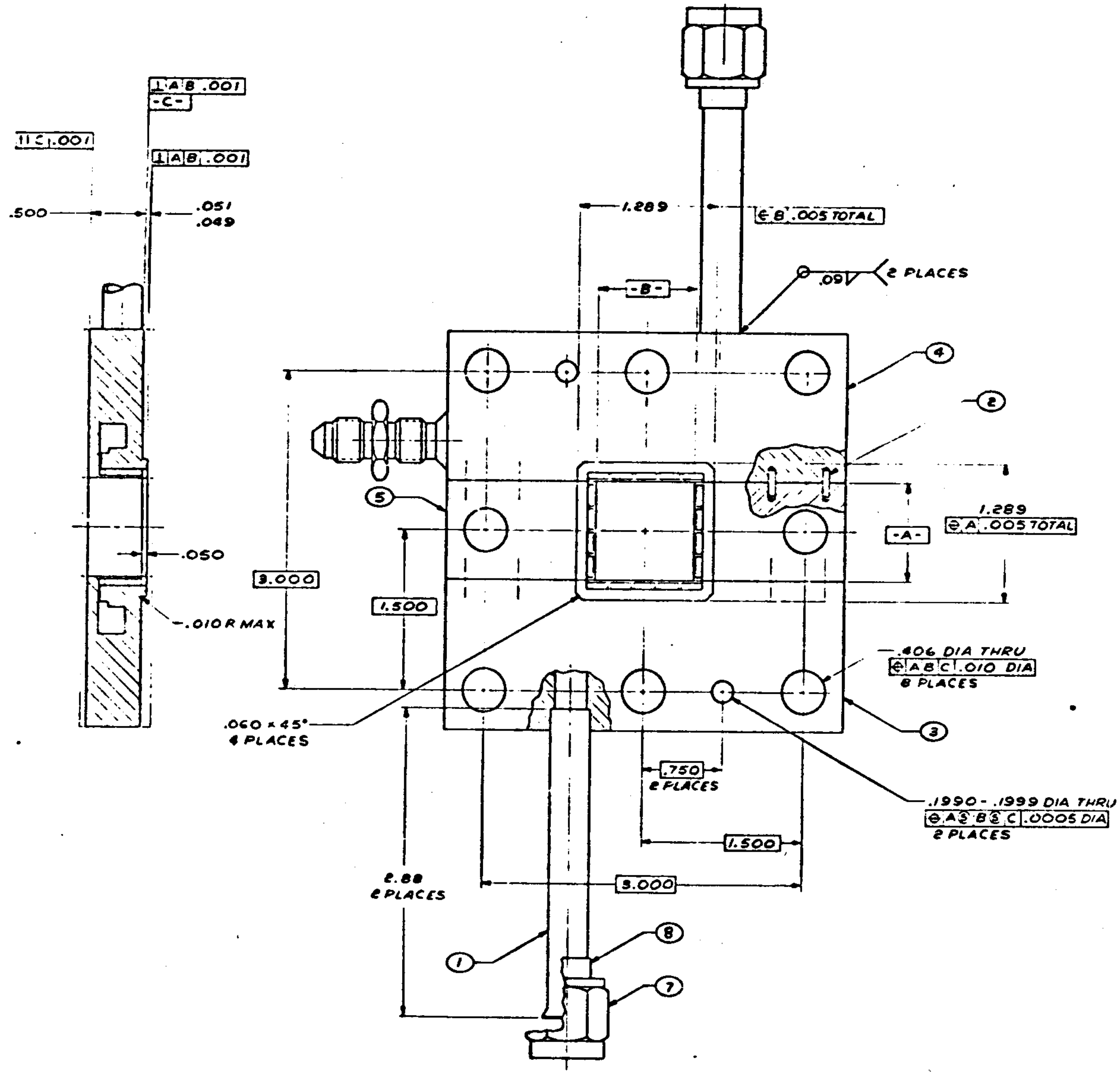

Figure 11. Square Injector Assembly

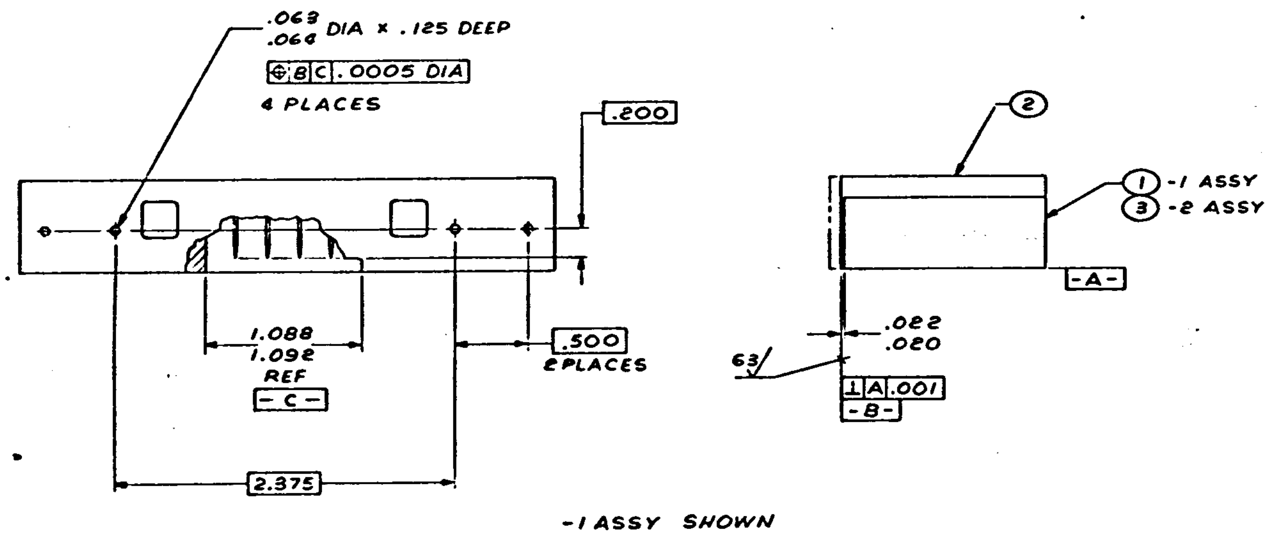

Figure 12. Square Injector - Plate No. 1 Assembly

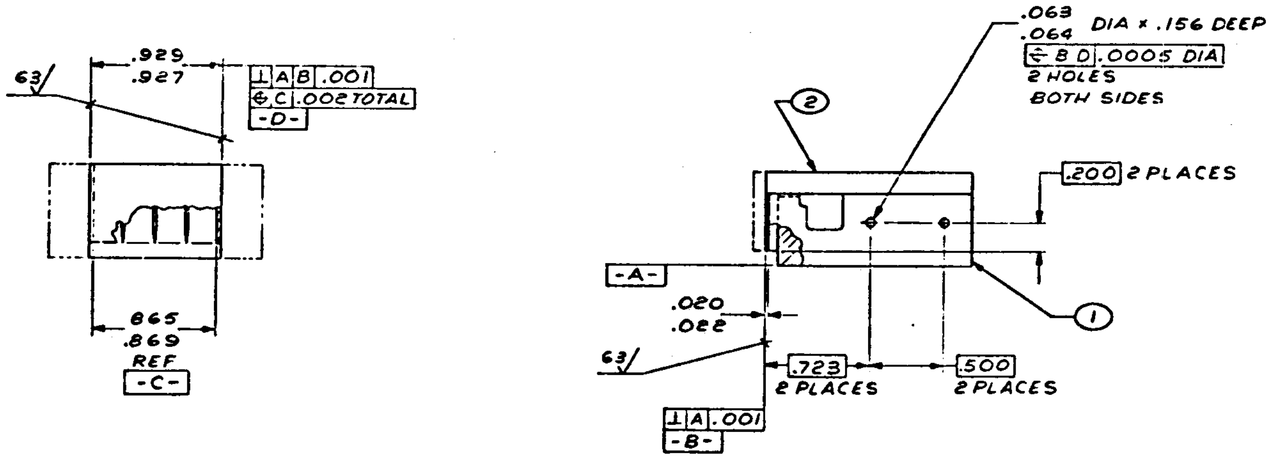

Figure 13. Square Injector - Plate No. 2 Assembly

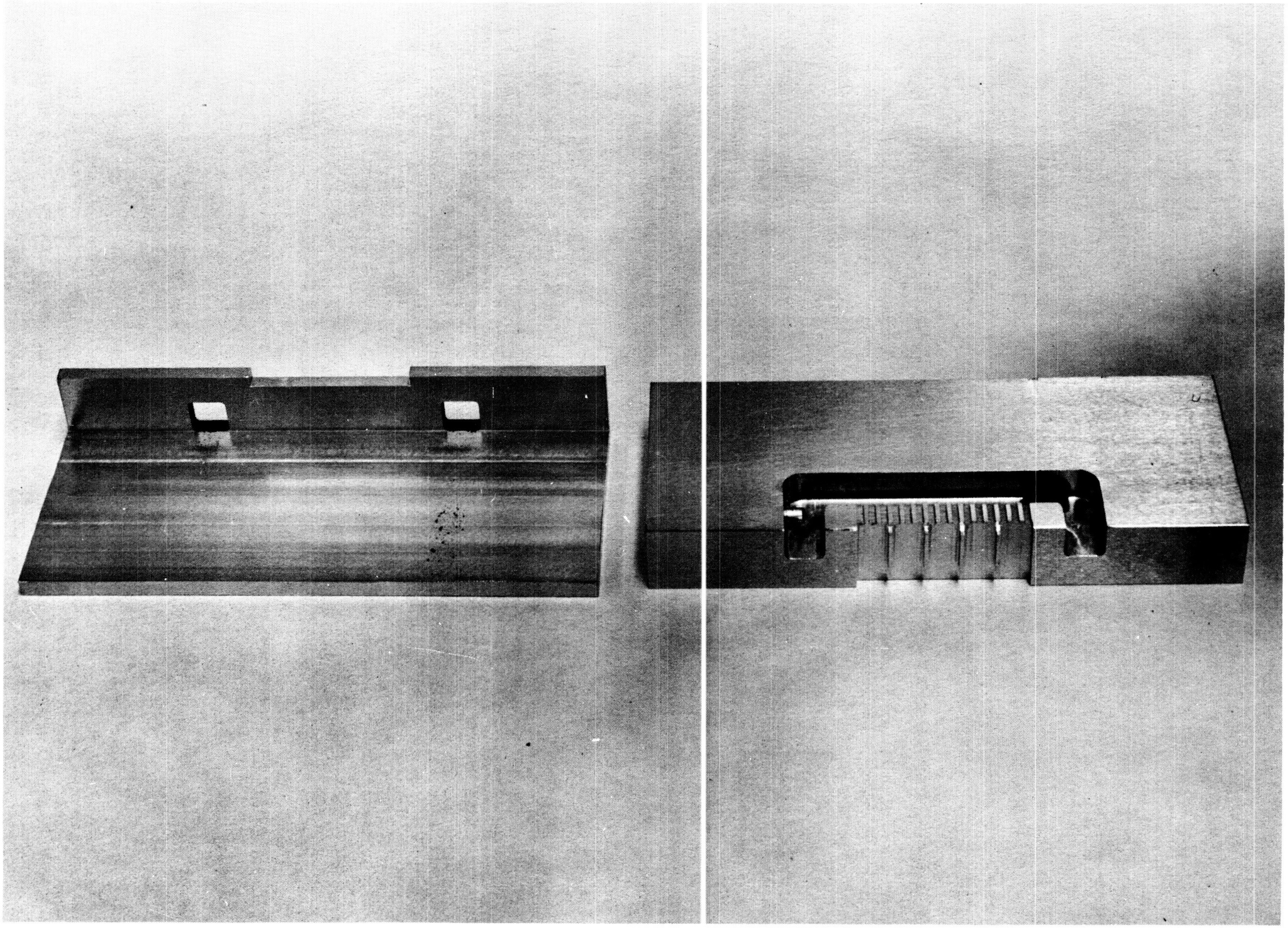

Figure 14. Five-Channel Metering Section and Cover Plate

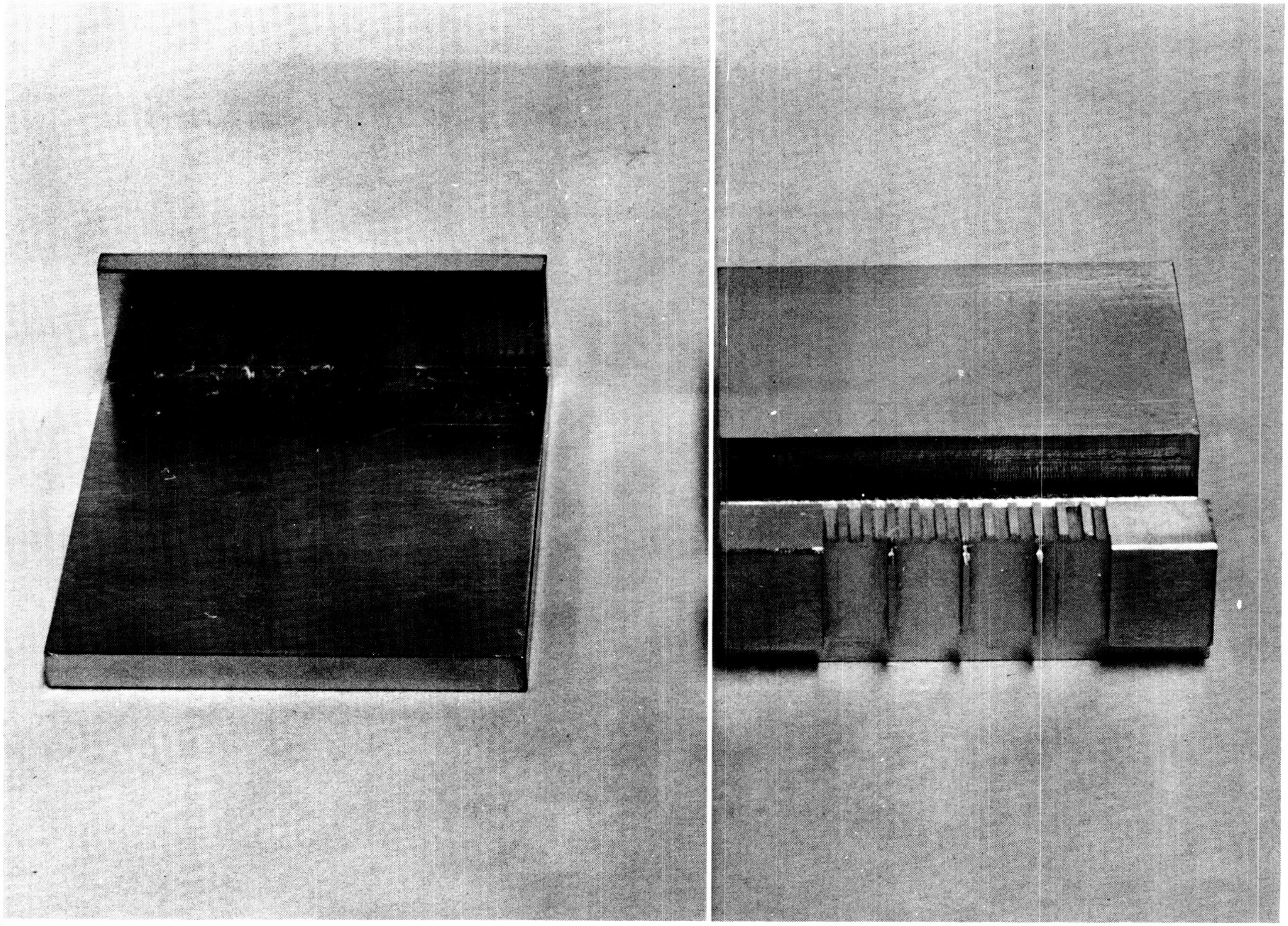

Figure 15. Four-Channel Metering Section and Cover Plate

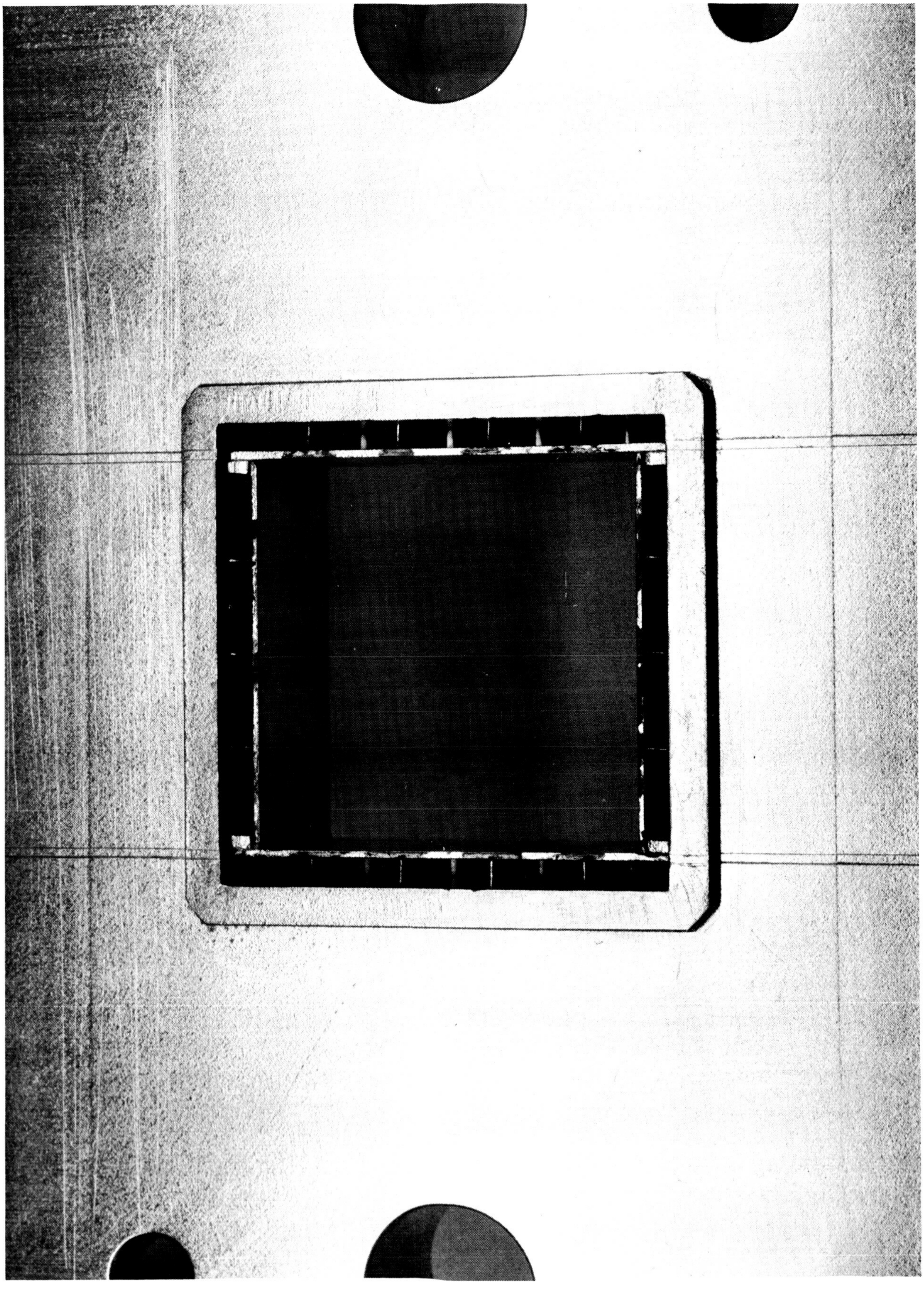

Figure 16. Square Injector Coolant Slot

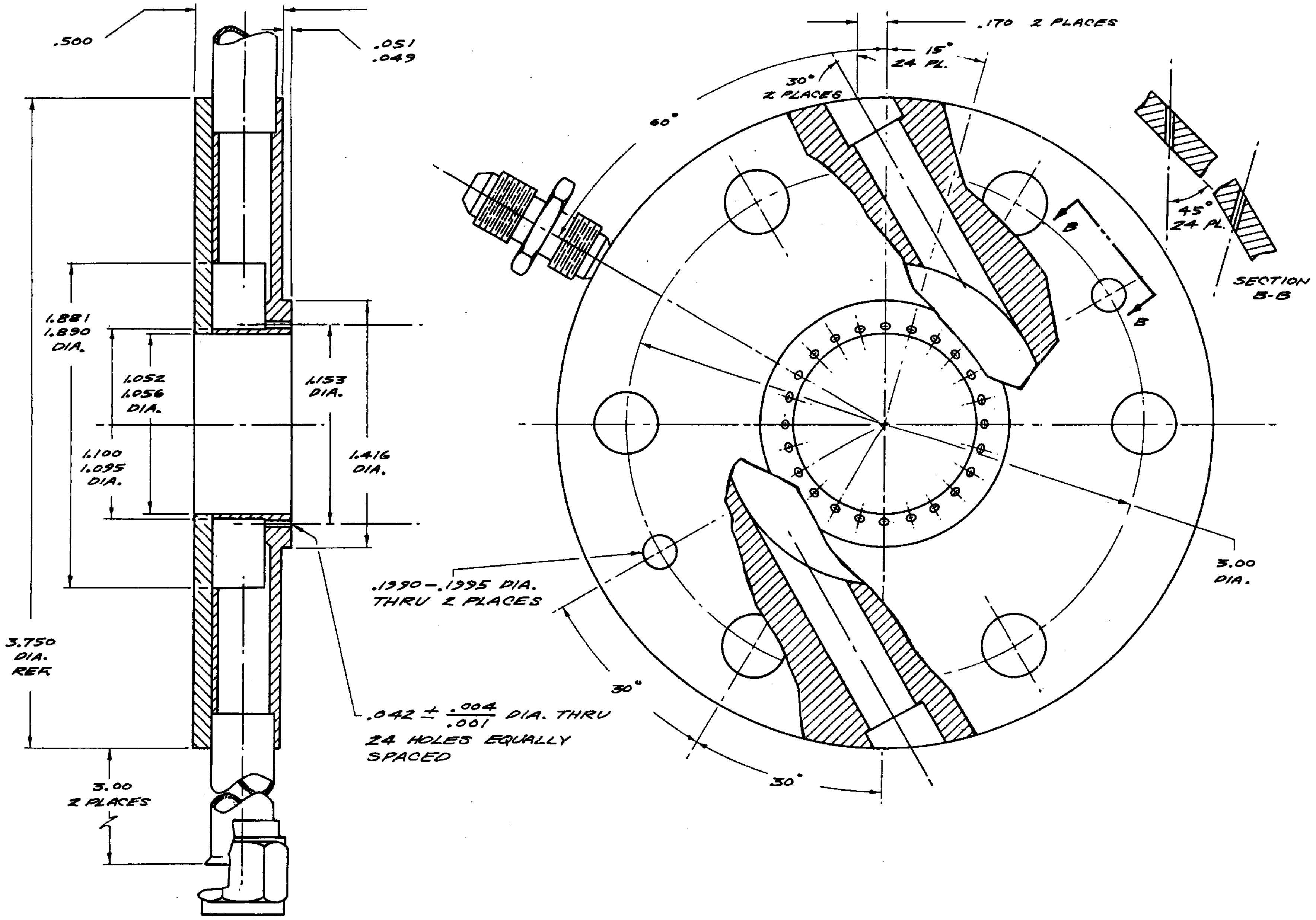

Figure 17. Liquid Coolant Injector Design

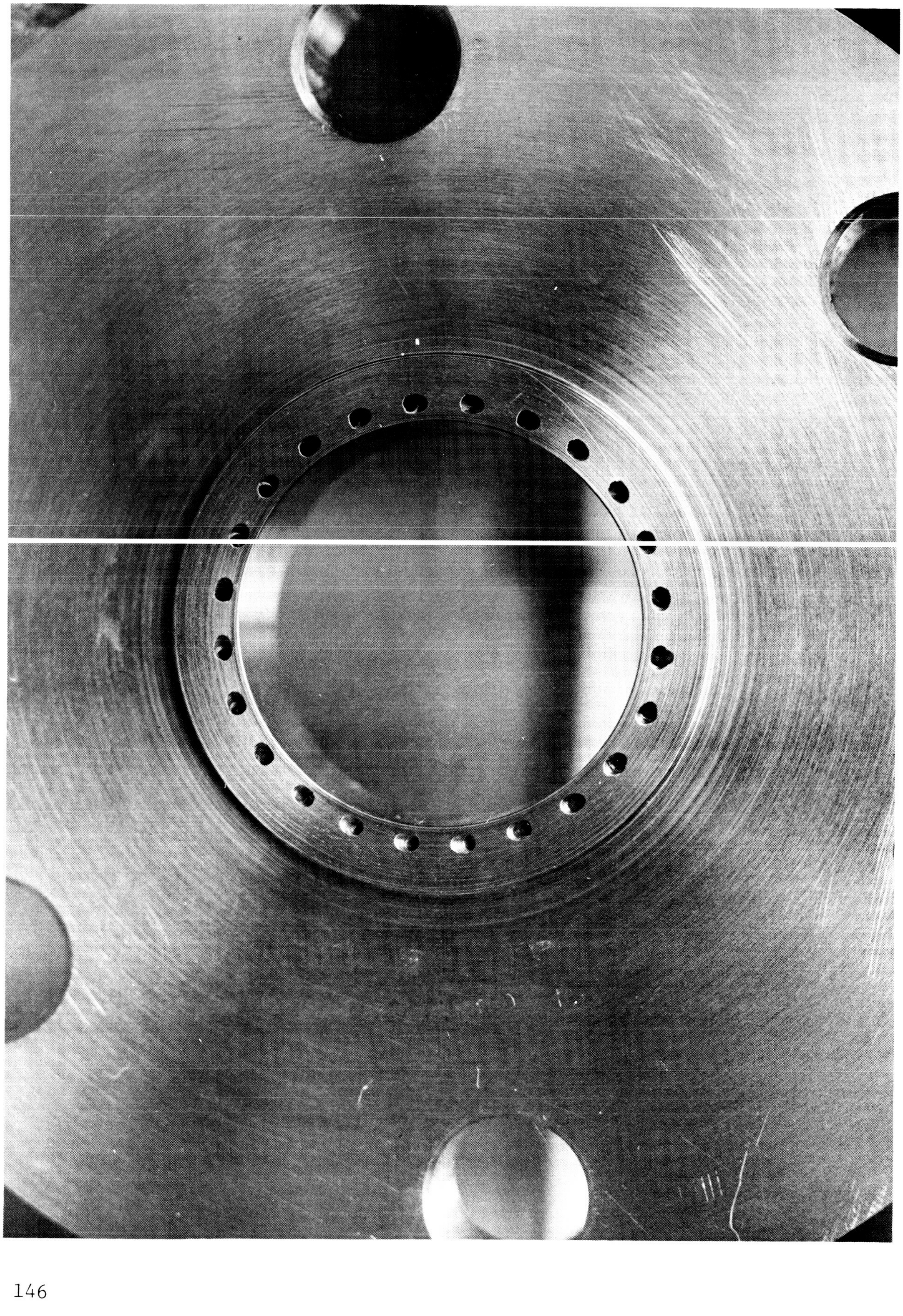

Figure 18. Liquid Coolant Injector

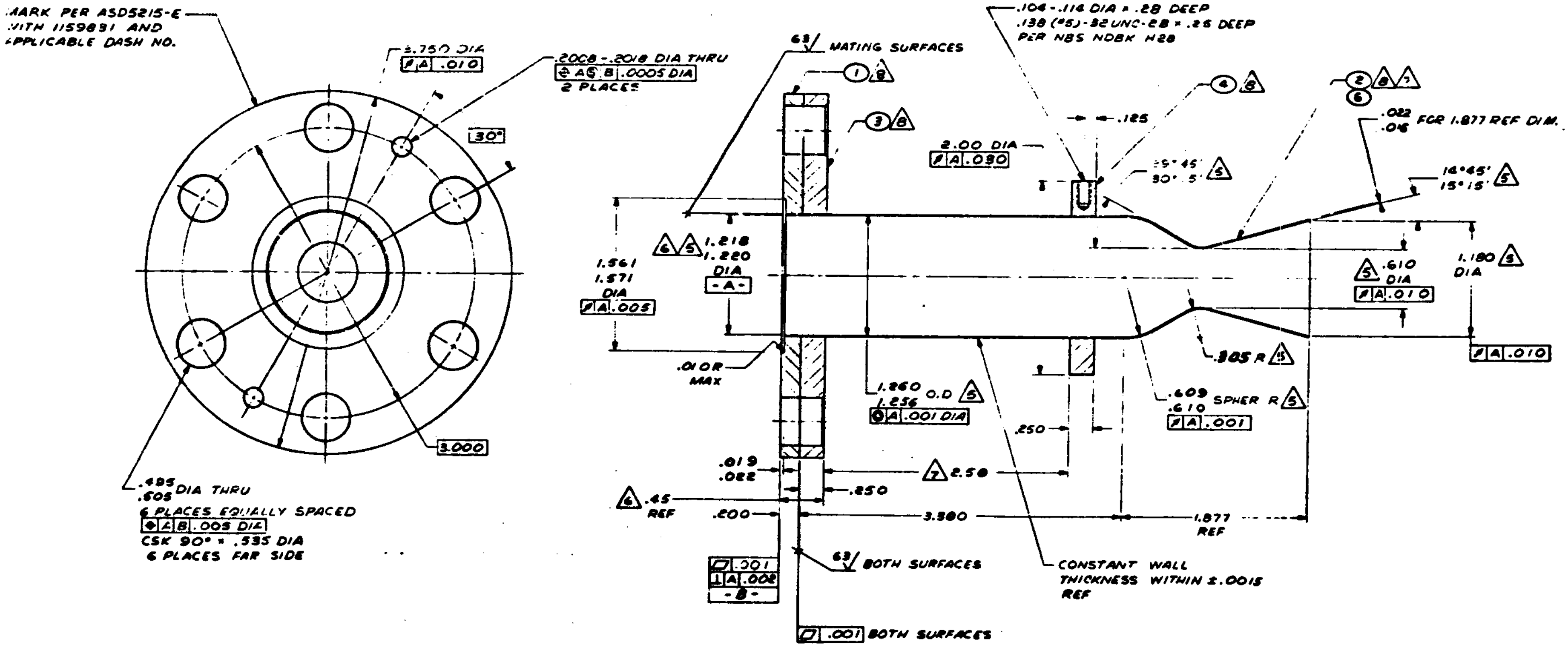

Figure 19. Cylindrical Chamber

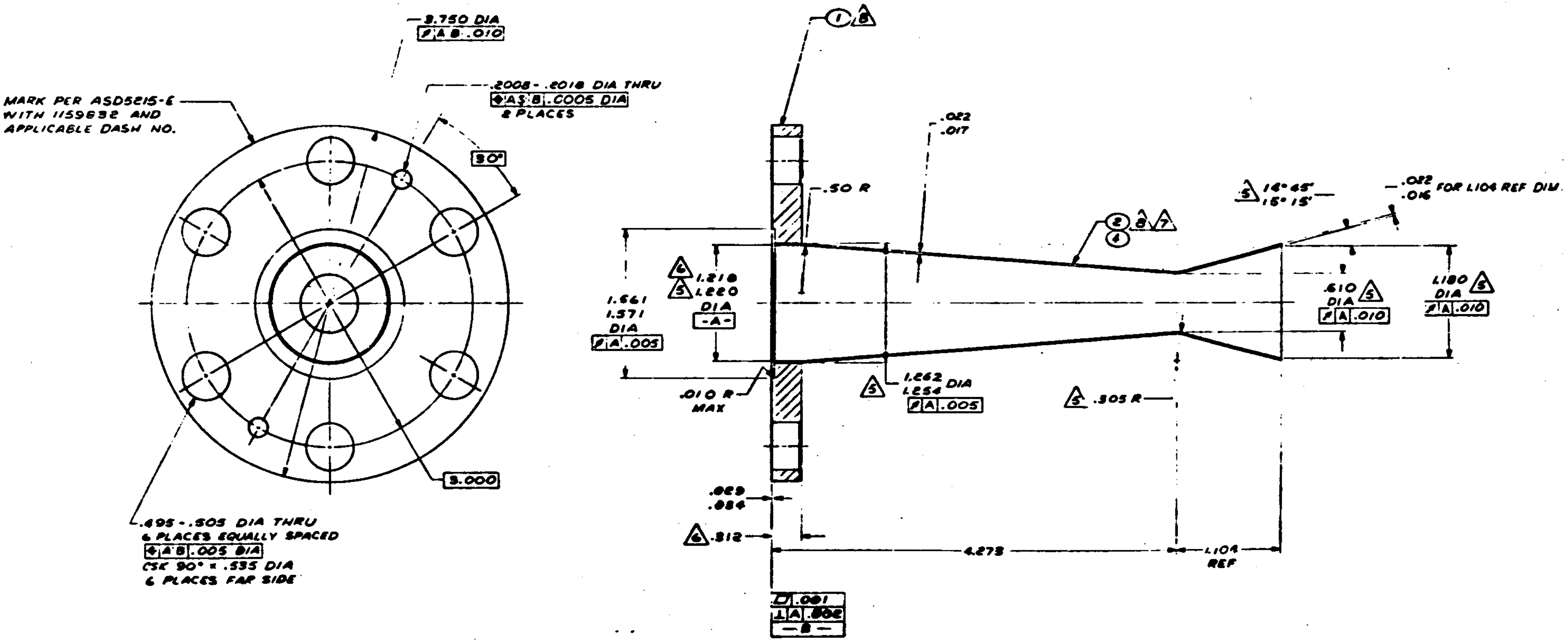

Figure 20. Conical Chamber

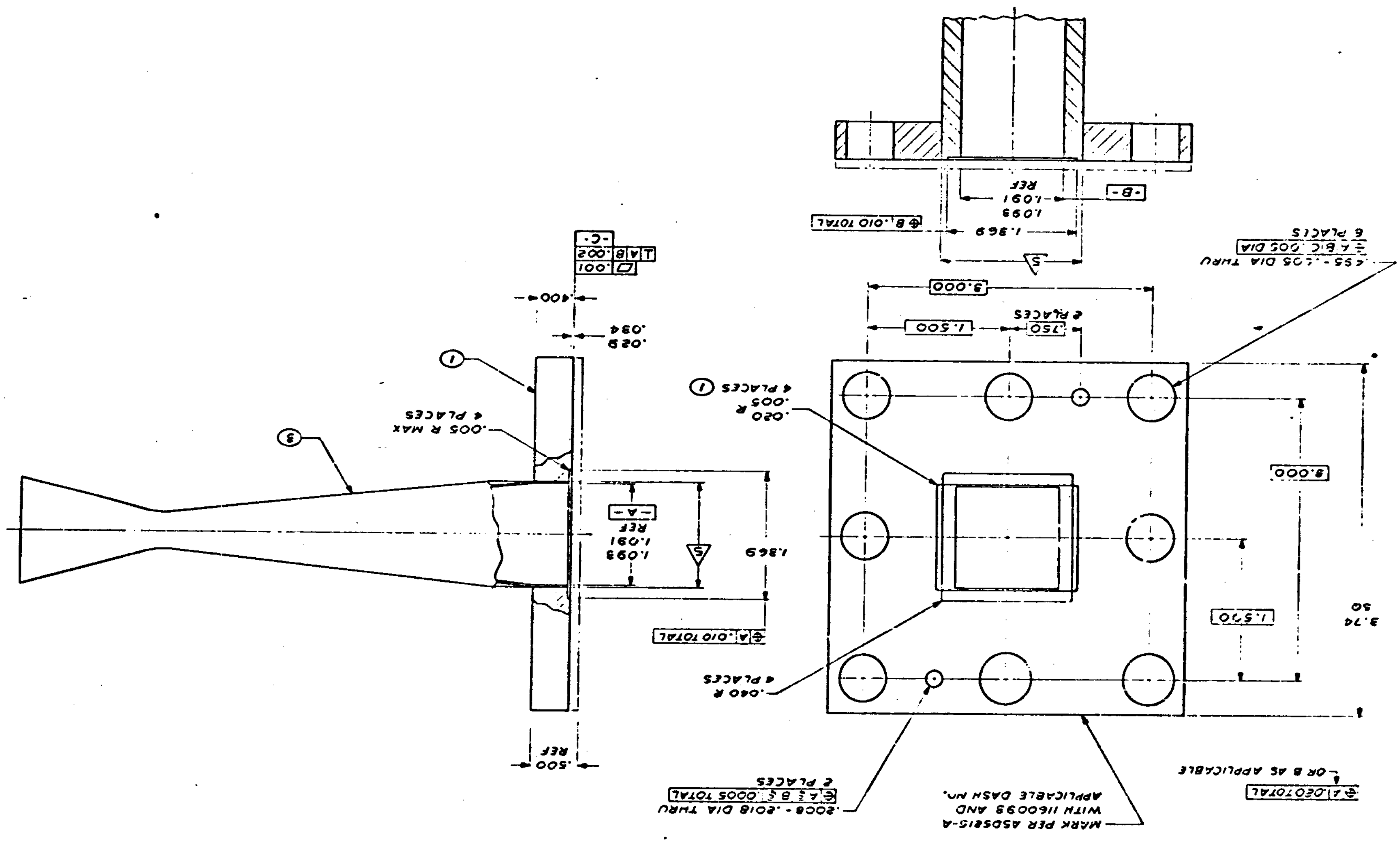

Figure 21. Rectangular Chamber Assembly

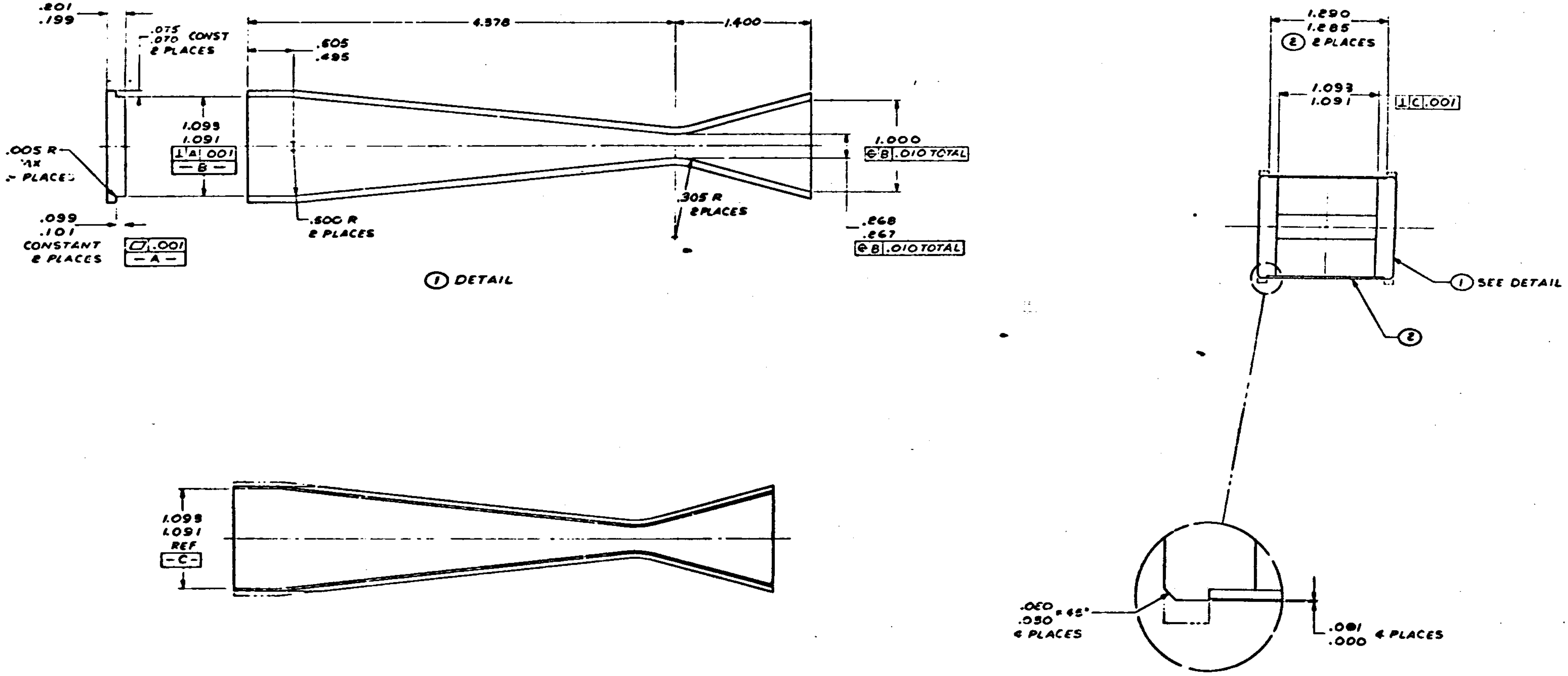

Figure 22. Rectangular Chamber

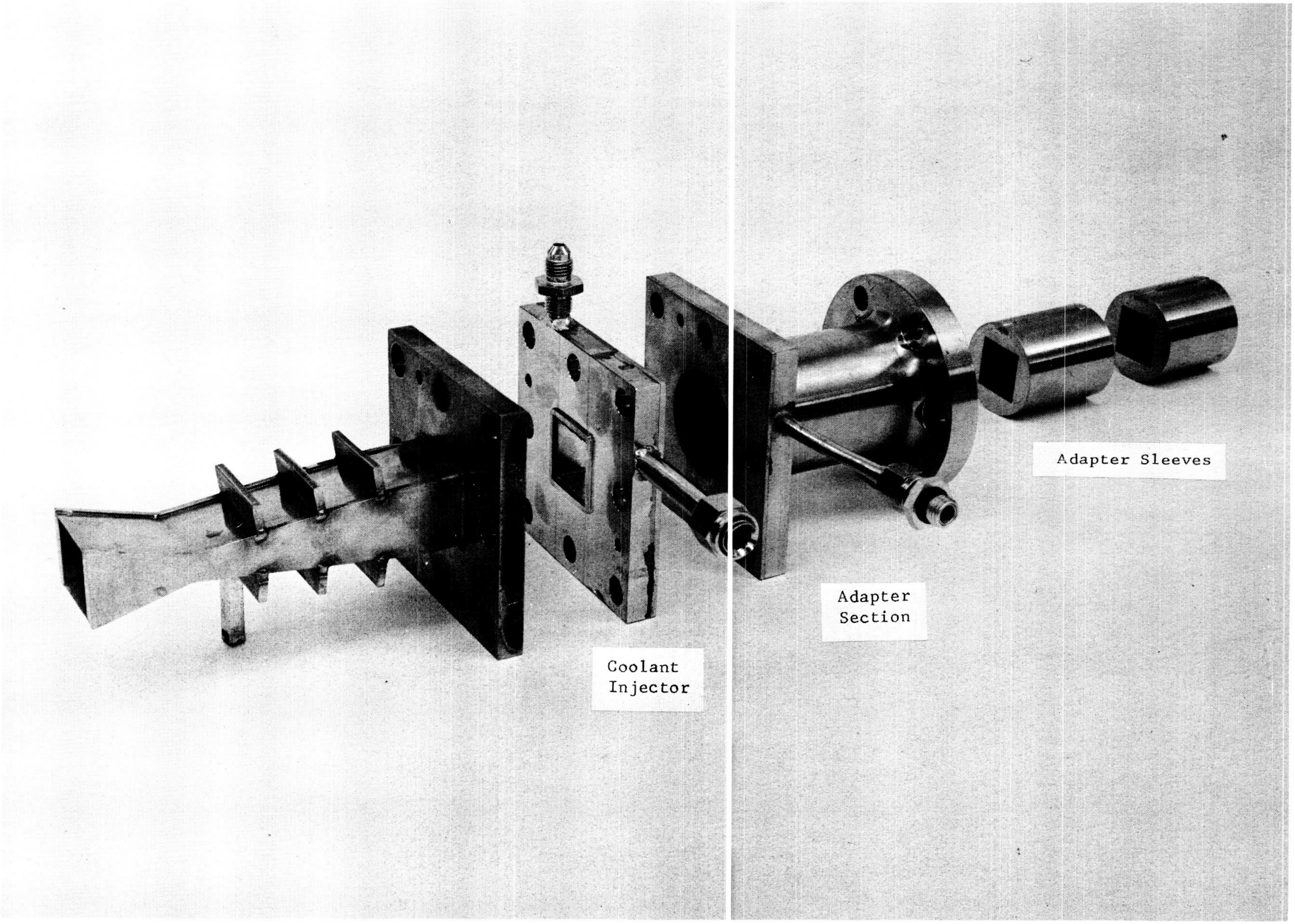

Figure 23. Rectangular Test Assembly Components

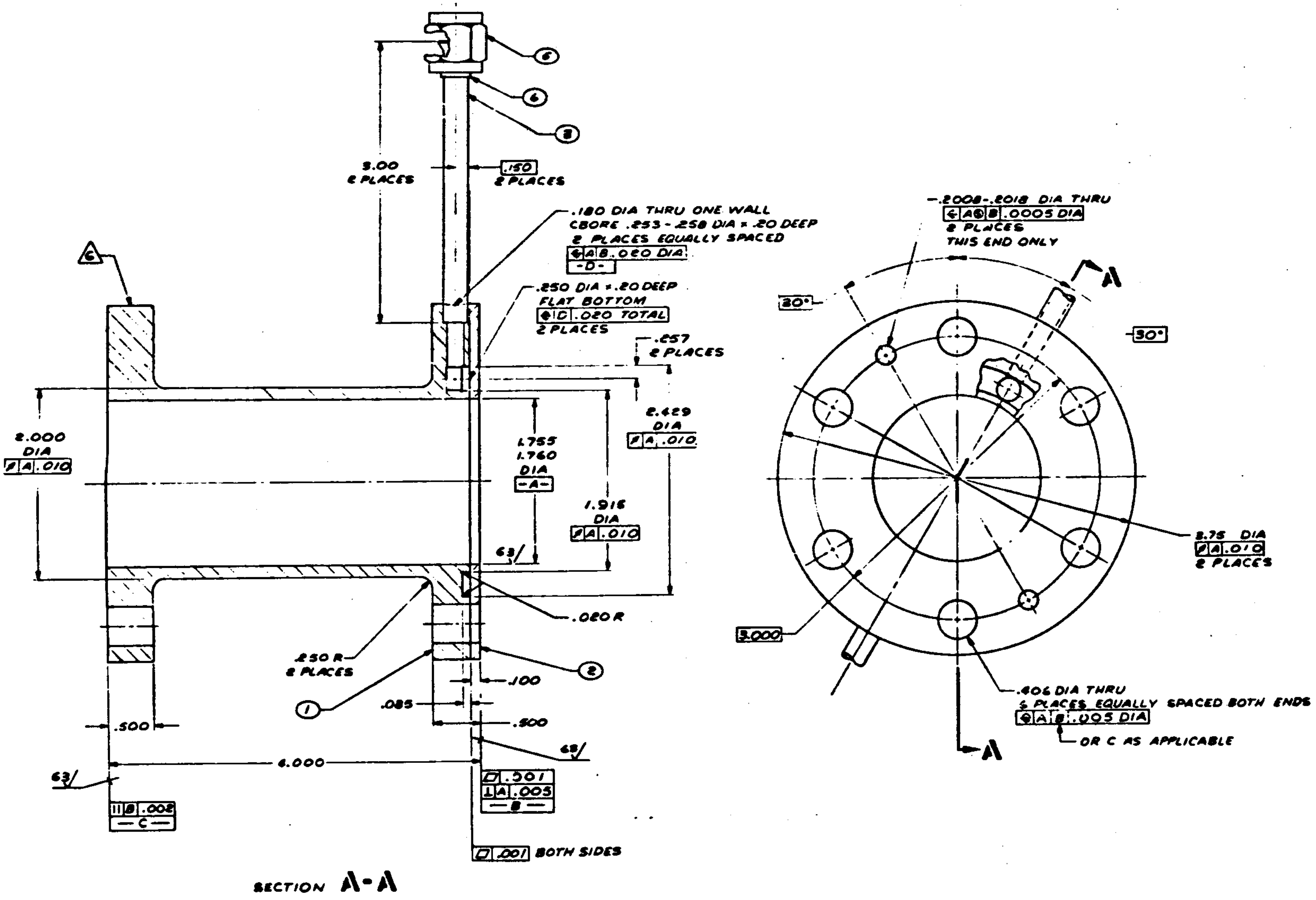

Figure 24. Adapter Housing

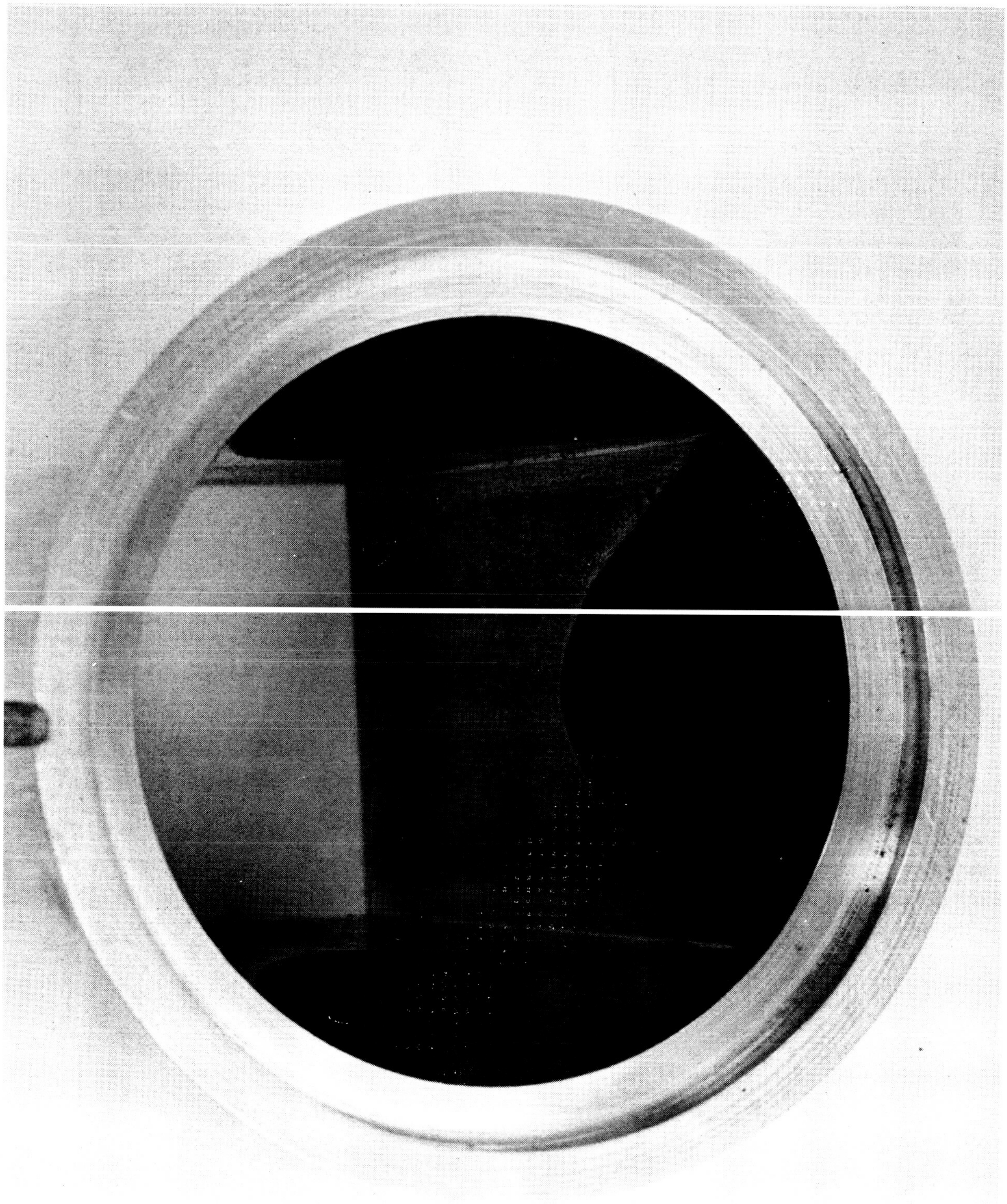

Figure 25. Flow Transition Sleeve

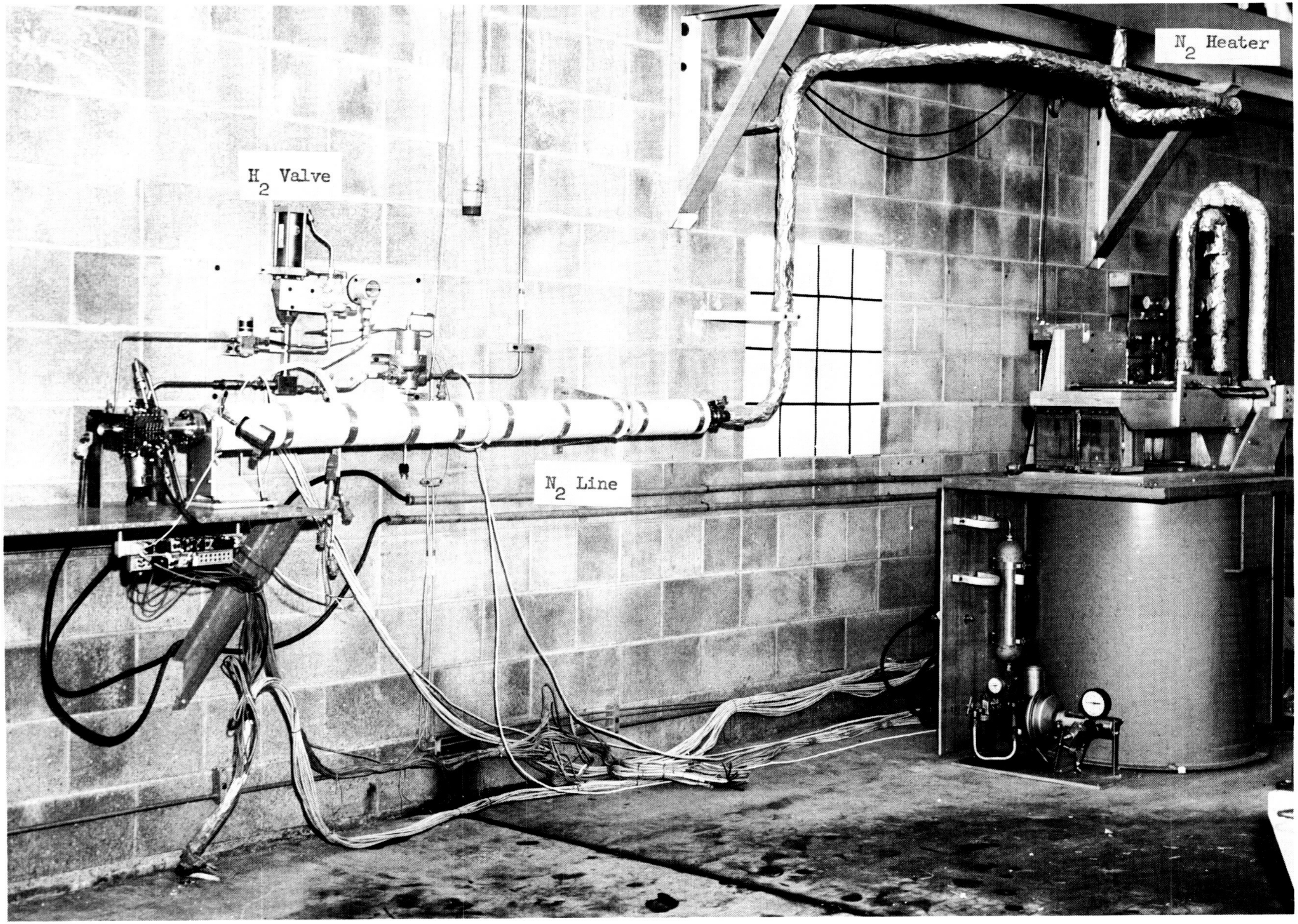

Figure 26. Overall View of the Test Area

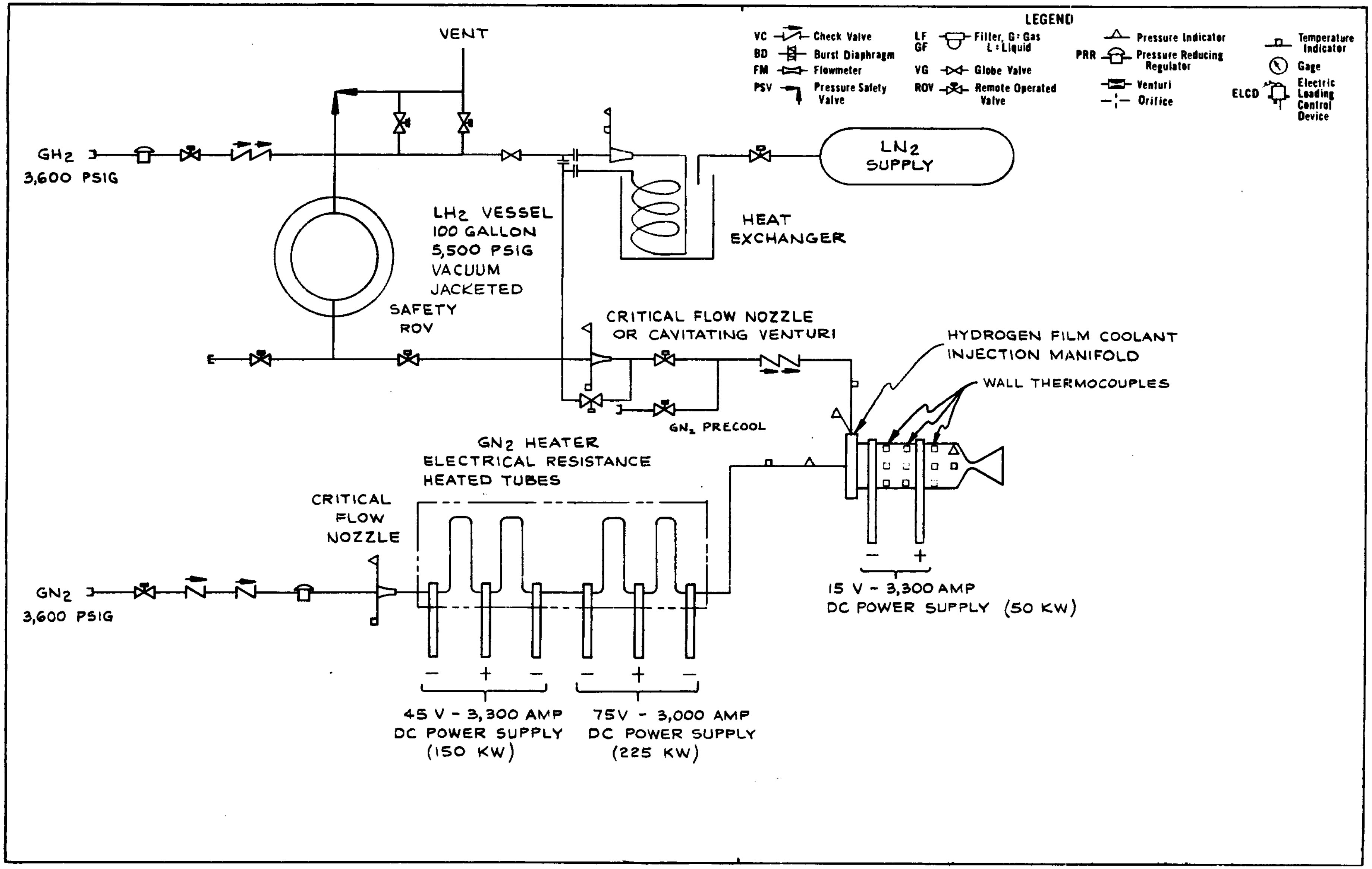

Figure 27. Test System Schematic Diagram

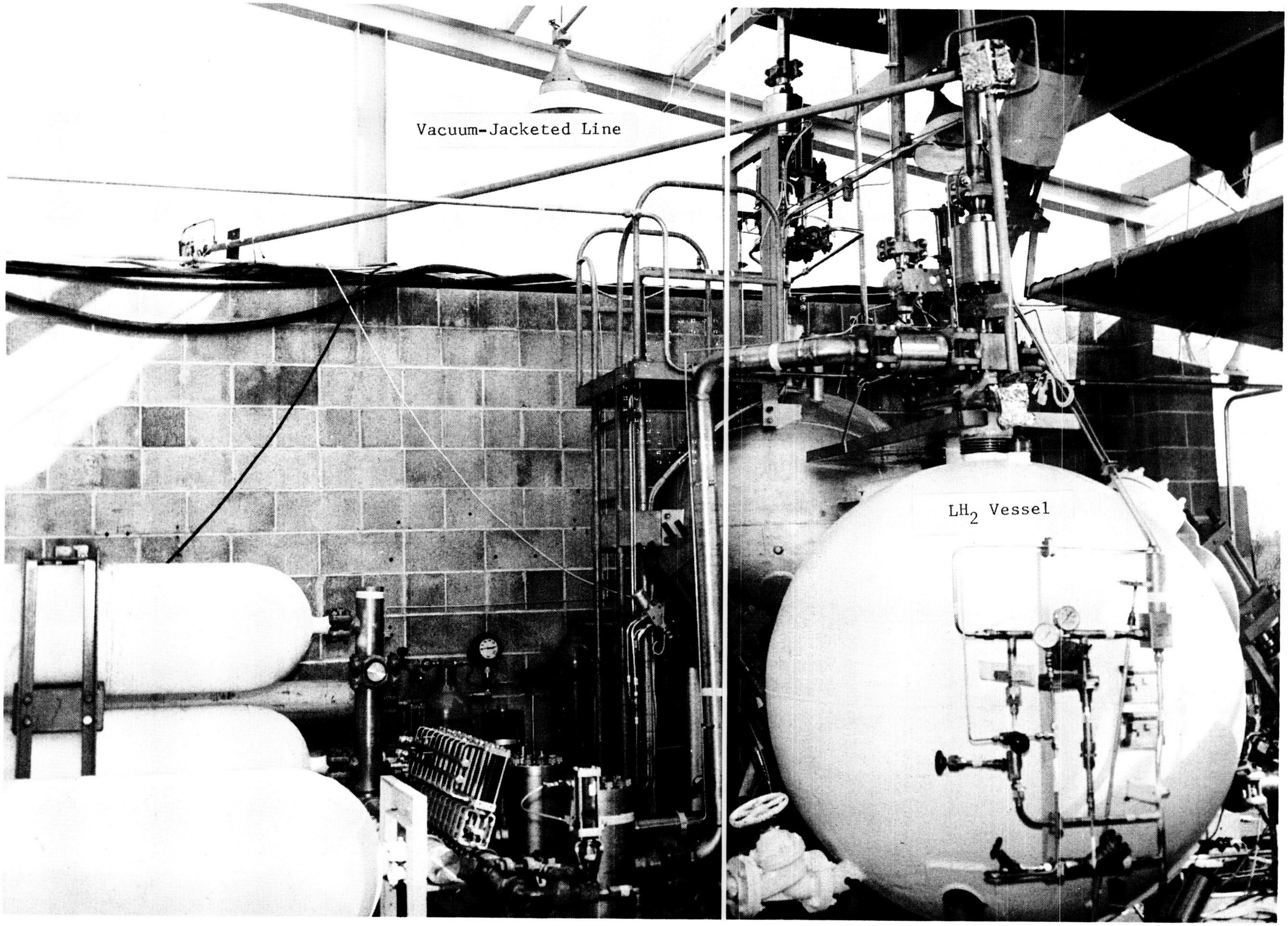

Figure 28. Liquid Hydrogen Vessel and Transfer Line

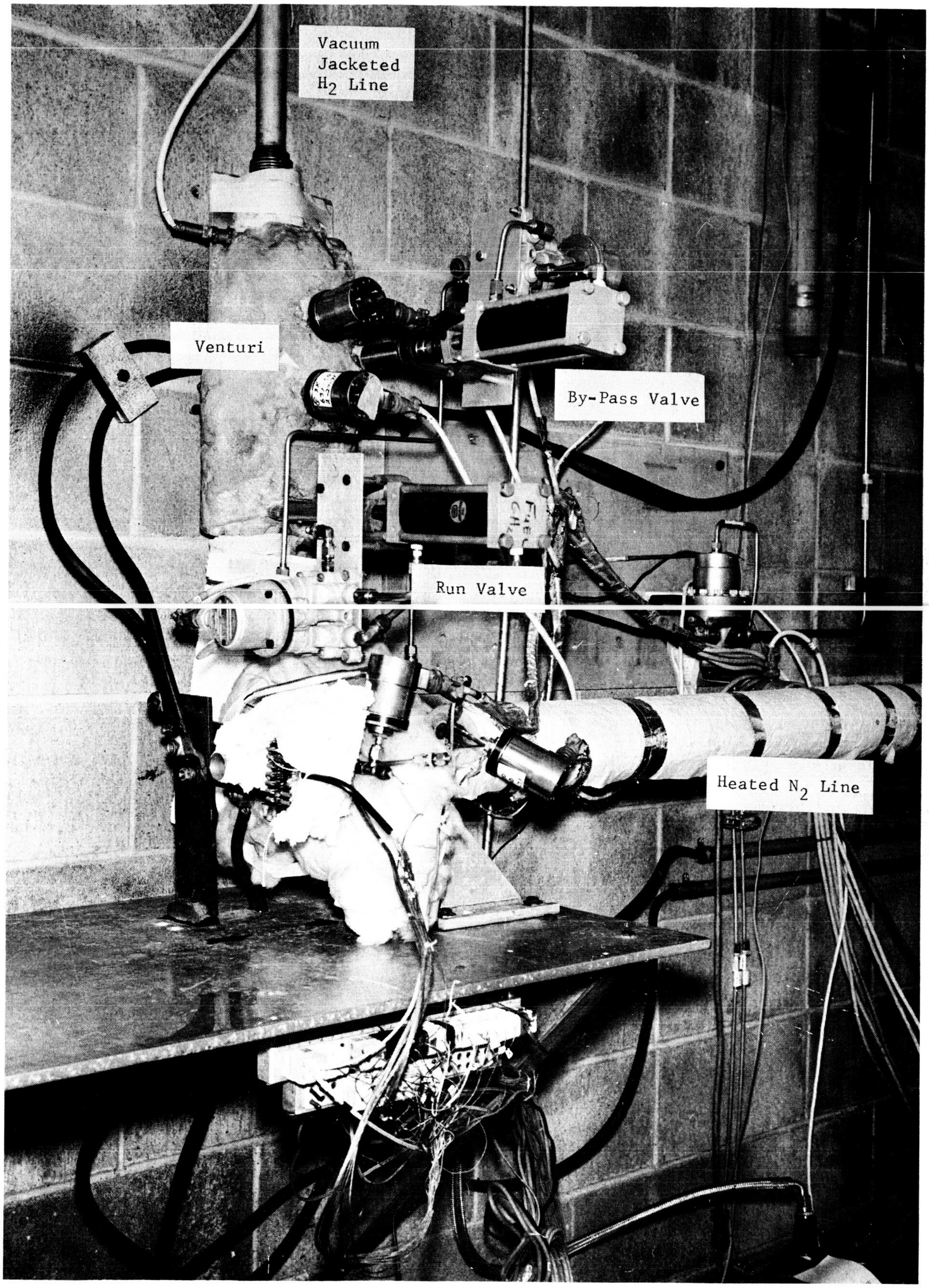

Figure 29. Liquid Hydrogen Test Setup

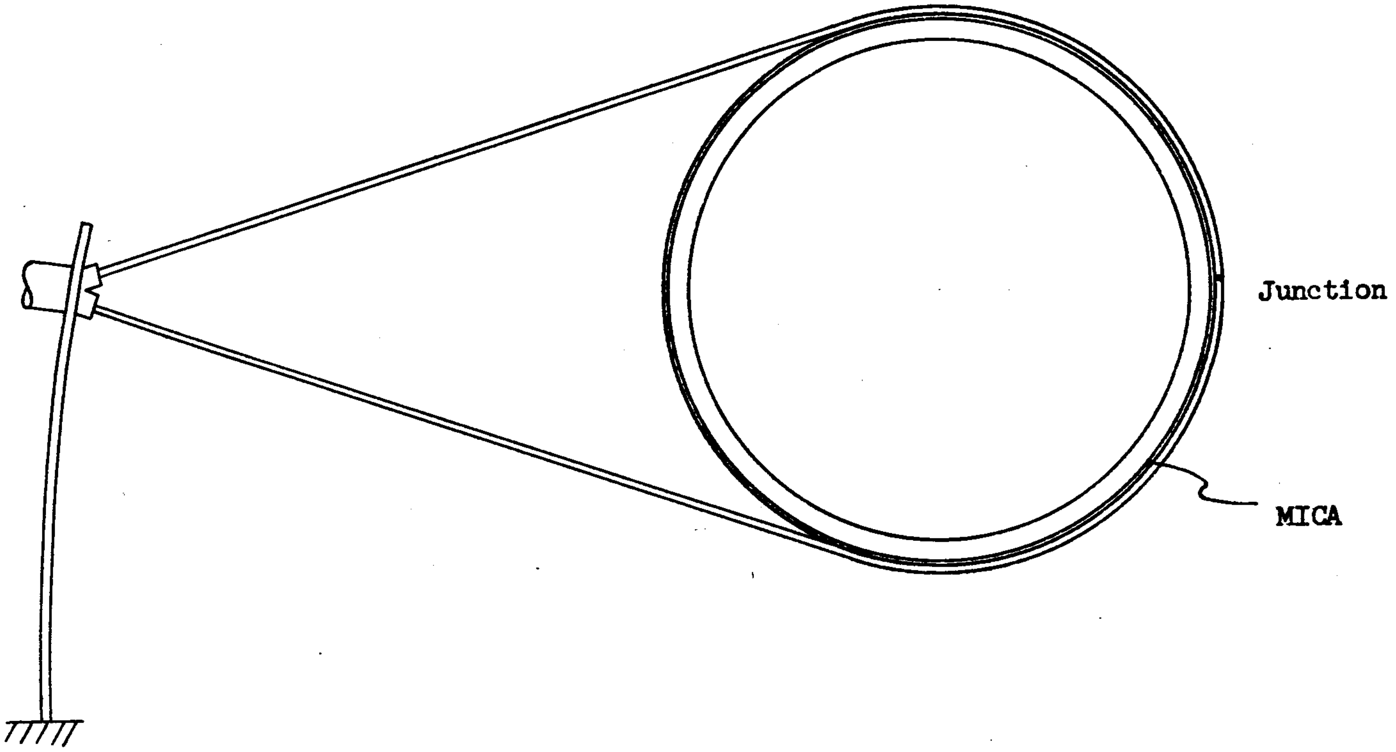

Figure 30. Spring Loaded Thermocouple

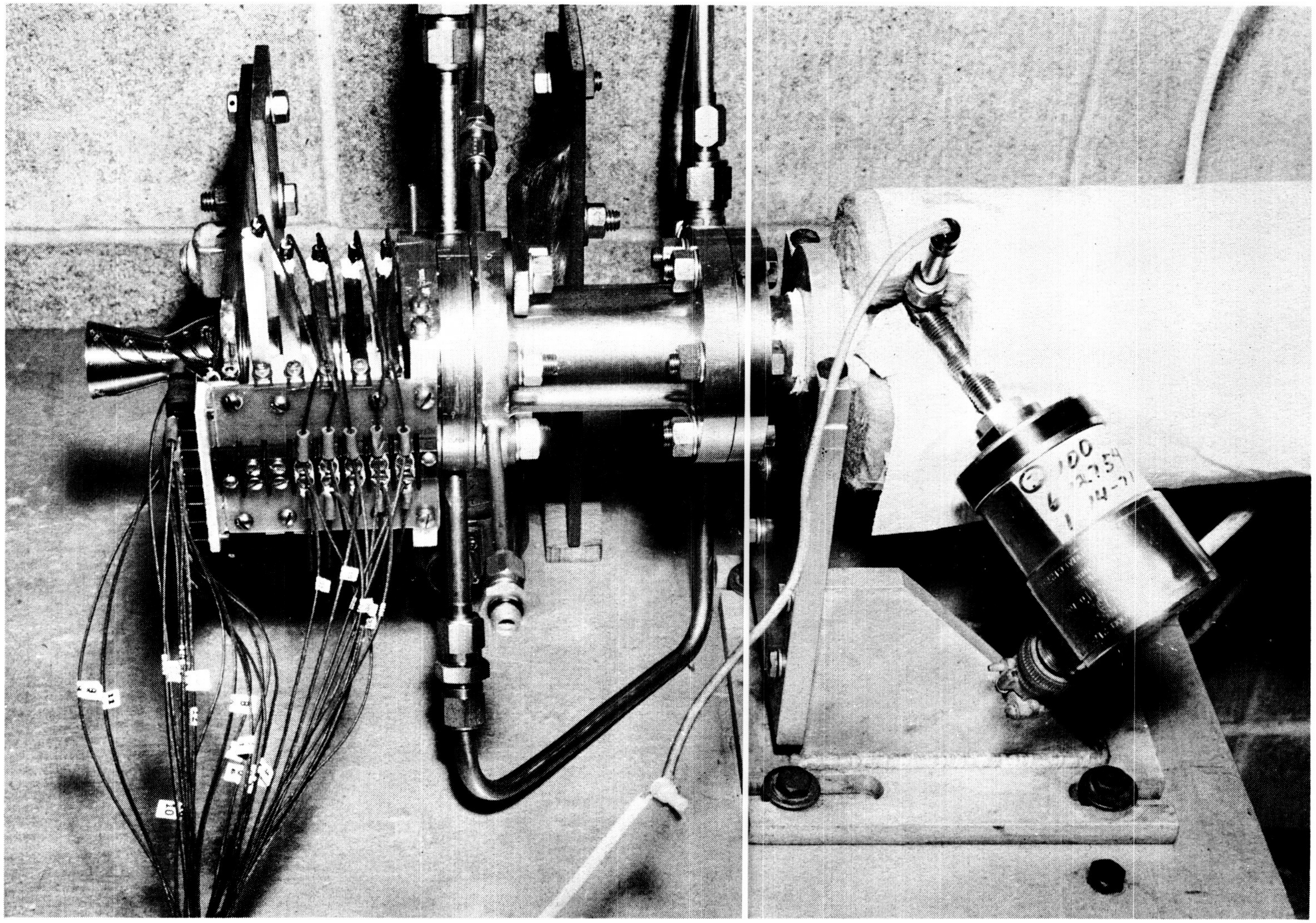

Figure 31. Test Assembly Before Insulation

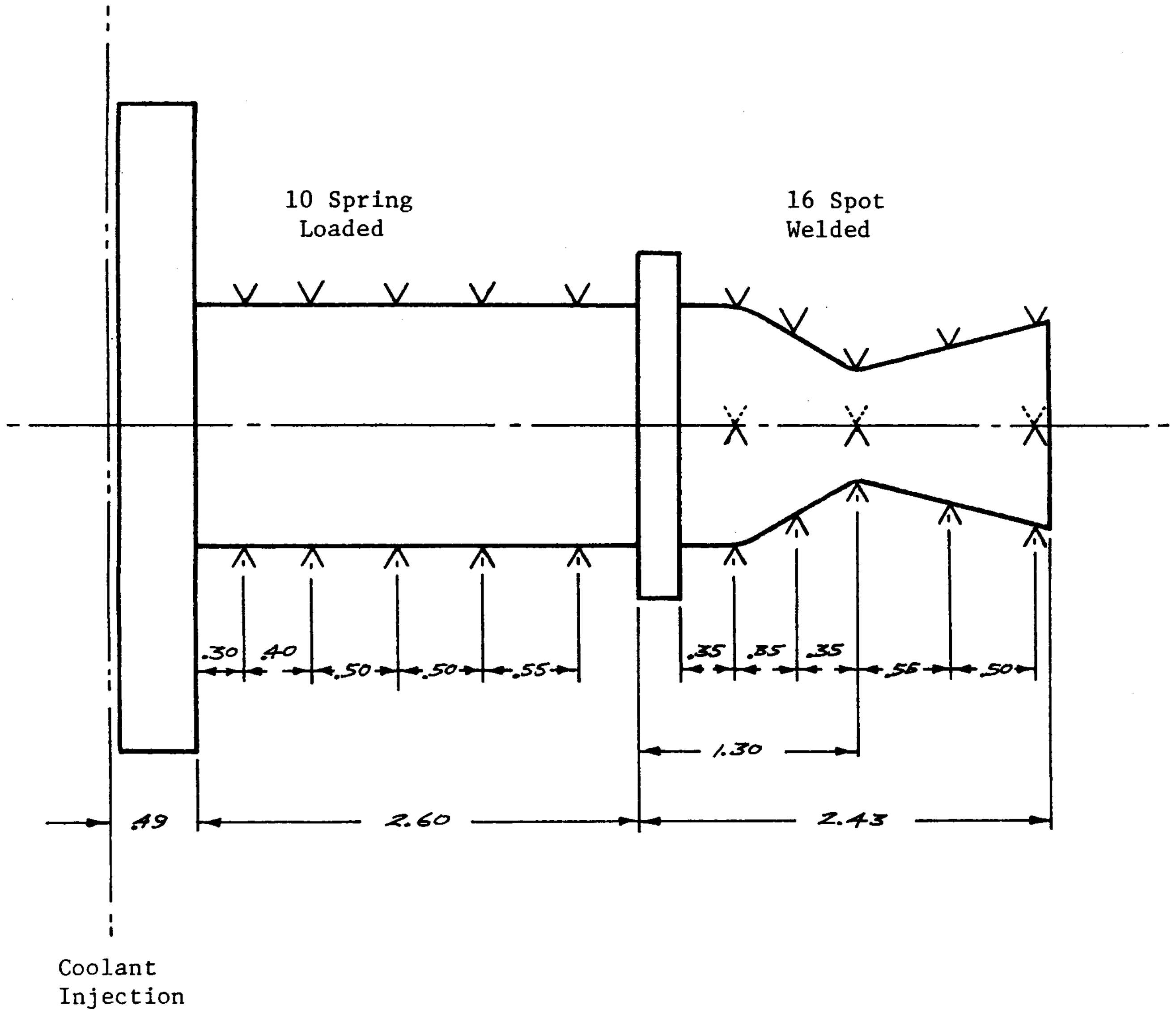

Figure 32. Cylindrical Chamber Thermocouple Locations

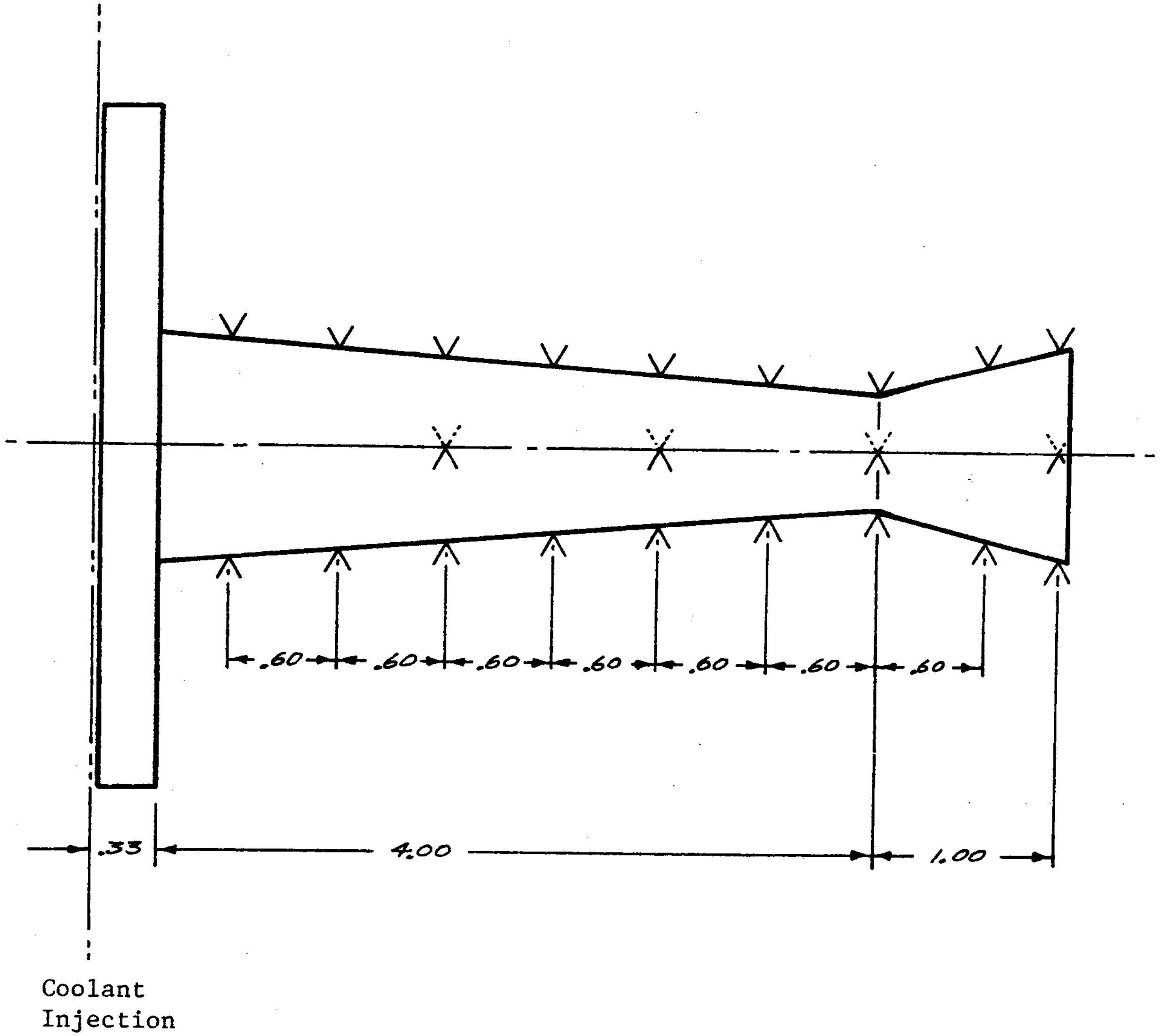

Figure 33. Conical Chamber Thermocouple Locations

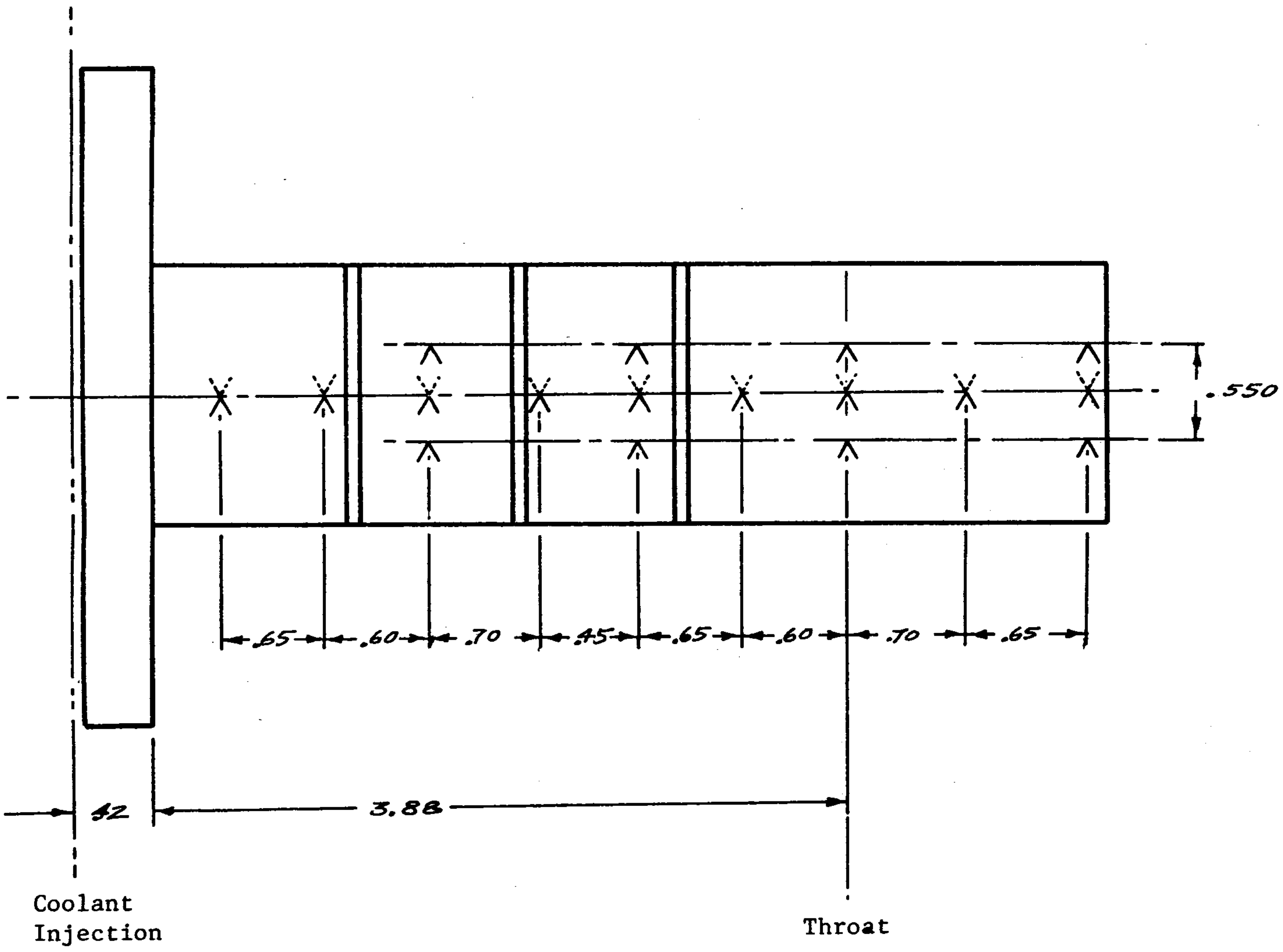

Figure 34. Rectangular Chamber Thermocouple Locations

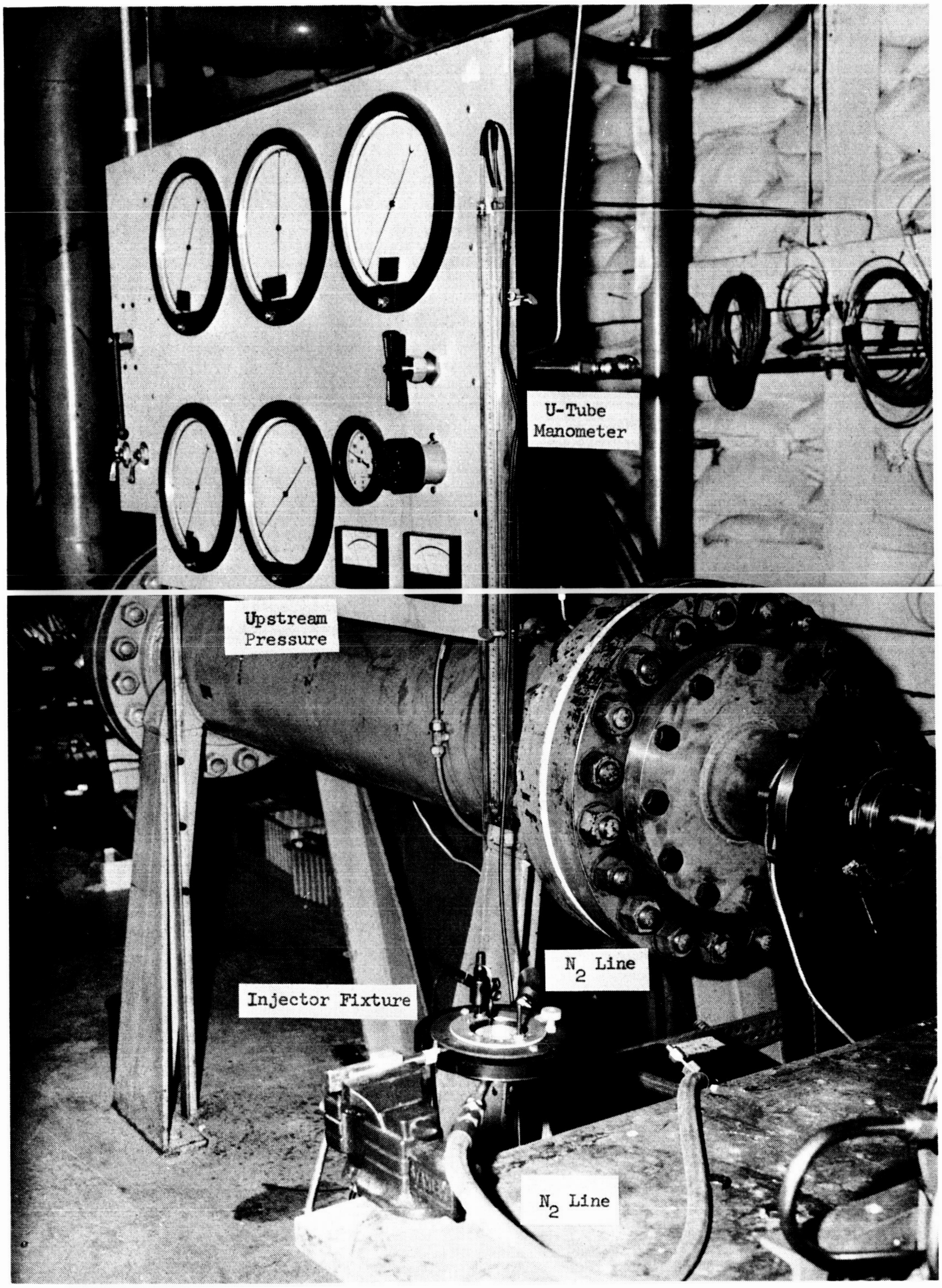

Figure 35. Injector Flow Distribution Test Setup

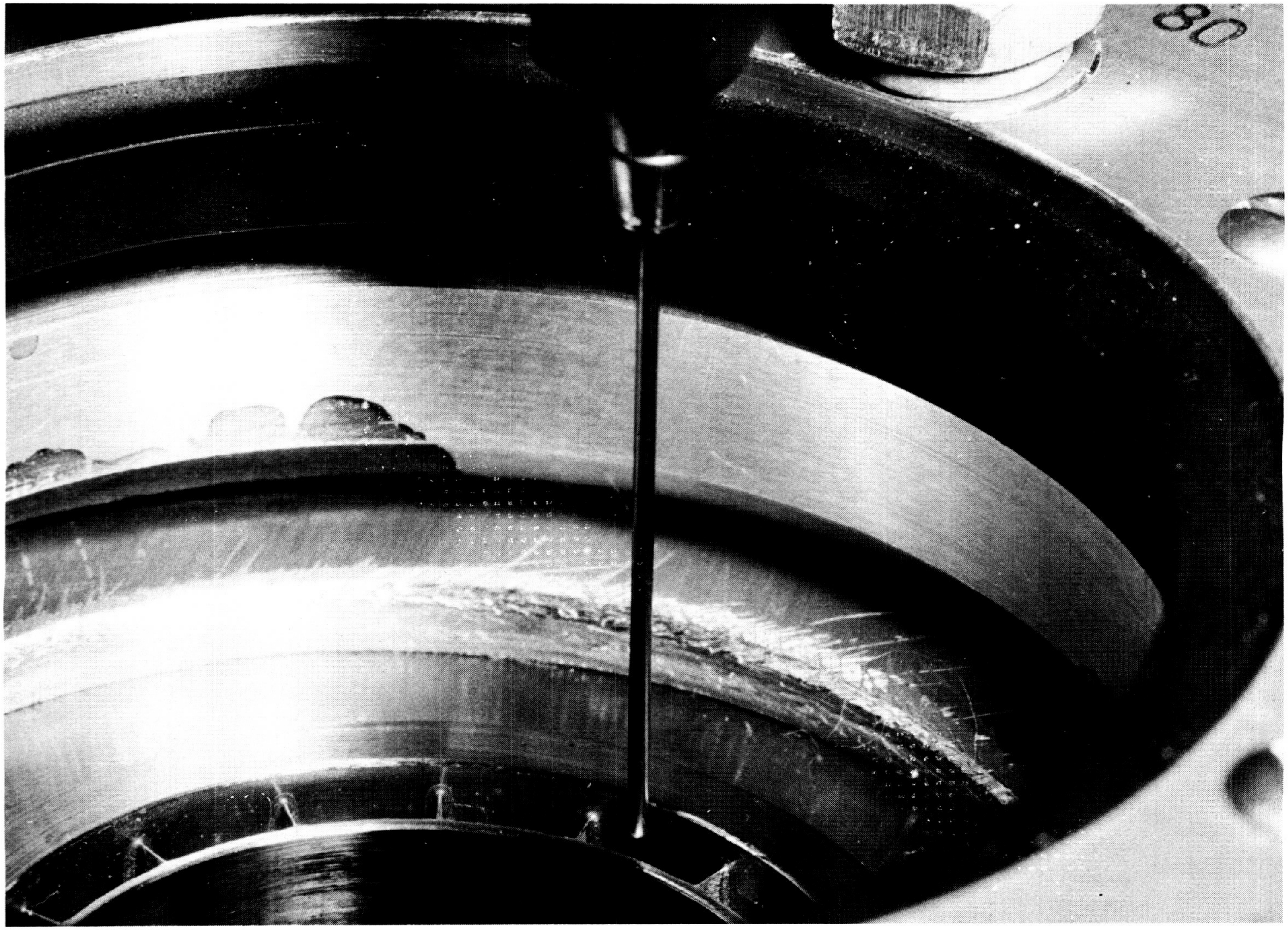

Figure 36. Axial Position of Probe Without Sleeve

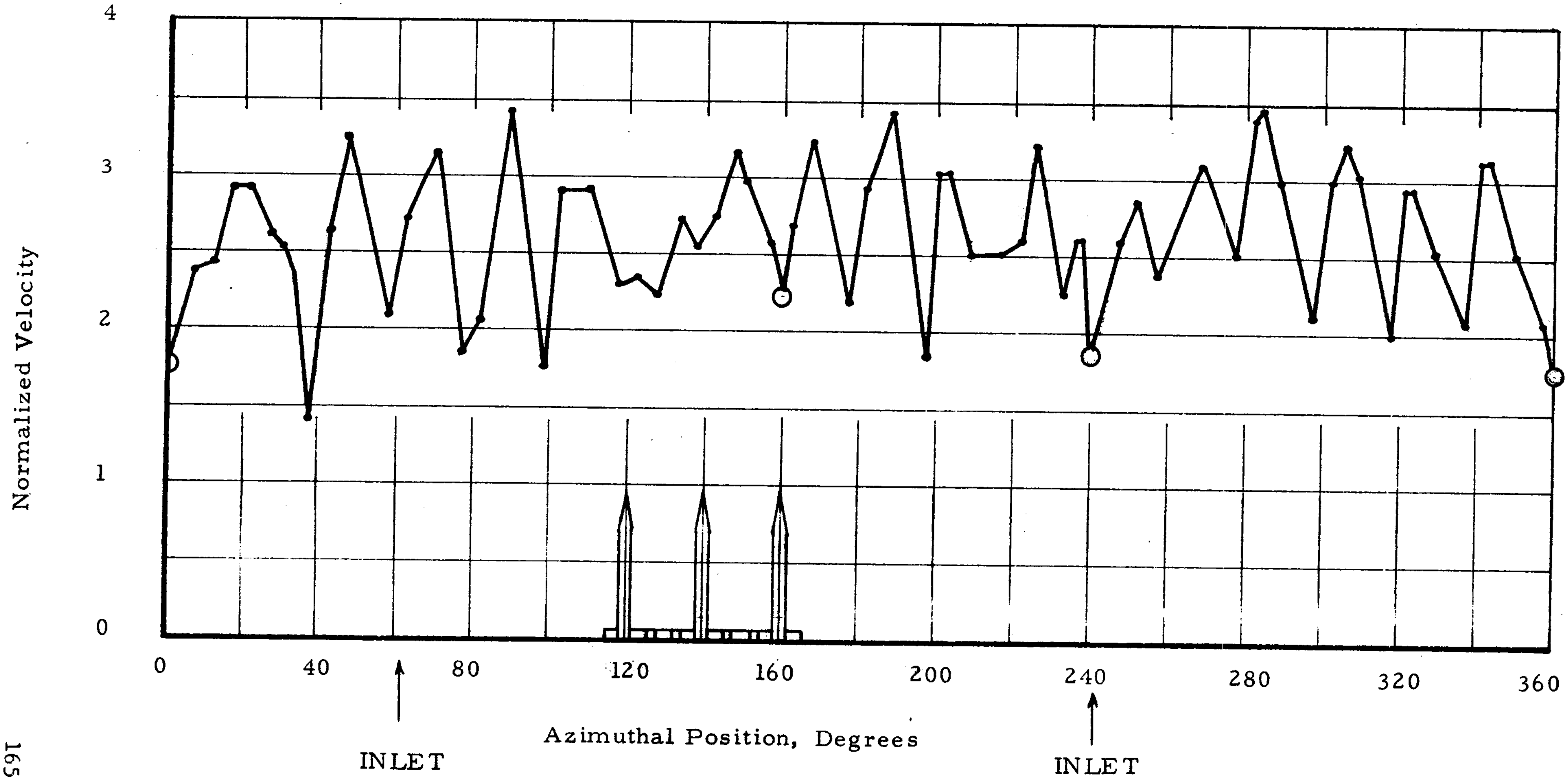

Figure 37. Flow Distribution - 0.060 in. Slot (No Sleeve)

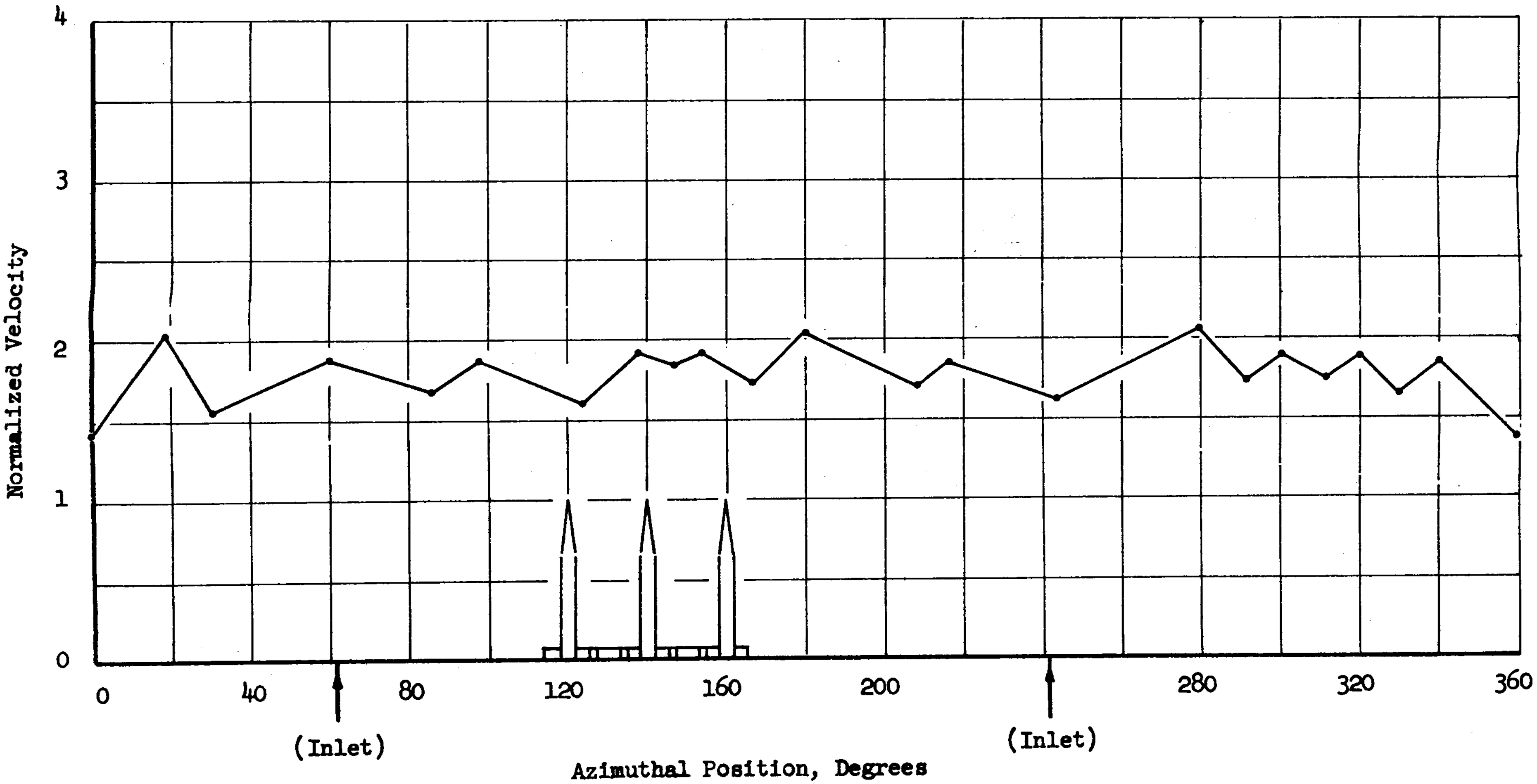

Figure 38. Flow Distribution - 0.060 in. Slot (With Sleeve)

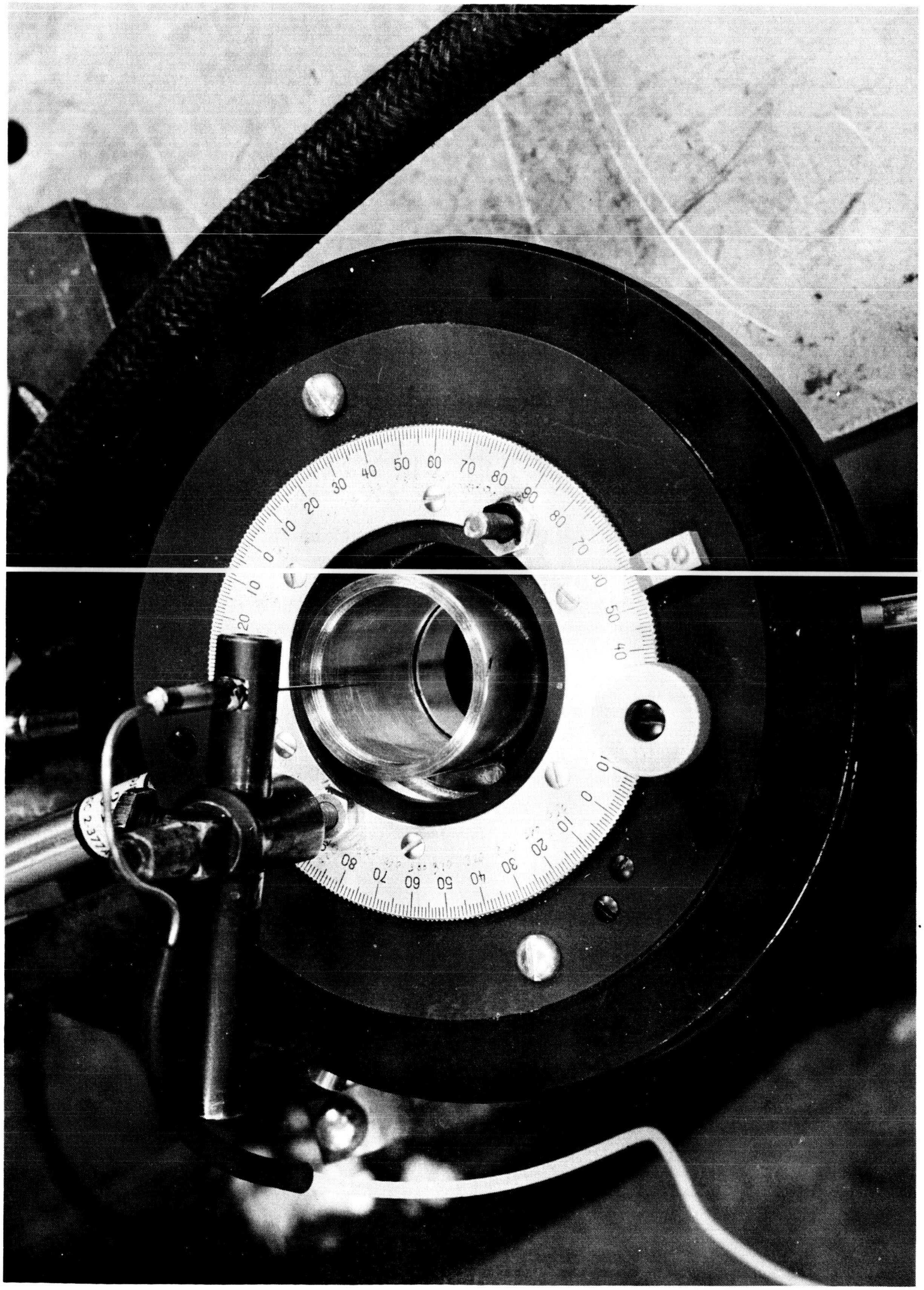

Figure 39. Flow Distribution Test of 0.015 in. Injector

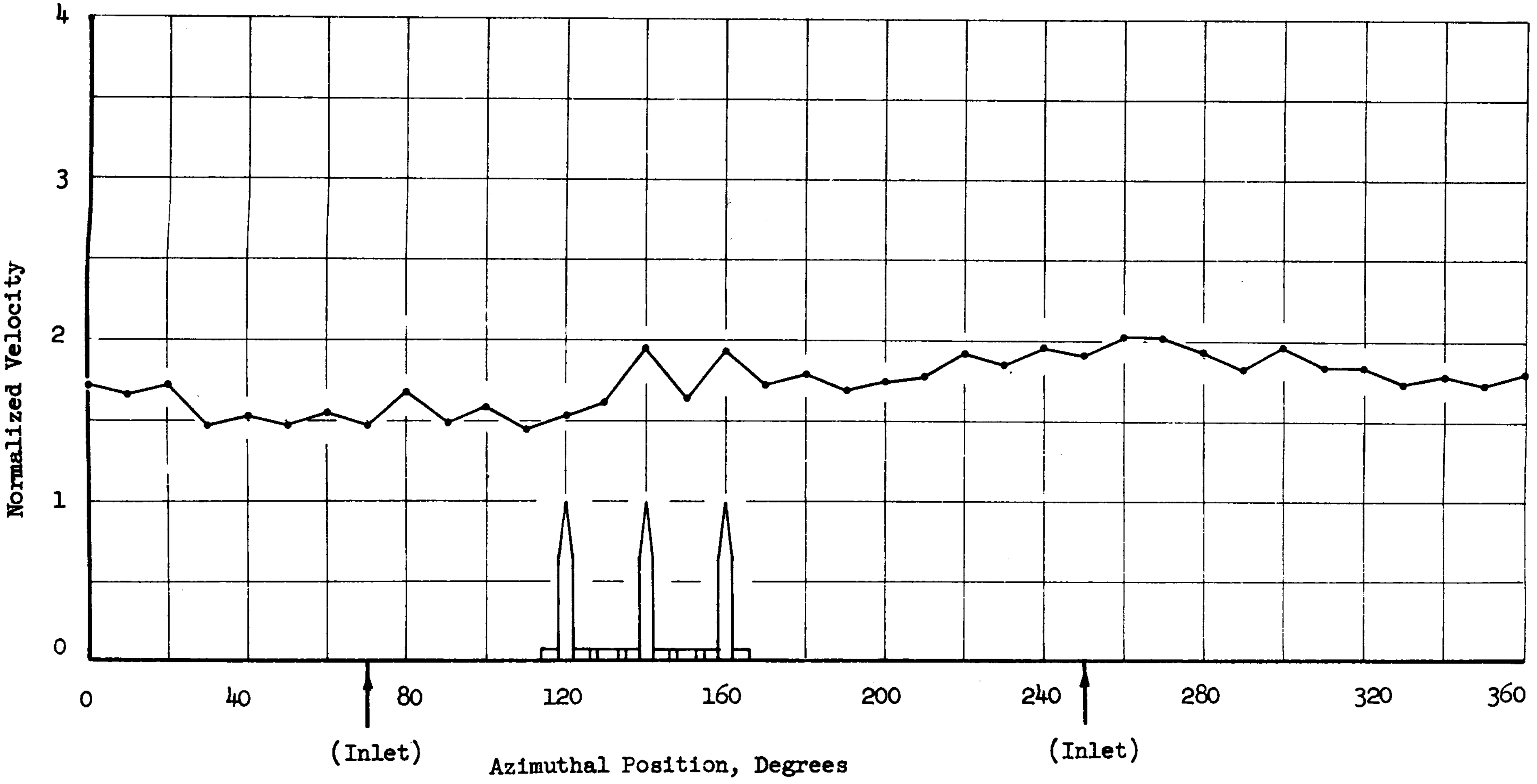

Figure 40. Flow Distribution - 0.015 in. Slot

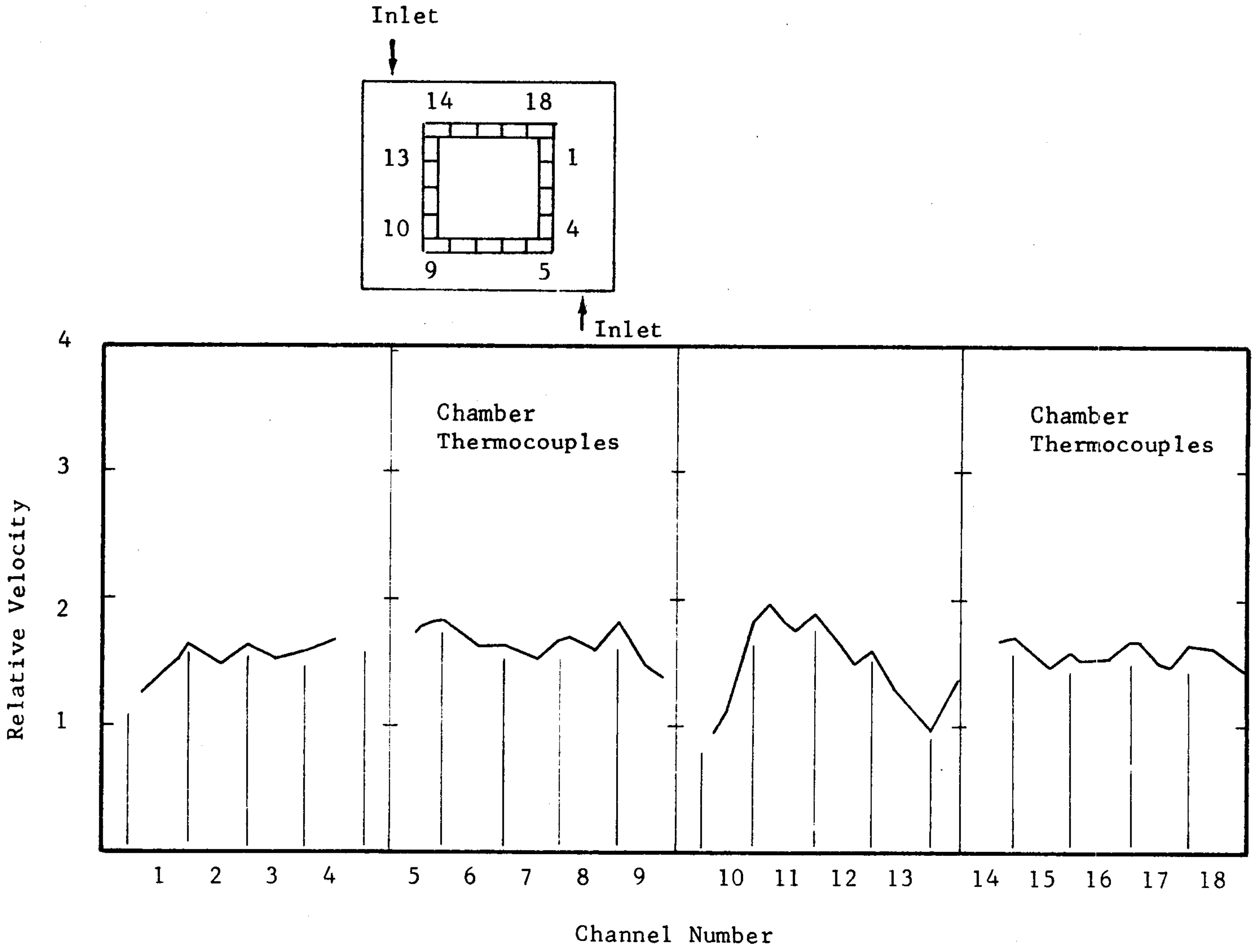

Figure 41. Square Injector Flow Distribution

Figure 42. Liquid Injector Water Flow Test

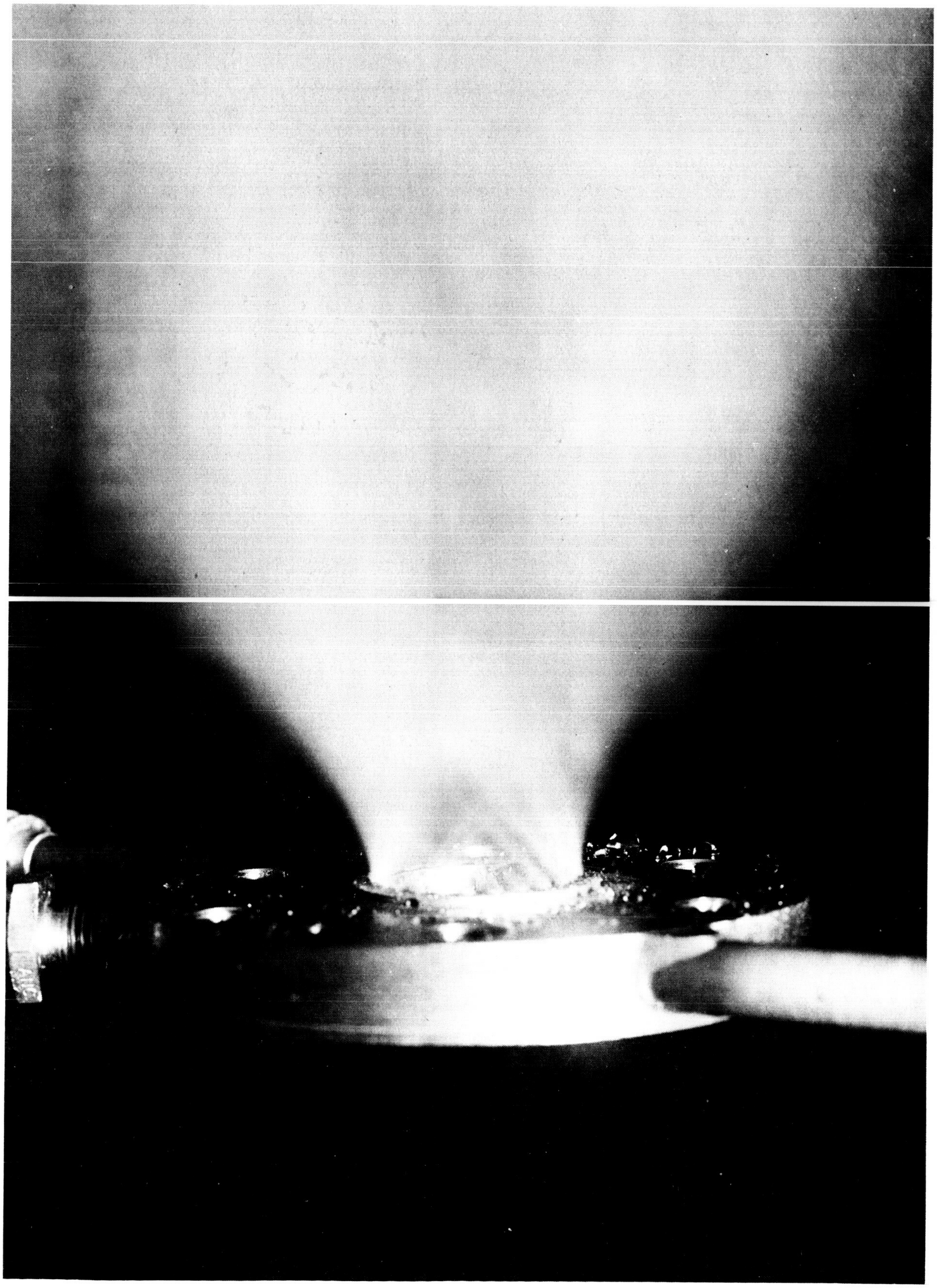

Figure 43. Liquid Injector Two-Phase Flow Test

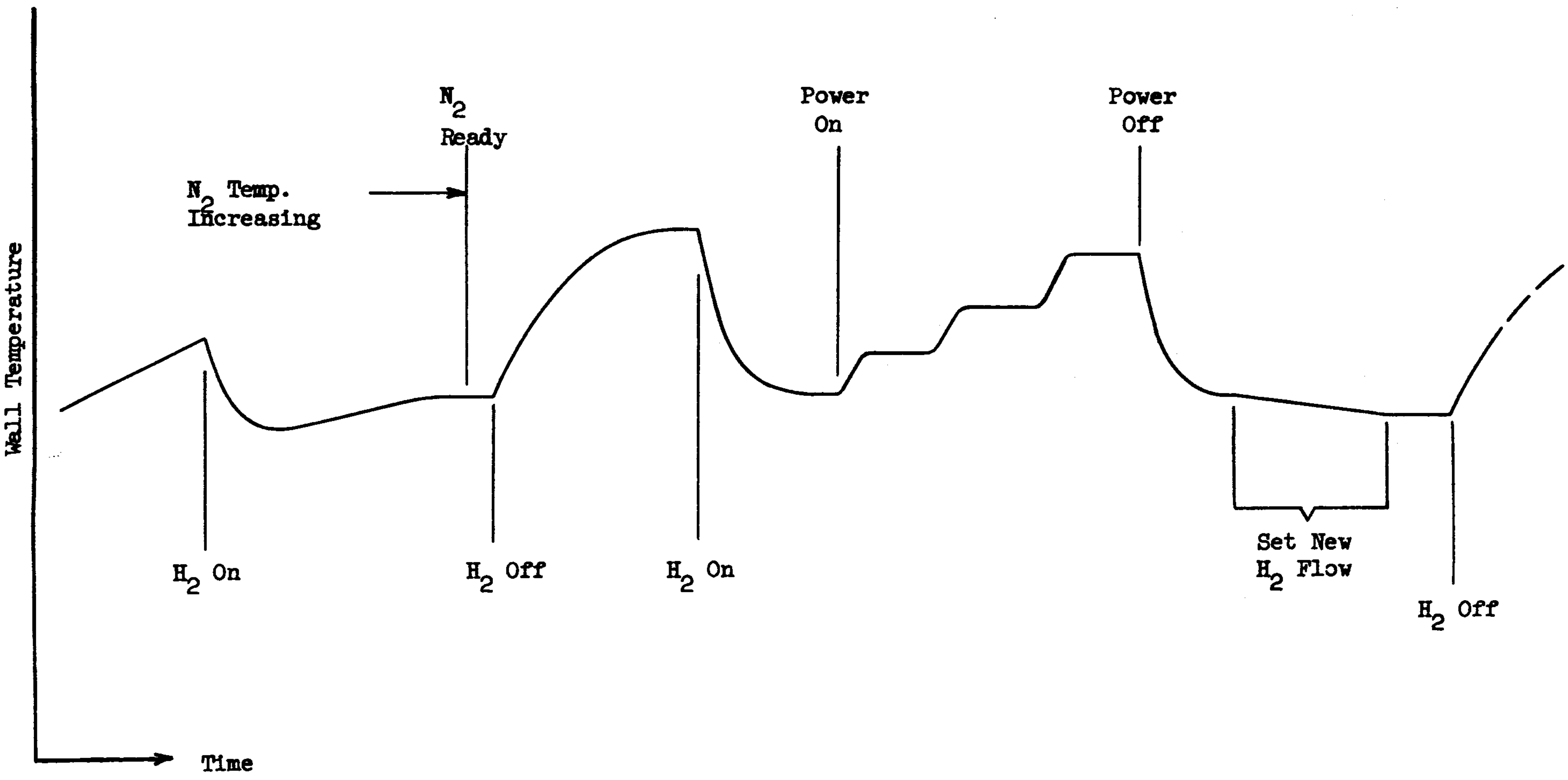

Figure 44. Test Procedure Schematic

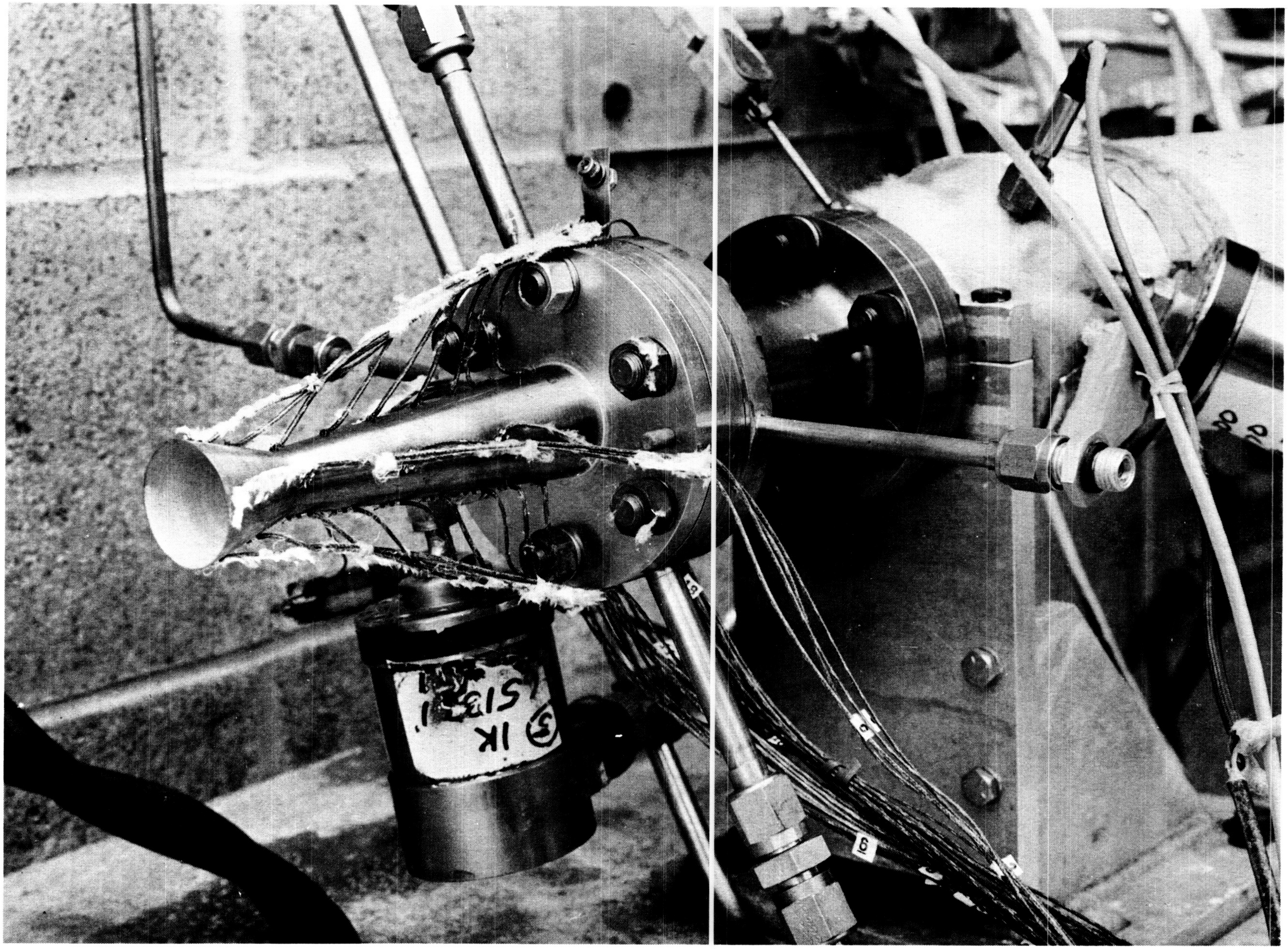

Figure 45. Test Assembly with Conical Chamber

Velocity Ratio ≈ 1.0

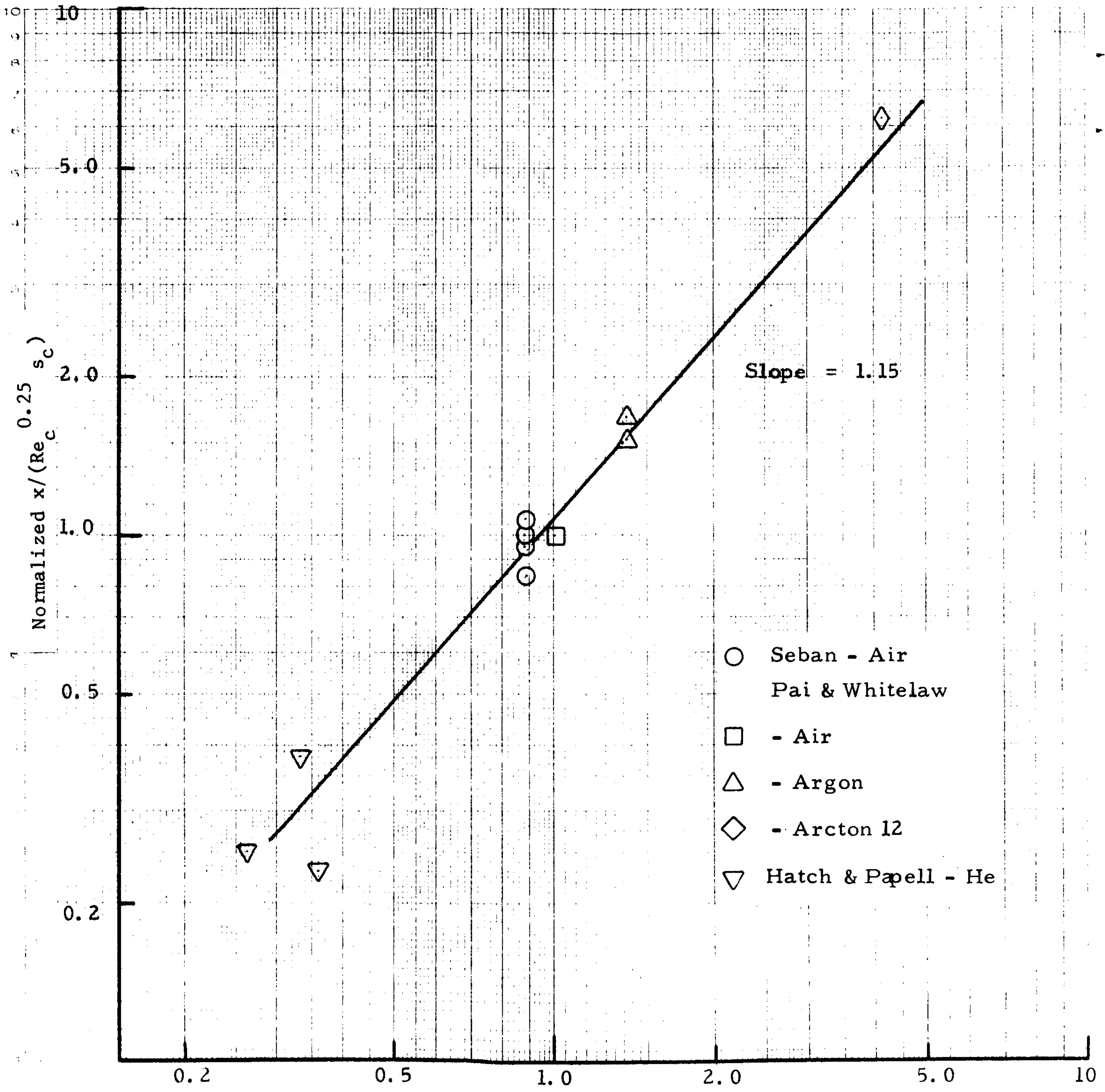

Figure 46. Density Ratio Correlation

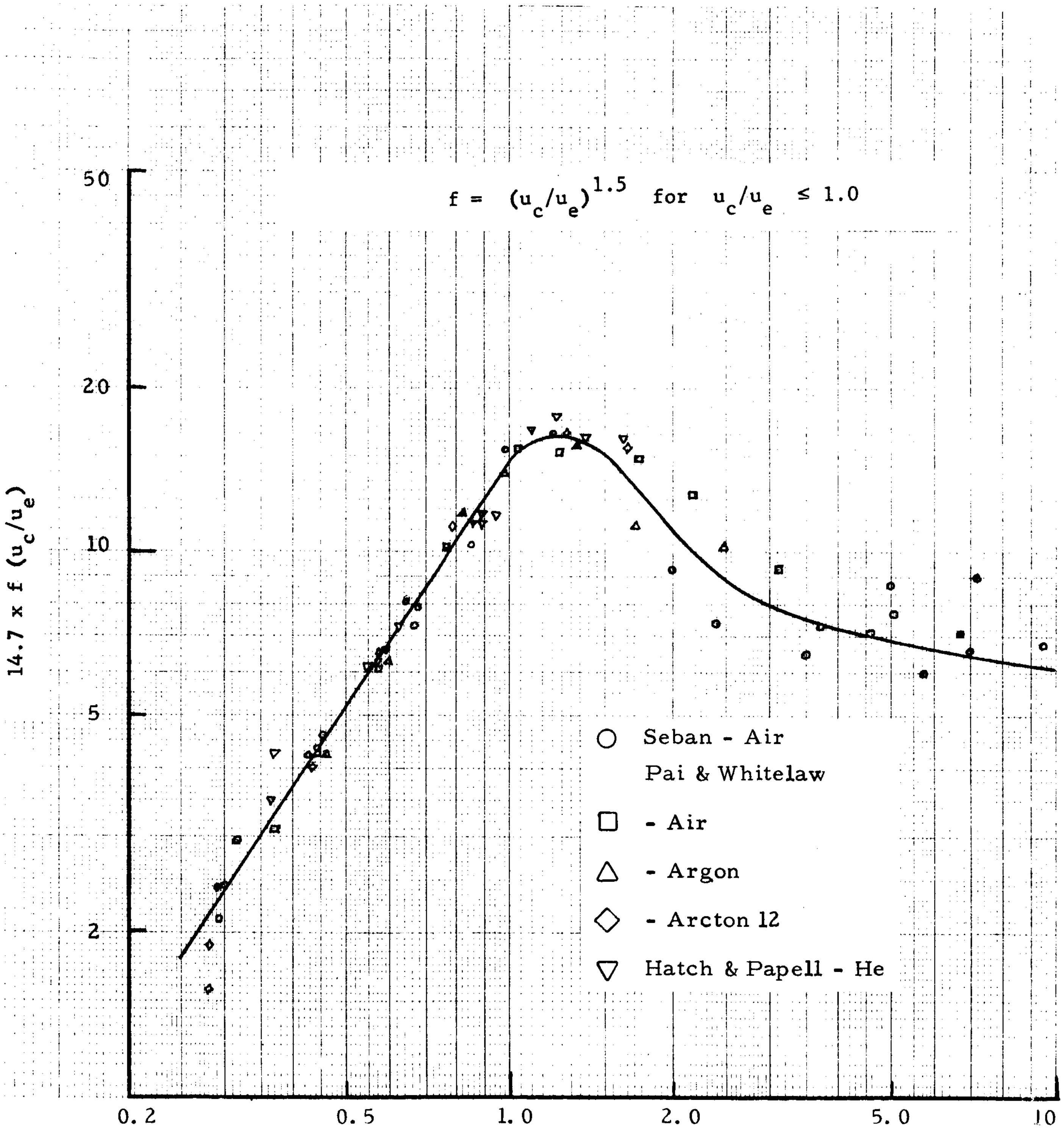

Figure 47. Velocity Ratio Correlating Function

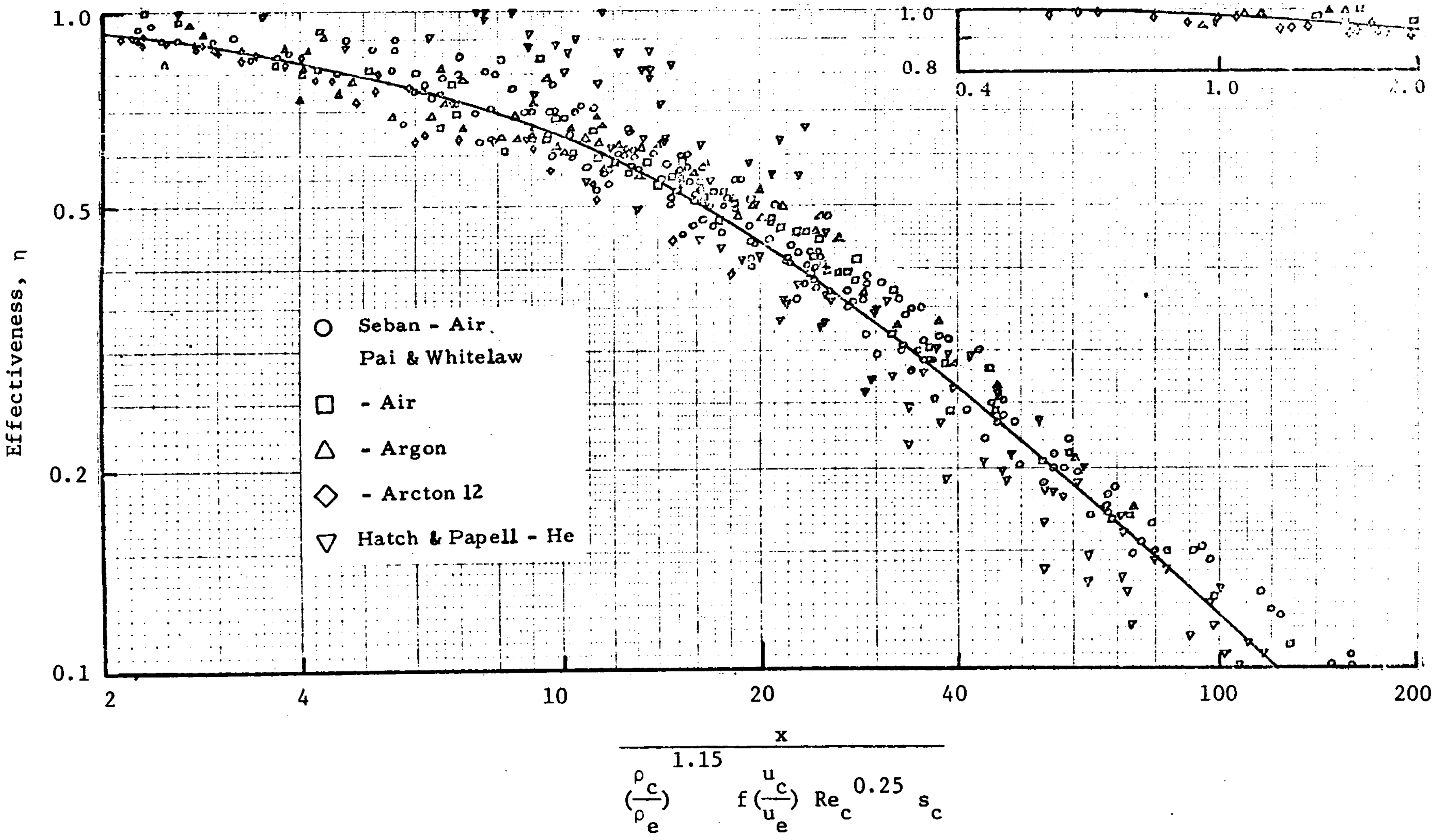

Figure 48. Gas Film Cooling Effectiveness Correlation for Plane, Unaccelerated Flow

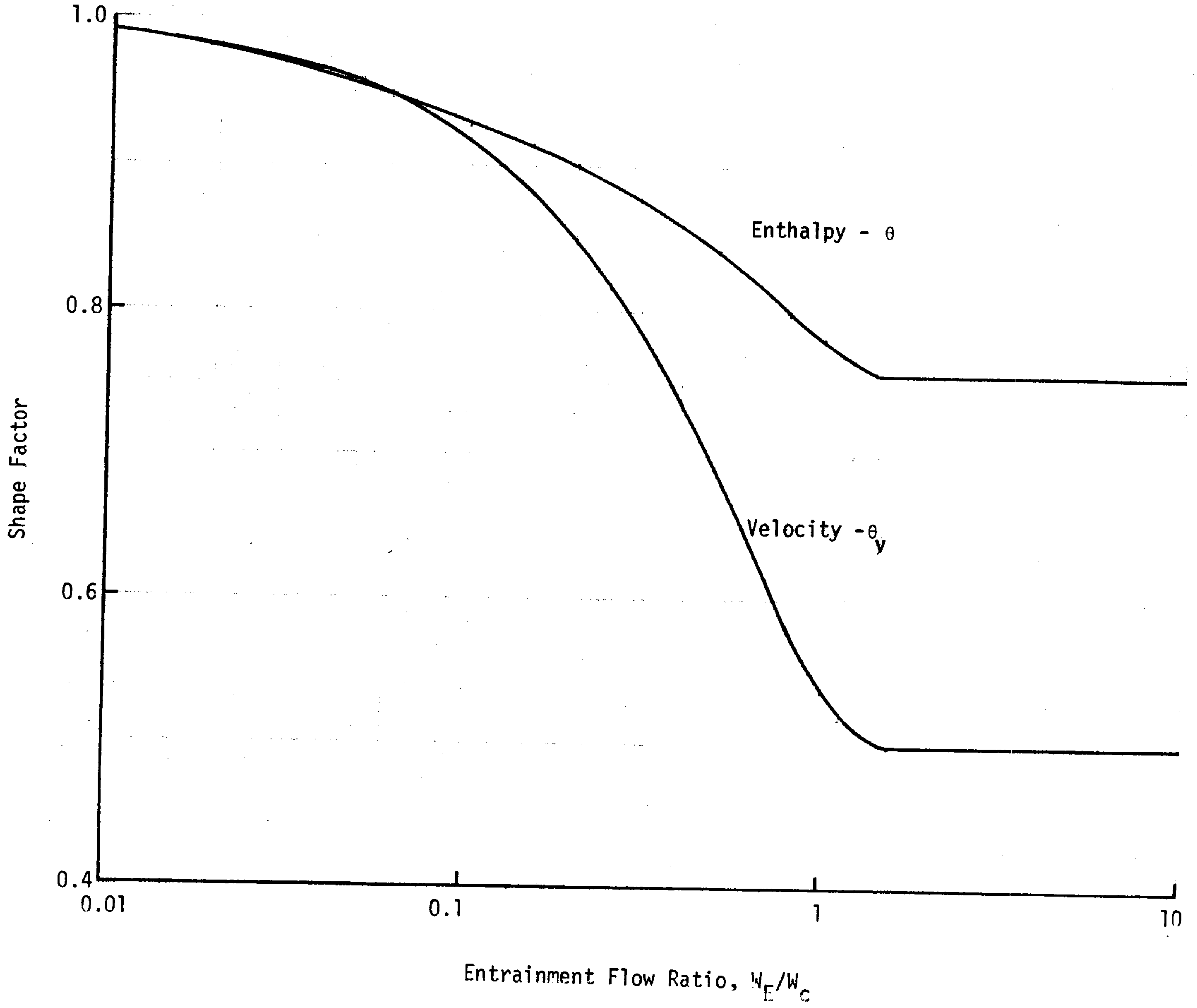

Figure 49. Mixing Layer Profile Shape Factors

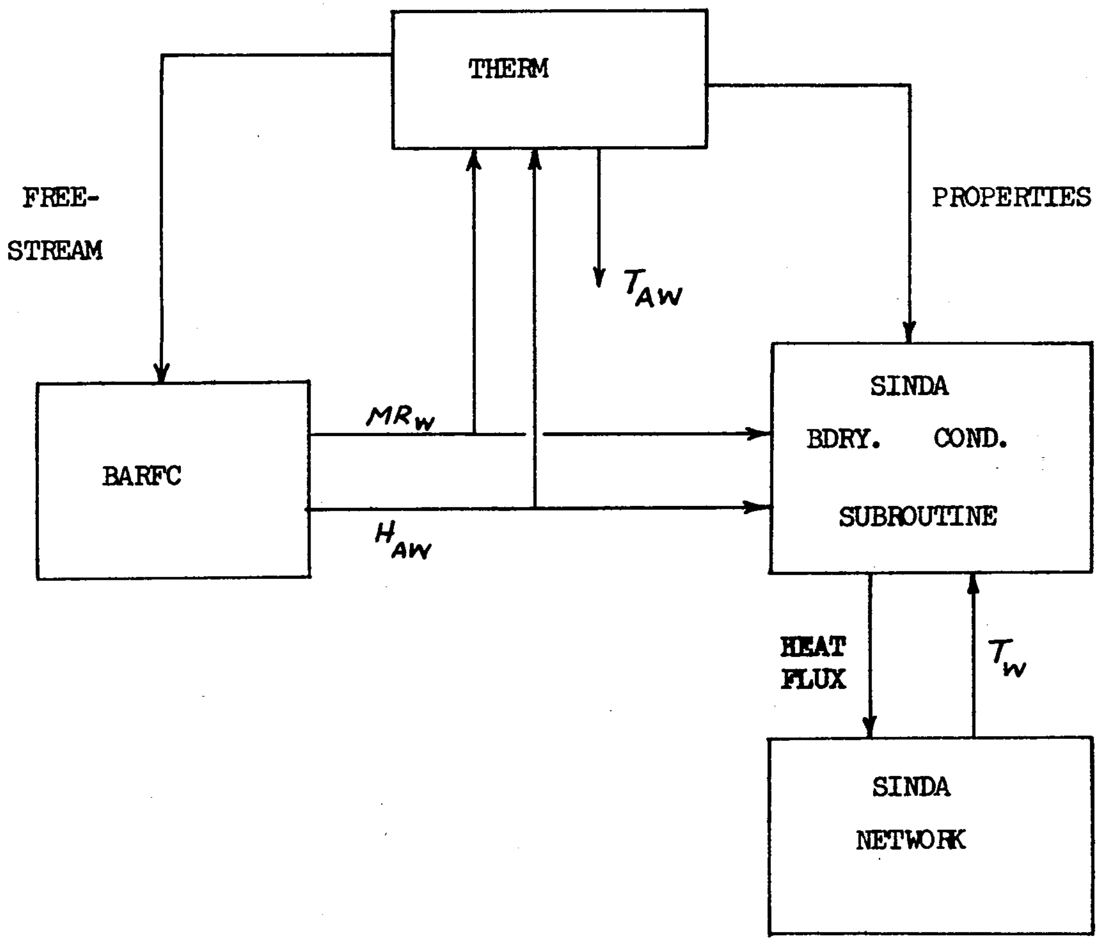

Figure 50. Gas Film Cooling Program

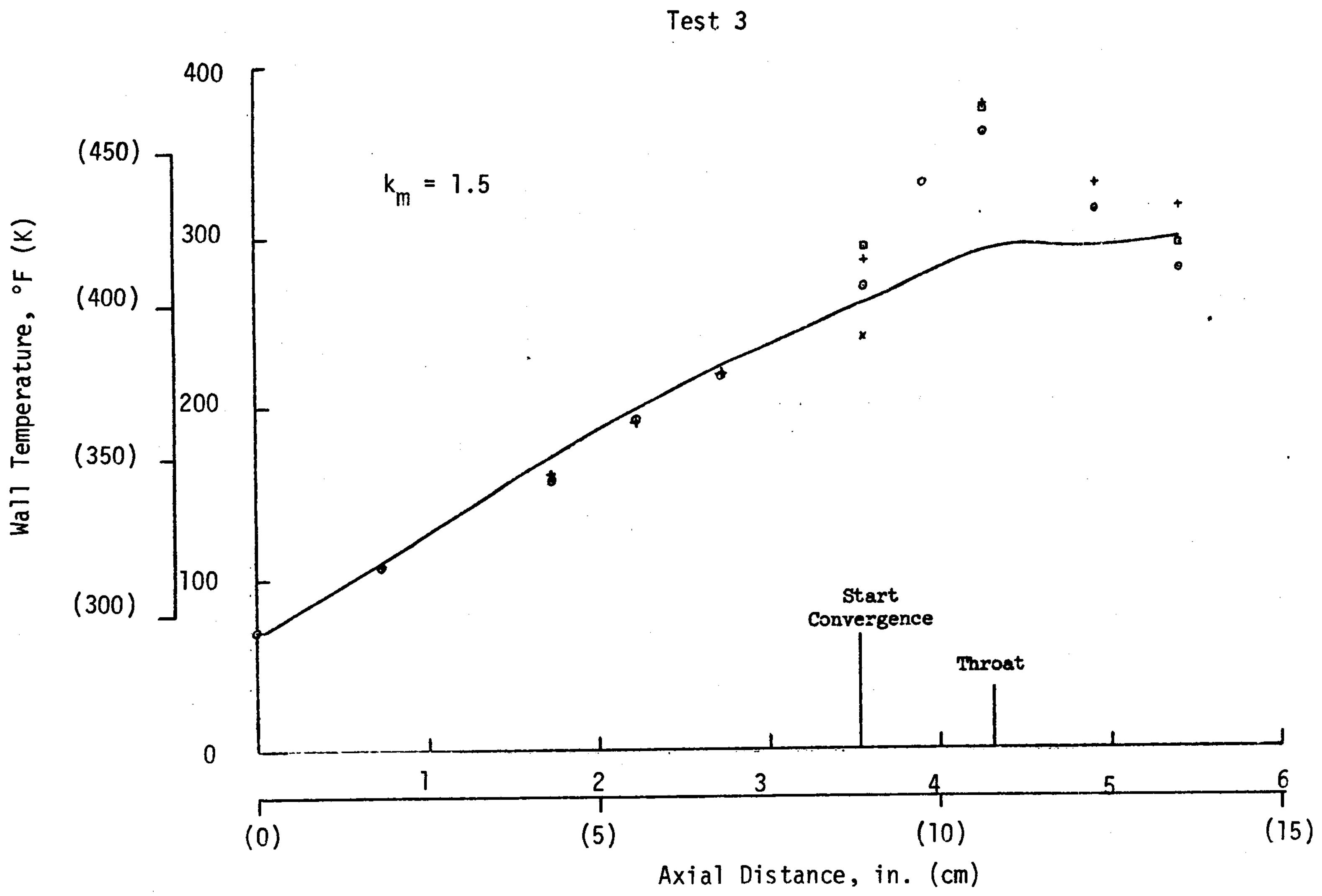

Figure 51. Comparison of Predicted and Measured Adiabatic Wall Temperatures

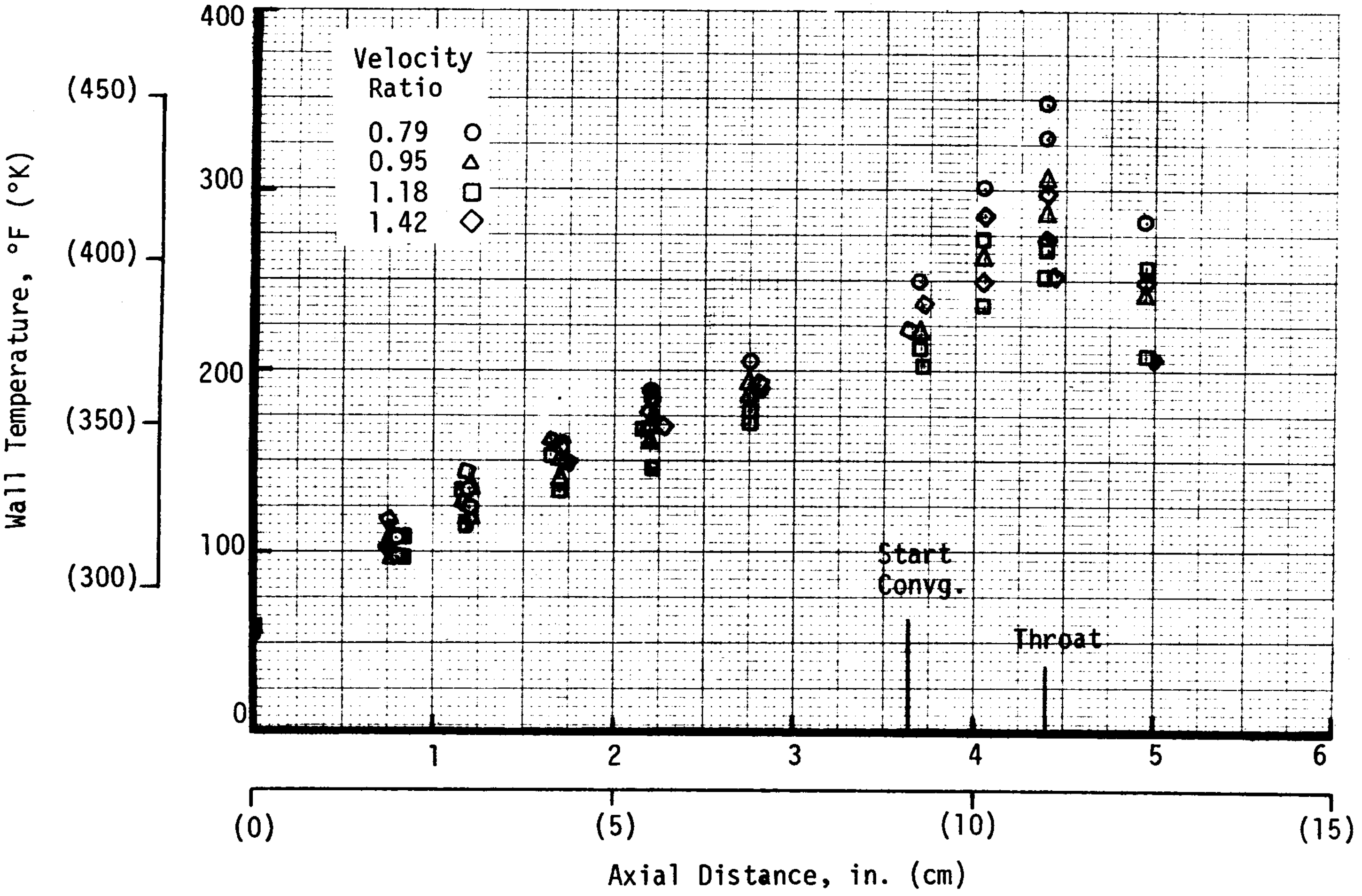

Figure 52. Cylindrical Chamber Adiabatic Wall Temperatures - Test 5

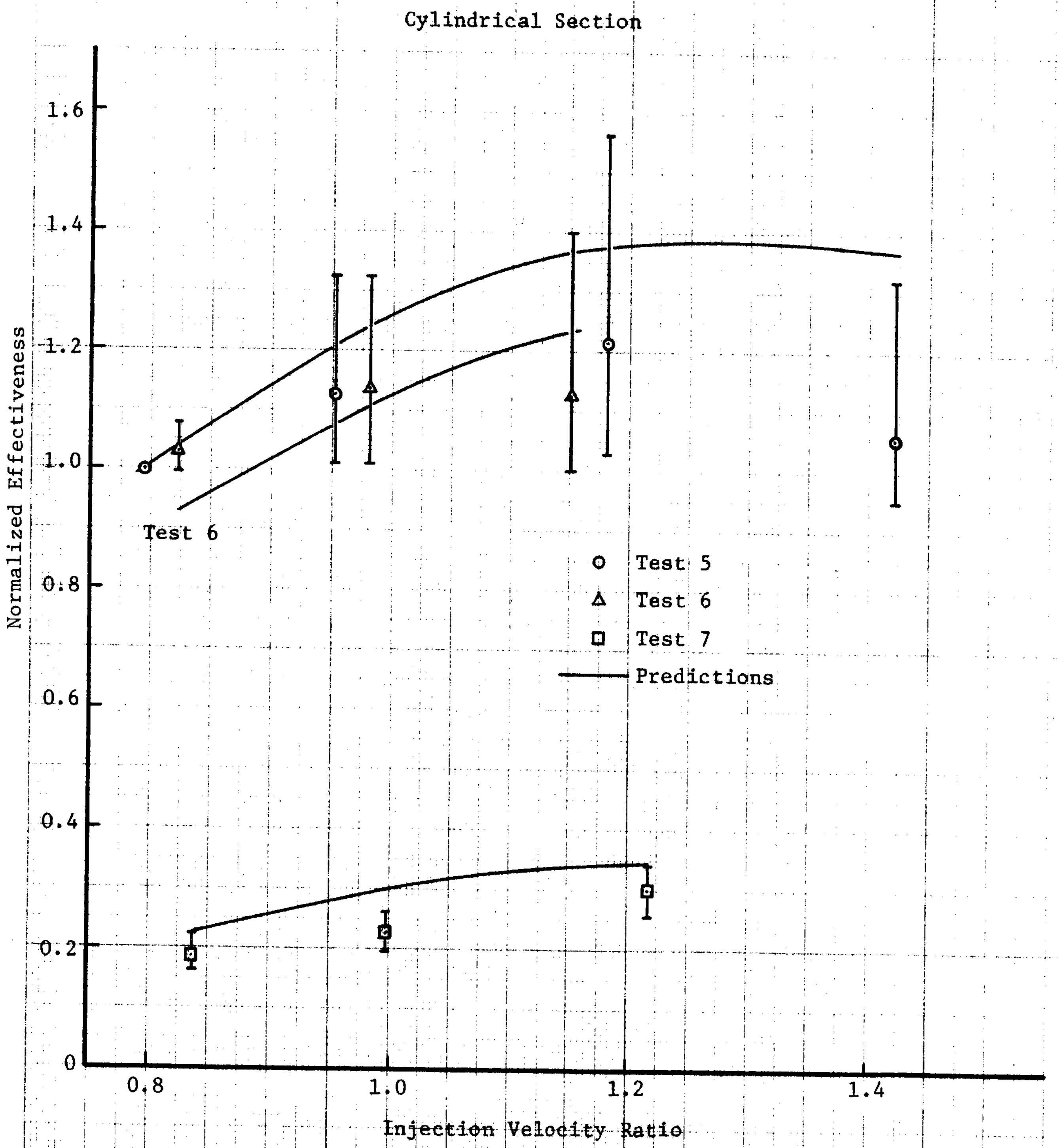

Figure 53. Effect of Velocity Ratio, Coolant Reynolds Number and Slot Height on Coolant Effectiveness - Cylindrical Section

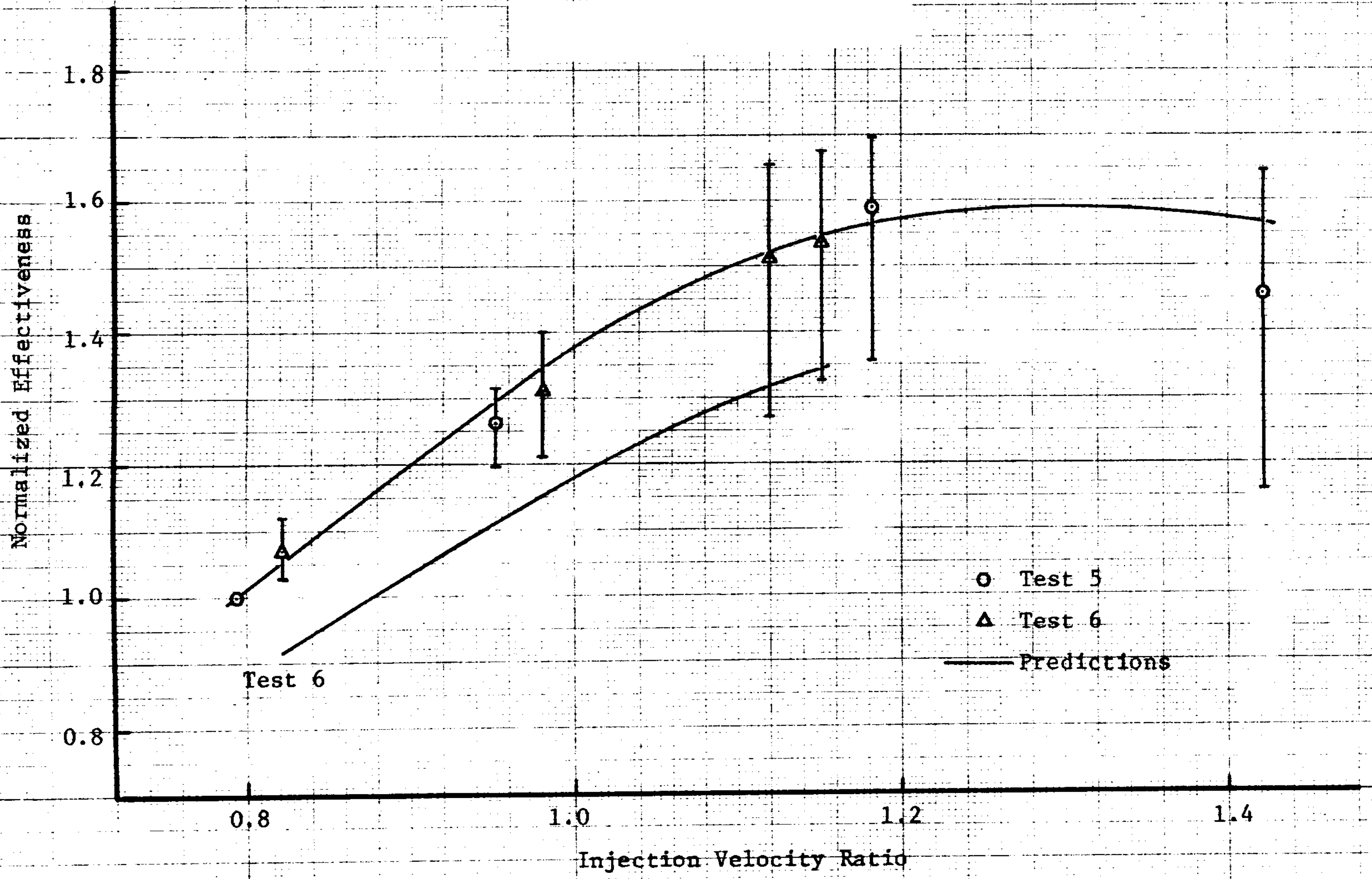

Figure 54. Effect of Velocity Ratio and Coolant Reynolds Number on Coolant Effectiveness - Nozzle Section

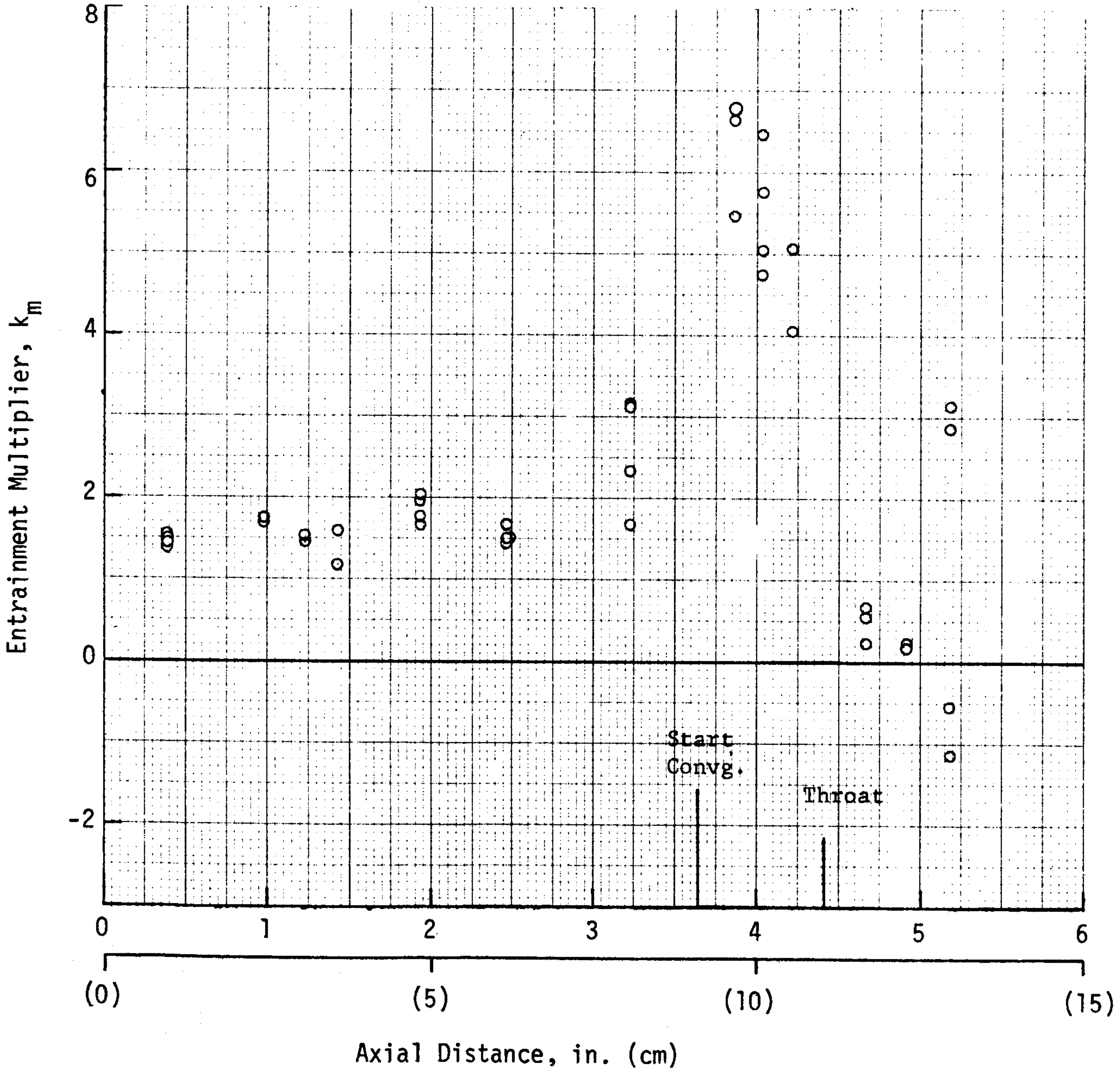

Figure 55. Entrainment Fraction Multipliers - Cylindrical Chamber Tests 3 and 4

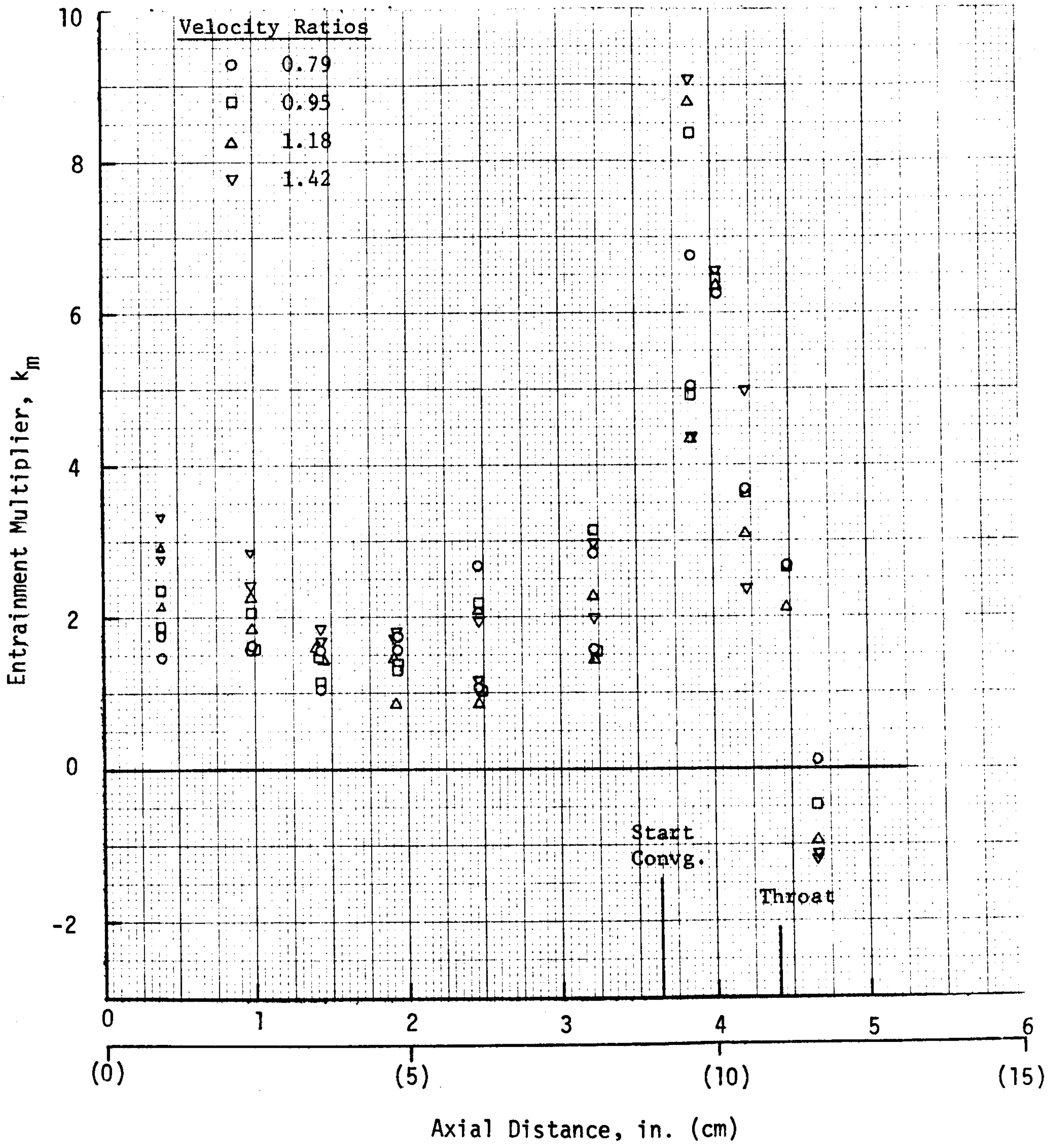

Figure 56. Entrainment Fraction Multipliers - Cylindrical Chamber Test 5

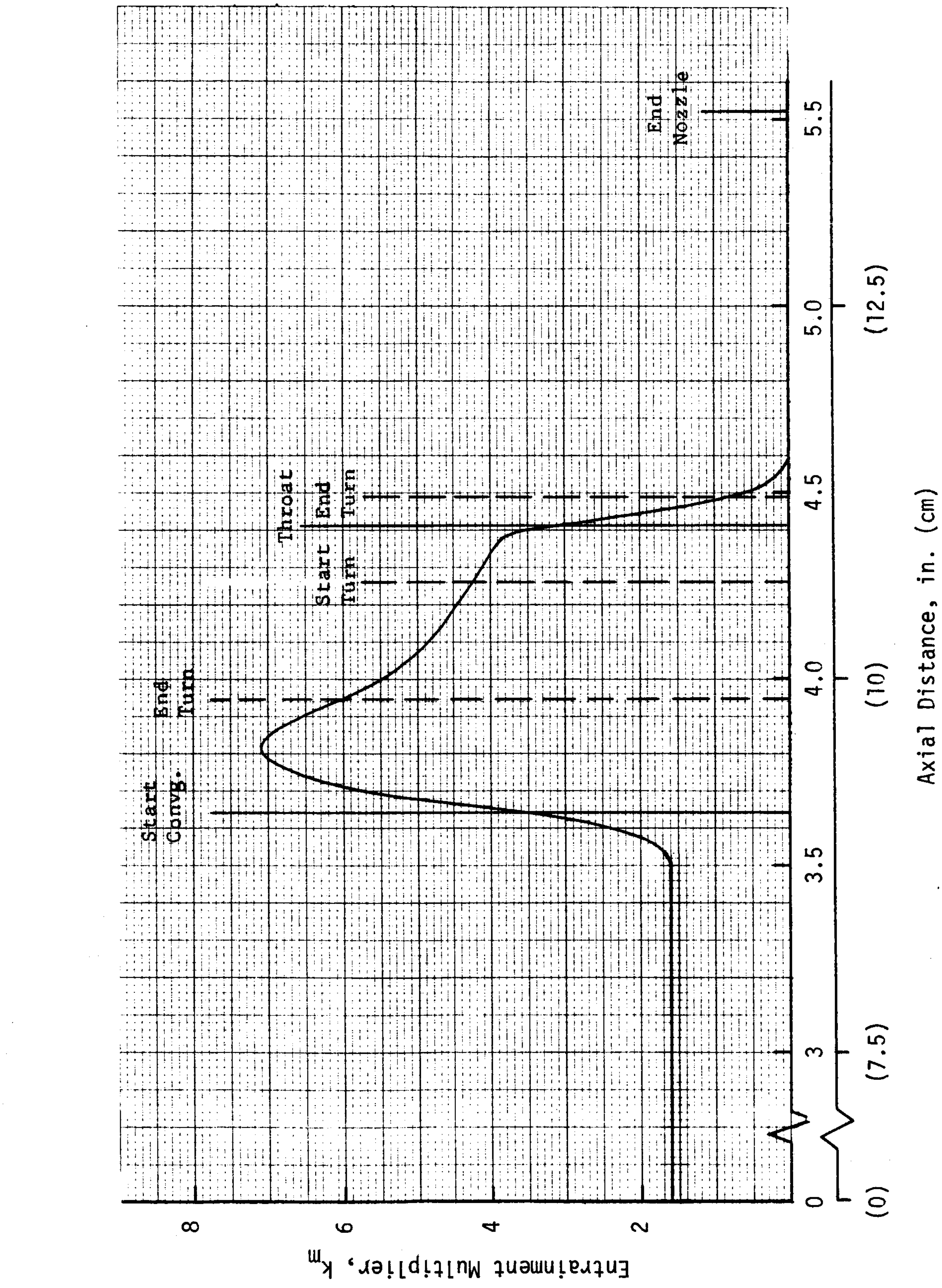

Figure 57. Entrainment Fraction Multiplier - Cylindrical Chamber

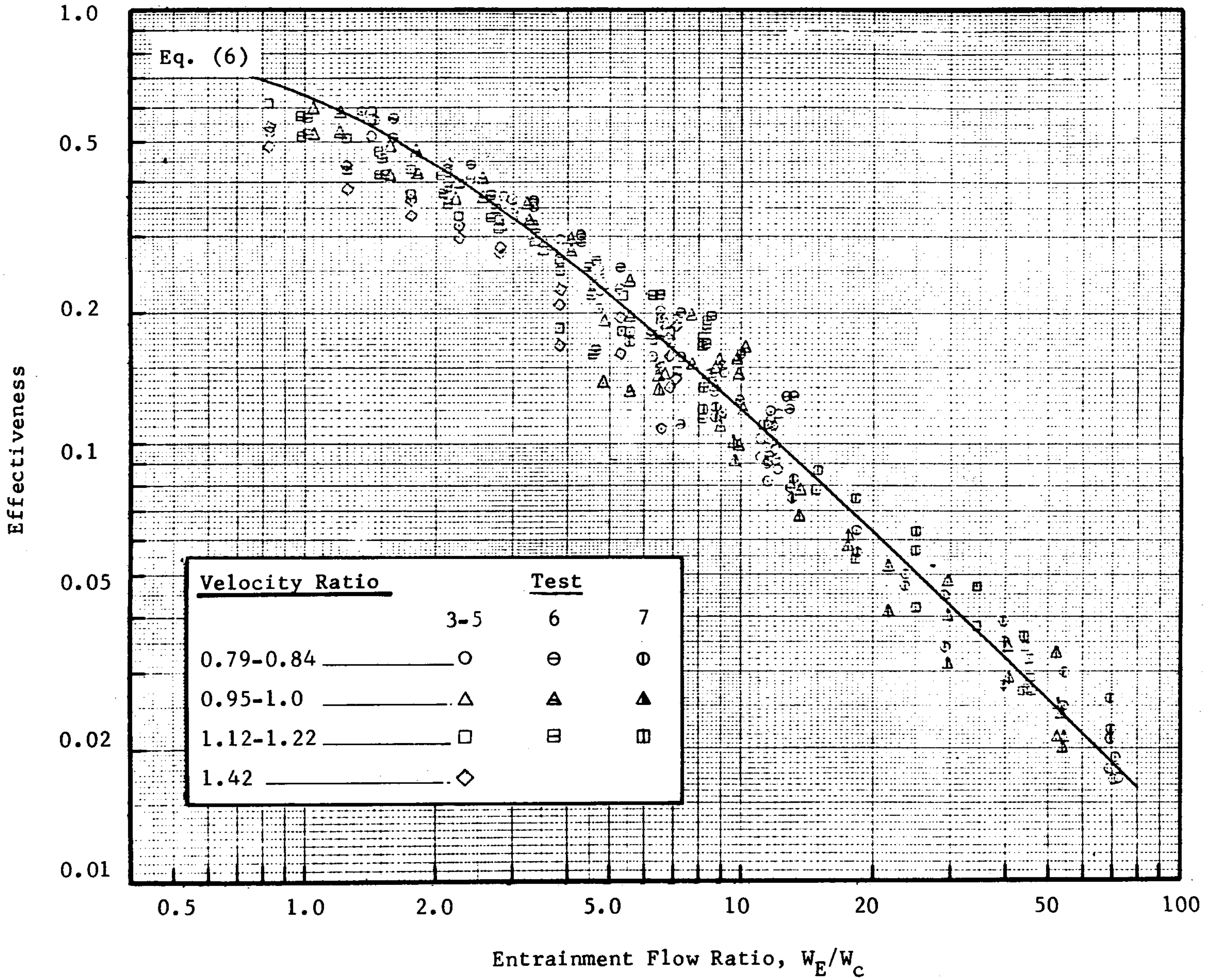

Figure 58. Film Coolant Effectiveness - Cylindrical Chamber, Ambient Coolant

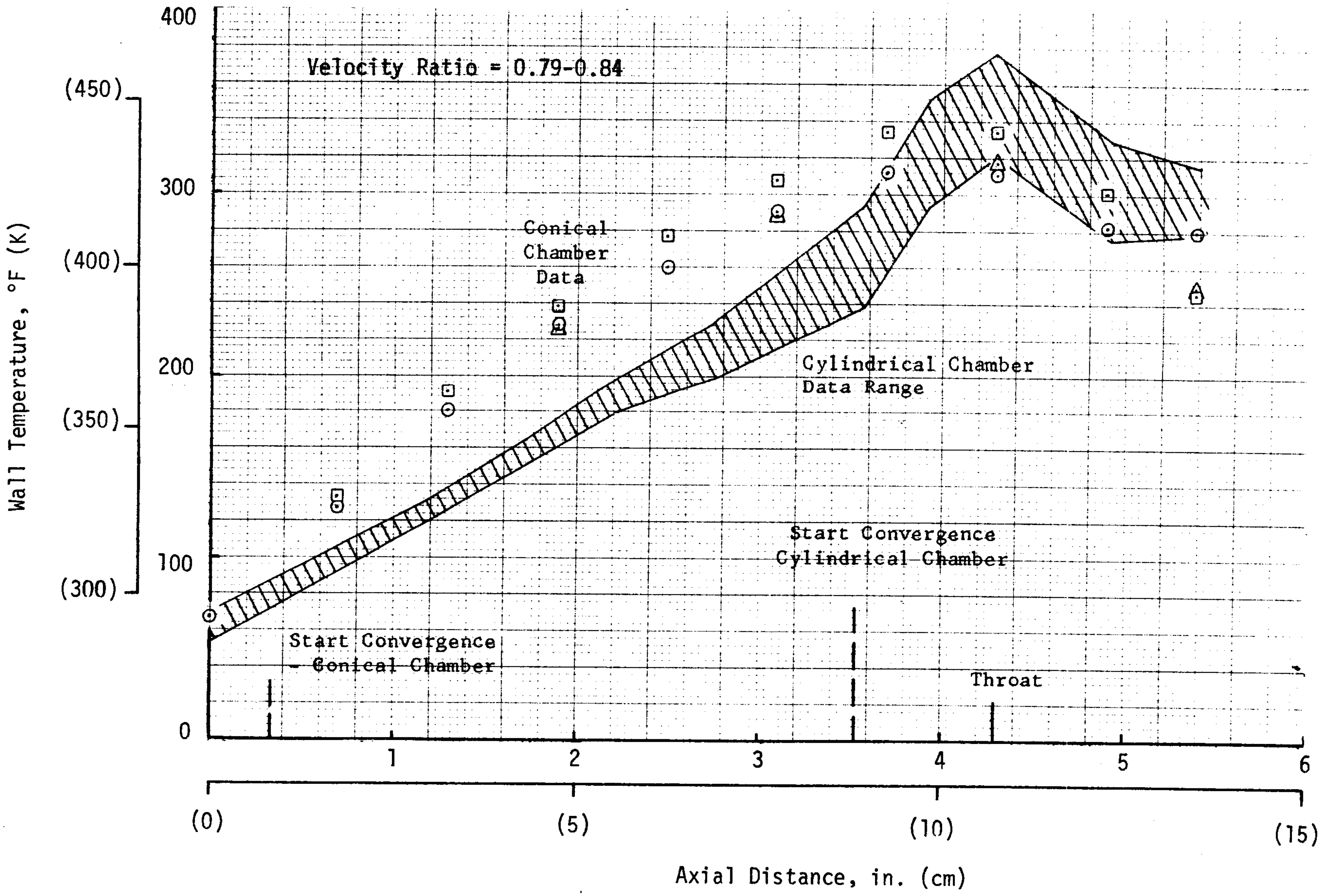

Figure 59. Comparison of Conical and Cylindrical Chamber Adiabatic Wall Temperatures

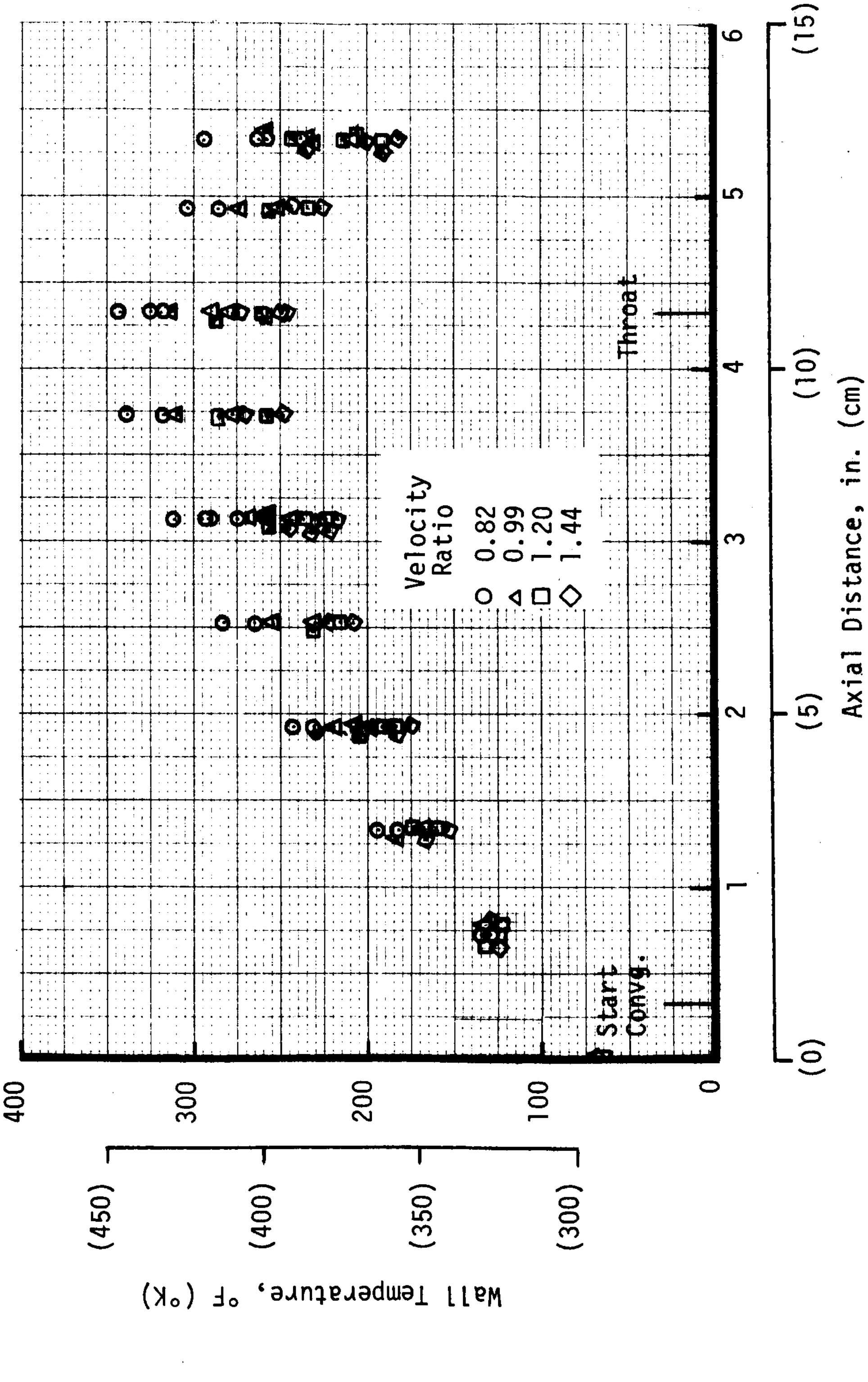

Figure 60. Conical Chamber Adiabatic Wall Temperatures

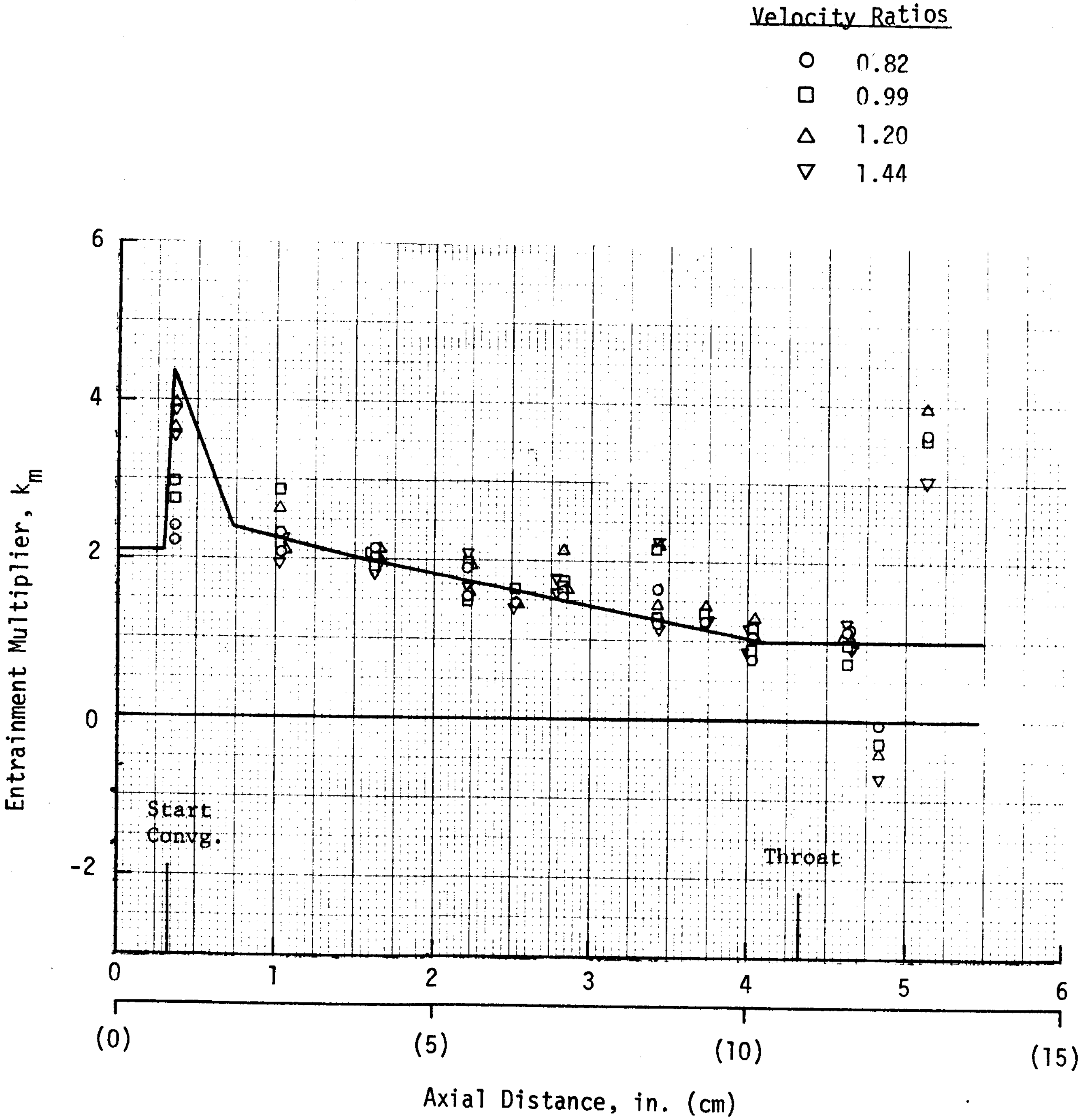

Figure 61. Entrainment Fraction Multiplier – Conical Chamber

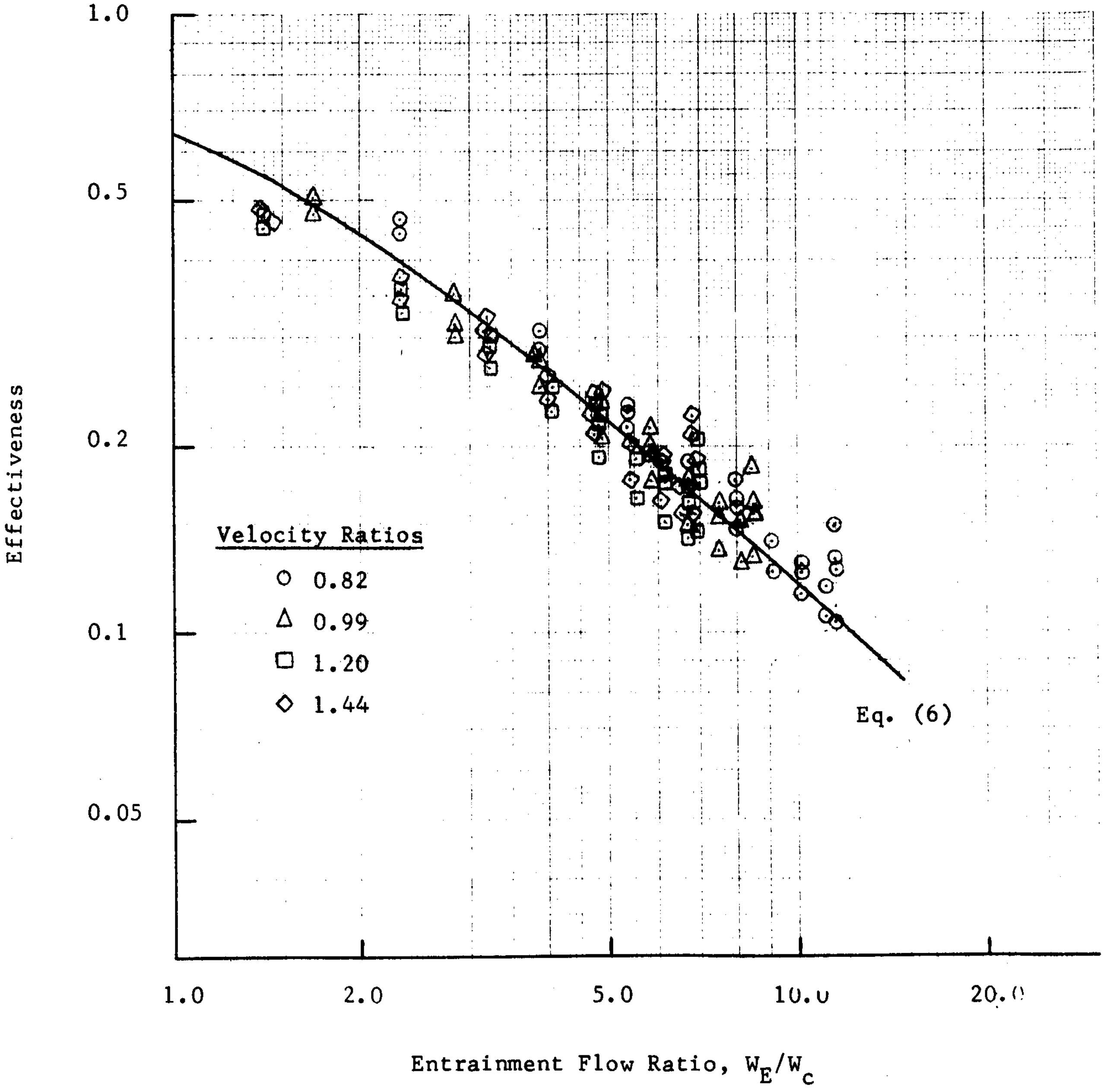

Figure 62. Film Coolant Effectiveness - Conical Chamber

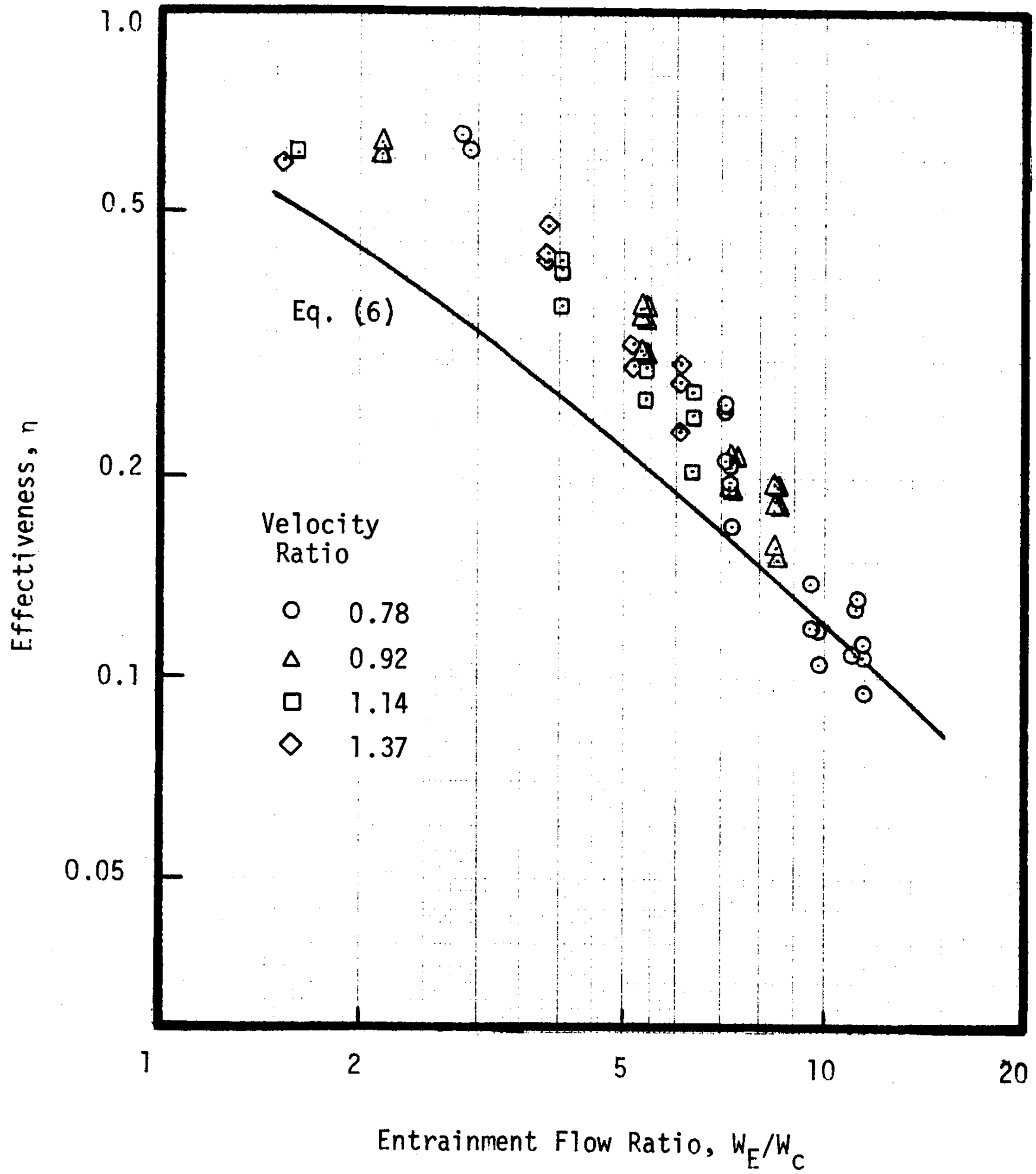

Figure 63. Film Coolant Effectiveness - Rectangular Chamber

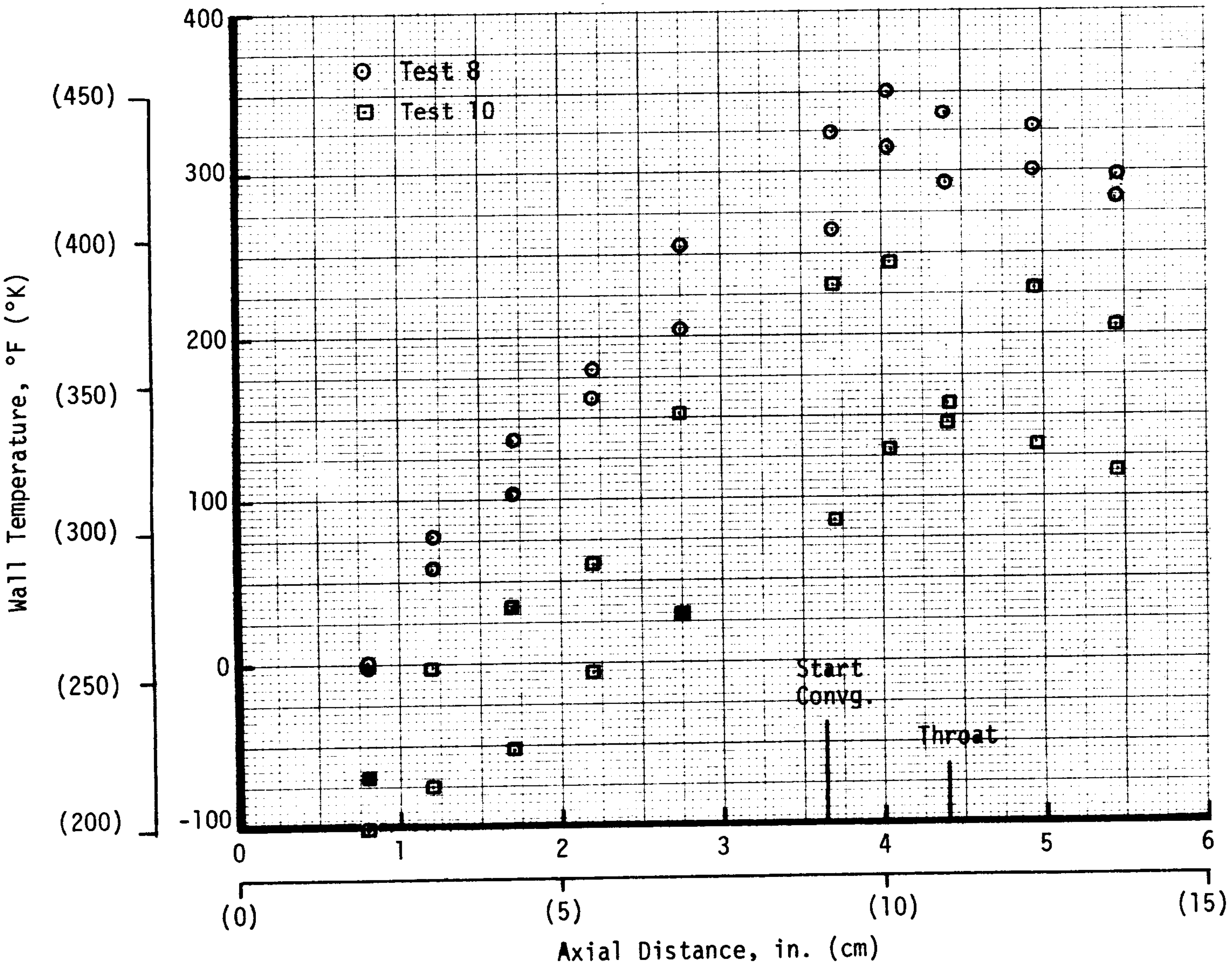

Figure 64. Wall Temperatures with Cold Gaseous Coolant

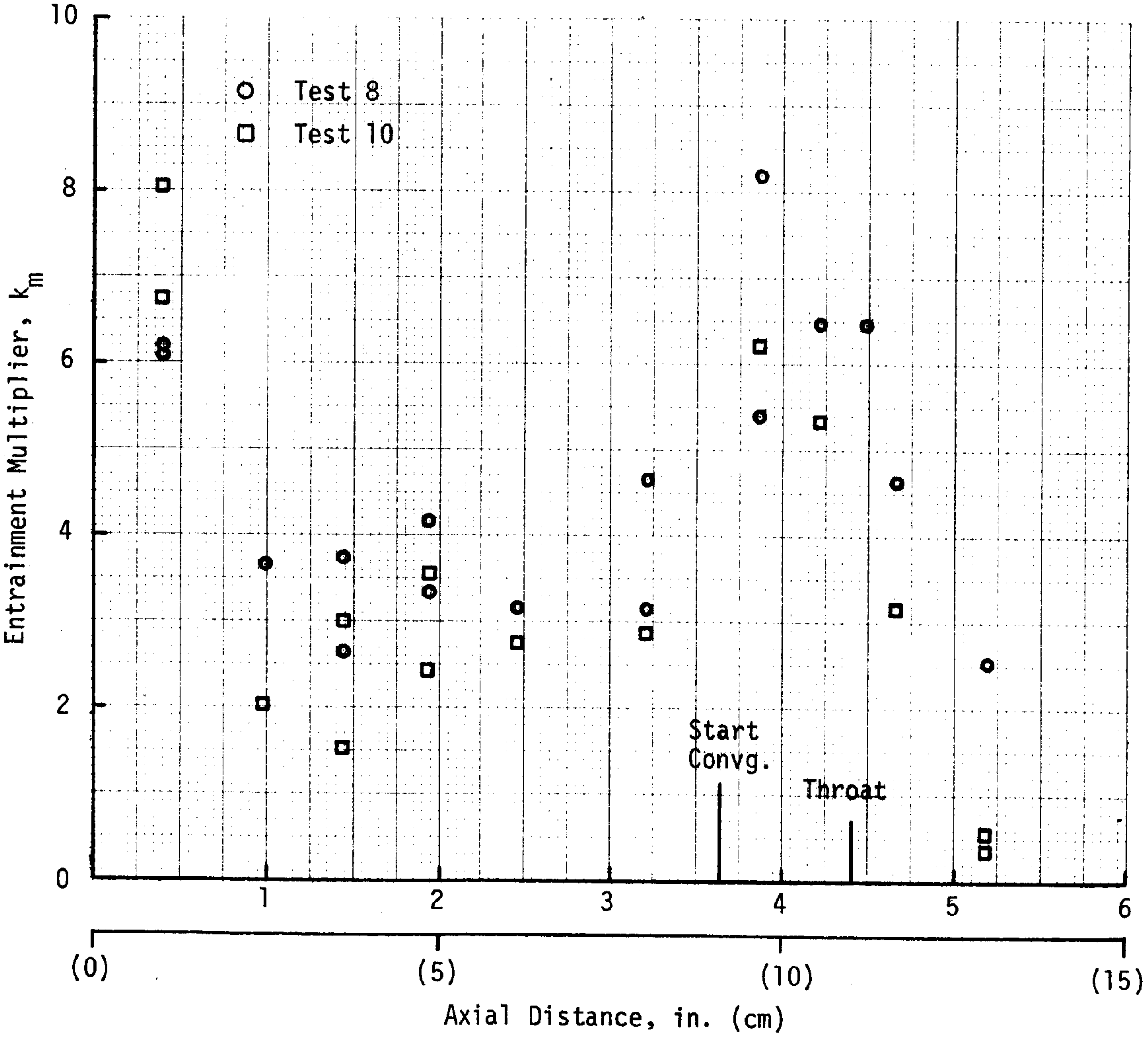

Figure 65. Entrainment Fraction Multipliers - Tests 8 and 10

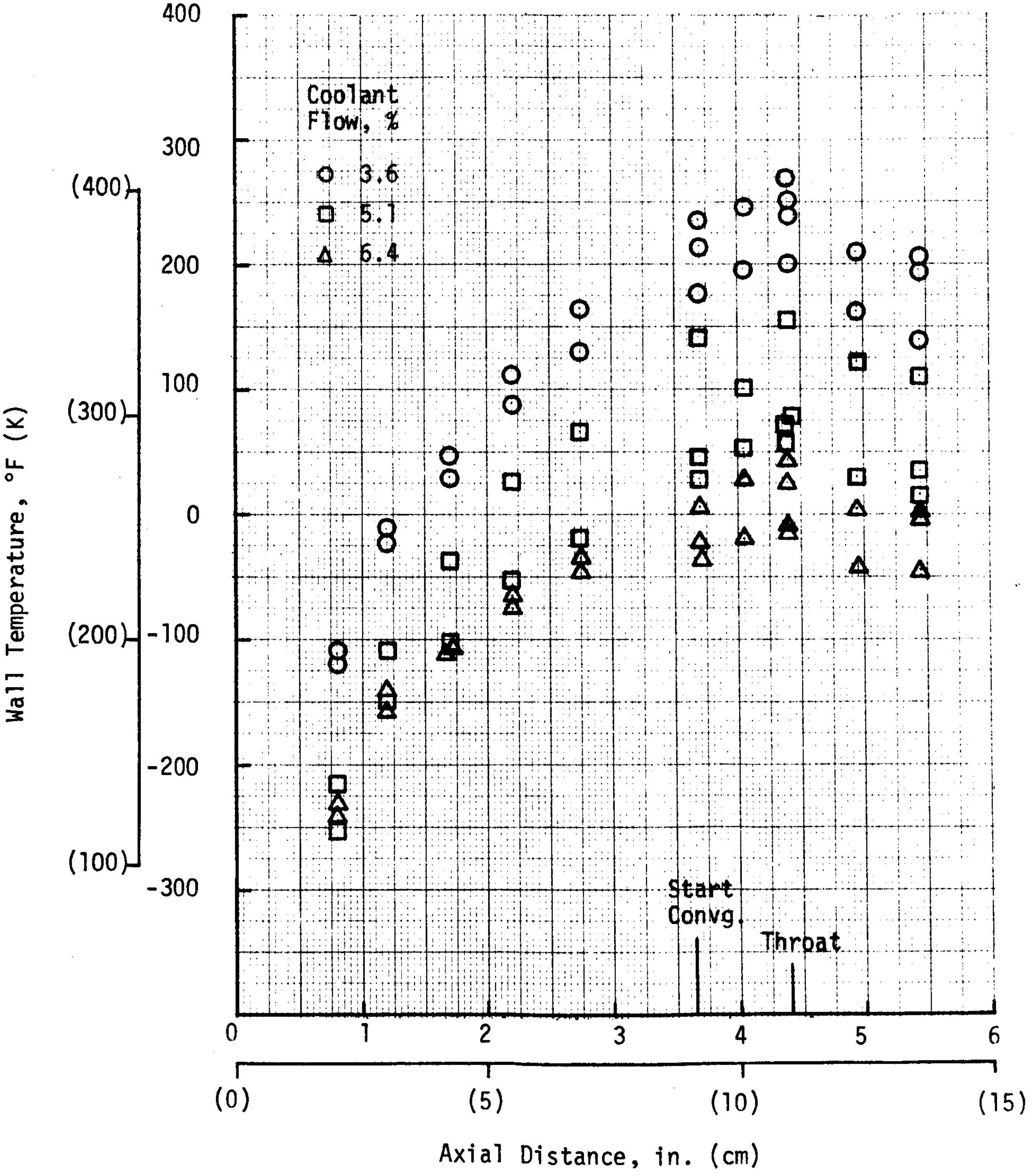

Figure 66. Wall Temperatures with Supercritical Liquid Hydrogen

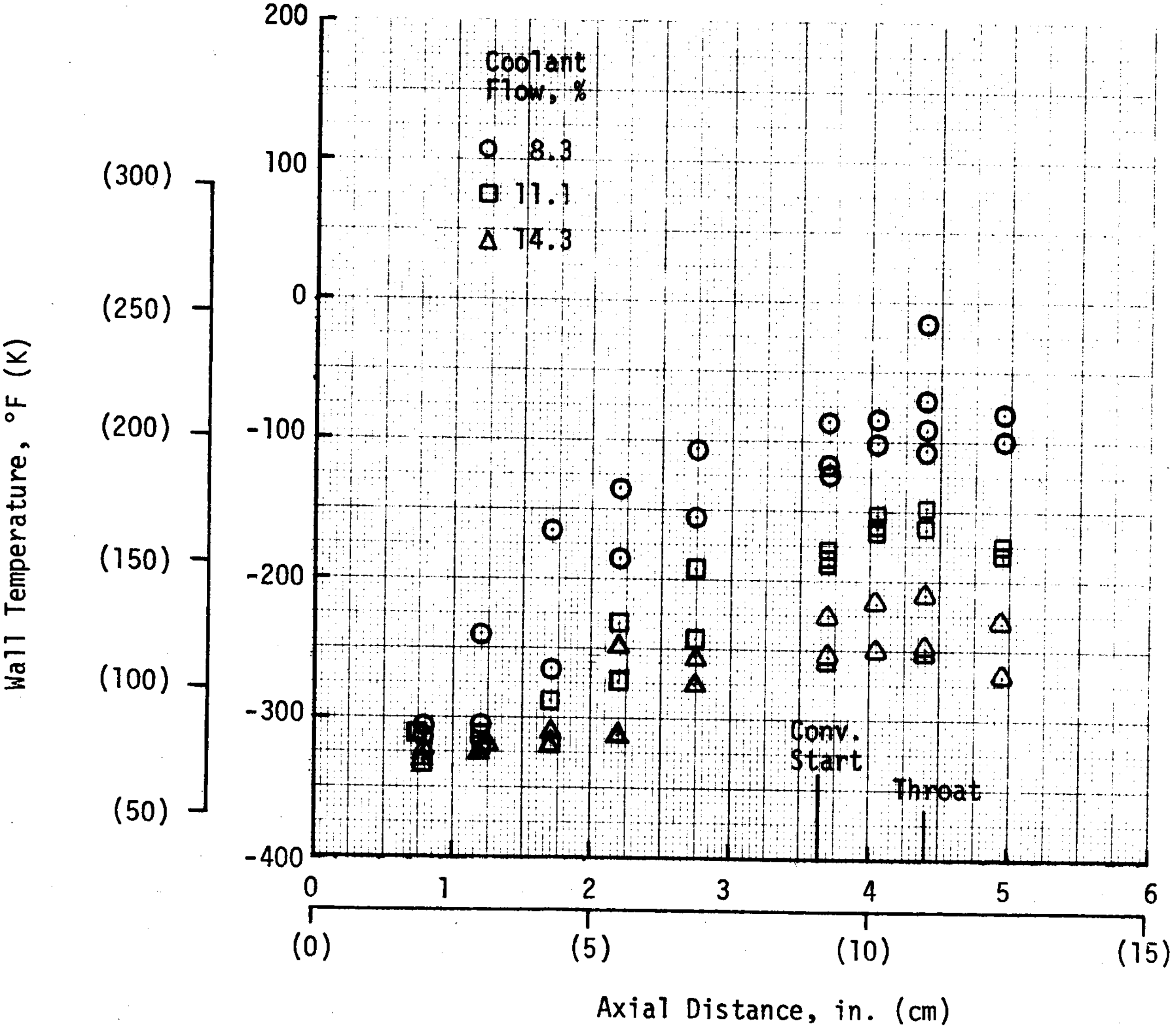

Figure 67. Wall Temperatures with Subcritical Liquid Hydrogen

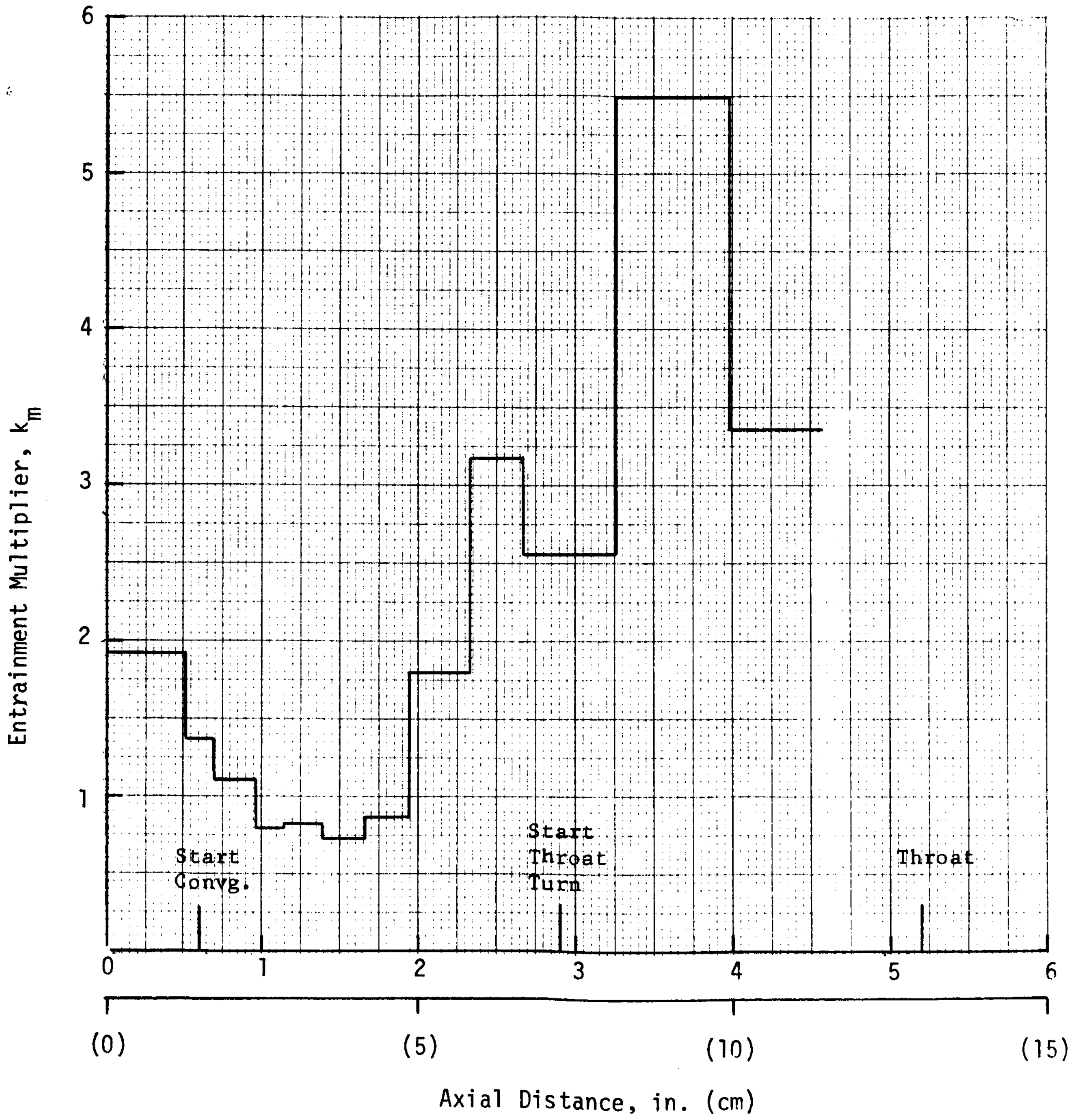

Figure 68. Entrainment Fraction Multipliers - Nozzle 3, Ref. 12

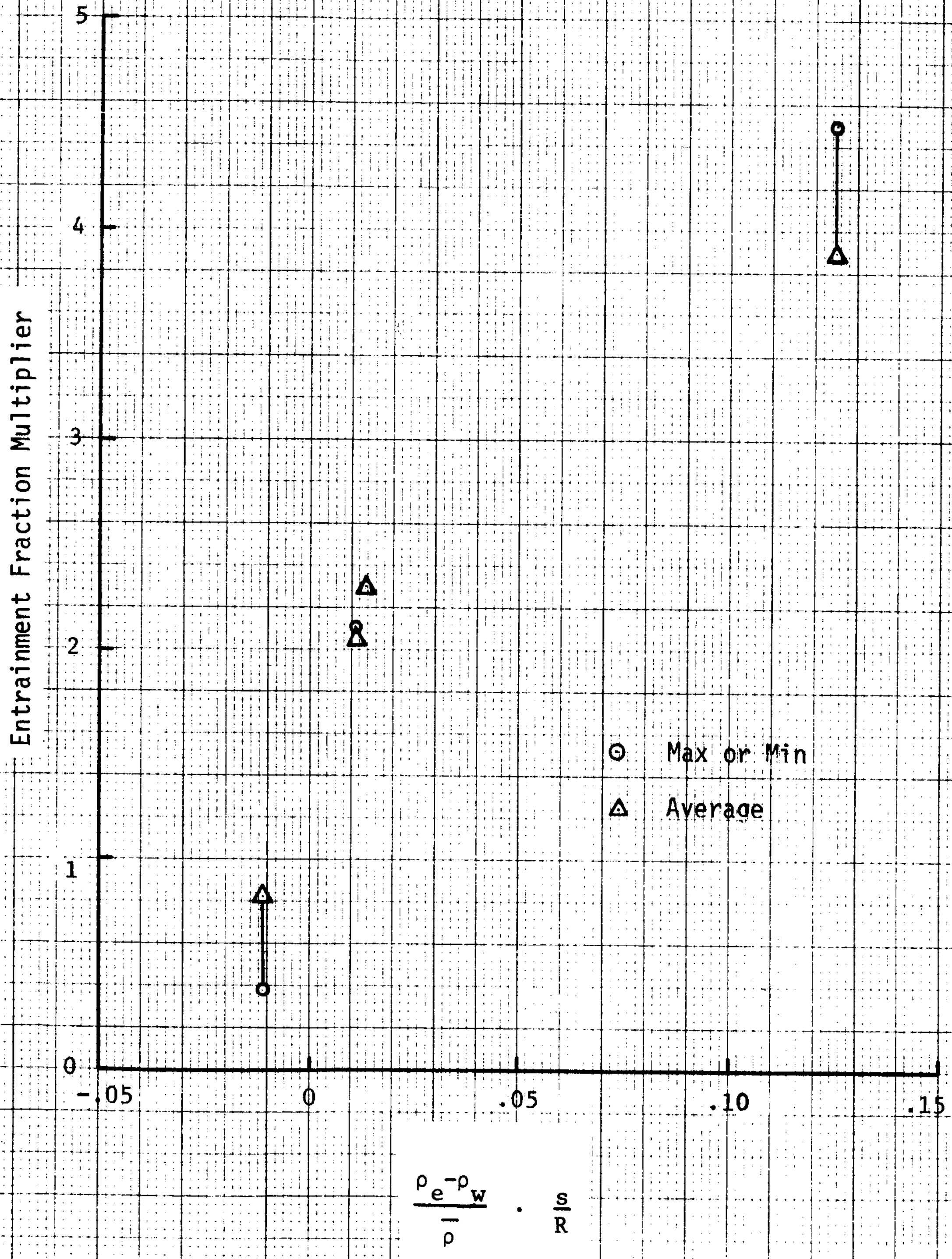

Figure 69. Entrainment Fraction Multiplier due to Flow Turning

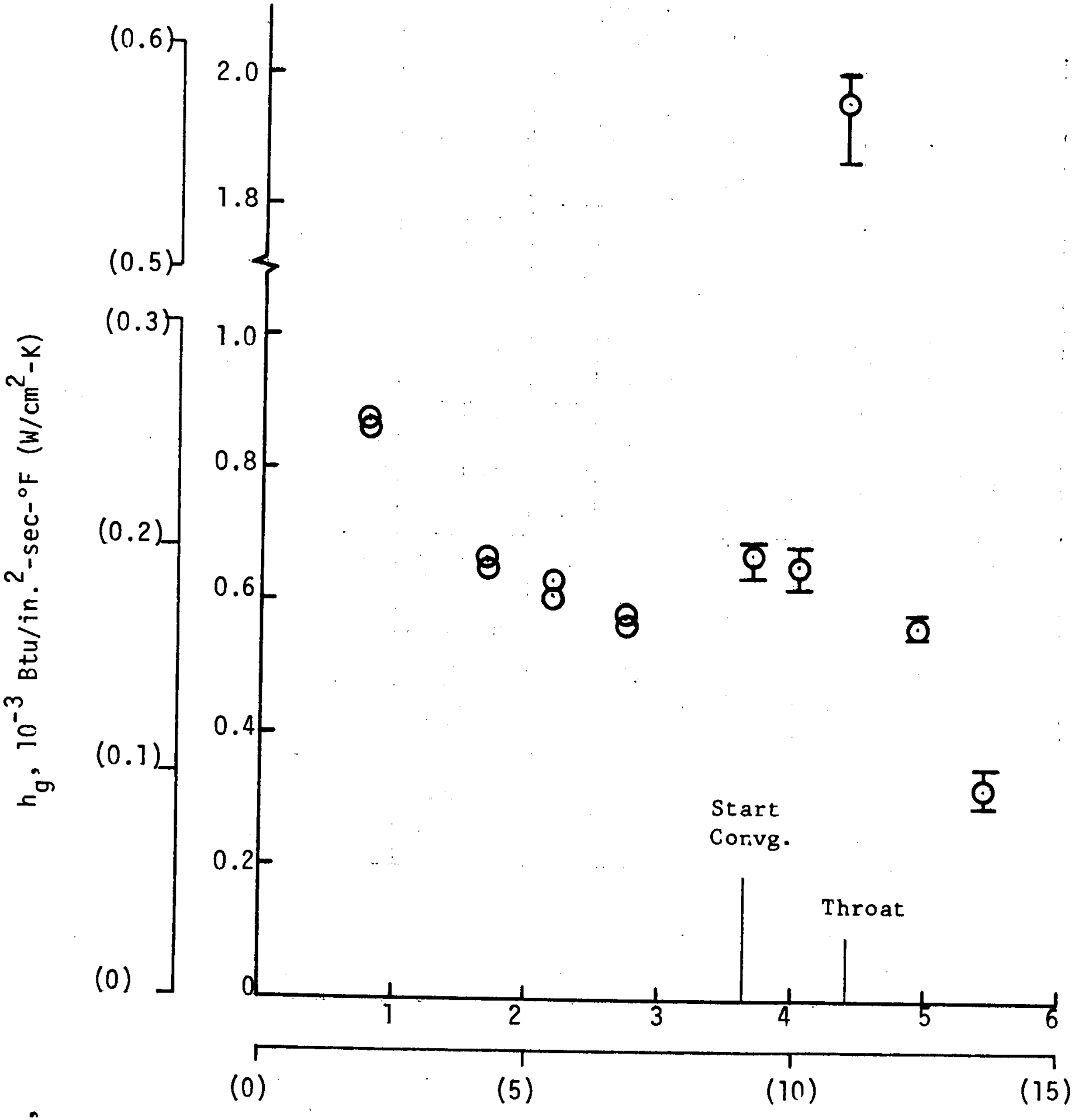

Figure 70. Heat Transfer Coefficients Without Film Cooling - Cylindrical Chamber Tests 3, 4 and 5A

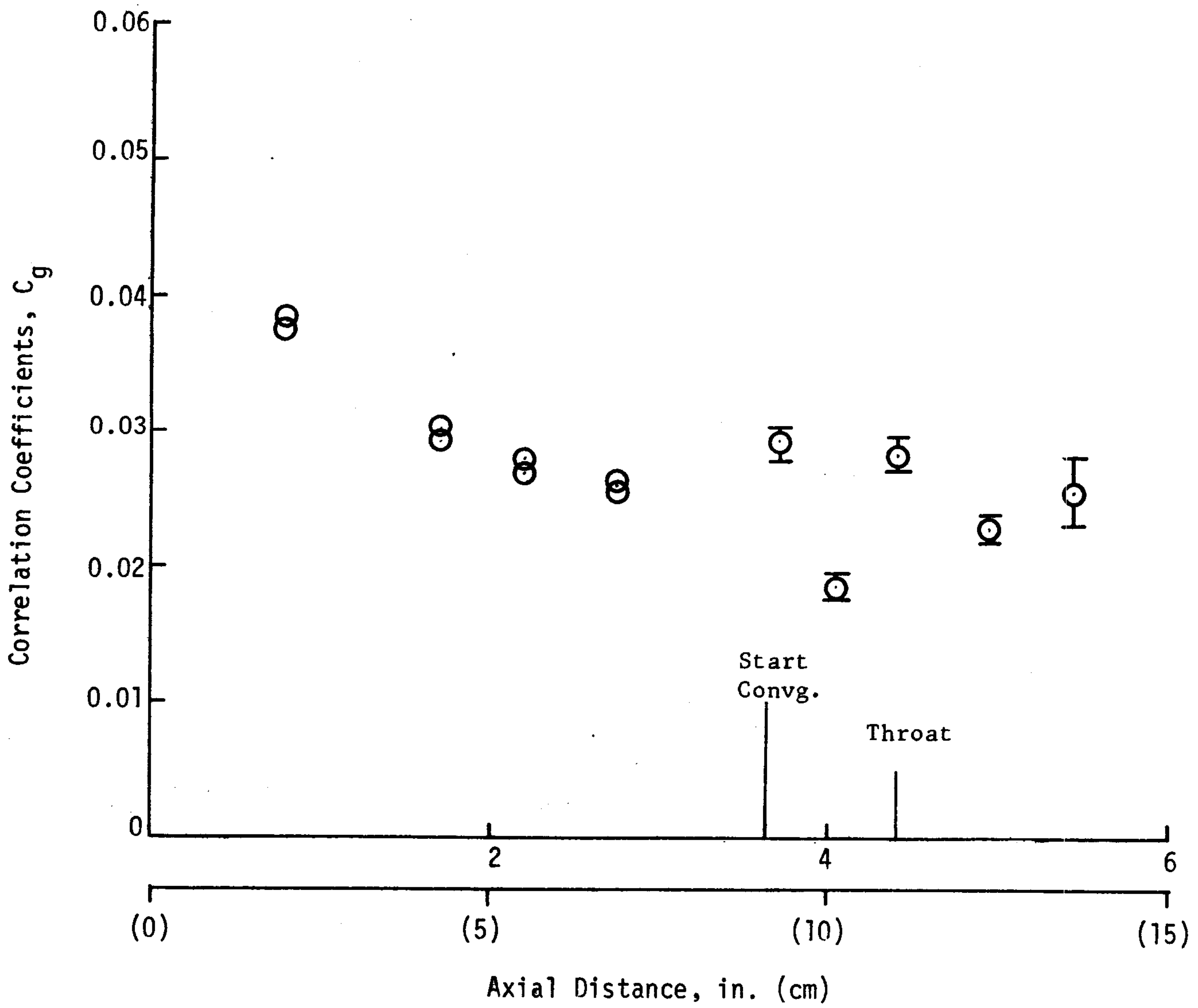

Figure 71. Heat Transfer Correlation Coefficients Without Film Cooling - Cylindrical Chamber Tests 3, 4, and 5A

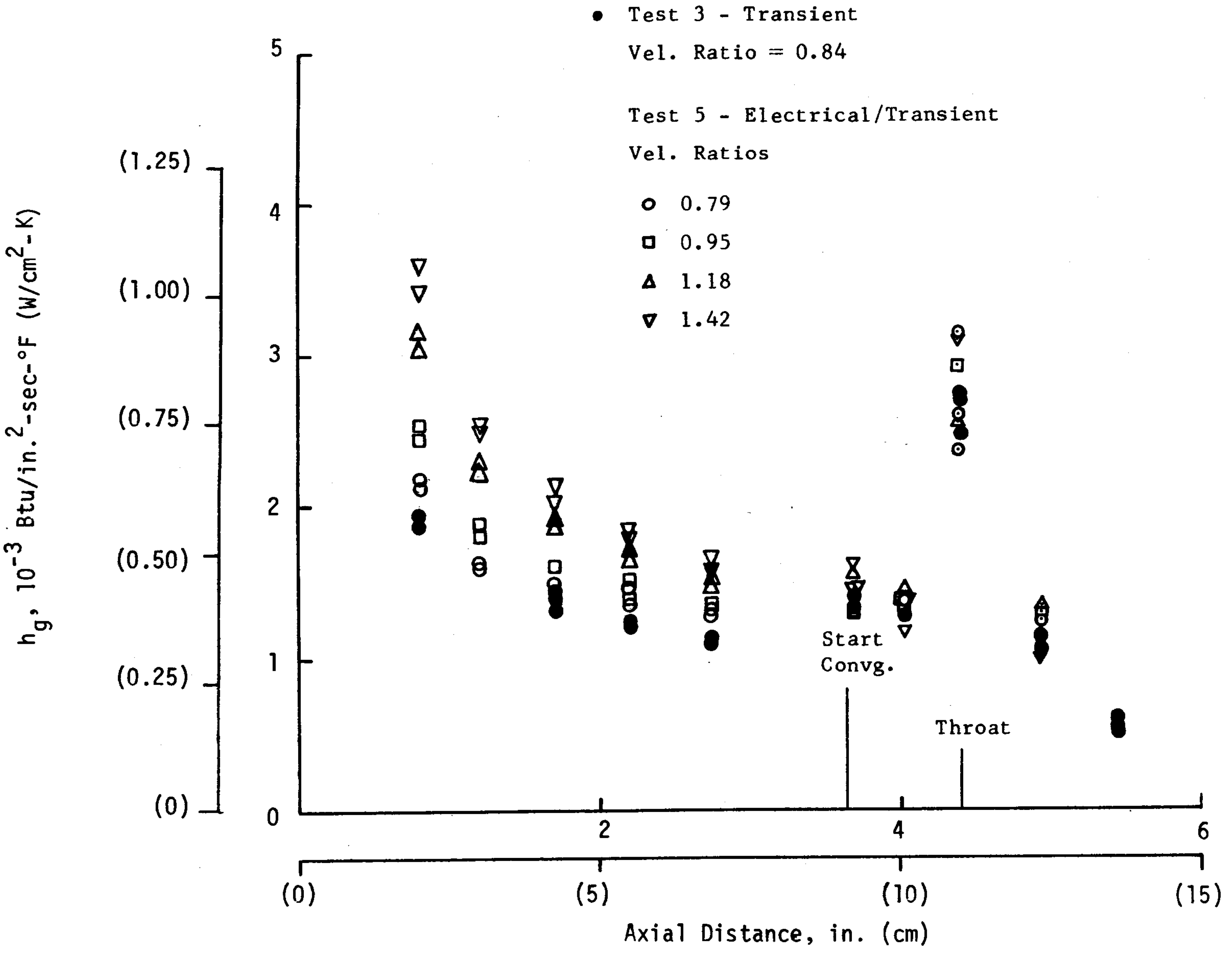

Figure 72. Heat Transfer Coefficients with Film Cooling - Cylindrical Chamber Tests 3 and 5

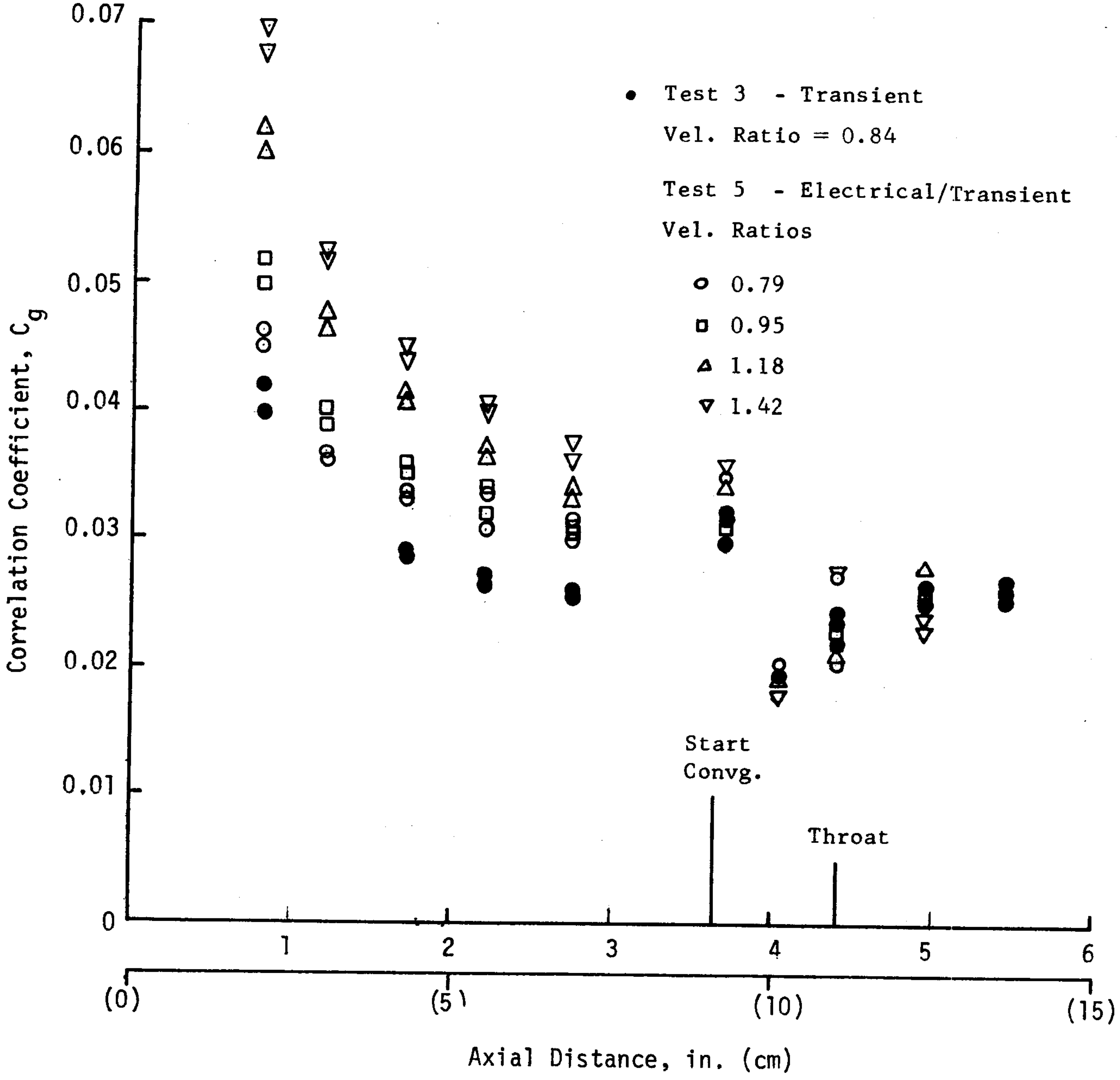

Figure 73. Heat Transfer Correlation Coefficients with Film Cooling - Cylindrical Chamber Tests 3 and 5

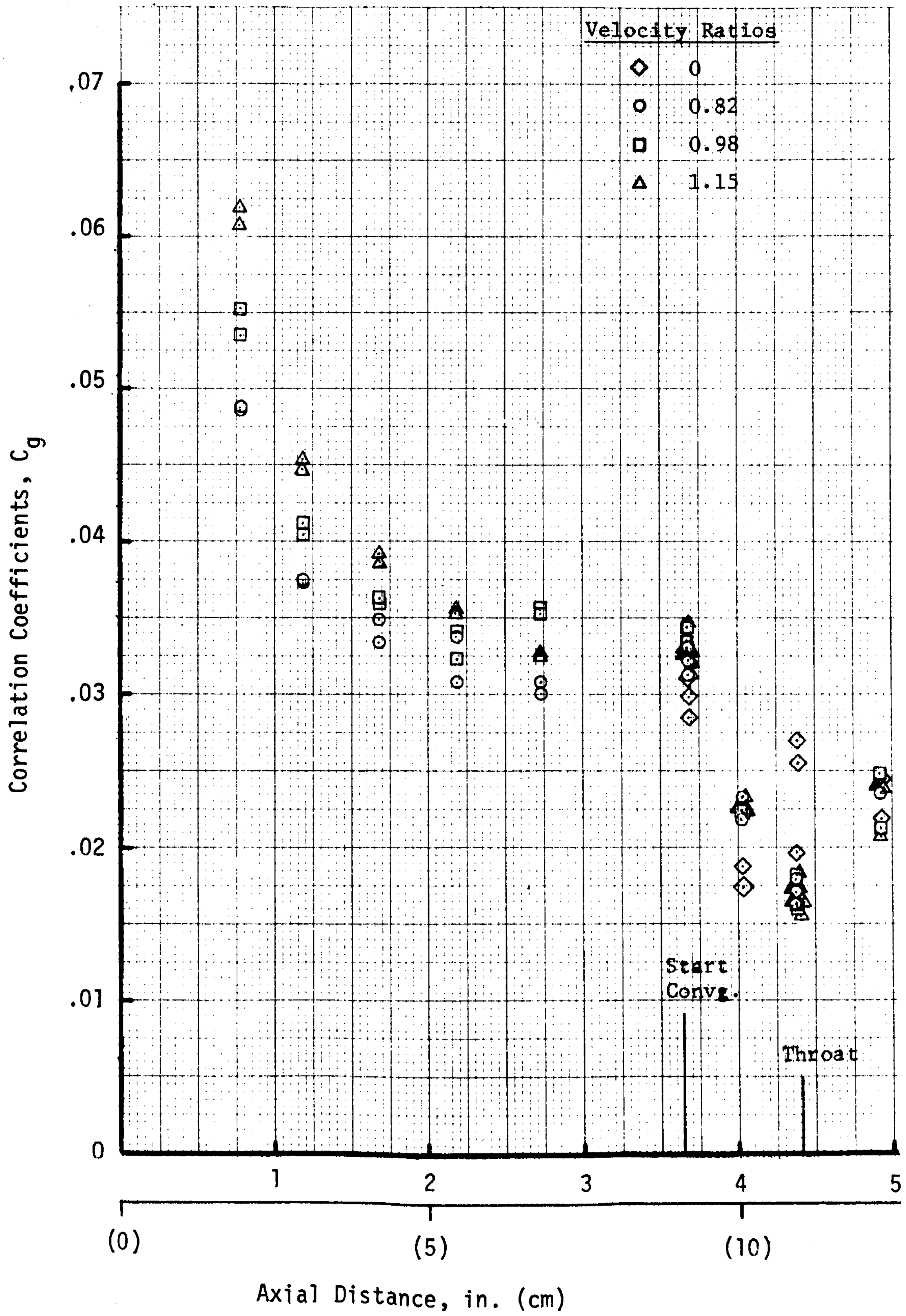

Figure 74. Heat Transfer Correlation Coefficients - Cylindrical Chamber Test 6

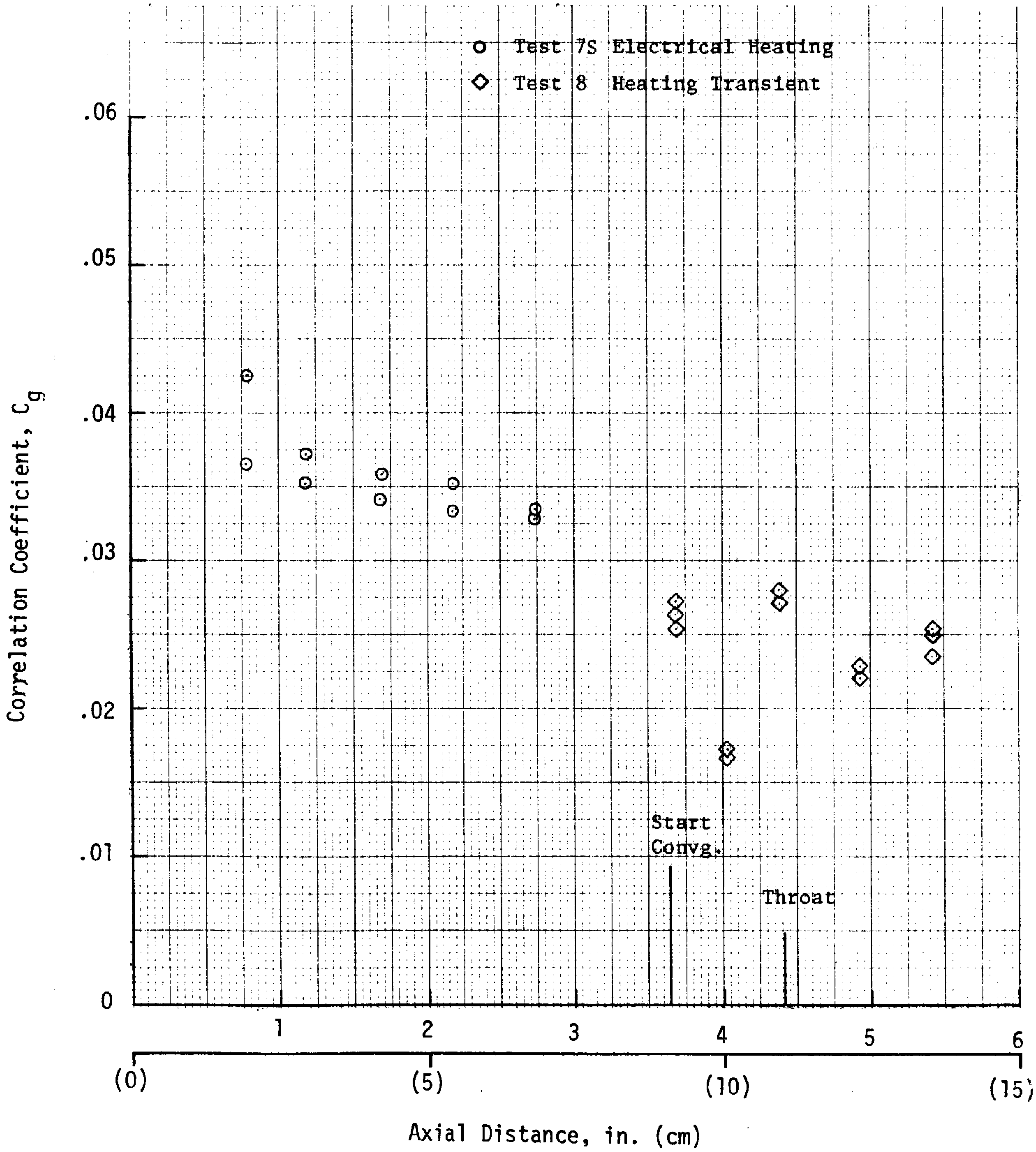

Figure 75. Heat Transfer Correlation Coefficients - 0.015 in. Slot Without Coolant

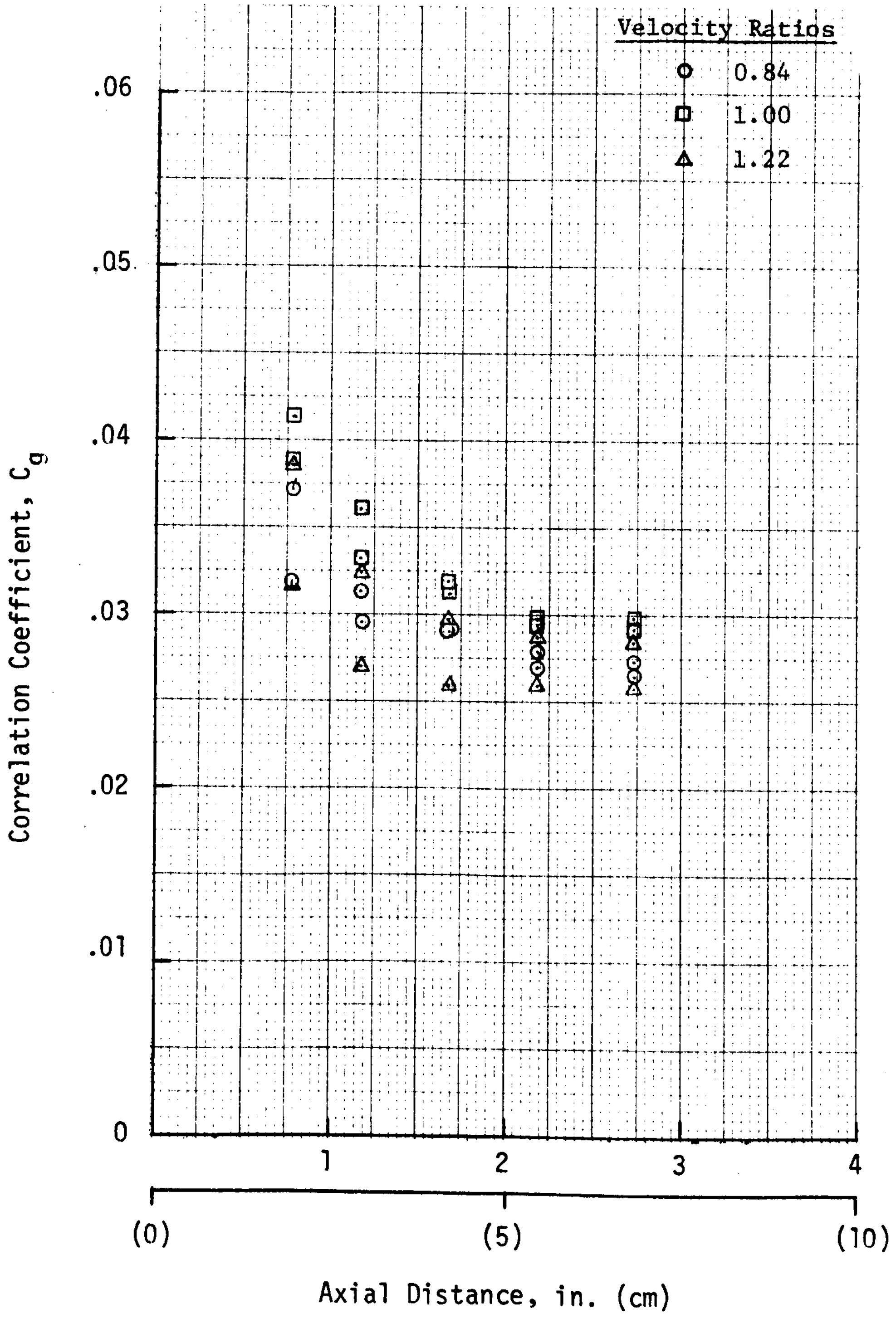

Figure 76. Heat Transfer Correlation Coefficients - 0.015 in. Slot, Ambient Coolant

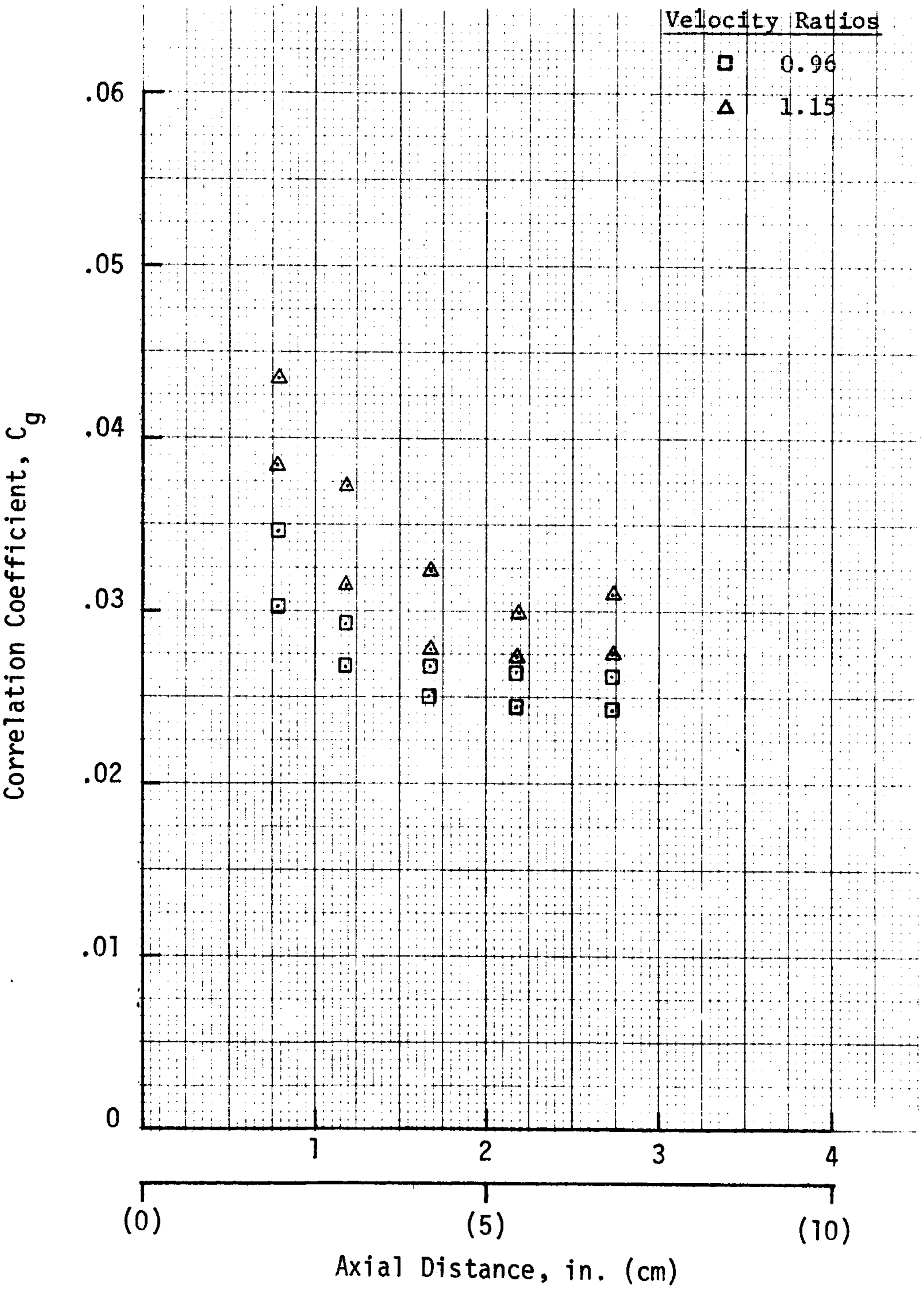

Figure 77. Heat Transfer Correlation Coefficients - 0.015 in. Slot, Cold Coolant

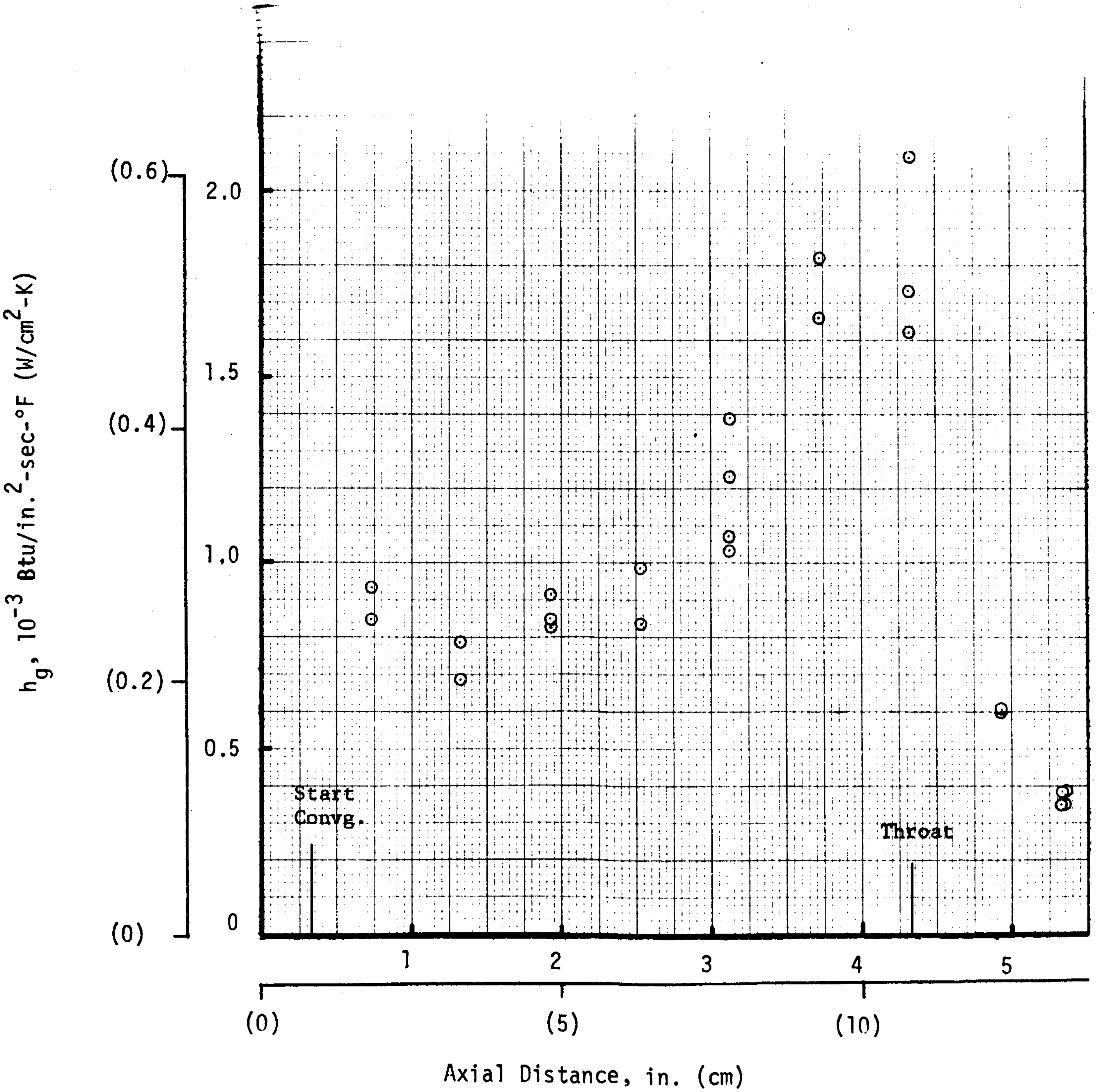

Figure 78. Heat Transfer Coefficients Without Film Cooling - Conical Chamber

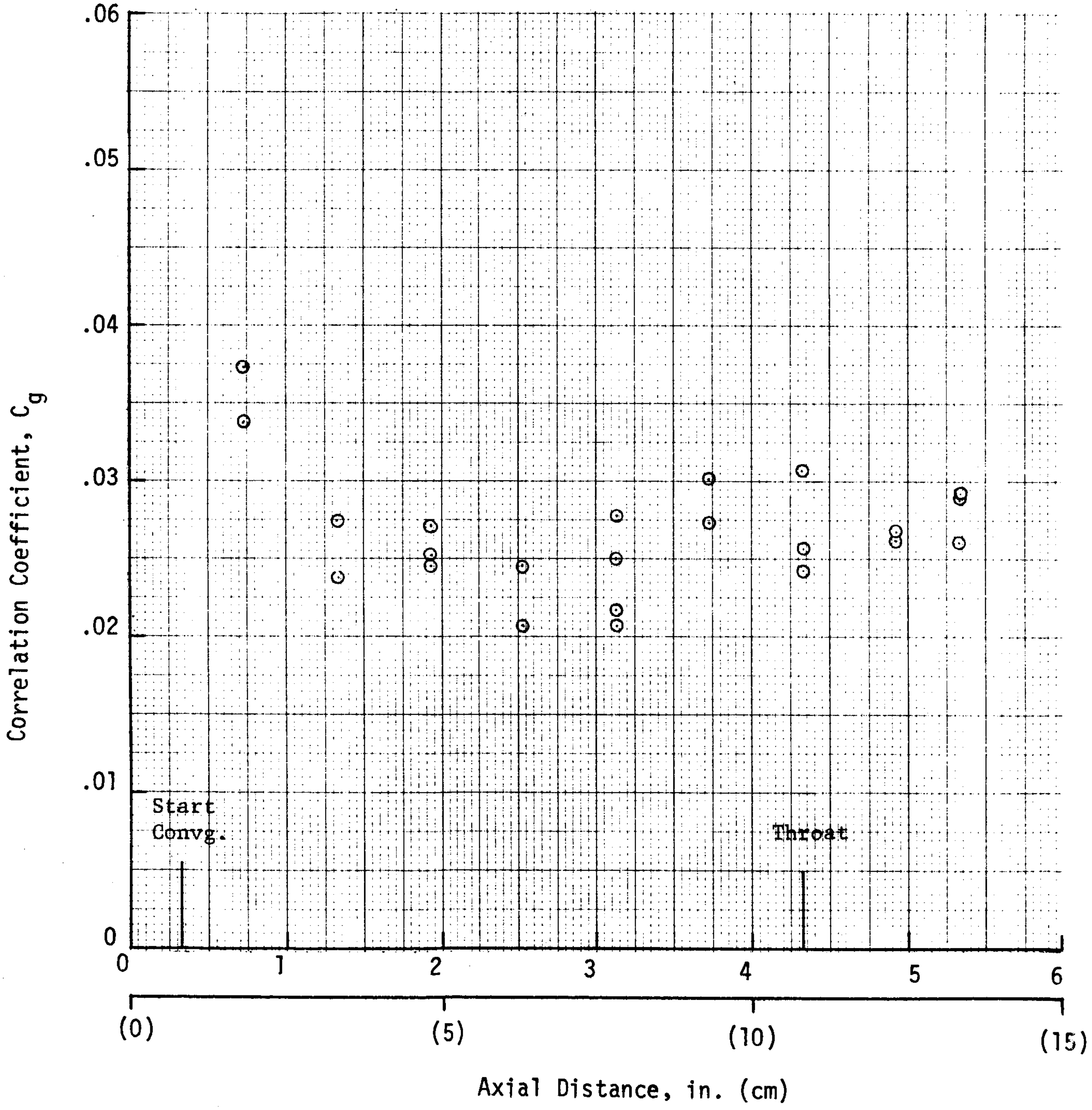

Figure 79. Heat Transfer Correlation Coefficients Without Film Cooling - Conical Chamber

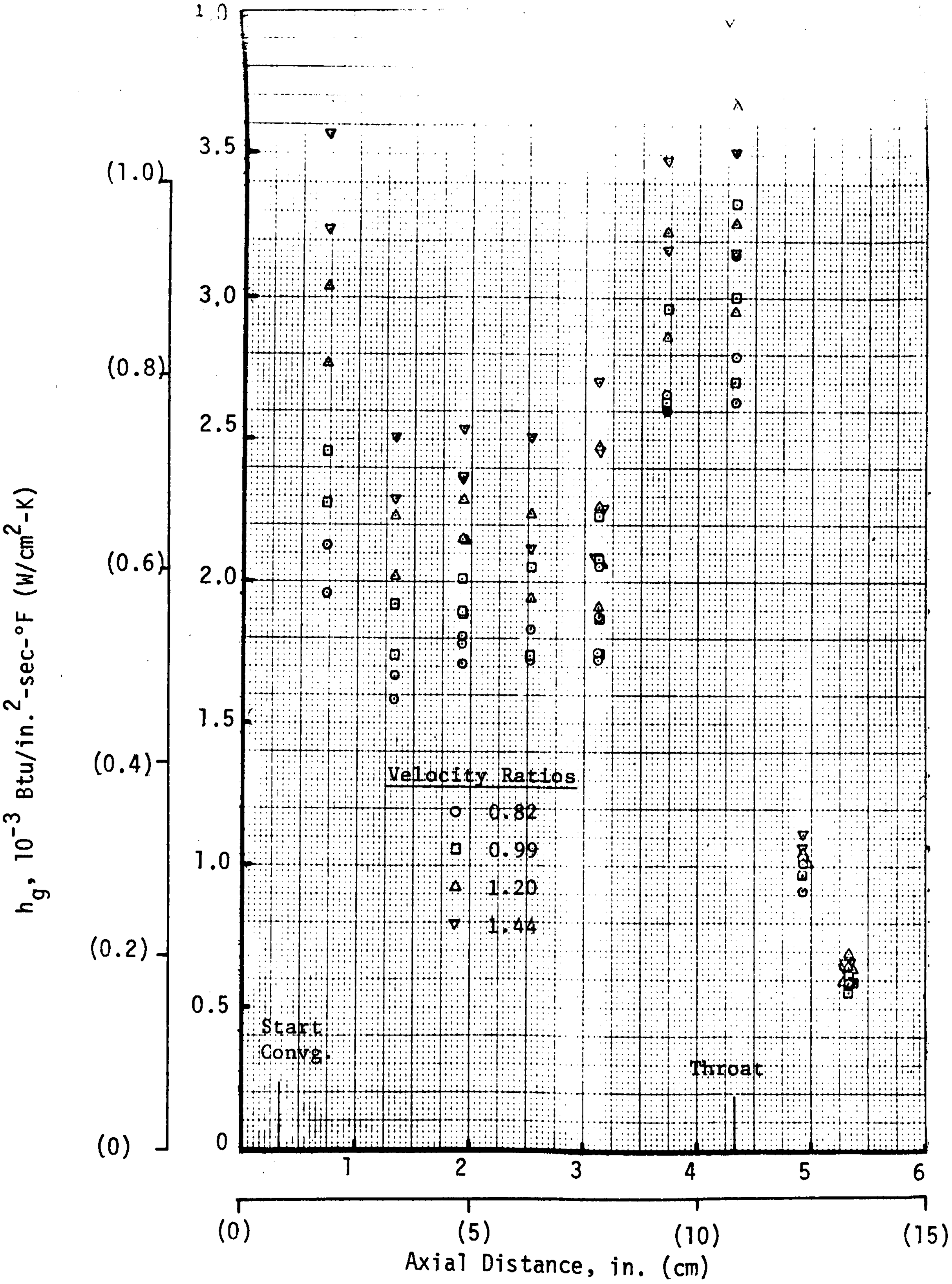

Figure 80. Heat Transfer Coefficients With Film Cooling - Conical Chamber

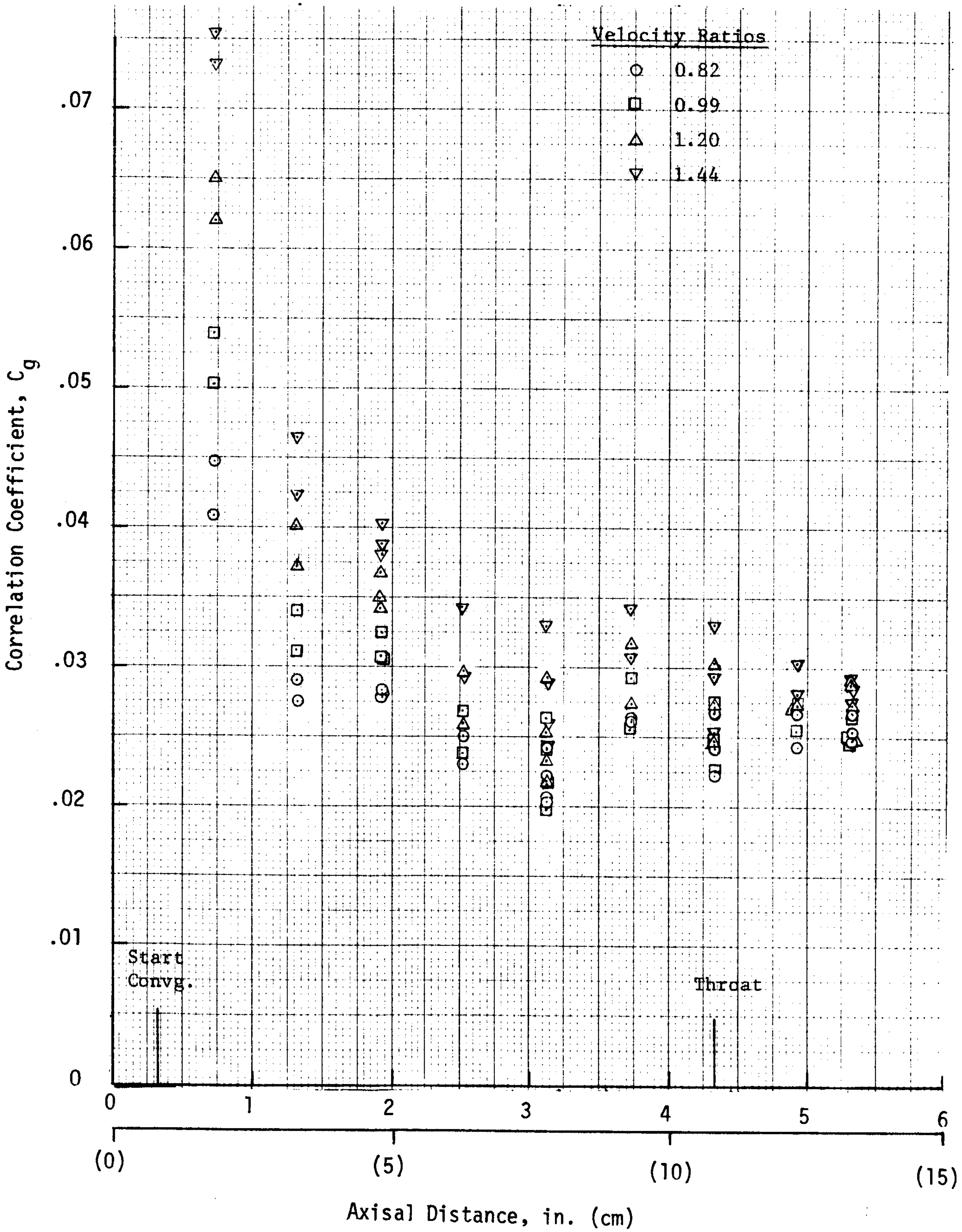

Figure 81. Heat Transfer Correlation Coefficients With Film Cooling - Conical Chamber

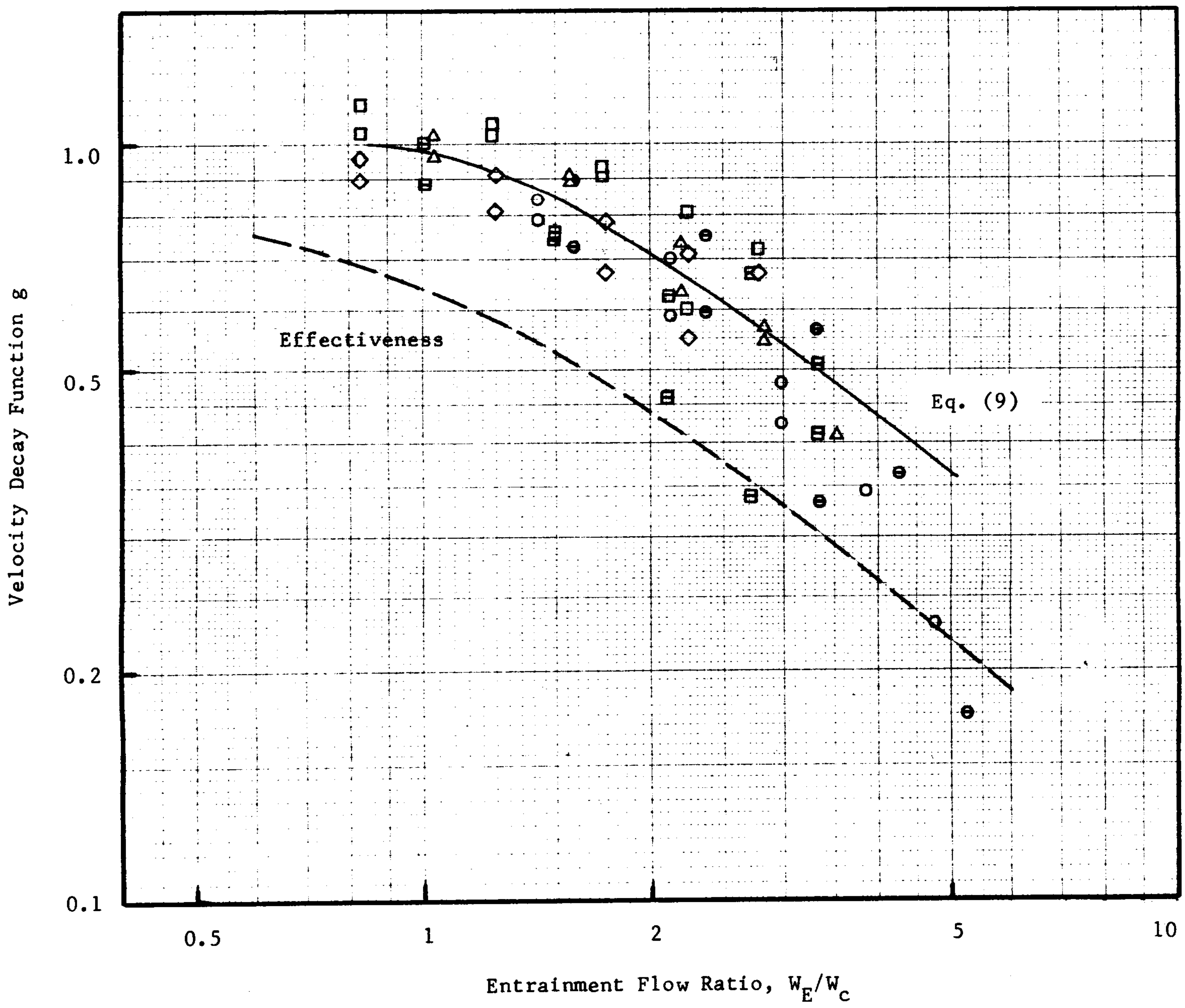

Figure 82. Velocity Decay Function - Cylindrical Chamber

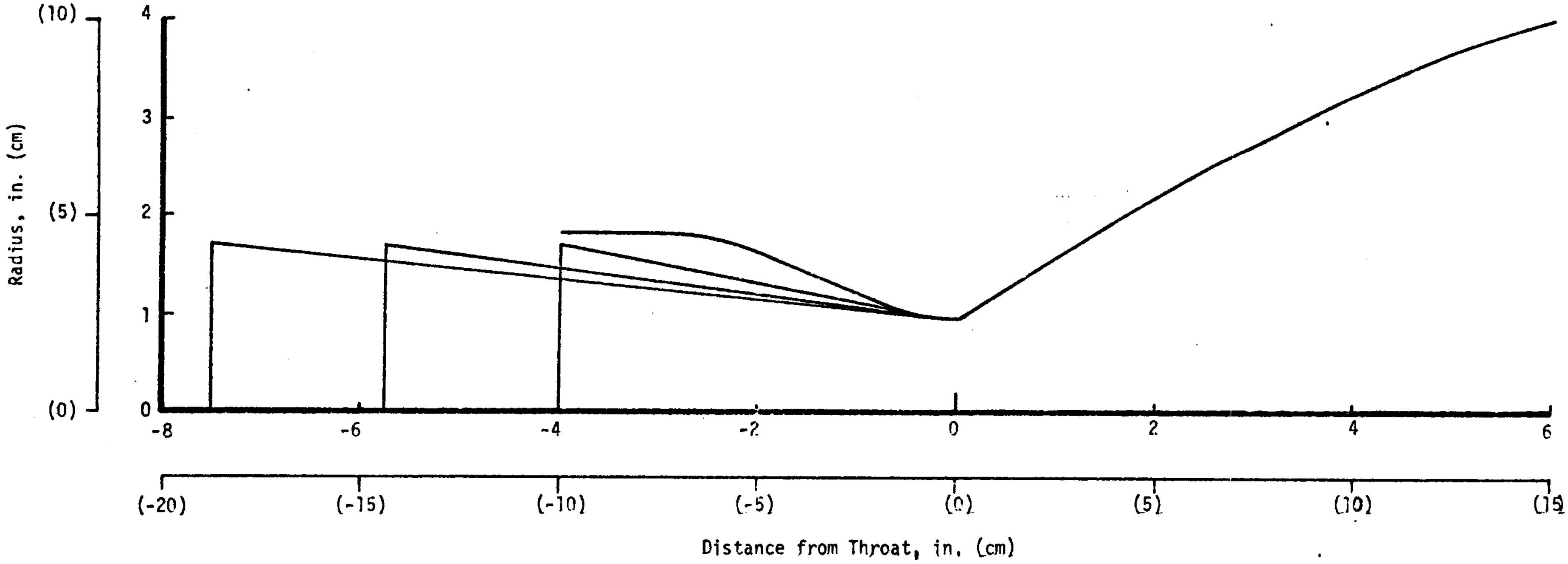

Figure 83. Design Study Chamber Contours

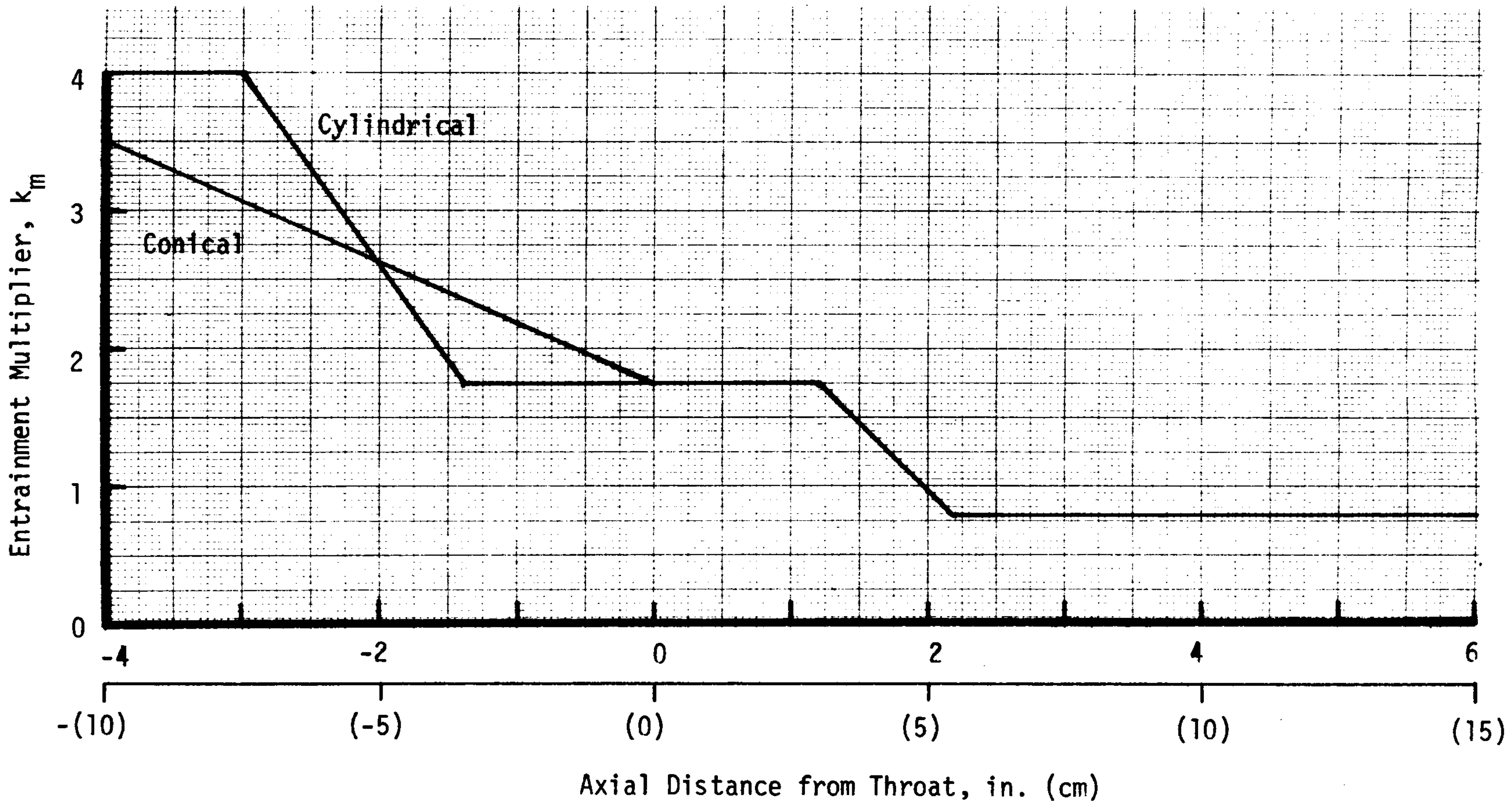

Figure 84. Design Study Entrainment Fraction Multipliers

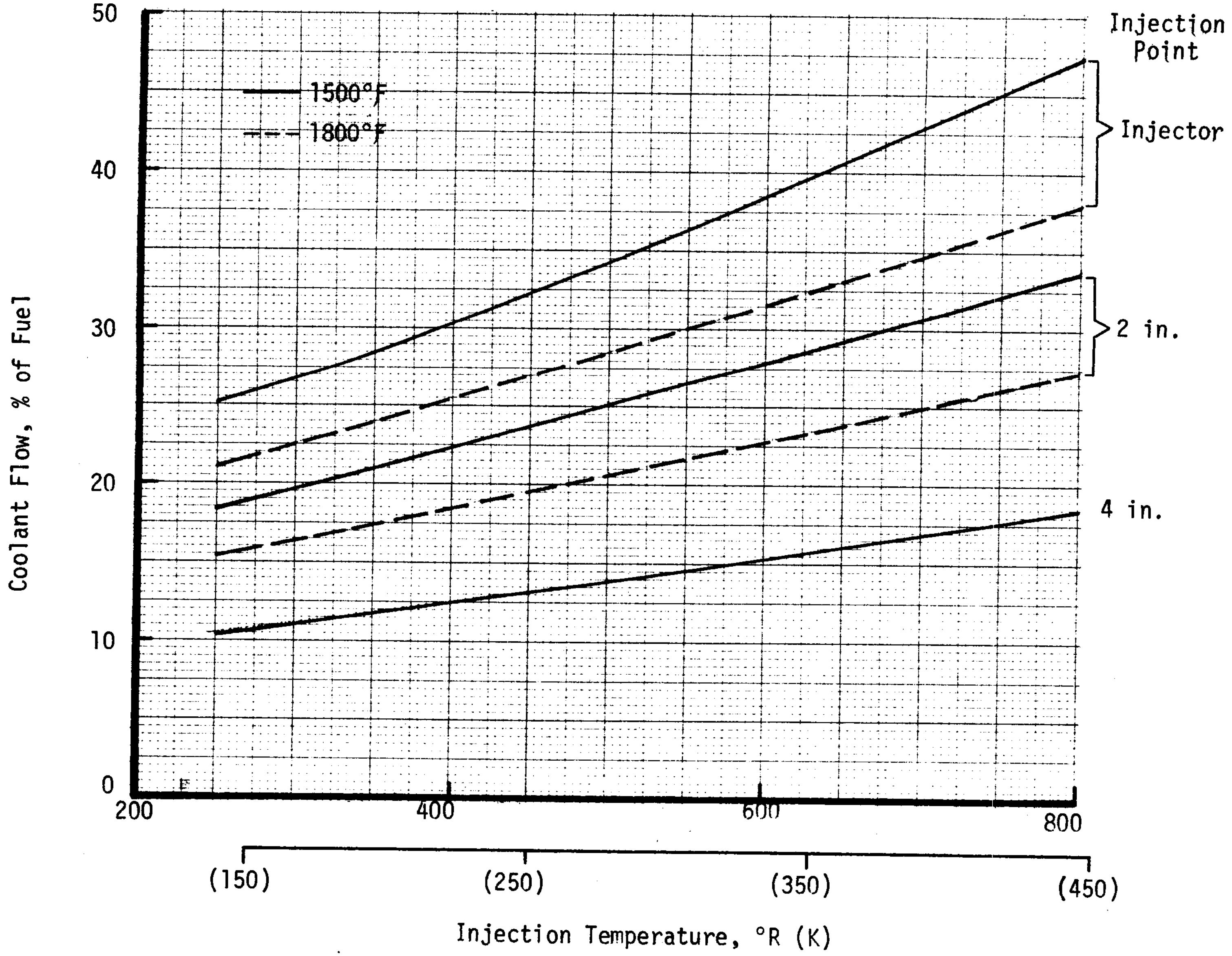

Figure 85. Adiabatic Wall Coolant Requirements - Throat Temperature Limit

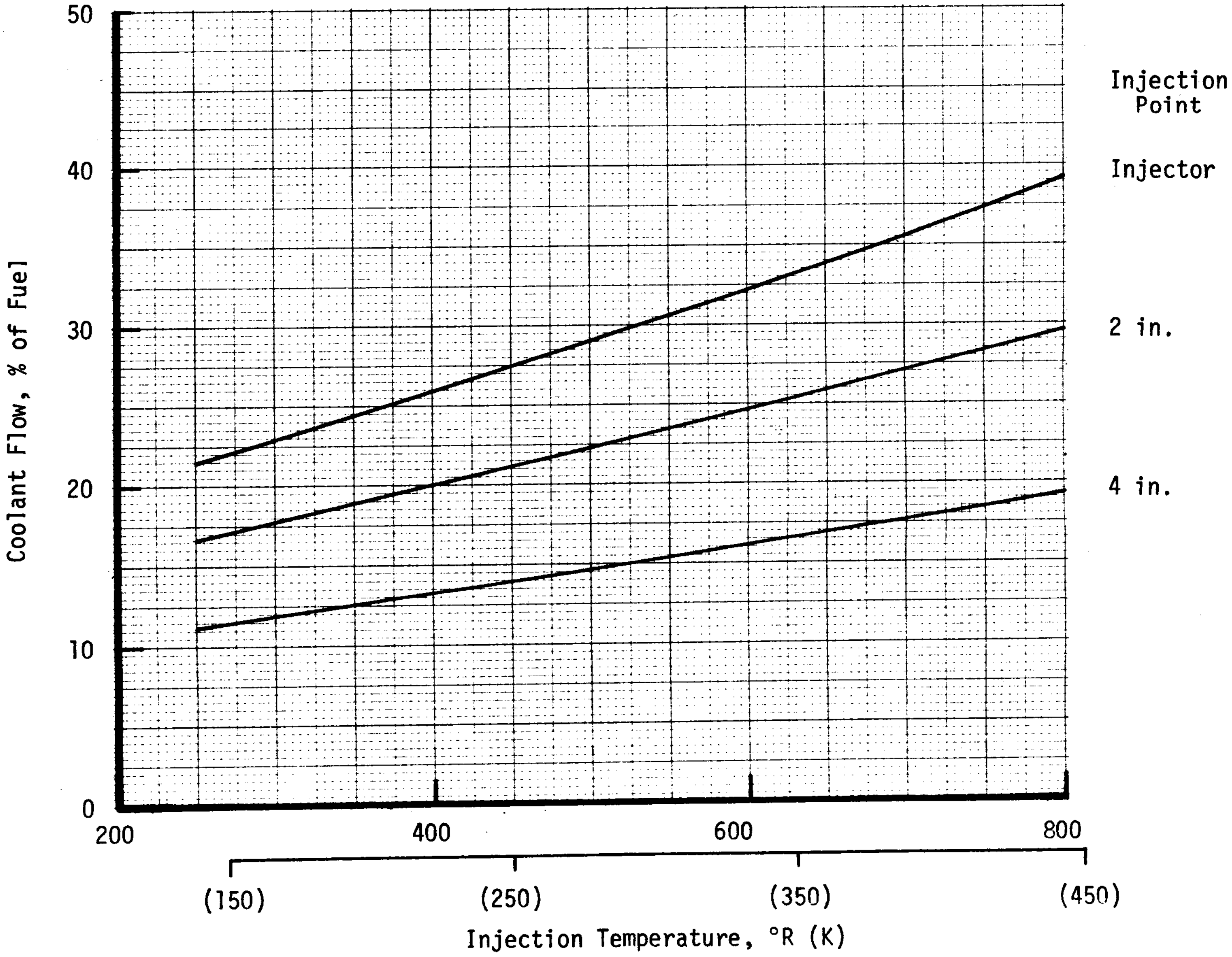

Figure 86. Adiabatic Wall Coolant Requirements - 1800°F Maximum Temperature

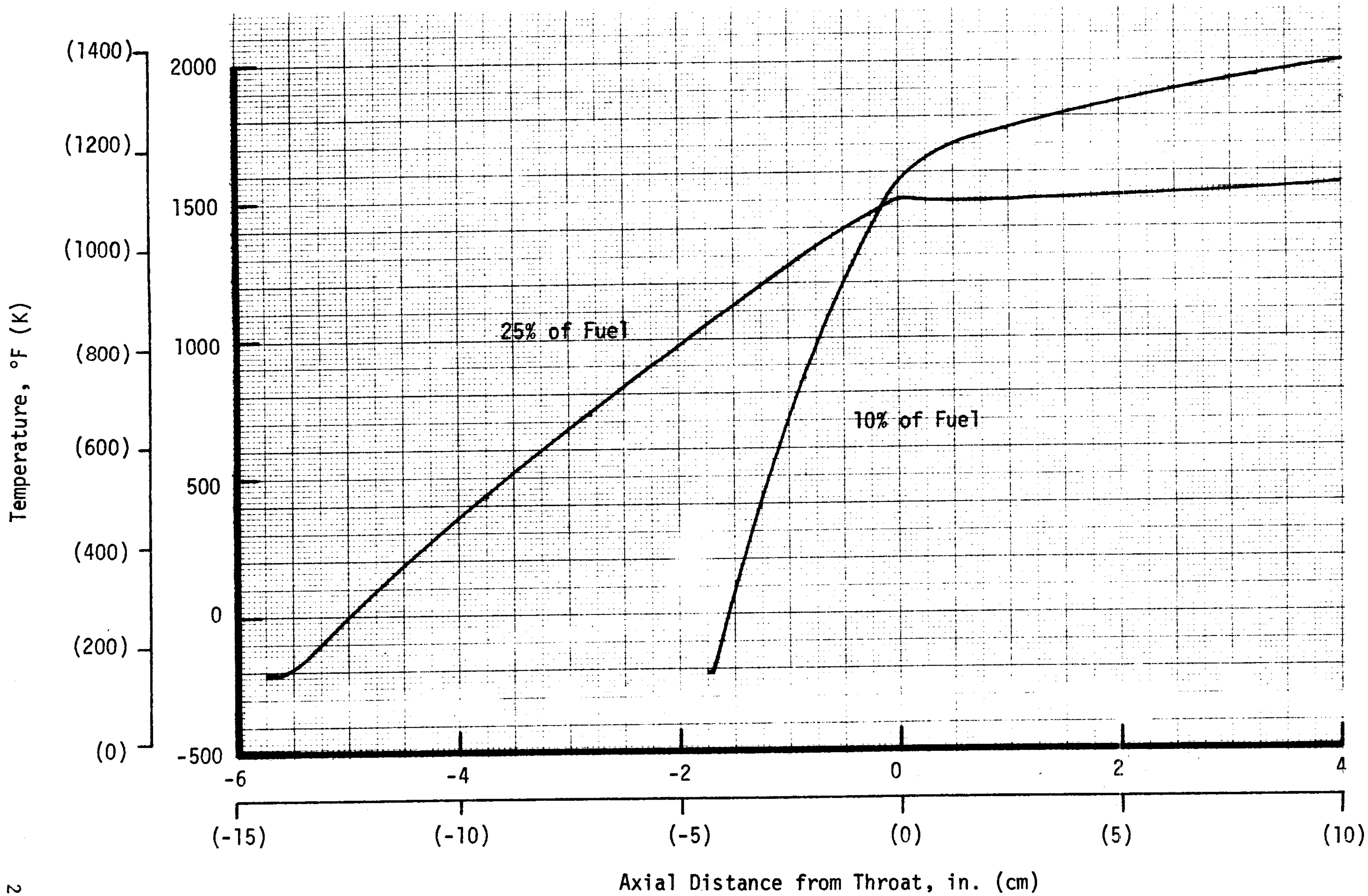

Figure 87. Adiabatic Wall Temperature Axial Variation

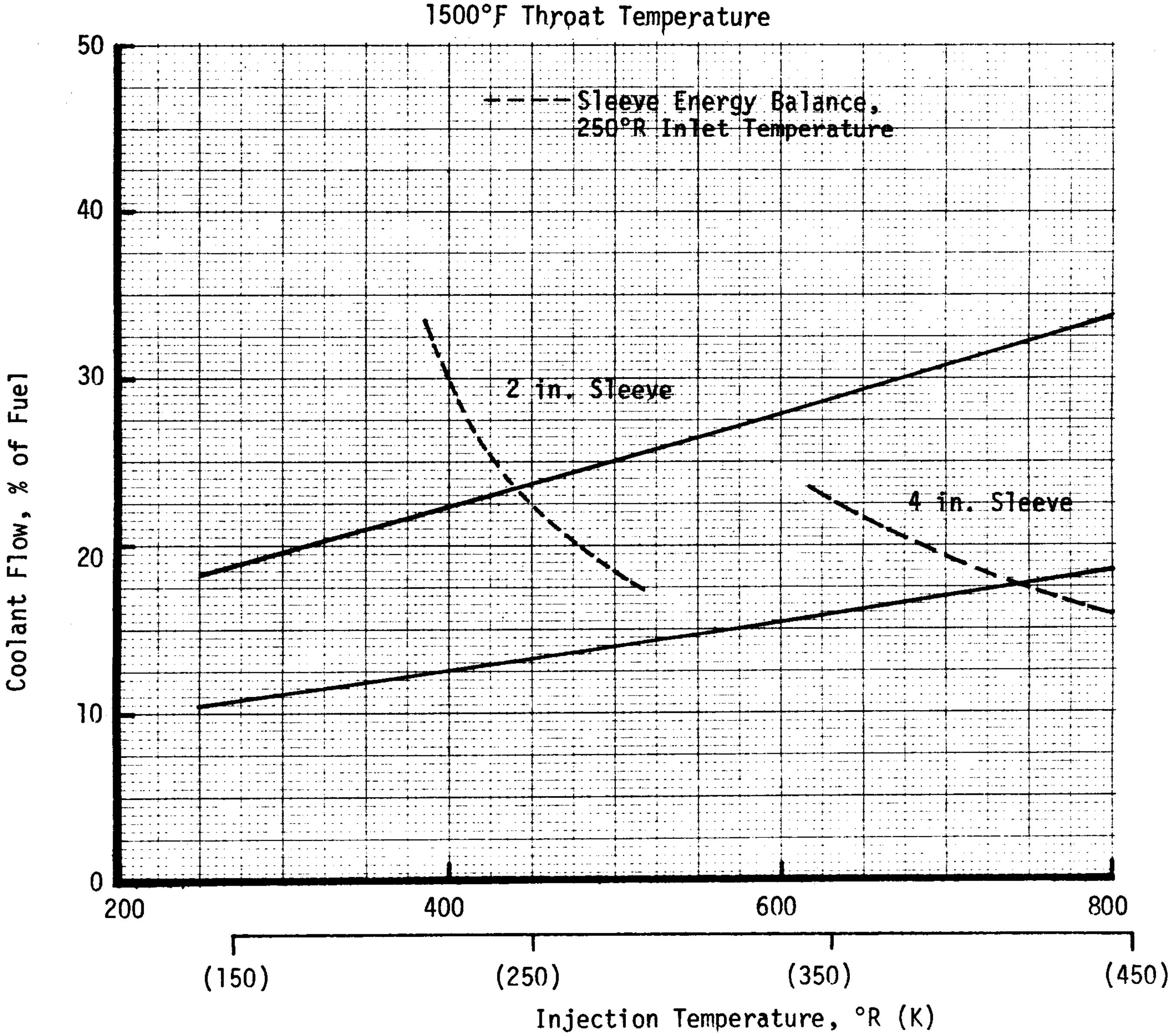

Figure 88. Adiabatic Wall Coolant Requirements With a Sleeve

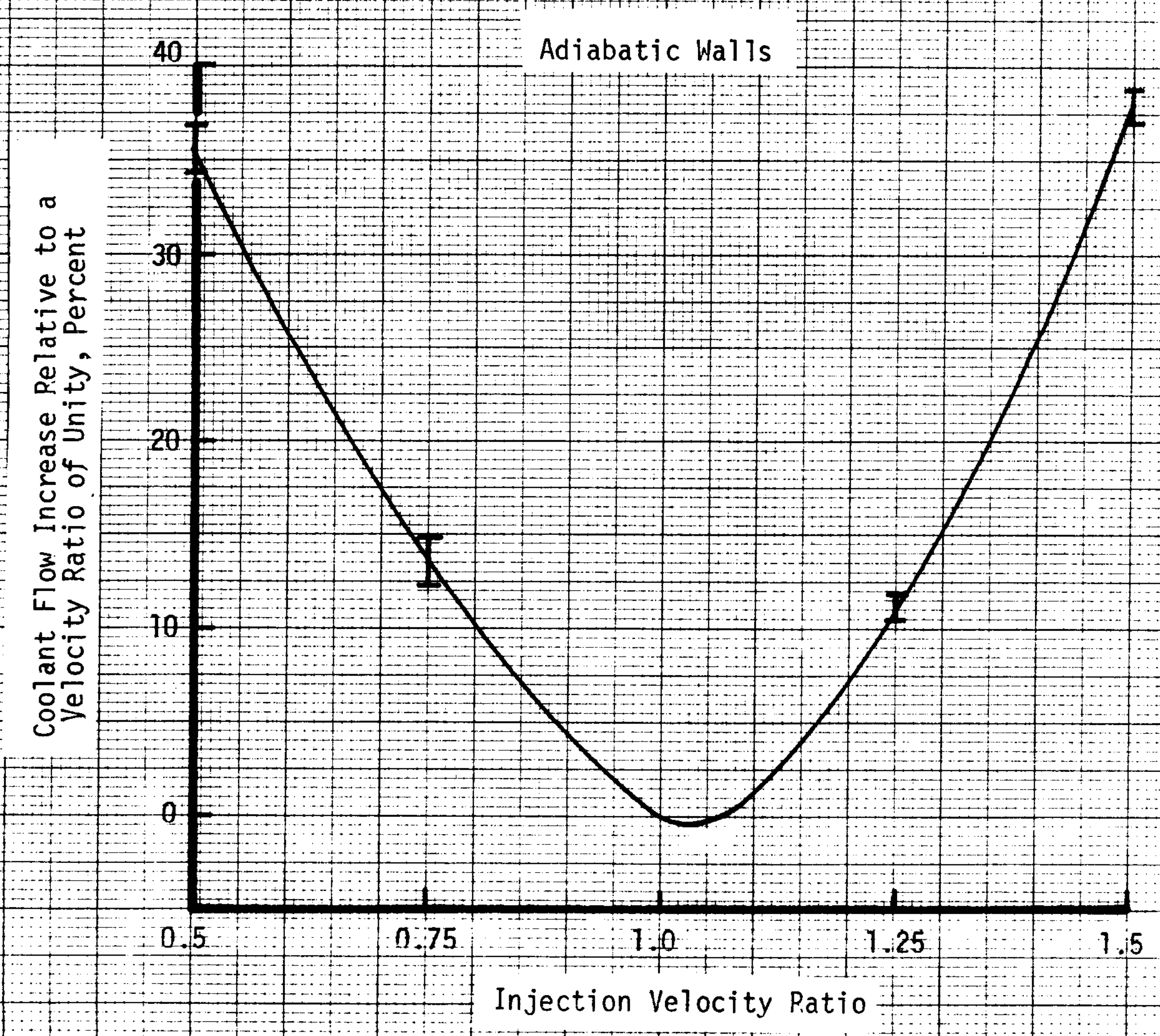

Figure 89. Effect of Velocity Ratio on Coolant Flow Requirements

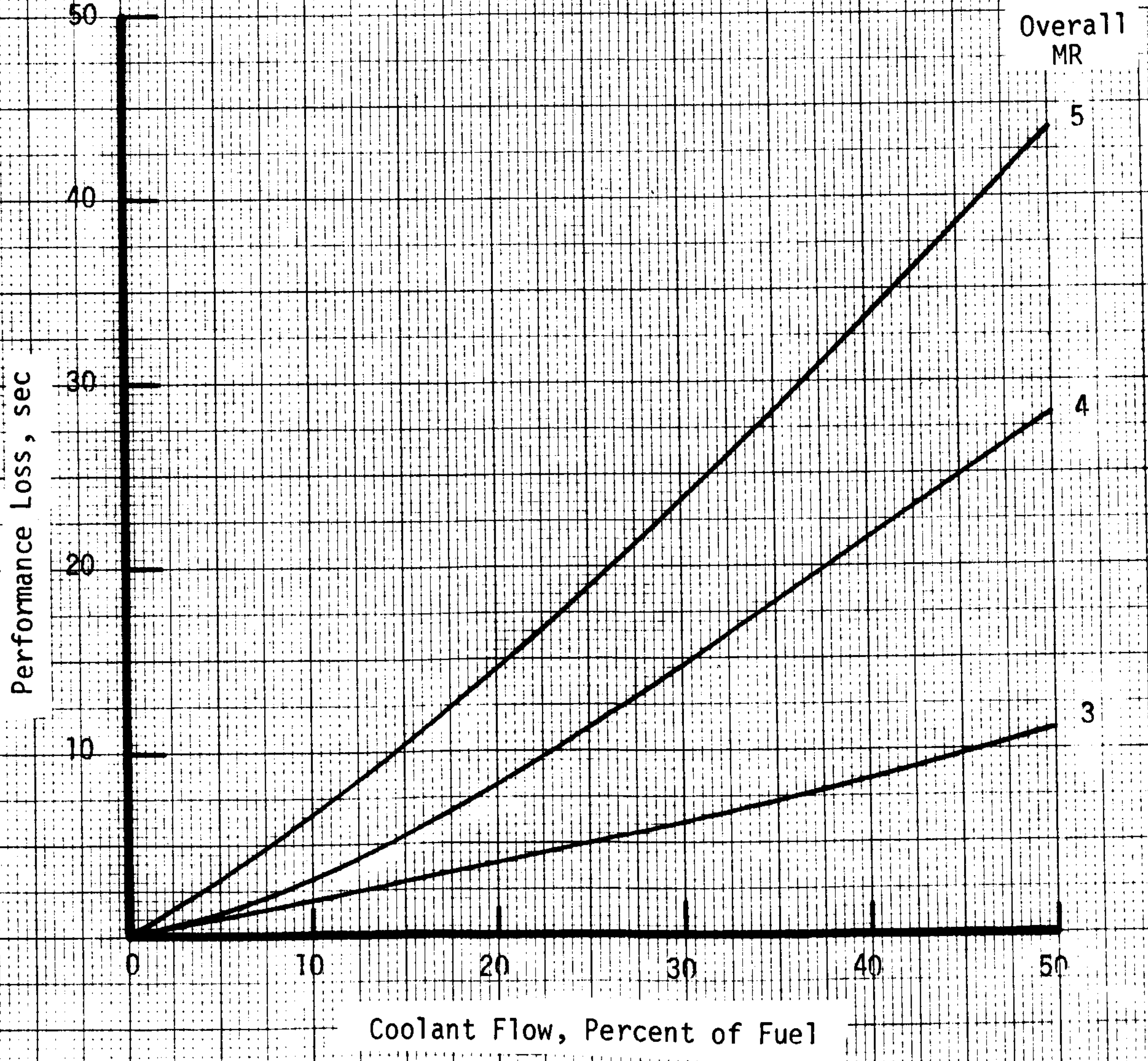

Figure 90. Performance Loss due to Film Cooling

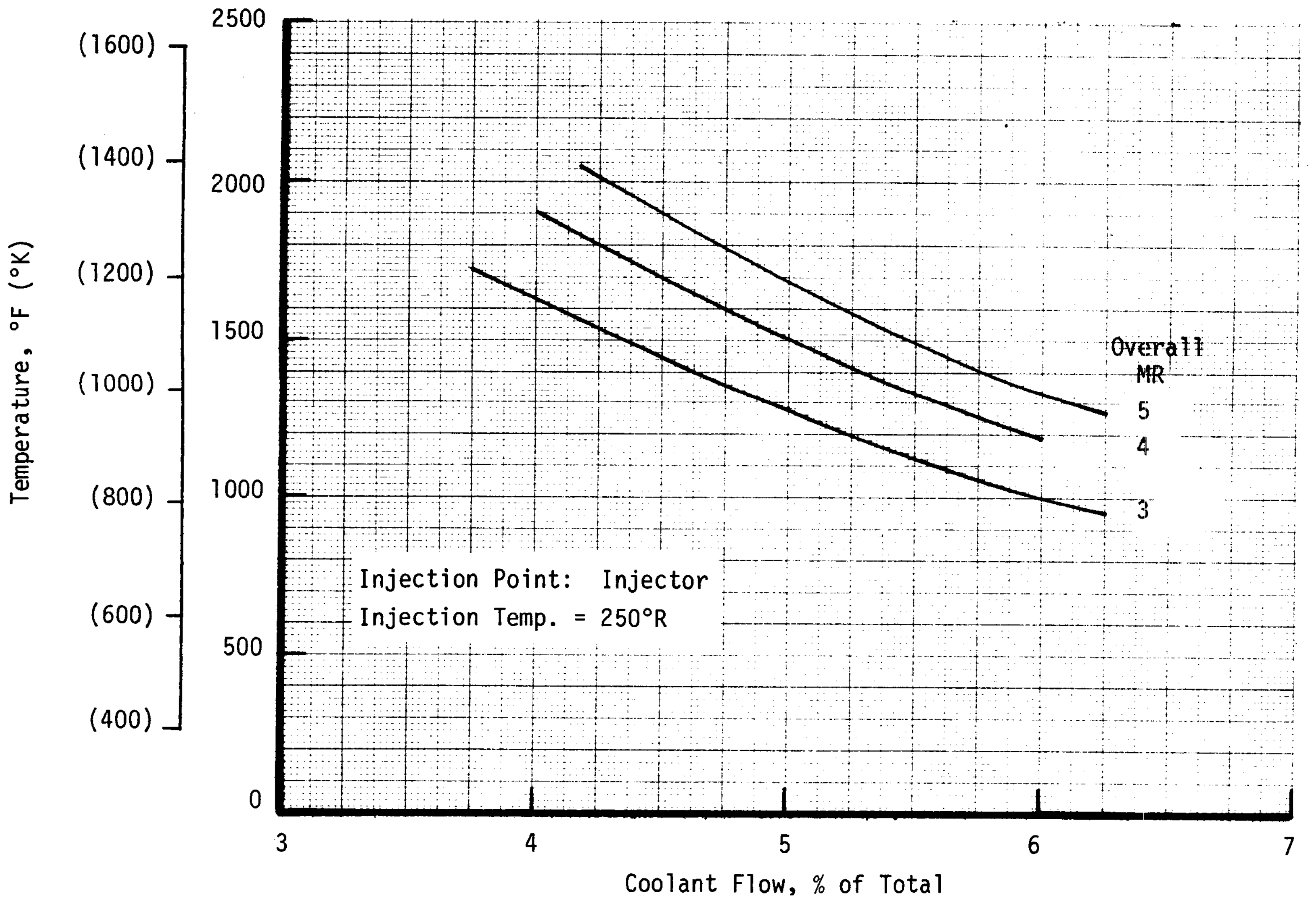

Figure 91. Adiabatic Wall Throat Temperature Variation with Coolant Flow

a. Coolant Flow

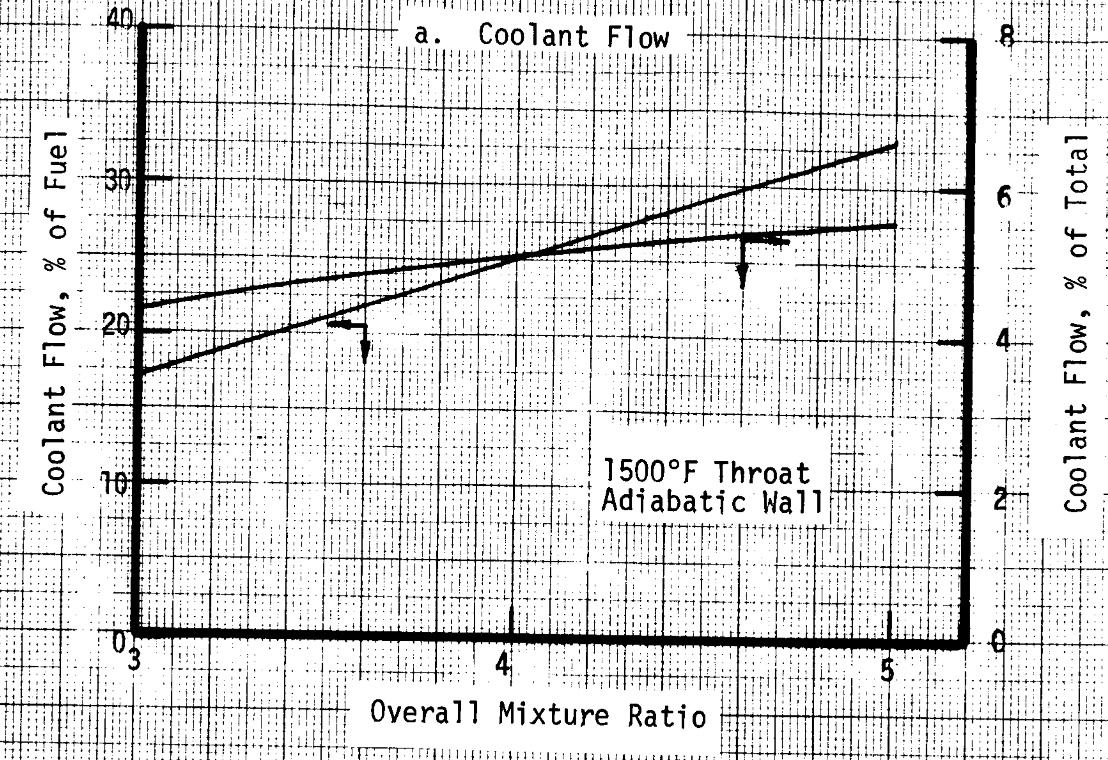

b. Resultant Performance

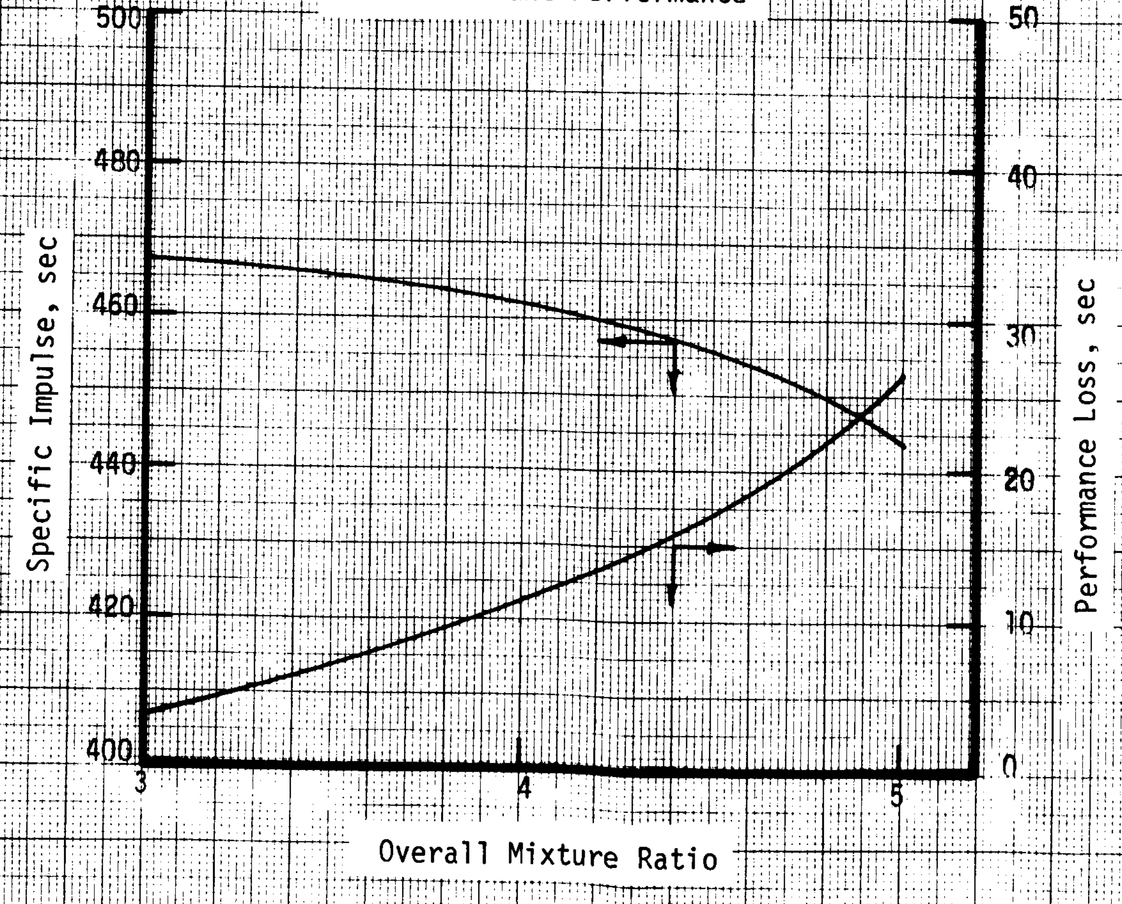

Figure 92. Effect of Overall Mixture Ratio on Coolant Flow and Performance

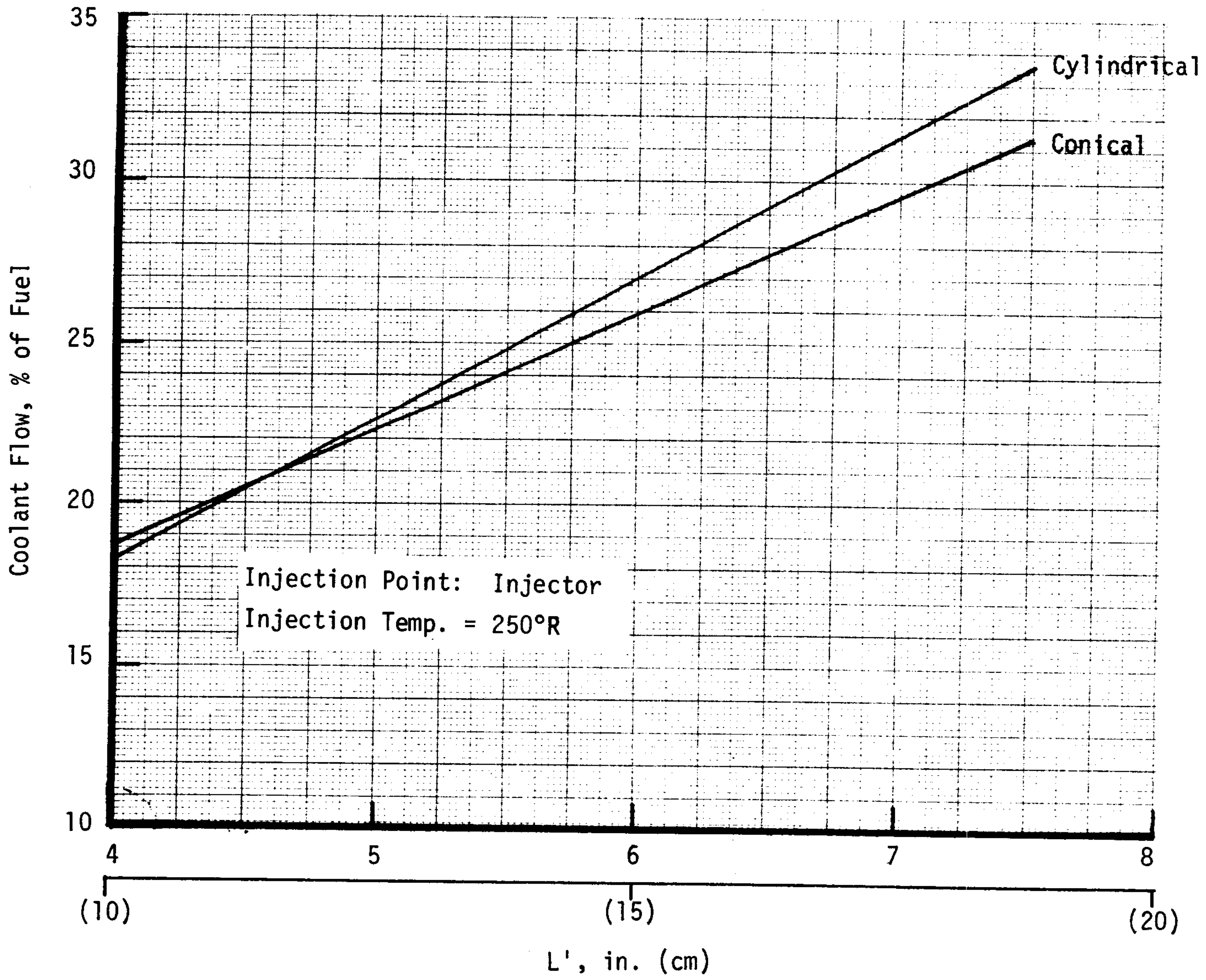

Figure 93. Adiabatic Wall Coolant Requirement Variation with Combustion Chamber Length

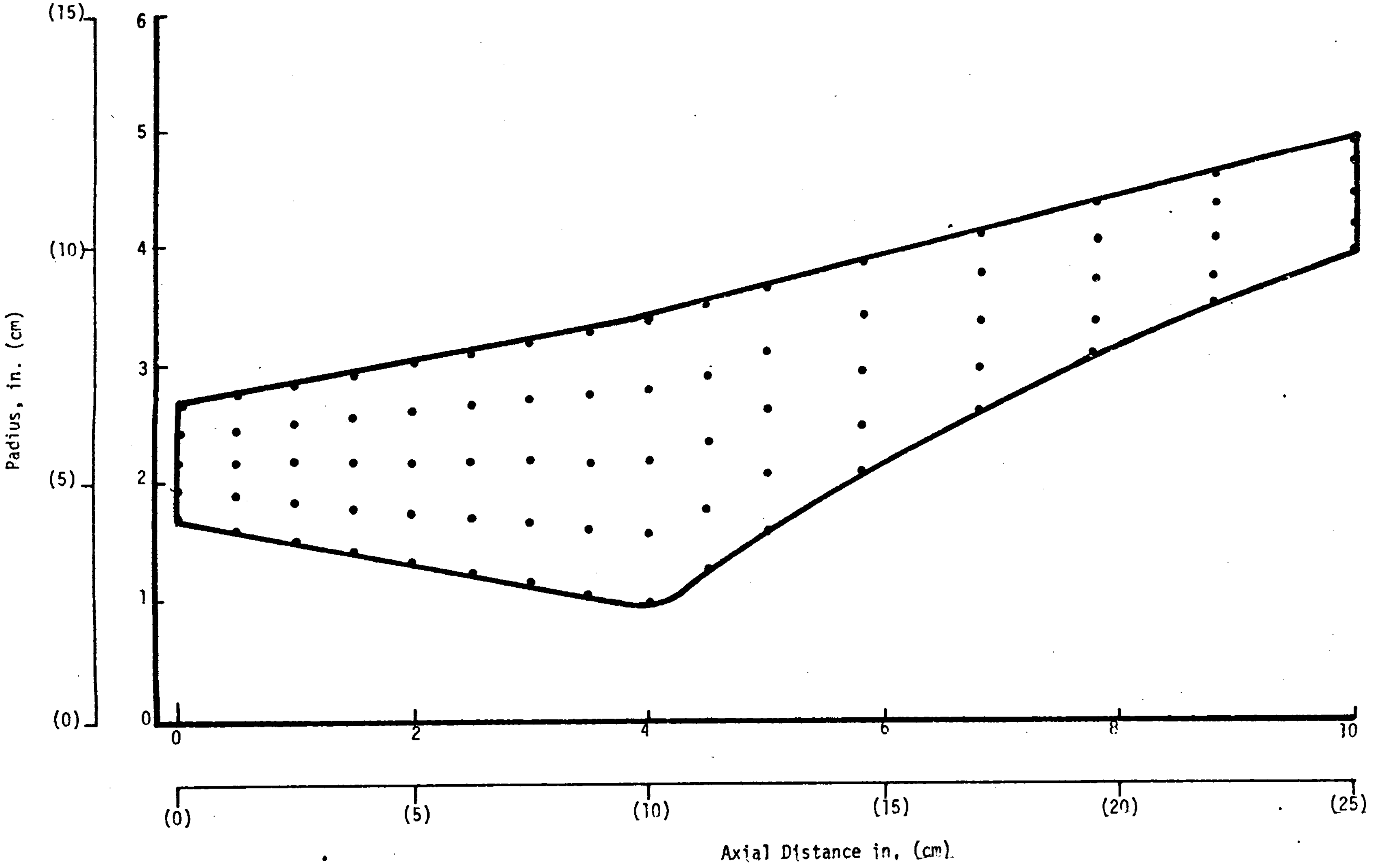

Figure 94. Internal Regenerative Cooling Node Network

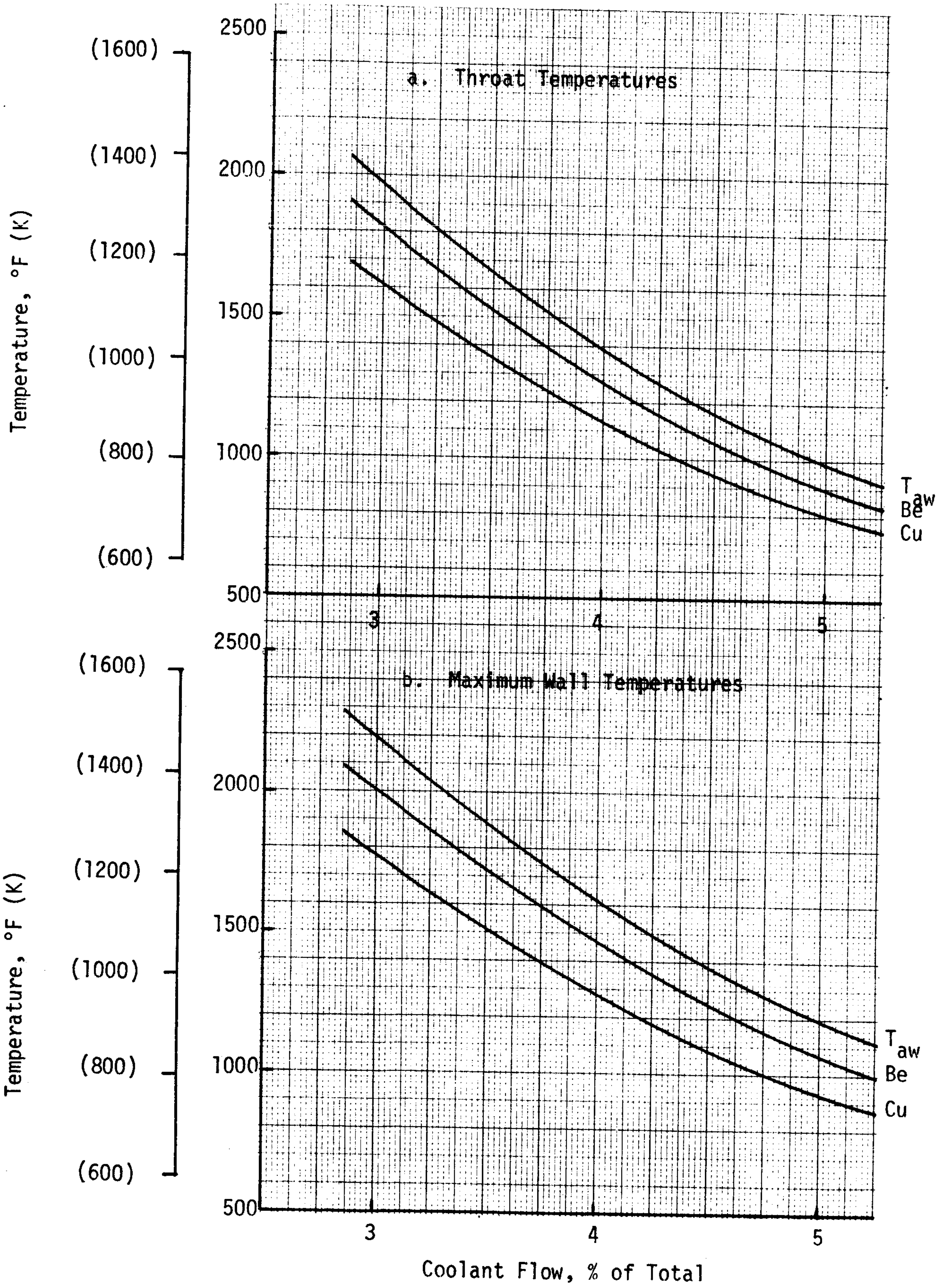

Figure 95. Comparison of Beryllium and Copper Chambers

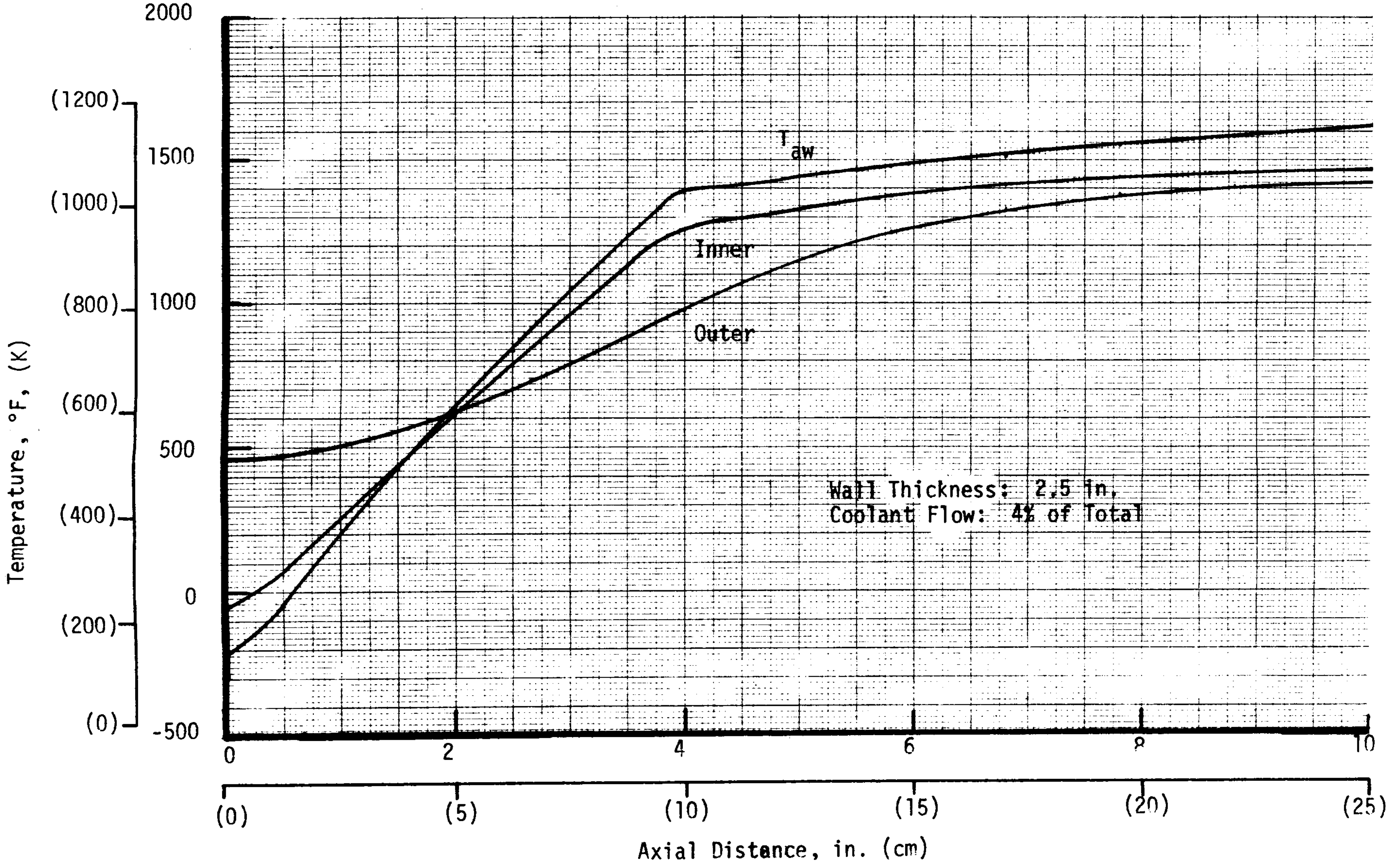

Figure 96. Beryllium Chamber Axial Temperature Variation

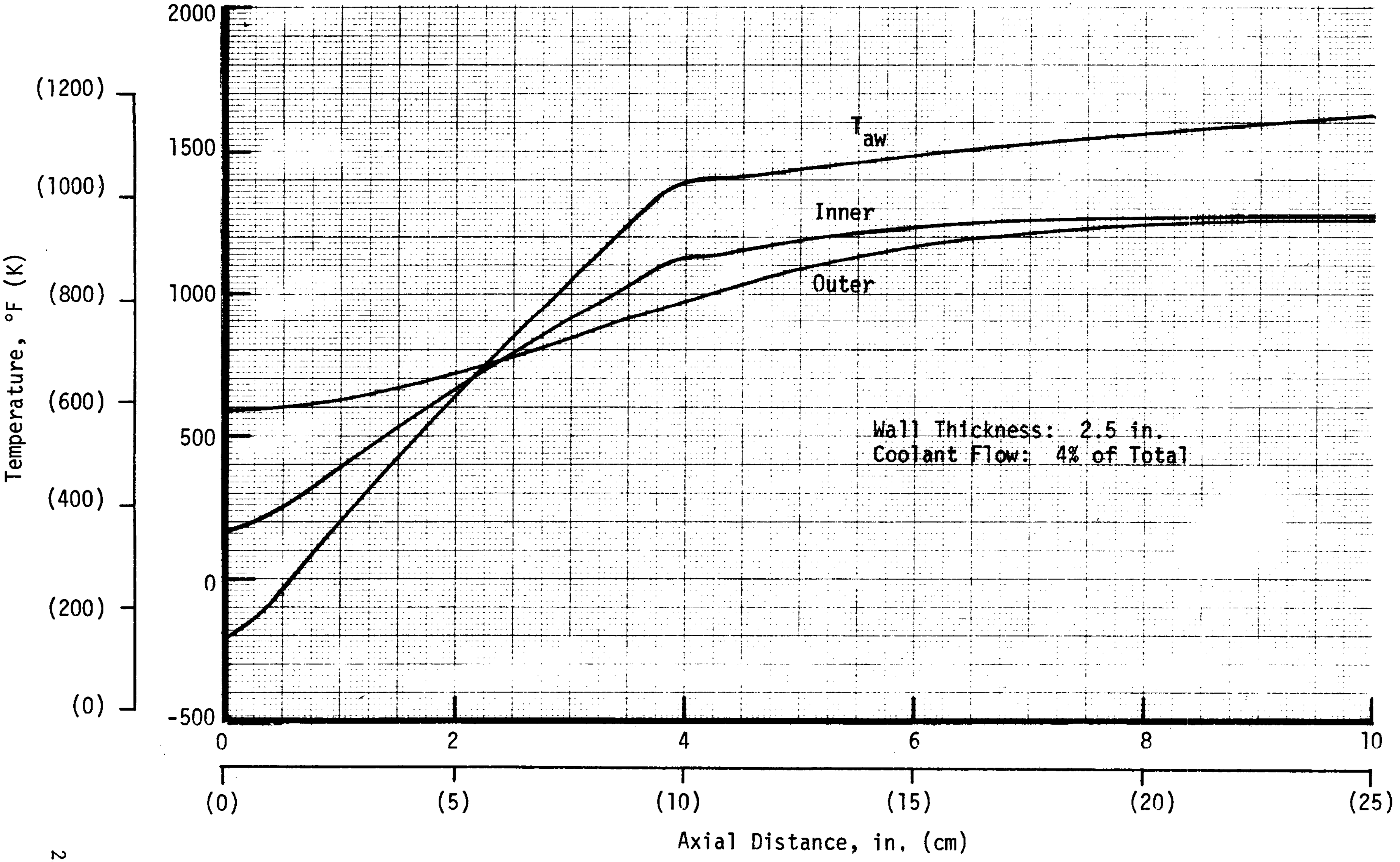

Figure 97. Copper Chamber Axial Temperature Variation

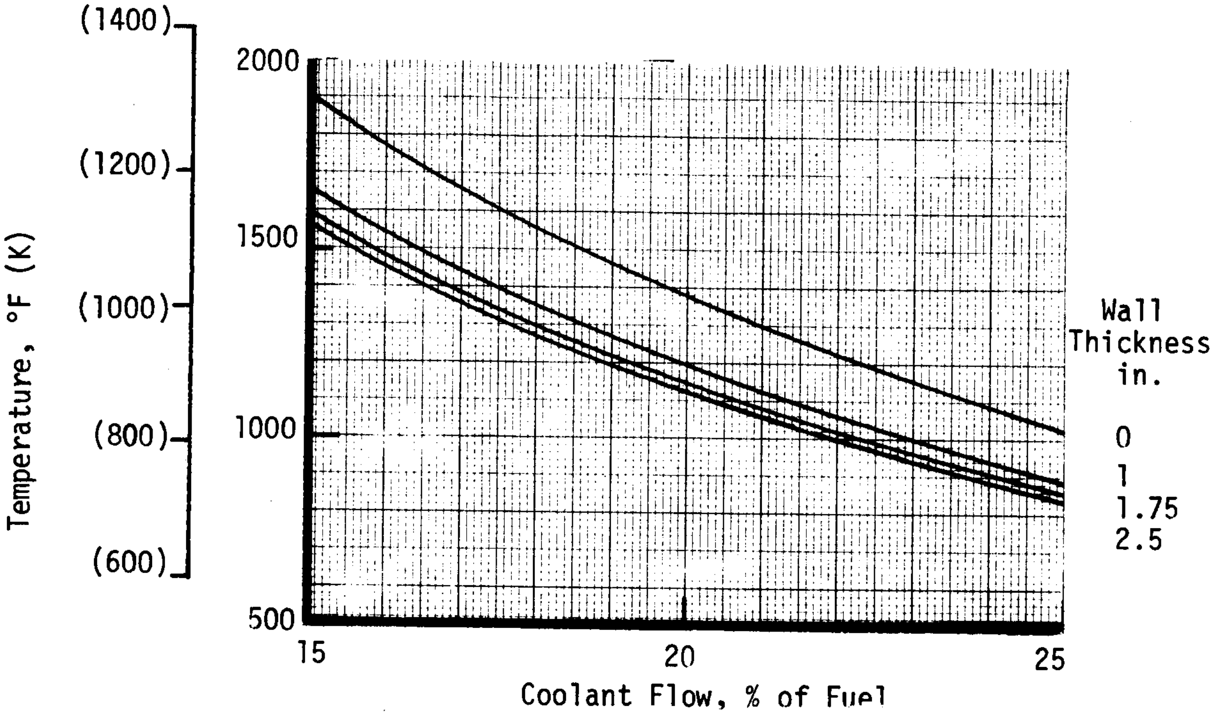

a. Throat Temperature

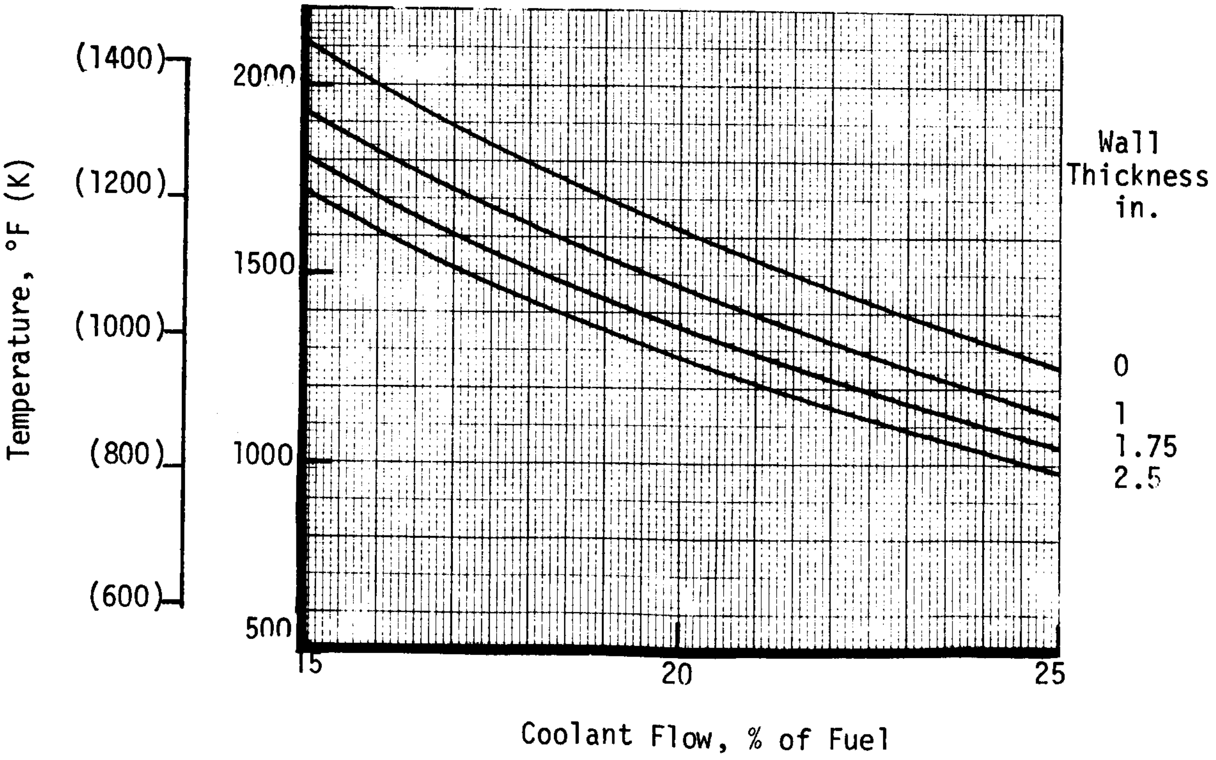

b. Maximum Temperature

Figure 98. Effect of Wall Thickness on Copper Chambers

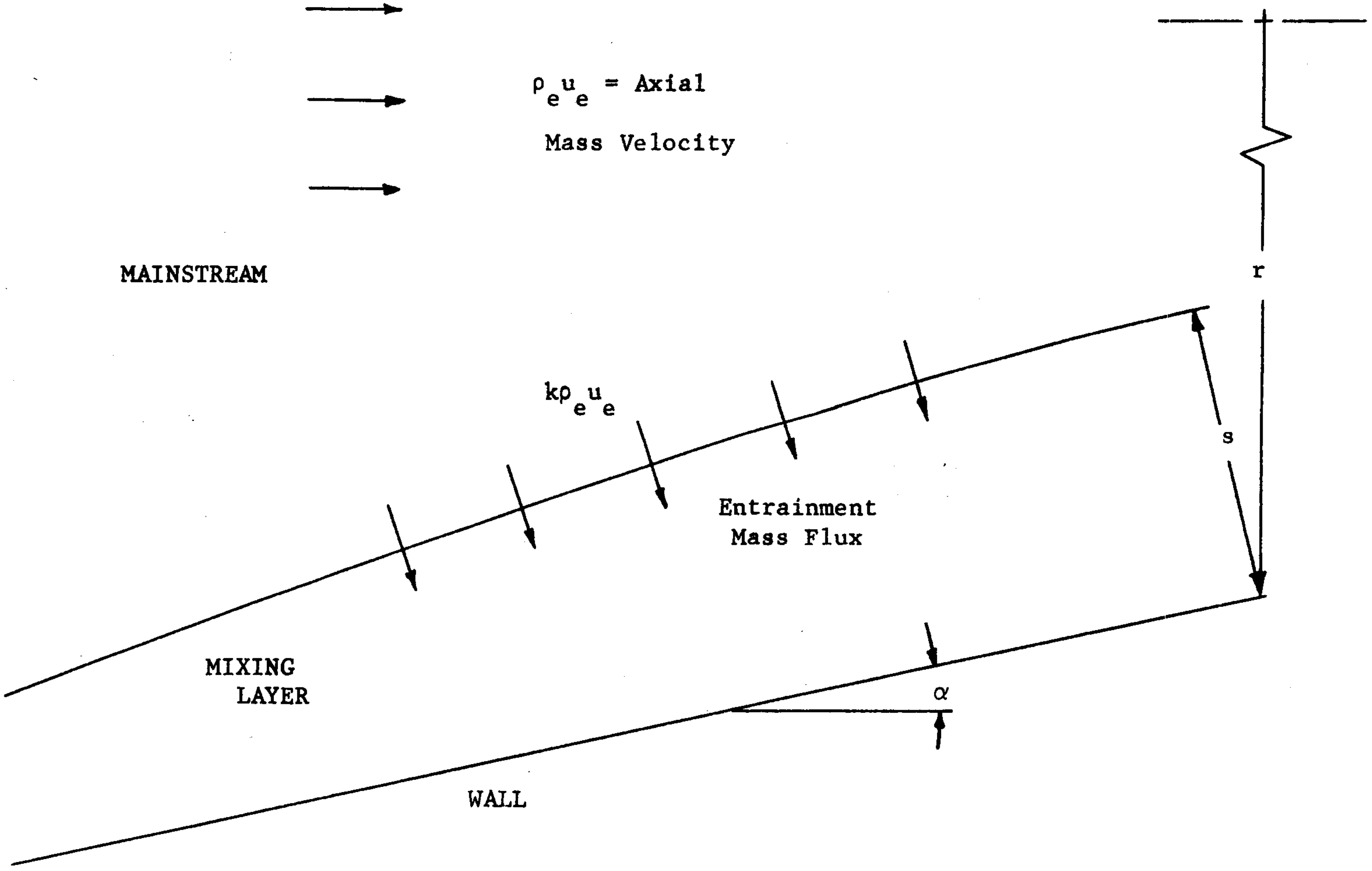

Figure 99. Entrainment Model Schematic

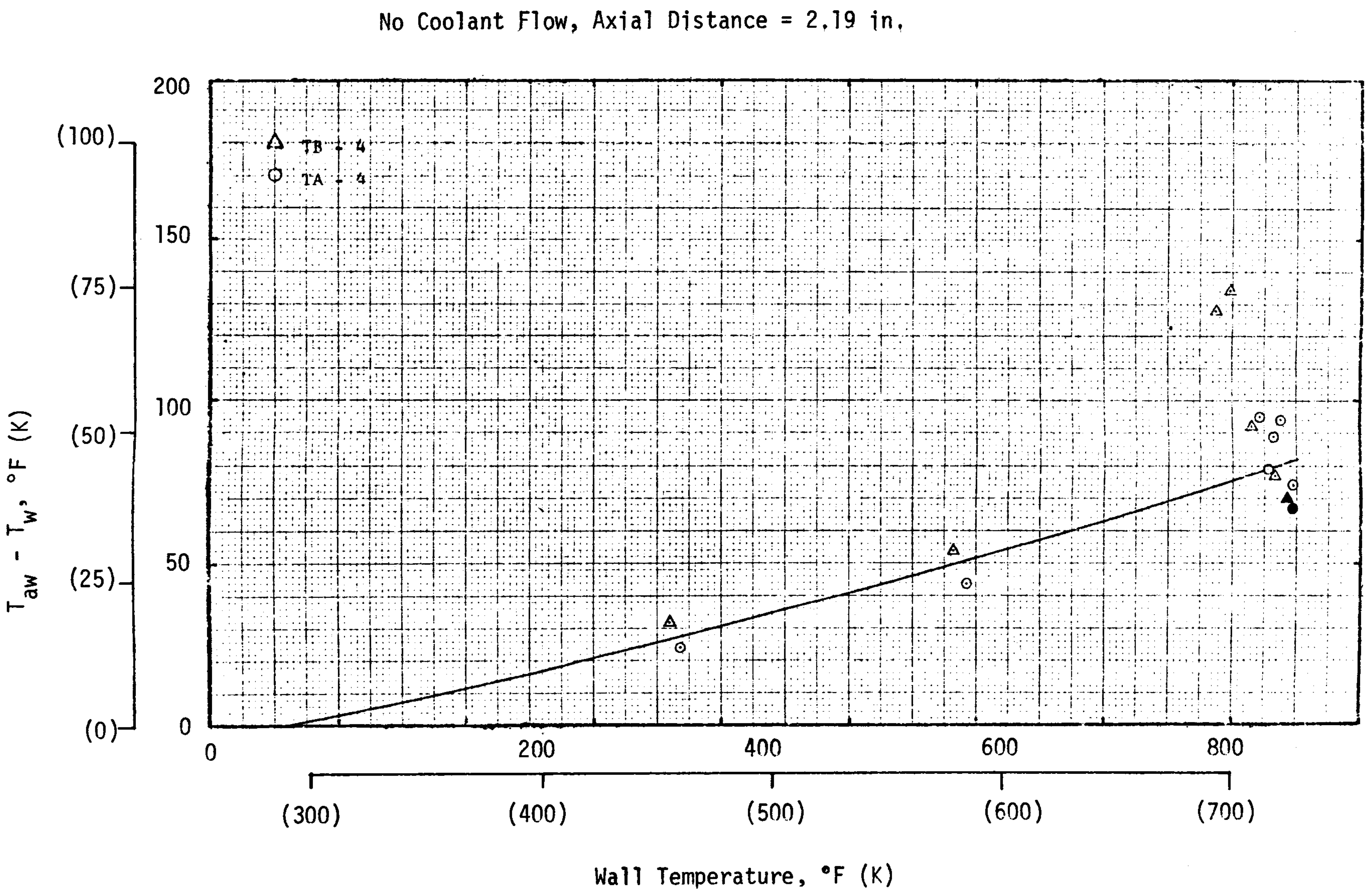

No Coolant Flow, Axial Distance = 2.19 in.

Figure 100. Wall Temperature Reduction due to Heat Loss

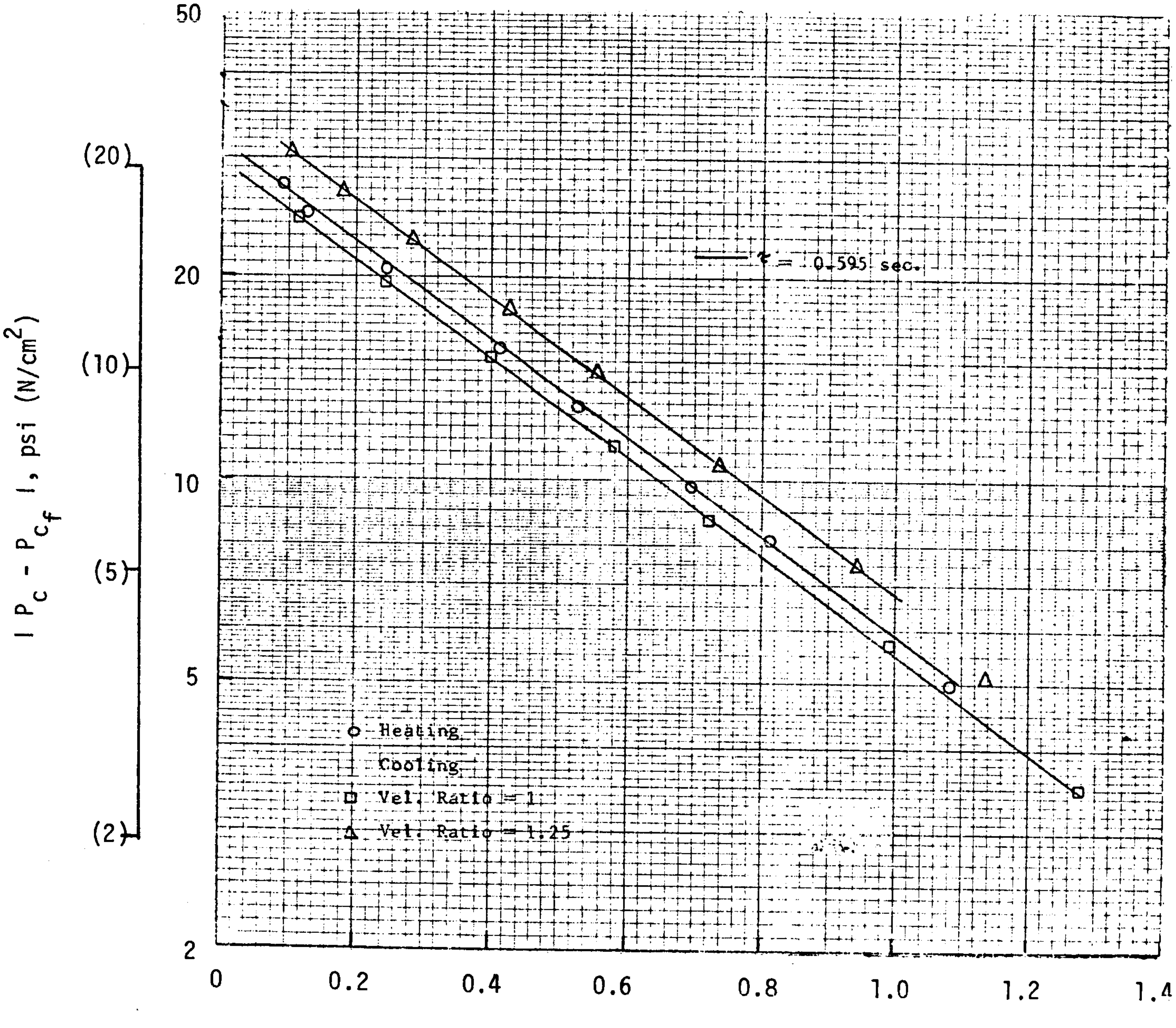

Figure 101. Determination of Chamber Pressure Time Constant

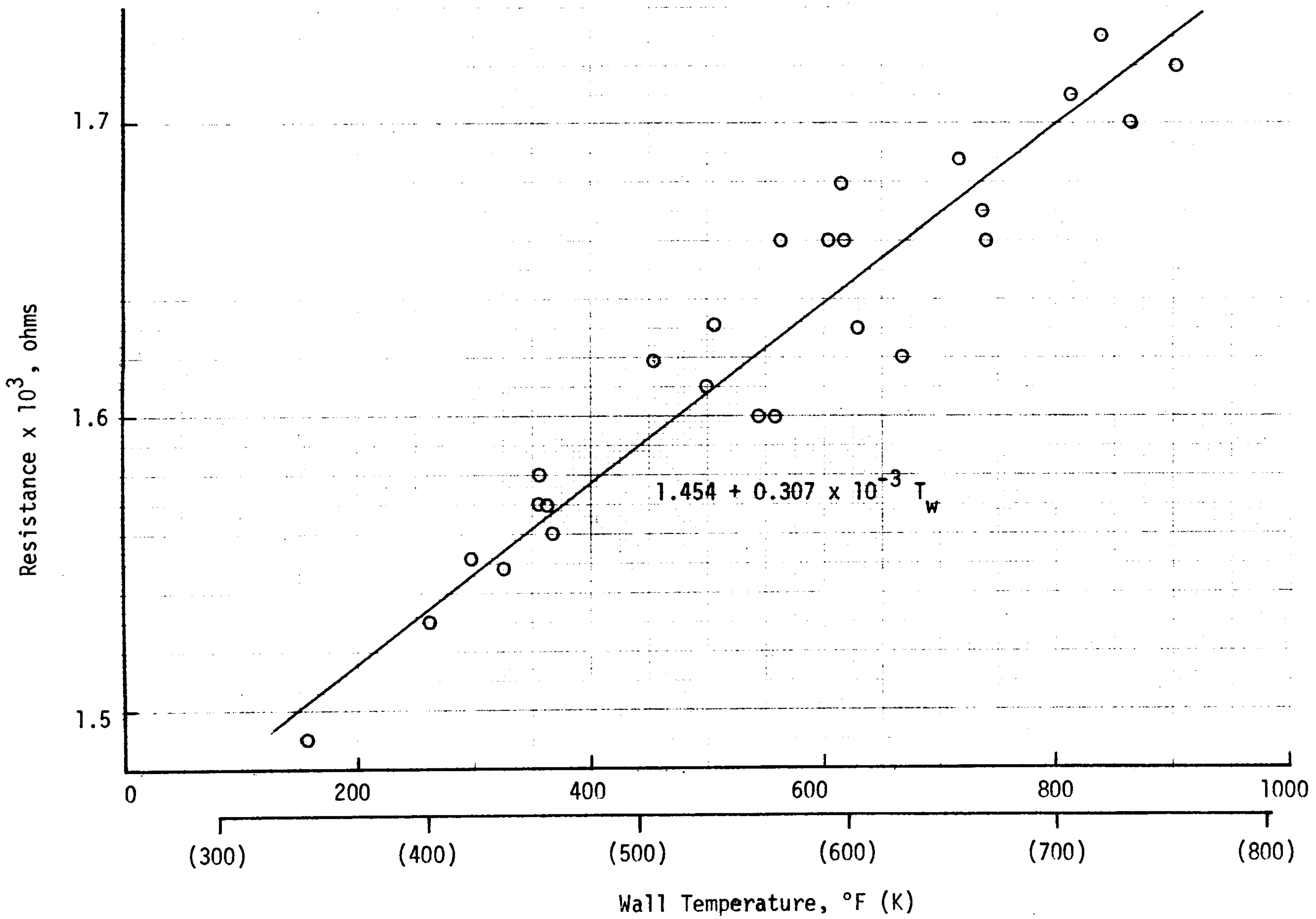

Figure 102. Test Section Electrical Resistance - High Temperature Range

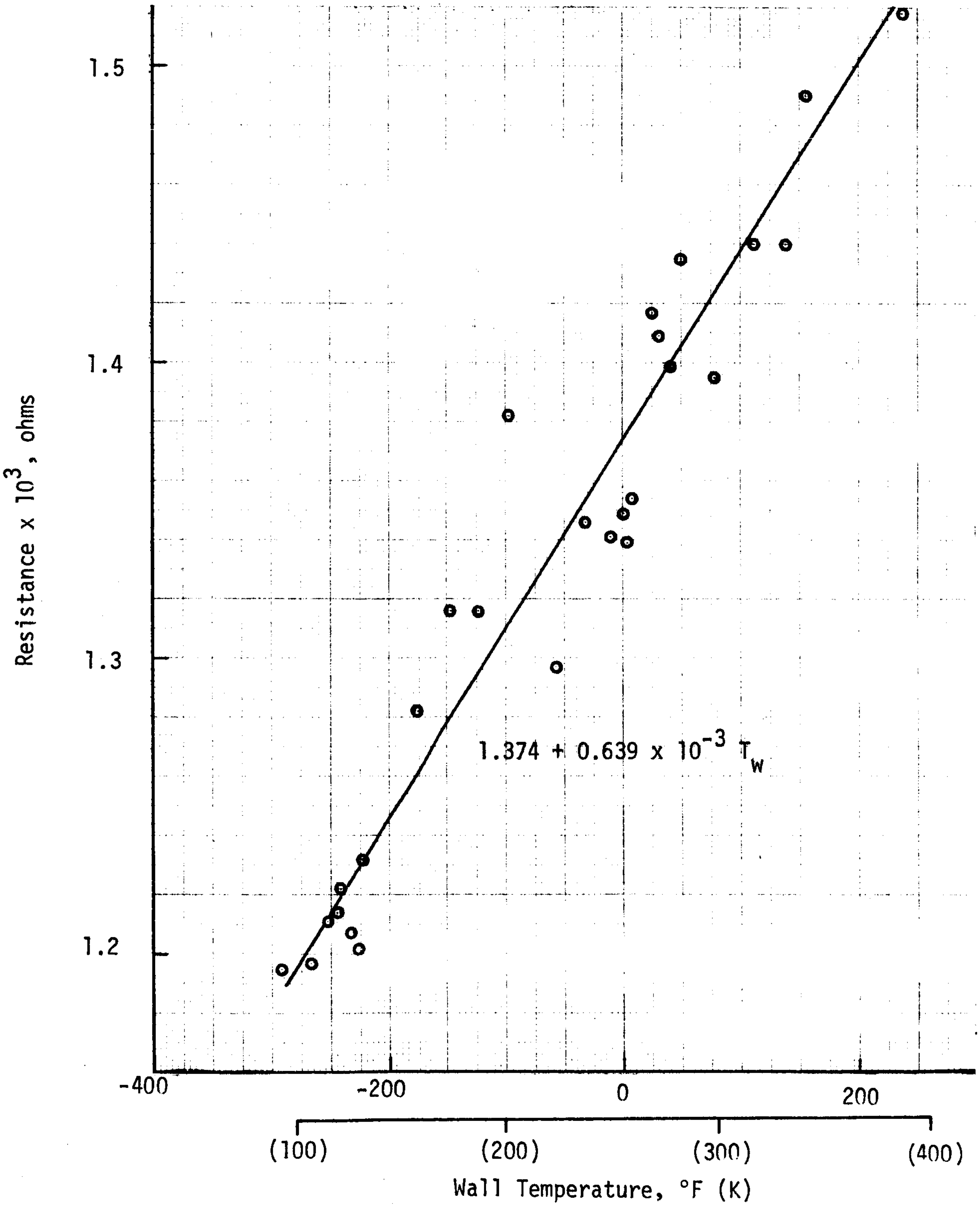

Figure 103. Test Section Electrical Resistance - Low Temperature Range

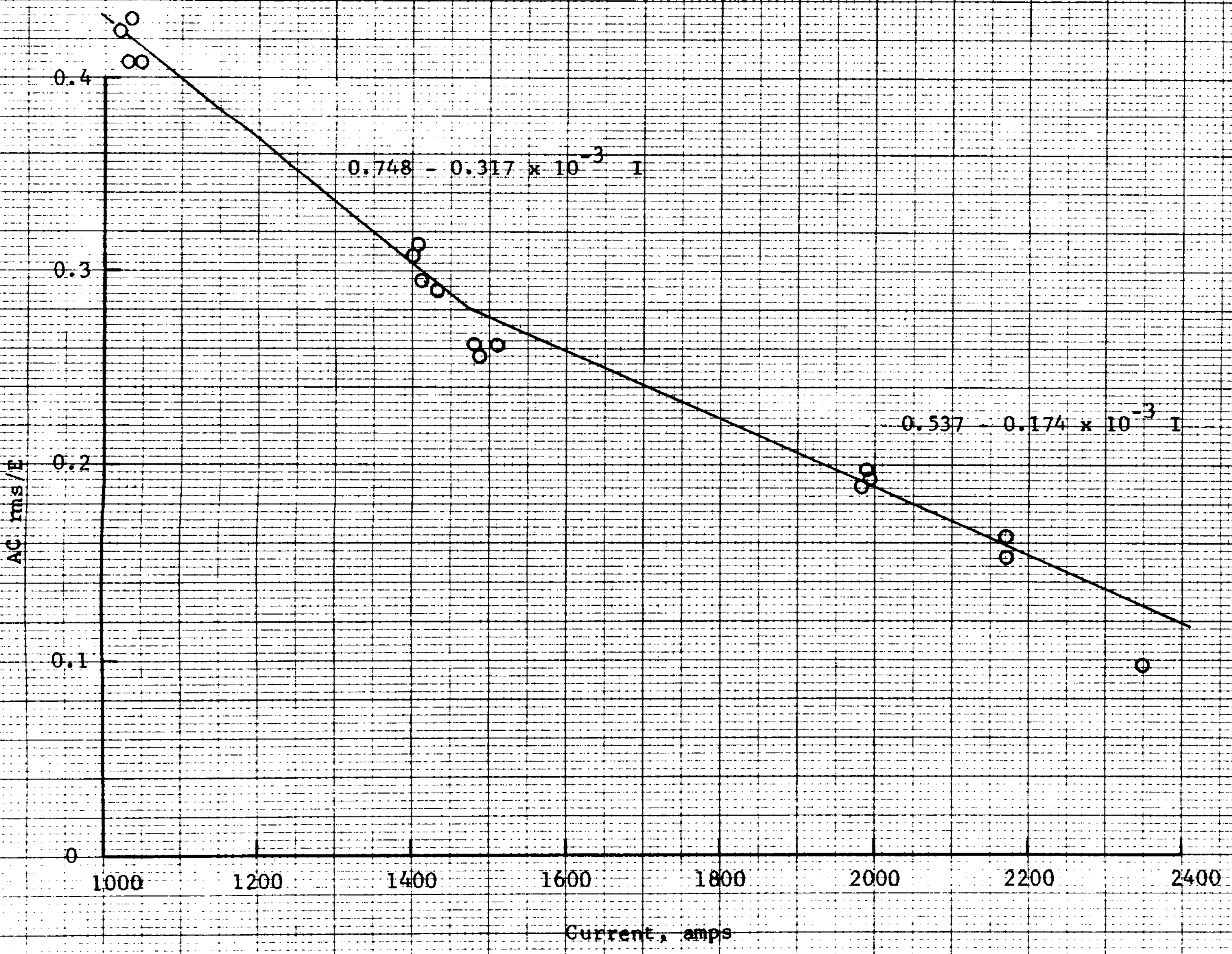

Figure 104. Correlation of the Relative AC RMS Voltage